

Anodic Treatments in an Ionic Liquid
for the Corrosion Protection of
Magnesium Alloy AZ31

by

Julie-Anne Latham

BEng (Hons. I)

ERRATA

p2-9 point 4: “magnesium is significantly easier to machine than aluminium” for “magnesium is significantly easier to machine than magnesium”

p2-25 para 2 line 8: “tetrafluoroborate” for “tetrafluorobotata”

ADDENDUM

The following points should be added in response to the examiners’ questions.

p4-45 to p4-46. Please note on page 4-45 and 4-46 the quantitative discussion around table 4.1 should be disregarded. As pointed out by the examiner, the assumption for this analysis was made on a quasi-reversible system, which is not correct. This discussion does not have any impact on the conclusions of this work.

p4-69: The following should also be added after the last paragraph:

“Alternatively, the behaviour observed may also be due to the breakdown of the amorphous film due to the build-up of internal stresses from thickening. Localised breakdown points in the film will act as lower resistance pathways for current flow and as a result localised heating of these areas will occur. The localised heating will then cause crystallisation of the surrounding amorphous film. The localised cracking of the film will also allow for corrosion of the underlying substrate through reaction with residual water in the IL. However, breakdown of the film in this manner is expected to be accompanied by heterogeneous areas of high reactivity. That is, localised pockets of crystallised film or corroded substrate. The appearance of the specimen in Figure 4.25 is highly heterogeneous, which is consistent with this behaviour but as the surface was exposed to the 3 V potential for an extended period of time, this breakdown may have occurred after the initial crystallisation process. On the other hand, Figure 4.26 shows the surface appearance of the film after shorter exposure (without erratic current behaviour). Whilst the entire exposed surface has not been reacted, there are no localised pockets that suggest points where the film has broken down (see section 4.2.3.3 for this morphology). Instead, the surface has reacted in a relatively uniform manner, which is not consistent with localised breakdown or corrosion. It is also observed in section 4.2.1.2.2 that highly uniform and dense films are formed, which are also not consistent with localised breakdown and corrosion of the surface.”

p4-103: After Figure 4.54

The table presents the corrosion potential and corrosion current density, obtained through Tafel extrapolation, of the potentiodynamic polarisation curves presented in Figure 4.51 to Figure 4.54. This table is added by request from an examiner.

Treatment	E_{corr} (mV)	i_{corr} (μAcm^{-2})
Control	-1557 ± 10	3.6 ± 1.1
0.05 mAcM^{-2} ; 18 V 15 min	-1561 ± 44	2.9 ± 0.2
0.05 mAcM^{-2} ; 18 V 30 min	-1553 ± 20	3.76 ± 0.03
0.05 mAcM^{-2} ; 18 V 60 min	-1577 ± 51	5 ± 3
0.05 mAcM^{-2}	-930 ± 590	4.8 ± 1.3
0.1 mAcM^{-2}	-1586 ± 19	5.6 ± 1.6

0.5 mAcm ⁻²	-1567	3.6
ILAN 0.05 mAcm ⁻²	-1522	2.4
ILAN 0.5 mAcm ⁻²	-1556	2.9
ILAN 1 mAcm ⁻²	-1582 ± 26	3.5 ± 0.5
ILAN 2 mAcm ⁻²	-1590	3.7
ILAN 3 mAcm ⁻²	-1579	3.1
ILAN 5 mAcm ⁻²	-1535	2.5
ILAN 10 mAcm ⁻²	-1563	3.2
0 V 3 hrs	-1551 ± 17	2.5 ± 1.1
0 V 6 hrs	-1580	5.2
1 V 1 hrs	-1507 ± 23	3.0 ± 1.1
1 V 3 hrs	-1552 ± 12	3.3 ± 1.6
1 V 6 hrs	-1569	3.6

Reviewer Questions and Answers

General Questions

1. How does the latent corrosion resistance of the coatings produced by IL anodization in this study compare with other common surface treatments used for Mg alloys such as spark anodization and conversion coatings?

The improvement factor of the IL coating in this work was approximately 3.3 (after pickling at 0.1 mAcm⁻²). In comparison, other conversion coatings can improve by 10 times (rare earth), 50 times (NTf₂ anion containing IL), up to a couple orders of magnitude (chromate). Standard anodising usually increases the corrosion resistance by approximately 30 times (HAE, DOW 17); while plasma (spark) anodising can increase the corrosion resistance by a couple orders of magnitude. Therefore, while the corrosion resistance was improved over the 'as-polished' AZ31 surface, currently the corrosion improvement is not as significant as other techniques.

2. Are there any other reasons besides prior local history with this IL, to indicate that it would be particularly well suited as a medium for the treatment of Mg alloys?

The process to produce this IL is similar to the processes used in the phosphine industry, which means that if tonnage levels of the IL were needed, this could be readily available at a cost effective price compared with other ILs.

Specific Questions

1. Page 3-40. On this page a discussion of the origins of inductance in EIS measurements is given with a focus on inductive response measured on corroding Mg alloys. Several interpretations are given. Is it important to indicate which of these interpretations was used in this study to understand the inductive responses observed? Is there anything to be learned about the surface films formed by IL treatment from a rigorous analysis of inductance? How inductance is analysed, if it is analysed should be stated here and in the relevant sections of the document that follow this page.

In this research inductive behaviour in EIS has been interpreted as caused by localised breakdown of the surface film and subsequent corrosion of the AZ31 substrate (as suggested in

the literature). This surface film may be either the natural hydroxide/oxide film or a film formed through treatment in an IL solution. No further analysis of the inductance was undertaken.

2. Page 4-44, 45. *On these pages there is a discussion of the effect of residual water in the cyclic voltammetry response. It seems that it would have been possible to add known amounts of water to the IL in a systematic manner and then measure the CV response. This may have helped clarify uncertainties in the IL reaction mechanism and response. Collecting more data is not needed to address this issue, but might there be data on hand not reported here that could help clarify the CV response here?*

A full study into the electrochemical behaviour of a wide range of water levels was not undertaken. Water levels of 1000-1500 ppm and 60,000 ppm were chosen and used to test two very different cases. In terms of electrochemistry, 1000-1500 ppm is considered as wet, and therefore it would have been most worthwhile to test the electrochemistry with levels < 100 ppm. However, we were unable to dry the IL to this level. Between 1000-4000 ppm (as the IL absorbed water through usage), there was no notable change in behaviour of the IL and no other water levels were examined.

3. Page 4-53. Section 4.1.3.2 describes dilution of the IL with acetonitrile and lithium triflate. Some explanation or rationale for why lithium triflate was added would be helpful here.

The compound lithium triflate was chosen as a comparison compound as it is a highly conductive and stable compound used extensively in electrochemistry (primarily as a compound of the electrolyte for lithium batteries). A comparative solution using this compound was prepared to contrast the specific interaction the IL has with AZ31 in growing a film on the surface, even when dilute (as presented).

4. Page 4-68 to 4-73. Section 4.2.1.2.1 discusses field crystallisation. Overall, arguments supporting this phenomenon need to be strengthened and the evidence given in support of field crystallisation should be scrutinized more deeply in the text. The evidence provided here is also consistent with cracking of the film as it thickens due to internal stresses and localized corrosion and the formation of localized corrosion product at longer treatment times. How these phenomena can be ruled out should be provided. It is not clear what Figure 4.26 is showing. How is it known that the rough raised regions in the OP images in Figure 4.29 are a crystallized deposit? It would seem that EIS of crystallized versus uncrystallised films would help to distinguish them? Was this done and if so, what do the data show?

A paragraph has been provided above to further address the question relating to breakdown and corrosion versus crystallisation.

5. Page 4-94 to 4-122. The general impression from this section is that the films formed are not persistent and therefore not corrosion resistant in dilute chloride solutions. Can persistence and protection offered by the coatings studied here be compared to other sorts of surface treatments such as cleaning, conversion coating, anodization? Where might treatments like this fall on the spectrum and therefore where might they find use?

With acid pickling and anodising at 0.1 mAcm⁻² we were able to form a film with persistence in a chloride media. This is represented by Figure 4.65, wherein the impedance and the phase angle of the surface remain highly stable over a 60 minute immersion in 0.01 M NaCl. In comparison, for bare AZ31 the impedance and phase angle increase as corrosion product is deposited onto the surface. It is highly likely that many films formed in this work are highly porous on the nano scale (based on their electrochemical behaviour) and thus these films need to be investigated further. As with other anodised coatings they may require sealing or these coatings may be used as part of a pre-treatment regime for subsequent coatings (e.g. an undercoat for a water based coating).

Anodic Treatments in an Ionic Liquid for the Corrosion Protection of Magnesium Alloy AZ31

by

Julie-Anne Latham

BEng (Hons. I)

A thesis submitted in the fulfilments of the requirements for the degree of
Doctor of Philosophy

at

Department of Materials Engineering
Monash University, Clayton, Victoria Australia, 3800

Submitted 18 June 2012

Under the Copyright Act 1968, this thesis must be used only under the normal conditions of scholarly fair dealing. In particular no results or conclusions should be extracted from it, nor should it be copied or closely paraphrased in whole or in part without the written consent of the author. Proper written acknowledgement should be made for any assistance obtained from this thesis.

I certify that I have made all reasonable efforts to secure copyright permissions for third-party content included in this thesis and have not knowingly added copyright content to my work without the owner's permission.

To my husband David who dealt with the mountains of paper strewn throughout the house, and my cat Lotus for helping spread the mess, this is for you.

Table of Contents

Abstract.....	ix
Statement of Originality	xi
Acknowledgements	xiii
List of Figures	xv
Chapter 1	xv
Chapter 3	xv
Chapter 4.....	xv
Chapter 5.....	xxi
Appendices.....	xxi
List of Tables.....	xxiii
Chapter 3.....	xxiii
Chapter 4.....	xxiii
Appendices.....	xxiii
List of Publications from PhD	xxv
List of Abbreviations	xxvii
Chapter 1	2-1
Introduction	2-1
1.1 Magnesium and AZ31 Alloy	2-1
1.2 Ionic Liquids and Corrosion	2-2
1.3 Research Problem, Hypothesis and Aims	2-3
1.3.1 Research Problem.....	2-3
1.3.2 Working Hypothesis and Aims	2-3
1.3.3 Research Plan.....	2-4
Chapter 2	2-7
Literature Review.....	2-7
2.1 Magnesium and Magnesium Alloys.....	2-7
2.1.1 A Brief History of Magnesium.....	2-7
2.1.2 Properties and Uses of Magnesium and its Alloys.....	2-8
2.1.3 AZ Series	2-10
2.1.3.1 AZ31.....	2-10
2.2 Corrosion of Mg and AZ Alloys	2-11
2.2.1 AZ31 Corrosion	2-14
2.3 Corrosion Protection for Mg Alloys.....	2-14
2.3.1 Surface Preparation: Cleaning & Acid Pickling.....	2-15
2.3.2 Conversion Coatings.....	2-15

2.3.2.1 Chromate Conversion Coatings.....	2-16
2.3.2.2 Alternative Conversion Coatings.....	2-17
2.3.2.2.1 Phosphate and Phosphate/Permanganate Conversion Coatings.....	2-17
2.3.2.2.2 Rare-Earth Conversion Coatings.....	2-17
2.3.2.2.3 Other Conversion Coatings.....	2-18
2.3.3 Sol-Gel Coatings.....	2-18
2.3.4 Plating and Electroplating.....	2-19
2.3.5 Anodising.....	2-20
2.3.5.1 Formation and Composition of Anodised Coatings	2-20
2.3.5.2 Corrosion Properties of Anodised Coatings.....	2-22
2.3.6 Organic and Polymer Coatings	2-22
2.3.7 Summary.....	2-23
2.4 Ionic Liquids.....	2-24
2.4.1 General Overview of Ionic Liquids	2-24
2.4.2 Ionic Liquids and Corrosion	2-24
2.4.3 Formation of Protective Coatings on Mg with Ionic Liquids.....	2-26
2.6 Summary.....	2-27
Chapter 3	3-29
Experimental Methodology.....	3-29
3.1 Materials	3-29
3.1.1 AZ31 Magnesium Alloy and Glassy Carbon (GC).....	3-29
3.1.2 [P _{6,6,6,14}][[(C ₈) ₂ PO ₂] Ionic Liquid.....	3-30
3.1.3 Dilute Solutions.....	3-30
3.2 Pipette Cells	3-31
3.3 Cyclic Voltammetry (CV)	3-32
3.4 Film Formation	3-33
3.4.1 Constant Current/Galvanostatic Anodising.....	3-33
3.4.2 Constant Potential/Potentiostatic Anodising.....	3-33
3.5 Electrochemical Impedance Spectroscopy (EIS) and Potentiodynamic Polarisation (PP) 3-	33
3.6 Surface Characterisation	3-34
3.7 Electrochemical Technique Theory.....	3-35
3.7.1 Cyclic Voltammetry	3-35
3.7.2 Electrochemical Impedance Spectroscopy	3-38
3.7.3 Potentiodynamic Polarisation and Tafel Curves.....	3-40
Chapter 4.....	4-43
Results and Discussion.....	4-43

Summary.....	4-43
4.1 Electrochemistry of $[P_{6,6,6,14}][(\overset{i}{C}_8)_2PO_2]$ IL on AZ31 and Glassy Carbon.....	4-43
4.1.1 Section Overview	4-43
4.1.2 Reactions in IL on AZ31 and GC: A Comparison.....	4-44
4.1.3 Passivation and Film Formation with Cyclic Voltammetry.....	4-47
4.1.3.1 Anodic Behaviour of AZ31 in Neat IL and Dilute IL	4-47
4.1.3.2 Anodic Behaviour of AZ31 in a Lithium Triflate Solution	4-53
4.1.3.3 Cathodic Behaviour of AZ31 in Neat IL.....	4-57
4.1.4 Effect of Air and Water.....	4-58
4.1.4.1 Condition 1 – Open-to-Air in Laboratory (wet IL)	4-58
4.1.4.2 Condition 2 – Argon Glovebox	4-61
4.1.5 Section Key Points	4-63
4.2 Electrochemical Film Formation in $[P_{6,6,6,14}][(\overset{i}{C}_8)_2PO_2]$	4-64
4.2.1 Section Overview	4-64
4.2.2 Constant Potential.....	4-64
4.2.1.1 Using EIS as a Diagnostic Tool	4-67
4.2.1.2 Higher Potentials and Field Crystallisation	4-68
4.2.1.2.1 Field Crystallisation at Room Temperature	4-68
4.2.1.2.2 Field Crystallisation at Elevated Temperature	4-71
4.2.3 Constant Current.....	4-76
4.2.3.1 Film Morphology of Constant Current Anodised Films	4-78
4.2.3.2 Film Breakdown.....	4-83
4.2.3.3 Morphology of Film Breakdown	4-84
4.2.3.3.1 Summary of Film Defects	4-88
4.2.3.4 Film Formation in Dilute IL Solution (ILAN)	4-88
4.2.3.5 Two-Step Process	4-92
4.2.4 Section Key Points	4-93
4.3 Corrosion Performance of Treated Specimens.....	4-94
4.3.1 Corrosion Performance of Field Crystallised Coatings on AZ31	4-94
4.3.2 Corrosion Behaviour of Films on Bare AZ31 via Potentiodynamic Polarisation .	4-100
4.3.2.1 Potentiodynamic Polarisation.....	4-100
4.3.2.2 EIS analysis of Film Behaviour of IL Films on As-Polished AZ31.....	4-103
4.3.3 The Effect of Surface Pre-Treatments on the Corrosion Behaviour of IL Treated AZ31 Surfaces	4-106
4.3.3.1 Surface Pre-treatment	4-106
4.3.3.2 Film Behaviour of IL Films on 60 s immersion HNO_3 & H_3PO_4 Acid Pickled AZ31.....	4-114

4.3.3.3 Film Behaviour of IL Films on 30 s immersion NaOH and 60 s immersion HNO ₃ & H ₃ PO ₄ Pickled AZ31	4-118
4.3.4 Summary	4-121
4.3.5 Section Key Points	4-122
4.4 Elemental Film Characterisation	4-123
4.4.1 Section Overview	4-123
4.4.2 XPS of IL Treated Surfaces	4-123
4.4.2.1 C 1s Region Spectra	4-124
4.4.2.2 O 1s Spectra	4-125
4.4.2.3 Mg 2p Spectra	4-126
4.4.2.4 P 2p Spectra	4-127
4.4.2.5 Summary	4-129
4.4.2 XRD	4-131
4.4.4 ATR-FTIR	4-134
4.4.4.1 ATR-FTIR of AZ31 Pre-Treatments	4-137
4.4.4.2 Summary	4-140
4.4.5 ToF-SIMS	4-141
4.4.6 Section Key Points	4-143
Chapter 5	5-145
Closing Discussion, Conclusions & Ways Forward	5-145
5.1 Overview of the Formation of the Anodic IL Film	5-145
5.2 Summary of Conclusions	5-149
5.3 What's Next?	5-150
References	152
Appendices	158
Appendix A: Electrochemical Behaviour of GC in Wet IL and in an Argon Glovebox.	158
Appendix B: XPS of Neat [P _{6,6,6,14}][(C ₈) ₂ PO ₂] IL and Untreated AZ31	160
Untreated AZ31	165
Appendix C: Table of XPS %area Fits	166
Appendix D: Fits of Equivalent Circuits of IL Films	167
Appendix E: SEM and EDS of Field Crystallised Films	168
Appendix F: [P _{6,6,6,14}][(C ₈) ₂ PO ₂] as an Inhibitor	171
Electrochemical Inhibitor behaviour: EIS and PP	171
Immersion Test Within the Pipette Cell	173
Key Points	179
Appendix G: ICP Analysis Results	183
Appendix H: Pt Pseudo Metal Reference Internal Referencing and Stability	184

Abstract

Recent work in our group found that applying a potential bias to magnesium alloys during immersion in ionic liquids (ILs) could improve the homogeneity and corrosion protection properties of the film (when immersed in 0.01 M NaCl). To gain an understanding of the effect of potential bias cyclic voltammetry was used to evaluate the behaviour of magnesium alloy AZ31 in the IL trihexyl(tetradecyl)phosphonium bis(2,4,4-trimethylpentyl) phosphinate ($[P_{6,6,6,14}][[(C_8)_2PO_2]$). The behaviour of the system was investigated using scan rates of 1, 10 and 100 mV/s, conditions of wet (6 wt% water) and dry (0.1 wt% water) IL, access to and absence of air and dilution of the IL in a solvent. These were all replicated on an inert glassy carbon (GC) substrate for comparison to AZ31. It was found that scanning the potential anodically resulted in anodic film growth under the “high field” mechanism of film growth. During film growth the IL was adsorbed into the oxide/hydroxide film to form a resistive film on AZ31. The presence of excess water in the system results in breakdown of the anion of the IL through hydrolysis.

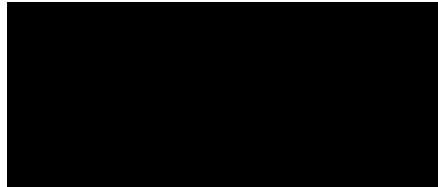
Ionic liquid films were formed on magnesium alloy AZ31 in ($[P_{6,6,6,14}][[(C_8)_2PO_2]$) ionic liquid using potentiostatic and galvanostatic anodising methods. We have found that galvanostatic and potentiostatic anodising in the IL is effective and can be used to control the dimensions of the film by varying the time of treatment and magnitude of potential. The films are comprised of both the anion and cation but the growth of the film is likely dominated by the anion whereas the cation is adsorbed. Film formation is still possible when the IL is diluted in a non-reactive solvent, but the morphology of the film is altered. In all cases, deposition under anodic bias was only effective over the α matrix-phase. Performing an acid pickling pre-treatment (mixture of nitric and phosphoric acid) coupled with galvanostatic anodising in the IL were effective in reducing the corrosion rate of AZ31 by a factor of 3 and reduced the anodic dissolution reaction by 1.5 orders of magnitude (vs. a blank ‘as-polished’ AZ31 surface).

The principal outcomes of this research provide an improved understanding of the formation of IL films on AZ31 for corrosion protection.

Statement of Originality

This thesis, except with the Research Graduate School Committee's approval, contains no material which has been accepted for the award of any other degree or diploma in any university or other institution and affirms that to the best of my knowledge the thesis contains no material previously published or written by another person, except where due reference is made in the text of the thesis.

Signed:

A large black rectangular box redacting the signature of the author.

Julie-Anne Latham

Date: 17/06/2012

Acknowledgements

First and foremost, I would like to express my gratitude and thanks to my supervisors Prof. Maria Forsyth and Dr. Patrick Howlett for all of their time, advice and guidance over the last three years. I would also like to thank Prof. Douglas MacFarlane for all his input into my work, allowing me to take advantage of his extensive knowledge in chemistry and the field of ionic liquids.

I would also like to acknowledge Anthony Somers who has dedicated time to help me obtain data using FIB-SEM, ToF-SIMS and XPS techniques. I would like to acknowledge Timothy Khoo, who has been a great friend throughout my candidature and help in the lab, as well as Tristan Simons and Angel Torriero whenever I required advice or assistance with chemistry or electrochemistry. Thank you also to Matthias Hilder and my husband David Latham for accepting to proof-read my thesis start to finish.

I want to acknowledge Deakin University and their staff for allowing me the use of their facilities over the last year and a half of my PhD candidature. I would like to thank Dr. Mark Nave from IFM, Deakin University in Geelong for assistance with FIB-SEM.

A thank you to my family and friends for their support and times I haven't been able to come out because I've been locked away working on my PhD, especially in the last few months during the writing stage.

Finally, thank you to the Australian Federal Government for scholarship through the Australian Postgraduate Award and the Materials Engineering Department at Monash University.

List of Figures

Chapter 1

Figure 1.1 – Flow diagram of research program in phase one: electrochemical behaviour of AZ31 in IL $[P_{6,6,6,14}][C_8]_2PO_2$	2-5
Figure 1.2 - flow diagram of research program in phase two: film forming via potentiostatic methods.	2-6
Figure 1.3 - flow diagram of research program in phase three: film forming via galvanostatic methods.	2-6

Chapter 3

Figure 3.1 - SEM image of etched AZ31 from both the edge of the DSC cylinder. Image courtesy of Steven Lin.	3-29
Figure 3.2 - Structure of trihexyl(tetradecyl)phosphonium bis(2,4,4-trimethylpentyl) phosphinate ($[P_{6,6,6,14}][C_8]_2PO_2$) IL.	3-30
Figure 3.3 – Photos of a) pipette cell set-up (incl. PE pipette, Pt wire pseudo metal reference, mixed oxide Ti-mesh counter electrode); b) mixed oxide Ti-mesh counter electrode.	3-31
Figure 3.4 – Schematic of special pipette cell for use in an argon glovebox.	3-32
Figure 3.5 – 3 electrode electrochemical cell, 1: saturated calomel electrode (SCE) and luggin attachment, 2: Working electrode holder, 3: mixed-oxide Ti mesh counter electrode.	3-34
Figure 3.6 – Schematic representation of potential response in a) linear sweep voltammetry and b) cyclic voltammetry. E_i is the initial pre-set potential and E_f is the final pre-set potential. ...	3-36
Figure 3.7 – Schematic EIS responses of a simple charge transfer process in a) Nyquist form and b) Bode form.	3-39
Figure 3. 8 – a) Randles circuit for diffusion processes, where R_s = solution resistance, C_{dl} = double layer capacitance, R_{ct} = charge transfer resistance, W = Warburg impedance; b) low frequency pseudo-inductance behaviour, where R_s = solution resistance, C = double layer capacitance, R_1 = charge transfer resistance, L = inductance.	3-40

Chapter 4

Figure 4.1 – Cyclic voltammograms of Glassy Carbon (GC) in $[P_{6,6,6,14}][C_8]_2PO_2$ IL between OCP and 3 V vs. Pt and OCP to -3 V vs. Pt at a) 1 mV/s, b) 10 mV/s, c) 100 mV/s and d) 1, 10 and 100 mV/s. Arrows indicate the scan direction.	4-44
Figure 4.2 – Cyclic voltammograms of AZ31 in $[P_{6,6,6,14}][C_8]_2PO_2$ IL between OCP and 3 V vs. Pt and OCP to -3 V vs. Pt at a) 1 mV/s, b) 10 mV/s, c) 100 mV/s and d) 1, 10 and 100 mV/s. Arrows indicate the scan direction.	4-46
Figure 4.3 – Cyclic voltammograms from OCP to 3 V vs. Pt at 10 mV/s for a) initial scan of AZ31 in dry neat IL and ILAN (0.1 M and 0.01 M IL in acetonitrile solutions) and repeat cycles b) $[P_{6,6,6,14}][C_8]_2PO_2$ IL and c) 0.1 M ILAN solution.	4-47
Figure 4.4 – Potential switching of AZ31 in a) $[P_{6,6,6,14}][C_8]_2PO_2$ IL and b) ILAN. Scans were performed progressively from OCP to potentials of 0, 1.5, 2.5, 3, 4 and 5 V at 10 mV/s. Two consecutive scans between OCP and 5 V were performed in neat IL after the initial scan to 5 V vs. Pt.	4-49
Figure 4. 5 – a) 100 hour long OCP of AZ31 in IL; b)cyclic voltammogram of AZ31 in IL cycled between OCP to 3 V vs. Pt at 1 mV/s after being held at OCP for 100 hours.	4-51
Figure 4.6 – Schematics of simulated CV responses of valve metals when a) no dissolution and perfect anodic film growth; b) effect of adsorption on anodic film growth. The incorporation of	

a compound from the anodising bath changes the potential distribution of the film and promotes dissolution, hence non-plateau behaviour; c) dissolution behaviour of the subsequent cycles – overlapping of the initial curve. Schematic images adapted from data presented in [119] and [118].	4-51
Figure 4.7 – Cyclic voltammograms of AZ31 polarised from OCP to 3 V vs. Pt in ANSO solution, a) cycle 1, b) cycle 2, c) cycle 3, d) cycle 4. The final potential was not achieved in any cycles due to the build-up of white precipitate on the Ti counter electrode.	4-54
Figure 4.8 - a) Photograph of white deposit (circled) formed on the Ti counter electrode after polarising AZ31 in ANSO solution (vertical lines at top of image correspond to 1 mm increments); b) Optical micrograph of AZ31 after cycling in ANSO; c) pH indication on litmus paper of ANSO after cycling with GC and AZ31; d) optical appearance of ANSO after cycling with AZ31.	4-55
Figure 4.9 – FTIR spectrum of deposit scraped from the counter electrode formed into a KBr disc.	4-56
Figure 4.10 – Cyclic voltammogram of GC cycled between OCP and 3 V vs. Pt in ANSO (4 cycles in total).	4-56
Figure 4.11 – CV of AZ31 in $[P_{6,6,6,14}][(\text{C}_8)_2\text{PO}_2]$ scanning between OCP and -3V vs. Pt at 1 mV/s.	4-57
Figure 4.12 – AZ31 polarised from OCP to 3 V vs. Pt and cycled between 3 V and -3 V vs. Pt at 1 mV/s in $[P_{6,6,6,14}][(\text{C}_8)_2\text{PO}_2]$ IL. Inset shows the zoomed in anodic side of the scans.	4-58
Figure 4.13 – CVs on AZ31 in IL with 6 wt% (60,000 ppm) H ₂ O between OCP and 3 V vs. Pt at 1 mV/s; a) initial cycle; b)-d) cycles 2-4. The purple arrows indicate the points of intersection between the forward and reverse scans.	4-59
Figure 4.14 – An optical micrograph of AZ31 cycled four times between OCP and 3 V vs Pt in IL containing 6 wt% (60,000 ppm) water. Arrow points to uncovered β -phase (light area). The dark area is the covered α -phase. The small black dots on the surface are due to grinding, not from pitting.	4-60
Figure 4.15 – Cyclic voltammogram of AZ31 in IL with 6 wt% (60,000 ppm) water. AZ31 was cycled at 1 mV/s from OCP and cycled between 3 V and -3 V vs. Pt. The inset show cycles 1-4 of the anodic portion of the scans (OCP to 3 V vs. Pt). Solid arrows indicate the direction of the scan, the dashed arrow indicates the progressive cathodic cycles.	4-61
Figure 4.16 – Cyclic voltammogram of AZ31 in IL cycled between OCP and -3 V vs. Pt at 1 mV/s in an argon glovebox. Water content of IL used was approximately 1000 ppm. All four cycles are shown in the graph, however the deviations in maximum current density in the repeats differ less than 10 $\mu\text{A}/\text{cm}^2$, and in no particular direction.	4-62
Figure 4.17 - Cyclic voltammogram of AZ31 in IL cycled between OCP and 3 V vs. Pt at 1 mV/s in an argon glovebox. Water content of IL used was approximately 1000 ppm.	4-63
Figure 4.18 - Current density vs. time for AZ31 in $[P_{6,6,6,14}][(\text{C}_8)_2\text{PO}_2]$ held at a) 1 and 0 V vs. Pt for 3 hours; b) 1 V vs. Pt for 96 hours. The noise in a) is not indicative of the actual behaviour on the electrode, it is more likely poor choice of current range on the equipment.	4-65
Figure 4.19 – FIB-SEM cross section of AZ31 anodised at a constant potential of 2.5 V vs. OCP (approx. 1 V vs. Pt) for 4 hours. b)-d) are EDS of parts 1-3 in a) respectively.	4-66
Figure 4.20 – a) Bode plot of AZ31 treated in $[P_{6,6,6,14}][(\text{C}_8)_2\text{PO}_2]$ at a potential bias of -0.2 V. An EIS spectrum was taken every 8 minutes; b) Z vs. t of AZ31 in IL biased at -0.2, -0.1, 0.1 and 3.5 V vs. OCP plotted at 139 mHz.	4-67
Figure 4.21 – Impedance values at 24 hours in IL for AZ31 biased at -0.2, -0.1, 0.1 and 3.5 V vs. OCP. Taken at 139 mHz.	4-67

Figure 4.22 - Impedance values at 30 minutes in 0.01 M NaCl for AZ31 biased at -0.2, -0.1, 0.1 and 3.5 V vs. OCP in IL for 24 hours. Taken at 1.8 Hz (due to erratic behaviour at lower frequencies).	4-68
Figure 4.23 – Current density vs. time for AZ31 held at 3 V vs. Pt for 96 hours in $[P_{6,6,6,14}][(\text{C}_8)_2\text{PO}_2]$. Inset is magnified current response between 0 and 10 hours.	4-69
Figure 4.24- Schematic representation of the field crystallisation process. Numbered steps correspond to the numbers in Figure 4.24.	4-70
Figure 4.25 – Optical micrographs of AZ31 treated at 3 V vs. Pt in $[P_{6,6,6,14}][(\text{C}_8)_2\text{PO}_2]$ for 96 hours at room temperature (approx. 22°C).	4-70
Figure 4.26 - Optical micrographs of AZ31 treated at 3 V vs. Pt in $[P_{6,6,6,14}][(\text{C}_8)_2\text{PO}_2]$ for 48 hours at room temperature (approx. 22°C).	4-70
Figure 4.27 – Behaviour of current density with time of AZ31 treated at 3 V vs. Pt and 50°C in $[P_{6,6,6,14}][(\text{C}_8)_2\text{PO}_2]$ at a) 24 hours, b) 48 hours and c) 96 hours.	4-71
Figure 4.28 - Optical micrographs of AZ31 treated at 3 V vs. Pt in IL at 50°C for a)&b) 48 hours, c)&d) 96 hours.....	4-72
Figure 4.29 – Optical profilometry of AZ31 after treatment at 3 V vs. Pt and 50°C for a) 24 hours b) 48 hours and c) 96 hours.	4-74
Figure 4. 30 – Optical profilometry of AZ31 ground to a P4000 grit finish.....	4-75
Figure 4. 31 – Current density behaviour over 48 hours of AZ31 treated at 1 V vs. Pt and 50°C.	4-75
Figure 4.32 – Cell potential vs. time for treatment of AZ31 using current densities of 0.005, 0.01, 0.05 and 0.1 mAcm ⁻² . The final potential set was 18 V.....	4-76
Figure 4.33 – a) Cell potential vs. time for treatment of AZ31 using current densities of 0.1 and 0.05mAcm ⁻² ; b) comparison of potential “jump” between AZ31 anodised at 0.1 mAcm ⁻² with and without iR compensation.	4-77
Figure 4.34 - Optical profilometry of constant current treated surfaces: a) 0.05 mAcm ⁻² and b) 0.1 mAcm ⁻²	4-79
Figure 4. 35 – FIB-SEM image of Ga ions on surface due to milling, a) ring of Ga ions around the sputtered area and b) thin light layer of Ga ions on surface make it difficult to confidently distinguish film.	4-81
Figure 4.36 – FIB-SEM cross section of AZ31 a) treated in IL at 0.05 mAcm ⁻² between a layer of deposited Pt (upper light layer) and AZ31 (lower dark layer). Thickness is approx. 80nm. b) cross-section of ‘as-polished’ AZ31 with a deposited Pt layer.	4-82
Figure 4.37 - Cell potential vs. time for treatment of AZ31 using a current density of 0.01 mAcm ⁻²	4-84
Figure 4.38 – Optical micrographs of AZ31 treated at 0.01 mA/cm ² A) successfully formed film at 4.0x and B) film after breakdown at 0.63x.....	4-85
Figure 4.39 – Potential transient and optical micrographs of the three different breakdown processes on the surface of AZ31 anodised in IL at 0.05 mAcm ⁻² : a) Potential transient; b) minor breakdown spot (1); c) & d) catastrophic breakdown spot (2); e) small areas of breakdown over remaining surface; f) as polished AZ31; g) AZ31 anodised in IL at 0.5 mAcm ⁻² ...4-86	4-86
Figure 4.40 – Secondary electron micrographs at 5 keV of a)-b) catastrophic breakdown point; c) Possible rupture point which caused breakdown (arrow); d)-e) cracks (indicated by arrows) over the surface away from the large breakdown sites (corresponding to areas like that represented in Figure 4.39 e)).....	4-87
Figure 4.41 – Potential transients of AZ31 treated in $[P_{6,6,6,14}][(\text{C}_8)_2\text{PO}_2]$ and ILAN at 0.05 mAcm ⁻² to a final cell potential of 18 V.	4-89

Figure 4.42 – Potential transients of AZ31 anodised to a final cell potential of 18 V in 0.1 M $[P_{6,6,6,14}]/[(C_8)_2PO_2]$ in acetonitrile at various current densities. Inset is full view of the potential transient for 0.05 mAcm ⁻² in comparison to the other applied current densities.....	4-90
Figure 4.43 – a) Potential transient of AZ31 anodised at 0.07 mAcm ⁻² to 18 V; b) FIB-SEM cross section of thin film (approx. 29 nm) formed in ILAN using a current density of 0.07 mAcm ⁻² . The film is less obvious than the film formed in neat IL. However it can be identified by the two thin dark lines above and below which signify interfaces between the Pt layer and the film, and the layer and the AZ31 alloy.	4-91
Figure 4.44 – Current decay during static application of 18 V after anodising at 0.05 mAcm ⁻² ...4-	92
Figure 4.45 – Optical micrograph change in appearance of film formed at 3 V vs. Pt, 50°C for 48 hours on AZ31 after exposure to 5 µL 0.01 M NaCl for 3 hours.....	4-95
Figure 4.46 – Microgalvanic corrosion around a cathodic particle in the microstructure of AZ31 after exposure to 5 µL 0.01 M NaCl for 3 hours on a) AZ31 treated in IL at 3 V vs. Pt and 50°C for 48 hours: optical micrograph; b) AZ31 ground to a P4000 surface finish: optical profile..	4-96
Figure 4.47 – Large pit likely formed from undercutting of a cathodic particle in the microstructure of AZ31 treated in IL at 3 V vs. Pt and 50°C for 48 hours, after exposure to 5 µL 0.01 M NaCl for 3 hours: a) optical micrograph; b) optical profile.....	4-97
Figure 4.48 - Large pit likely formed from undercutting of a cathodic particle in the microstructure of AZ31 ground to a P4000 grit surface finish, after exposure to 5 µL 0.01 M NaCl for 3 hours: a) optical micrograph; b) optical profile.	4-98
Figure 4.49 – Localised pitting corrosion over the α phase of AZ31 after exposure to 5 µL 0.01 M NaCl for 3 hours: a) AZ31 treated in IL at 3 V vs. Pt and 50°C for 48 hours; b) AZ31 ground to a P4000 grit surface finish. Pitting cluster on b) indicated by circle.	4-98
Figure 4.50 – Optical profilometry of Small surface pit clusters over α phase in a) control P4000 grit polished AZ31 exposed to 5 µL 0.01 M NaCl for 3 hours; b) AZ31 treated at 3 V vs. Pt and 50° C for 48 hours exposed to 5 µL 0.01 M NaCl for 3 hours. Inset in a) is ‘as-polished’ AZ31 (as seen in Figure 4.29) prior to corrosion: notice the lack of pitting ‘bumps’ over this surface..	4-99
Figure 4.51 – PP curves obtained in 0.01 M NaCl for AZ31 treated at constant potentials of a) 0 V and 1 V vs. Pt for 6 hours; b) 0 V vs. Pt for 3 and 6 hours and 1 V vs. Pt for 1 and 6 hours; c) 1 V vs. Pt for 3 hours. The same control PP curve is used in a, b and c.....	4-100
Figure 4.52 – PP curves obtained in 0.01 M NaCl for ‘as-polished’ AZ31 (P4000 grit finish) and AZ31 anodised in IL at 0.05, 0.1 and 0.5 mAcm ⁻²	4-101
Figure 4.53 - PP curves obtained in 0.01 M NaCl for ‘as-polished’ AZ31 (P4000 grit finish) and AZ31 anodised in IL at 0.05 mAcm ⁻² followed by the static application of 18 V for 15, 30 and 60 minutes.....	4-102
Figure 4.54 – PP curves obtained in 0.01 M NaCl for ‘as-polished’ AZ31 (P4000 grit finish) and AZ31 anodised in ILAN (0.1 M IL in acetonitrile) at 0.05, 0.5, 1, 2, 3, 5 and 10 mAcm ⁻² to a final cell potential of 18 V.	4-103
Figure 4.55 – EIS response of as-polished AZ31 (blank) and as-polished AZ31 after anodising in IL at 0.1 mAcm ⁻² and ILAN at 1 mAcm ⁻² in 0.01 M NaCl after 0 and 60 minutes immersion: a) Nyquist plot; b) Bode plot of impedance with frequency; c) Bode plot of phase angle with frequency.	4-105
Figure 4.56 – Optical profilometry of AZ31 surfaces after immersion in a) HNO ₃ & H ₃ PO ₄ for 60s and b) NaOH for 30s followed by HNO ₃ & H ₃ PO ₄ for 60s. Units of the inset are µm. .	4-107

Figure 4.57 – AZ31 ‘as-polished’ to a P4000 grit surface finish a) SEM image; b) EDS map of Mg; c) EDS map of Al; d) EDS map of Zn. The EDS maps were obtained over the area shown in a).....	4-108
Figure 4.58 - AZ31 pickled in a mixture of HNO ₃ and H ₃ PO ₄ for 60 seconds a) SEM image; b) EDS map of Mg; c) EDS map of Al; d) EDS map of Zn. The EDS maps were obtained over the area shown in a).....	4-109
Figure 4.59 - PP curves obtained in 0.01 M NaCl for a) ‘as-polished’ AZ31 (P4000 grit finish) and AZ31 anodised in IL at 0.05 mAcm ⁻² ; 18V 15min, and 0.1 mAcm ⁻² ; b)AZ31 immersed in a mixture of HNO ₃ and H ₃ PO ₄ for 60s (technique 1 – Table 4.10) blank and anodised in IL at 0.05 mAcm ⁻² ; 18V 15min, and 0.1 mAcm ⁻²	4-110
Figure 4.60 – Electrochemical impedance spectroscopy of as-polished AZ31, AZ31 after 60s immersion in a mixture of HNO ₃ & H ₃ PO ₄ and AZ31 after 30s immersion in NaOH and 60s in a mixture of HNO ₃ & H ₃ PO ₄ ; a) 0 minutes after immersion in 0.01 M NaCl; b) 60 minutes after immersion in 0.01 M NaCl.....	4-111
Figure 4.61 – Proposed equivalent circuits for a) as polished AZ31 immediately after immersion in 0.01 M NaCl; b) as polished AZ31 60 minutes after immersion in 0.01 M NaCl; c) acid and base treated AZ31 immersed in 0.01 M NaCl. R _s = solution resistance; Q _{dl} = double layer capacitance; R _{dl} = double layer resistance; Q _t /C _t = film capacitance; R _t = film resistance/charge transfer resistance; R ₃ = resistance through film defects; L = inductance.....	4-112
Figure 4.62 – Bode plot of phase angle against frequency of as-polished AZ31, AZ31 after 60s immersion in a mixture of HNO ₃ & H ₃ PO ₄ and AZ31 after 30s immersion in NaOH and 60s in a mixture of HNO ₃ & H ₃ PO ₄ 0 and 60 minutes after immersion in 0.01 M NaCl.....	4-113
Figure 4.63 - PP curves obtained in 0.01 M NaCl for ‘as-polished’ AZ31 (P4000 grit finish) blank and AZ31 immersed in a mixture of HNO ₃ and H ₃ PO ₄ for 60s (technique 1 – Table 4.10) blank and anodised in IL at 0.1 mAcm ⁻² and 0.05 mAcm ⁻² with a static 18 V hold for 15 minutes.....	4-115
Figure 4.64 - PP curves obtained in 0.01 M NaCl for ‘as-polished’ AZ31 (P4000 grit finish) blank and anodised in ILAN at 1 mAcm ⁻² and AZ31 immersed in a mixture of HNO ₃ and H ₃ PO ₄ for 60s (technique 1 – Table 4.10) blank and anodised in ILAN at 1 mAcm ⁻²	4-115
Figure 4.65 - EIS response of 60s acid pickled AZ31 (blank) and 60s acid pickled AZ31 after anodising in IL at 0.1 mAcm ⁻² and 0.05 mAcm ⁻² with a 15min 18V hold and ILAN at 1 mAcm ⁻² in 0.01 M NaCl after 0 and 60 minutes immersion: a) Bode plot of impedance with frequency; b) Bode plot of phase angle with frequency.....	4-117
Figure 4.66 - PP curves obtained in 0.01 M NaCl for ‘as-polished’ AZ31 (P4000 grit finish) and AZ31 immersed for 30s in NaOH and 60s in a mixture of HNO ₃ and H ₃ PO ₄ (technique 2 – Table 4.10) blank and anodised in IL at 0.05 mAcm ⁻² ; 18V 15min, and 0.1 mAcm ⁻² and a constant potential of 2.5 V vs. OCP for 4 hours.....	4-118
Figure 4.67 - EIS response of 30s NaOH immersion followed by 60s acid pickled AZ31, blank, and after anodising in IL at 0.1 mAcm ⁻² and 0.05 mAcm ⁻² with a 15min 18V hold and ILAN at 1 mAcm ⁻² in 0.01 M NaCl after 0 and 60 minutes immersion: a) Bode plot of impedance with frequency; b) Bode plot of phase angle with frequency.....	4-120
Figure 4.68 – Survey spectrum of AZ31 treated in [P _{6,6,6,14}][(C ₈) ₂ PO ₂] at a constant current density of 0.1 mAcm ⁻² to 18 V.....	4-123
Figure 4.69 – C 1s spectra obtained at 1486 eV of AZ31 treated at constant potentials of -0.4, 1.5 and 2.5 V vs. OCP for 4 hours: a) region spectra; b) survey spectra.....	4-124
Figure 4.70 – C 1s spectra obtained at 1486 eV of AZ31 treated at current densities of 0.01, 0.1 and 0.5 mAcm ⁻² to a final cell potential of 18 V. The broadness of some of the fits is likely due	

to the presence of additional species on the surface, which were not able to be accurately fit and identified.....	4-125
Figure 4.71 – O 1s spectra obtained at 1486 eV of surfaces treated at constant potentials of -0.4, 1.5 and 2.5 V vs. OCP for 4 hours. a) region scans and b) survey spectra.....	4-126
Figure 4.72 – O 1s spectra at 1486 eV of surfaces treated using constant current densities of 0.01, 0.1 and 0.5 mAcm ⁻² to a final cell potential of 18 V.....	4-126
Figure 4.73 - Mg 2p spectra obtained at 1486 eV of AZ31 treated at constant potentials of -0.4, 1.5 and 2.5 V vs. OCP for 4 hours. a) region spectra; b) survey spectra.	4-127
Figure 4.74 – Mg 2p spectra obtained at 1486 eV for AZ31 surfaces treated at constant current densities of 0.01, 0.1 and 0.5 mAcm ⁻² to a final cell potential of 18 V. The larger intensity of the peak at high binding energies probably reflects a thinner film, resulting in greater contribution of the carbonate (see C 1s).....	4-127
Figure 4.75 – P 2p spectra obtained at 1486 eV of a) region spectra of AZ31 treated at -0.4 V vs. OCP for 4 hours; b) survey spectra of AZ31 treated at constant potentials of -0.4, 1.5 and 2.5 V vs. OCP for 4 hours.	4-128
Figure 4.76 – P 2p region spectra obtained at 1486 eV for AZ31 treated at constant current densities of 0.01, 0.1 and 0.5 mAcm ⁻² to a final cell potential of 18 V.....	4-129
Figure 4.77 – XRD of “as-polished” AZ31 (P4000 grit finish) and AZ31 treated in IL for 3 hours at a constant potential of 0 V vs. Pt (green) and 3 V vs. Pt (blue).	4-132
Figure 4.78 - XRD of “as-polished” AZ31 (P4000 grit finish) and AZ31 treated in IL at a constant current of 0.05 mAcm ⁻² in IL (green) and ILAN (blue).....	4-133
Figure 4.79 - XRD of “as-polished” AZ31 (P4000 grit finish) and AZ31 treated in IL treated at a constant current of 0.5 mAcm ⁻² (green), 0.1 mAcm ⁻² (blue) and 0.01 mAcm ⁻² (pink).	4-134
Figure 4.80 - ATR-FTIR of neat [P _{6,6,6,14}][(C ₈) ₂ PO ₂] IL with approximately 1000 ppm water and bare AZ31 anodised at 0.5 mAcm ⁻² in IL.	4-135
Figure 4.81 – ATR-FTIR of AZ31 anodised at 0.5 mAcm ⁻² in neat IL (black) and 0.05 mAcm ⁻² in IL containing 6 wt% water (blue). Breakdown occurred in the wet system, leading to a final potential of 4 V with this treatment, as the system could no longer support anodic film growth.	4-136
Figure 4.82 – ATR-FTIR of AZ31 cycled between OCP and 3 V vs. Pt (black) and anodised at 0.05 mAcm ⁻² to a final potential of 4 V (blue) in wet IL.....	4-137
Figure 4.83 – ATR-FTIR of AZ31 after pre-treatment using techniques 1 (red) and 2 (purple) including a surface immersed only in 0.1 M NaOH for 30 s (black).....	4-138
Figure 4.84 – ATR-FTIR of AZ31 anodised in IL at 0.1 mAcm ⁻² after 60s pickling in a solution of nitric and phosphoric acid (red line). A comparison is provided by the pickled AZ31 surface from Figure 4.76 (black).	4-139
Figure 4.85 - ATR-FTIR of AZ31 with no films (bare - black), AZ31 anodised in IL at 0.1 mAcm ⁻² after pre-treatment in the acid mixture (red line) and AZ31 anodised in IL at 0.1 mAcm ⁻² after pre-treatment in NaOH and the acid mixture (green).	4-139
Figure 4.86 – Positive ion ToF-SIMS 2D elemental mapping of AZ31 anodised at 0.1 mAcm ⁻² to 18 V of a) ‘as-polished’ AZ31; b) acid pickled (60s HNO ₃ and H ₃ PO ₄) AZ31. C ₃₂ H ₆₈ P is the cation molecule.....	4-142
Figure 4.87 - Negative ion ToF-SIMS 2D elemental mapping of AZ31 anodised at 0.1 mAcm ⁻² to 18 V of a) ‘as-polished’ AZ31; b) acid pickled (60s HNO ₃ and H ₃ PO ₄) AZ31. C ₁₆ H ₃₄ PO ₂ is the anion molecule.....	4-143

Chapter 5

Figure 5.1 – Possible film structures for a) IL film composed of the phosphinate anion and b) magnesium phosphate (taken as $\text{Mg}_3(\text{PO}_4)_2$) film on the alloy surface. Corresponding reaction of the phosphinate with Mg: $\text{Mg}^{2+} + \text{O}_2\text{PR}_2^- \rightarrow \text{MgO}_2\text{PR}_2^+$	5-146
Figure 5.2 – Possible film composition due to deposition of the phosphinate anion onto a pickled surface with a magnesium phosphate ($\text{Mg}_3(\text{PO}_4)_2$) film.....	5-147

Appendices

Figure A. 1 – Cyclic voltammogram of two separate scans on glassy carbon: 1) polarised from OCP (approx 0 V vs. Pt) to 3 V vs. Pt at 1 mV/s and 2) polarised from OCP to -3 V vs. Pt at 1 mV/s. C1 and C2 denote the cathodic reaction peaks and A1 and A2 the anodic peaks. Arrows indicate the direction of the scans. Dashed line indicates OCP.	158
Figure A. 2 - Cyclic voltammograms of glassy carbon in dry IL in glovebox a) OCP to 3 V \leftrightarrow -3 V vs. Pt at 1 mV/s (old IL batch), b) OCP to 3 V at 1 mV/s (new IL batch) and c) OCP to -3 V at 1 mV/s (new IL batch).	160
Figure B. 1 – Structure of $[\text{P}_{6,6,6,14}][(\text{C}_8)_2\text{PO}_2]$	161
Figure B. 2 – XPS survey of purified neat IL on Au foil at a) 1486 eV and b) 790 eV.	162
Figure B. 3 – XPS spectra of P2p region at a) 180 eV; b) 330 eV; c) 530 eV; d) 1486 eV.	163
Figure B. 4 – XPS spectra of C1s region at a) 335 eV; b) 1486 eV.	163
Figure B. 5 – XPS spectra of O1s region at a) 580 eV; b) 1486 eV.	164
Figure B. 6 – O 1s spectra obtained at 790 eV of untreated AZ31 and AZ31 treated in IL at 1.5 V vs. OCP for 4 hours. O_2PR_2 = phosphinate.	165
Figure B. 7 – Mg 2p spectra obtained at 790 eV of untreated AZ31 and AZ31 treated in IL at 1.5 V vs. OCP for 4 hours. O_2PR_2 = phosphinate.	166
Figure D. 1 - Example of the correlation of the proposed model of the equivalent circuit in Figure 4.61 a) and b) on as-polished AZ31.	167
Figure D. 2 – Example of the correlation of the proposed model of the equivalent circuit in Figure 4.61 c) on AZ31 surfaces showing low frequency inductive behaviour.	167
Figure E. 1 – a) Secondary electron image of AZ31 anodised at a constant voltage of 3 V vs. Pt at 50°C for 96 hours after field crystallisation; b) EDS of point 1 and c) EDS of point 2.....	169
Figure E. 2 – a) Secondary electron image of AZ31 anodised at a constant voltage of 3 V vs. Pt at 50°C for 48 hours after field crystallisation; b) EDS of point 1; c) EDS of point 2; d) EDS of point 3 and e) EDS of point 4.	170
Figure F. 1 – Nyquist plots of AZ31 immersed in 0.01 M NaCl with and without 1, 1.2, 6.4 and 10×10^{-4} M IL after a) immediate immersion and b) 3 hours after immersion.	172
Figure F. 2 - Bode plot of phase angle of AZ31 immersed in 0.01 M NaCl with and without 1, 1.2, 6.4 and 10×10^{-4} M IL for 0 and 3 hours after immersion.	172

Figure F. 3 – Potentiodynamic polarisation of AZ31 in solutions containing 0.01 M NaCl and 0 (control), 100 and 500 ppm added $[P_{6,6,6,14}][C_8]_2PO_2$.	173
Figure F. 4 – Optical micrographs of AZ31 immersed for 3 hours in a) 0.01 M NaCl; b) 0.01 M NaCl and 10^{-4} M IL; c) 0.01 M NaCl and 1.2×10^{-4} M IL; d) 0.01 M NaCl and 6.4×10^{-4} M IL; e) 0.01 M NaCl and 10^{-3} M IL.	175
Figure F. 5 – Optical profilometry of AZ31 after 3 hours immersion in neutral 0.01 M with a) 0 M IL; b) 10^{-4} M IL; c) 1.2×10^{-4} M IL; d) 6.4×10^{-4} M IL; e) 10^{-3} M IL.	177
Figure F. 6 – SEM images at 5 keV of AZ31 after 3 hours immersion in a)-b) 0.01 M NaCl; c) 0.01 M NaCl + 10^{-4} M IL; d)-e) 0.01 M NaCl + 1.2×10^{-4} M IL.	178
Figure F. 7 – SEM images at 5 keV of AZ31 after 3 hours immersion in a)-b) 0.01 M NaCl + 6.4×10^{-4} M IL; c)-d) 0.01 M NaCl + 10^{-3} M IL.	179
Figure F. 8 – SEM images of AZ31 exposed to a 5 μ L droplet of 0.01 M NaCl for 24 hours at 80-90 %R.H. a) the entire droplet (lighter area) b) corrosion product over a large pit surrounded by mud-cracking of magnesium hydroxide/oxide.	180
Figure F. 9 - SEM images of AZ31 exposed to a 5 μ L droplet of 0.01 M NaCl containing 1.2×10^{-4} M $[P_{6,6,6,14}][C_8]_2PO_2$ for 24 hours at 80-90 %R.H. a) a large pit and surrounding area b) zoomed in image of corrosion product over the large pit, surrounded by mud-cracking of magnesium hydroxide/oxide.	181
Figure F. 10 - SEM images of AZ31 exposed to a 5 μ L droplet of 0.01 M NaCl containing 6.4×10^{-4} M $[P_{6,6,6,14}][C_8]_2PO_2$ for 24 hours at 80-90 %R.H. a) a large pit and surrounding area b) zoomed in image of corrosion product over the large pit, surrounded by mud-cracking of magnesium hydroxide/oxide.	182
Figure H. 1 – Cyclic voltammetry of $[P_{6,6,6,14}][C_8]_2PO_2$ on glassy carbon with the addition of 5 mM ferrocene. Scanned from OCP \rightarrow 3 V \rightarrow -3 V. Inset is zoomed portion of the curve.	184
Figure H. 2 - Cyclic voltammetry of $[P_{6,6,6,14}][C_8]_2PO_2$ on glassy carbon with the addition of 10 mM cobaltocenium. Scanned from OCP \rightarrow -2.5 V \rightarrow 2.5 V.	185
Figure H. 3 – Open Circuit Potential vs. time curves for Pt reference electrode immersed in $[P_{6,6,6,14}][C_8]_2PO_2$ IL. “After 24hrs” and “After 48hrs” refer to electrodes stored in IL prior to this test for 24 and 48 hours respectively. “Fresh Pt” refers to Pt polished just prior to the test.	186

List of Tables

Chapter 3

Table 3.1 - Elemental composition of commercial AZ31[33].	3-29
Table 3.2 – Compositions of dilute IL solutions prepared.	3-31
Table 3.3 – Scan bounds used for evaluating electrochemical behaviour of AZ31 and GC. All scans were repeated 3 times (total of 4 cycles).	3-32

Chapter 4

Table 4.1 – Relationships calculated from Figure 4.1.	4-45
Table 4.2 – Surface roughness values for constant-voltage treated surfaces obtained from optical profilometry data over a 937.5 x 1249.7 μm area.	4-72
Table 4.3 - Surface roughness values for constant-current treated surfaces obtained from optical profilometry data over a 94 x 125.3 μm area.	4-80
Table 4.4 – Charge densities passed during anodising.	4-83
Table 4.5 – Roughness values obtained through optical profilometry of sites of breakdown in Figure 4.35.	4-85
Table 4.6 – solutions and technique used to pre-treat AZ31 prior to application of IL film formation processes.	4-106
Table 4.7 – Film resistance and capacitance obtained from fitting of equivalent circuits. The qualities of the fits for these models are presented in Appendix D. Capacitance was calculated from resistance using an online calculator[142].	4-112
Table 4.8 – Tafel extrapolations pre-treated AZ31 surfaces tested in 0.01 M NaCl solution. Measurements were made 20 mV either side of E_{corr} over 20 mV lengths.	4-121
Table 4.9 - at% of elements found in XPS survey for specimens anodised in IL at constant potentials (vs. OCP) for 4 hours.	4-124
Table 4.10 - at% of elements found in XPS survey for specimens anodised in IL at constant current densities to a cut-off potential of 18 V.	4-124
Table 4.11 – Bond positions and peak identities for neat IL.	4-134

Appendices

Table B. 1 - at% of elements found in XPS survey and the expected quantity based on chemical composition.	161
Table C. 1 - % area of separate peaks in the C 1s and O 1s spectrums at 790 and 1486 eV for CP 1 and 2. Binding energies for the peaks are indicated in brackets in eV.	166
Table C. 2 - %area composition of numerous species from the C1s and O 1s spectra. Binding energies for the peaks are indicated in brackets in eV.	166
Table F. 1 – Tafel extrapolations of solutions of 0.01 M NaCl containing no (control), 100 and 500 ppm IL.	173
Table G. 1 - impurities between as received Cytec IL and purified IL. (1mL IL: 1000mL solution)	183

List of Publications from PhD

Journal Papers

J.-A. Latham, P.C. Howlett, D.R. MacFarlane, M. Forsyth, *Electrochim. Acta*, **56** (2011) 5328-5334

“Electrochemical reactivity of trihexyl(tetradecyl)phosphonium bis(2,4,4-trimethylpentyl)phosphinate ionic liquid on glassy carbon and AZ31 magnesium alloy”

J.-A. Latham, P.C. Howlett, D.R. MacFarlane, M. Forsyth, *Electrochem. Comm.*, **19** (2012) 90-92

“Passive film formation in dilute ionic liquid solutions on magnesium alloy AZ31”

Conference Proceedings

J.-A. Latham, P.C. Howlett, D.R. MacFarlane, M. Forsyth, *Proceedings of the 18th ICC conference*, (2011) paper 116

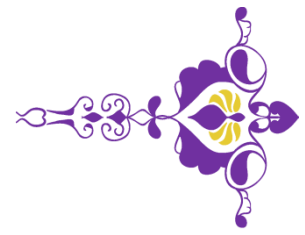
“Anodic Oxidation of AZ31 Mg Alloy in Ionic Liquid”

List of Abbreviations

ANSO	0.1 M Lithium Triflate in Acetonitrile
ATR-FTIR	Attenuated Total Reflectance Fourier Transform Infra-Red
CV	Cyclic Voltammetry
Dilute ILAN	0.01 M IL in Acetonitrile
E	Potential
E_{corr}	Corrosion Potential
EDS	Energy Dispersive X-Ray Spectroscopy
EIS	Electrochemical Impedance Spectroscopy
E_{pf}	Forward Peak Potential
E_{pr}	Reverse Peak Potential
FIB-SEM	Focused Ion Beam Scanning Electron Microscopy
FTIR	Fourier Transform Infra-Red
GC	Glassy Carbon
I	Current
i_{corr}	Corrosion Current
IL	Ionic Liquid
ILAN	0.1 M IL in Acetonitrile
i_{pf}	Forward Peak Current
i_{pr}	Reverse Peak Current
J	Current Density
Mg(OH) ₂	Magnesium Hydroxide
MgO	Magnesium Oxide
OCP	Open Circuit Potential
PP	Potentiodynamic Polarisation
SEM	Scanning Electron Microscope
ToF-SIMS	Time of Flight Secondary Ion Mass Spectroscopy
ν	Scan Rate
XPS	X-Ray Photoelectron Spectroscopy
XRD	X-Ray Diffraction
Z	Impedance
Z'	Real Impedance
Z''	Imaginary Impedance



Chapter 1



Introduction

1.1 Magnesium and AZ31 Alloy

Magnesium and its alloys have a wide range of attractive properties. These include high specific strength and stiffness, low density, good fluidity, hot formability, easy machinability and good damping[1]. In particular, the light weight of magnesium alloys makes them very attractive for applications in the transportation industries.

AZ31 (3% Al 1% Zn, Mg alloy) belongs to the AZ (magnesium-aluminium-zinc) class of magnesium alloys, which are the most common magnesium alloy family[2]. AZ alloys are very versatile, used in both casting and wrought applications. The microstructure is comprised of two main phases: the solid solution α phase matrix and the $Mg_{17}Al_{12}$ β phase, which form a network along the grain boundaries[2]. The addition of aluminium allows solid-solution strengthening, precipitate hardening and improves the castability of magnesium[2]. Zinc acts as a weak grain refiner in magnesium but also allows precipitation hardening and, like aluminium, it improves the castability of the alloy.

Unfortunately, the use of magnesium alloys, primarily the wrought alloys such as AZ31, is limited due to poor corrosion properties. Magnesium is very active thermodynamically, such that it will spontaneously and rapidly oxidise in environments containing oxygen or water[3]. The presence of moisture in the air will cause the oxide (MgO) to react with water to form $Mg(OH)_2$, which results in both species present on the surface[3, 4]. Due to the hexagonal unit cell of magnesium, mismatching exists between the metal and the structure of hydroxide and oxide films[5]. The passive layer also possesses a greater molar volume than the metal[6] which, alongside the mismatching, results in the passive layer being under compressive stress which leads to rupture and cracking[5-7]. With cracks present in the passive layer, ingress of electrolytes can occur which leads to corrosion. In small amounts both aluminium and zinc do little to improve the corrosion resistance of AZ31 versus pure magnesium. Studies have shown that the aluminium content in solid solution can work to significantly increase the corrosion resistance of these alloys[4]. The corrosion properties are improved as aluminium oxide (Al_2O_3) is incorporated into the surface film. Al_2O_3 is far more stable than MgO and $Mg(OH)_2$, which improves the overall corrosion resistance of the alloy. However, at only 3 wt% Al (in AZ31) not enough aluminium is incorporated into the surface film and the aluminium is actually detrimental as it acts as cathodes in the microstructure, in the form of β phase. Consequently, higher aluminium containing AZ91 and AZ80 alloys show better corrosion properties than AZ31[4].

As a result, steps need to be taken to prevent or minimise the corrosion of magnesium alloys. Whilst a considerable amount of research has been done into optimising the microstructure to minimise microgalvanic corrosion processes between the α phase and cathodic particles, the

very anodic potential of magnesium metal means that these alloys will still undergo significant galvanic corrosion when in contact with other metals and alloys (in the presence of an electrolyte). Alterations to the alloying and microstructure of magnesium alloys do not and cannot address this problem. Hence, it is necessary to apply a protective coating which will provide a barrier against both the electrolyte and contact with another metal. In addition, to make magnesium competitive, the coating needs to be economical and simple to apply. Up until recently the most common methods of cheaply improving the corrosion performance of magnesium alloys was through the use of chromate compounds. Chromates have been used for surface activation (through immersion in chromic acid) to form a base for other coatings (e.g. paint, sol-gels), to form chemical conversion layers (CCC), and as a component in electrolytes for anodising. However, this compound has since been found to be highly toxic and carcinogenic[8, 9]. Environmental concern and regulations has led to development of alternative environmentally friendly solutions[9]. This results in the need for new protective systems to be developed for magnesium alloys, particularly wrought magnesium alloys.

1.2 Ionic Liquids and Corrosion

Ionic liquids (ILs) are salts which contain very large or unsymmetrical organic and/or inorganic anions and cations. The size and unsymmetrical nature of these molecules restrict their capability to order into a solid phase and hence, by definition, exhibit a melting temperature below 100°C. Room temperature ionic liquids (RTILs) are ILs which are liquid at room temperature and hence exhibit considerably low melting temperatures. The fact that these materials are liquid at room temperature means they can behave as an electrolyte (due to the charged anion and cation molecules) without the need of a solvent (such as water). This lends these materials exclusive properties over other, 'classical', liquid electrolytes. Due to the unique combination of properties including the low vapour pressure[10], high thermal and chemical stability, high electrochemical stability[11] and high ion conductivity[12] ILs are an attractive material for use as electrolytes in a number of applications, including batteries[13, 14], dye sensitised solar cells (DSSCs)[15, 16] and electroplating/electrodeposition[16-18].

The use of ionic liquids (ILs) to form corrosion protective films on magnesium alloys is still very new and has only had minor investigation in the last decade. Some research has also gone into studying the corrosive effects of ILs against different alloys rather than their ability to form films on alloy surfaces. The first extensive study on the corrosion properties of ILs was undertaken with commercial alloys by Uerdingen *et al*[19]. This study involved a range of materials including carbon steel, Hastelloy C22 (Ni-base), stainless steel, brass, copper, and aluminium (AlMg3), which were exposed to a range of imidazolium and quaternary ammonium based ILs at 90°C under flow conditions. The authors found that the ILs were generally non-corrosive but that the corrosive effect was controlled by the anion of the IL[19]. In dry IL, even the reactive aluminium alloy experienced low corrosion rates[19]. In another study, the effect of IL on magnesium alloy AZ91D was investigated by Caporali *et al*[20] and found that the rate of corrosion of AZ91D in the IL was slow, particularly at room temperature. XPS analysis of the AZ91D surface after exposure to 1-butyl-3-methyl-imidazolium bis(trifluoromethanesulfonyl)amide [BMIm][Tf₂N] IL at 200°C ranging from 1 to 30 days revealed breakdown products of the IL anion ([Tf₂N]) on the AZ91D surface[20]. In addition to this, Howlett *et al*. [13, 14], in studies of lithium batteries using an IL, found a passive solid electrolyte interphase formed on the lithium electrode from the reduction products of the IL anion during cycling.

After it was established that a passive film formed on lithium metal[13, 14], interest in the use of ionic liquids to mitigate corrosion on reactive magnesium alloys emerged. One of the most beneficial properties regarding ILs and their potential for dealing with reactive metals for corrosion purposes is that they are non-aqueous. In a pure IL the water content is negligible and thus it would be expected that the standard aqueous based corrosion reactions will not occur in well dried ILs. Early work into the protective quality of films formed from ILs was performed using tri(hexyl)tetradecyl phosphonium bis(trifluoromethanesulfonyl)amide ($[P_{6,6,6,14}][NTf_2]$) on Mg alloy AZ31[21]. Significant reduction in the corrosion current in 0.1 M NaCl was experienced after 17 hours of IL treatment. In addition, self-healing behaviour was witnessed. The surface films formed from this IL were able to withstand 21-30 days in 100% humidity without significant evidence of corrosion[21]. Following work found that extended treatment times (24 hours vs. 1 hour) could lead to a defective film, which performed worse in corrosion conditions[22]. Work using this IL has found that the $[NTf_2]$ anion plays a direct role in the film composition as EDS analysis of the films registered significant levels of F, C, P and S[21, 22].

More recently, a number of studies have focused on the influence of applying a potential bias to the system. In a study by Howlett *et al* [23] on AZ31 and ZE41 using trihexyl(tetradecyl)phosphonium bis(2,4,4-trimethylpentyl) phosphinate $[P_{6,6,6,14}][iC_8)_2PO_2]$ AZ31 was polarised to -0.1 and 0.1 V vs. OCP and ZE41 was polarised to potentials up to 0.5 V vs. Ag/AgCl. In both cases an anodic potential led to increased surface resistance (measured by EIS). XPS analysis of ZE41 treated with $[P_{6,6,6,14}][iC_8)_2PO_2]$ at 0.25 V vs. Ag/AgCl for an hour found evidence of phosphate species, magnesium hydroxide and magnesium oxide. The authors concluded that the film formed on the surface was a composite between the oxide and hydroxides and the IL anion.[23] Efthimiadis *et al* [24] studied the effect of a potential bias on ZE41 with trihexyl(tetradecyl)phosphonium diphenylphosphate ($[P_{6,6,6,14}][DPP]$) IL. ToF-SIMS revealed that the application of a -0.2 V vs. OCP bias provided a more uniform film deposition than a treated surface at OCP.

1.3 Research Problem, Hypothesis and Aims

1.3.1 Research Problem

Due to environmental concerns, the demand for improved fuel economy in our transportation sector is growing. This demand requires materials which possess good strength-to-weight ratios, of which magnesium alloys, including AZ31, fulfil. Indeed, if wrought magnesium alloys can replace steel and aluminium as the main components constructing the body of cars, buses, planes, etc. the weight savings would be significant. However, to be used in these applications the magnesium alloy needs to have sufficient corrosion resistance to perform in coastal and industrial areas with corrosive airborne pollutants. Herein lays the problem. Protecting magnesium alloys from corrosion is not easy and with the banning of chromates the solution to this problem has become more difficult. New solutions to the problem of corrosion must be environmentally conscious as well as relatively cheap, easy and controllable. However, of most importance is the ability to adequately protect the alloys from corrosion. Research into a number of possible solutions has so far not resulted in a technique which satisfies these conditions.

1.3.2 Working Hypothesis and Aims

Previous research has shown improvement on the ability to form a corrosion protective surface film on Mg alloys in ionic liquids by applying a small, static potential bias to the alloy[23, 24]. Depending on the alloy and the IL used in these studies the polarity of the potential bias which

yielded the best film could be either anodic or cathodic. As yet, there is no understanding of the specific effect of the application of these potential biases on the film forming process.

Hence, three main working hypotheses were developed for this PhD:

1. *The application of electrochemical techniques, such as a potential bias, during immersion in an ionic liquid will allow for control over the formation of a passive IL film on magnesium alloys.*
2. *Homogeneity of the film formed on AZ31 can be enhanced through the application of an appropriate potential bias.*
3. *Film deposition will be dependent not only on the polarised potential of the working electrode, but also the way in which the potential is applied (including time and rate etc).*

These hypotheses were tested using magnesium alloy AZ31 and ionic liquid tetradecyltrihexylphosphonium bis(2,4,4-trimethylpentyl)phosphinate ($[P_{6,6,6,14}][[(C_8)_2PO_2]$).

The specific project aims can therefore be summarised as the following:

- To understand and characterise the electrochemical behaviour between AZ31 and the IL, and how these affect the formation of the film.
- To determine the effect of different polarities and magnitude of potential, immersion time and water and oxygen content on the film forming process.
- To investigate applying the potential by current control.
- To characterise the composition and morphology of the films formed and gain an insight into the mechanism of film formation.
- To determine, through corrosion testing, the optimum process for forming a corrosion resistive film on AZ31 in $[P_{6,6,6,14}][[(C_8)_2PO_2]$.

The research scope of this project was very wide. In addition, deviations in the research direction were often made due to significance in certain results. However, these aims were broken down into three phases which describe the basic experimental regime of this PhD.

1.3.3 Research Plan

The first phase of the project involved gaining an understanding of the electrochemical behaviour of AZ31 in tetradecyltrihexylphosphonium bis(2,4,4-trimethylpentyl)phosphinate ($[P_{6,6,6,14}][[(C_8)_2PO_2]$) using cyclic voltammetry and a non-reactive glassy carbon electrode as a comparison. This was done to determine the effects of polarity, water and oxygen in the film forming process. By first gaining an idea of the behaviour of the IL on AZ31, this would allow for improved selection of the techniques used for actively forming the films. The basic structure of this is represented graphically in Figure 1.1.

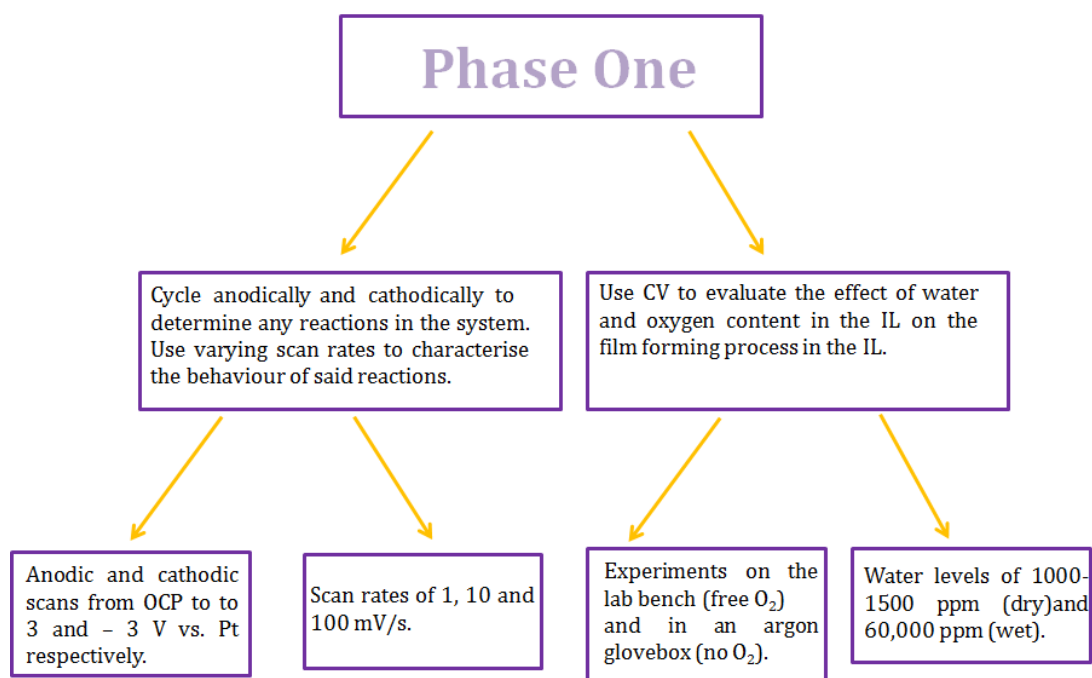


Figure 1.1 – Flow diagram of research program in phase one: electrochemical behaviour of AZ31 in IL [P_{6,6,6,14}][(tC₈)₂PO₂].

The second phase (Figure 1.2) of the project involved using constant potential techniques to form films on AZ31. This included using relatively low (< 2 V vs. Pt) and relatively high (3 V vs. Pt) potentials for a range of exposure times. These films were then characterised (where possible) for their composition, morphology and corrosion resistance. The aim was to understand the effect of the magnitude of the potential in addition to the time of exposure on the ability to form a protective film. With high potentials the phenomenon of field crystallised films was investigated to determine whether these films could be used in corrosion settings.

The third phase (Figure 1.3) involved using a constant current approach to film formation rather than constant voltage. This was because it is generally considered that anodising using a constant current is more controllable (hence films more reproducible) than constant voltage anodising. In addition, static application of high voltages can lead to unpredictable crystallisation processes.

This was done by applying a number of different current densities to a final potential of 18 V. The effect of the different current densities on film formation was investigated, including changes to film composition, morphology and corrosion performance. The effect of an acid pre-treatment was also investigated with respect to the process film formation corrosion protection.

Phase 2 and 3 were used comparatively to determine if one method was superior to another for film formation in this IL on AZ31.

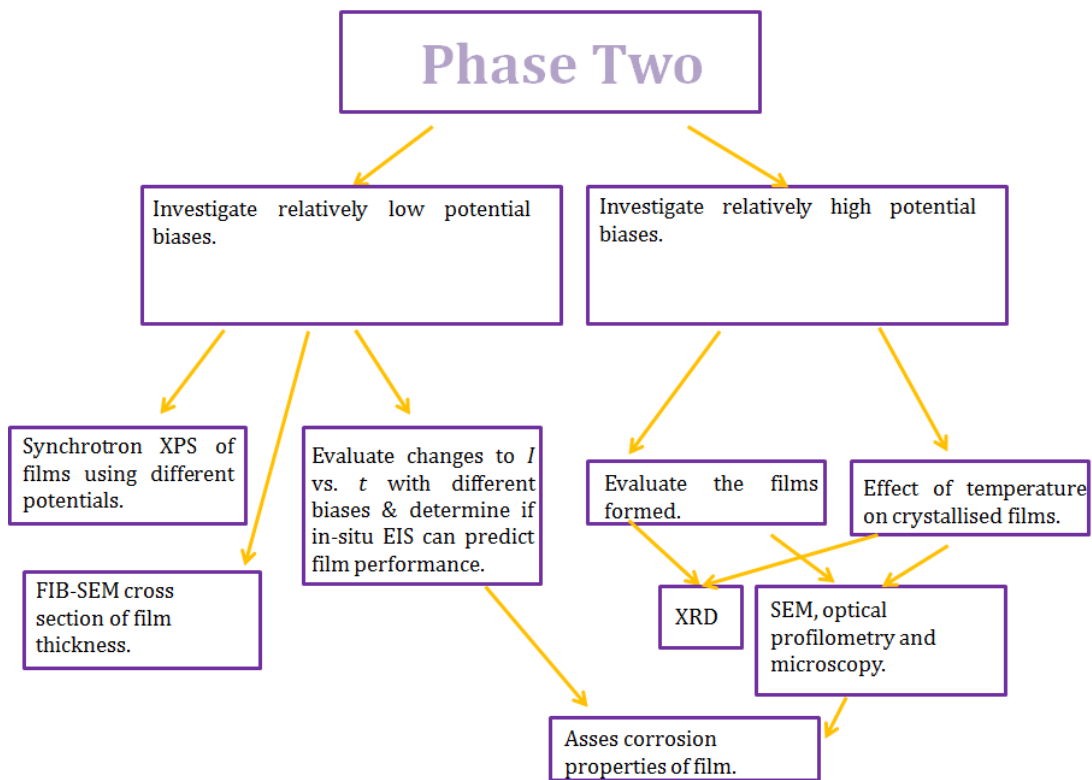


Figure 1.2 - flow diagram of research program in phase two: film forming via potentiostatic methods.

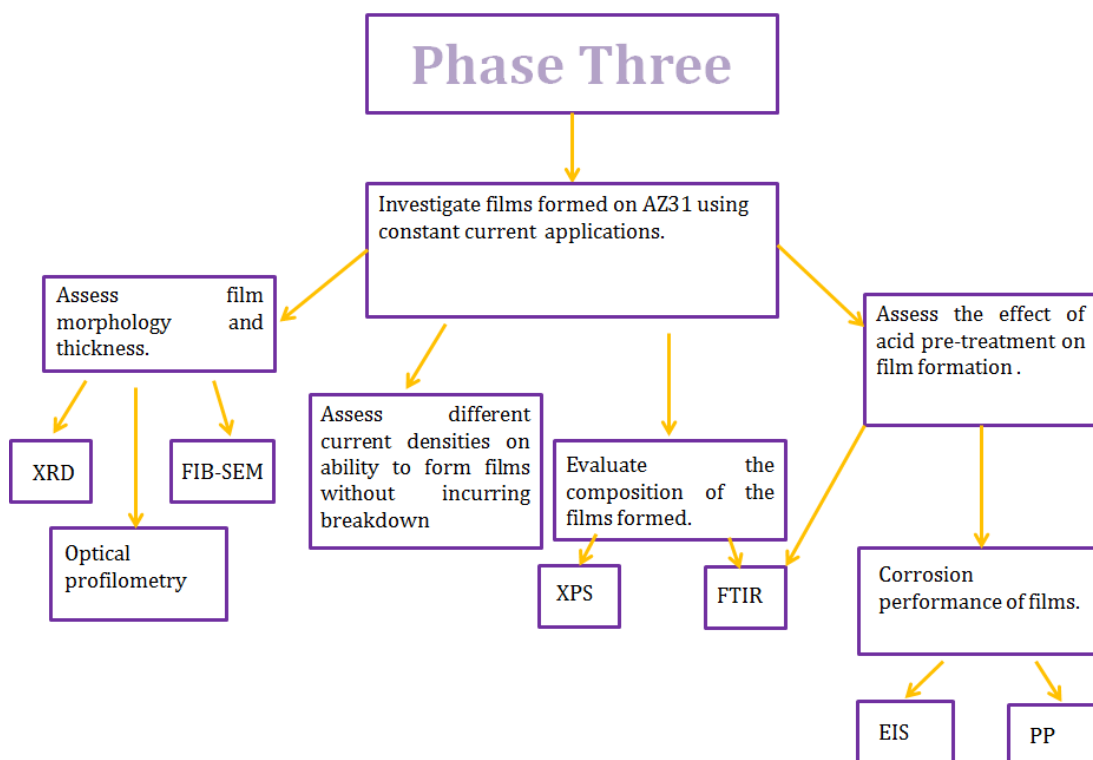


Figure 1.3 - flow diagram of research program in phase three: film forming via galvanostatic methods.



Chapter 2



Literature Review

2.1 Magnesium and Magnesium Alloys

2.1.1 A Brief History of Magnesium

The following has been adapted from K. Harbodt, in *Magnesium Technology - Metallurgy, Design Data, Applications*.pp. 1-25[25].

Magnesium is the eighth most abundant element in the universe and the seventh most abundant in Earth's crust, constituting 2% of the crusts total mass[26]. Magnesium was first discovered in 1774[26], but was first isolated in England by Sir Humphrey Davy in 1808; however it was not entirely pure. Pure magnesium was first produced by Antoine Bussy in 1830, using the same technique to produce pure aluminium: reacting magnesium chloride with potassium at elevated temperatures. However, it wasn't until the process of electrolytically extracting magnesium was discovered that the metal could be produced commercially. Nonetheless, magnesium was not widely used, only being produced in Germany, which was the only manufacturer of magnesium from 1868 to 1915.

The first AZ alloys (2.5-3.0% Al & 3.0-4.0% Zn) were produced and used in automobile pistons in Germany in 1924. Cast magnesium alloys found further applications in automobiles by Prof. Porsche. These included the 8-cylinder Tatra motor and 20 kg worth of magnesium used in the newly designed Volkswagen Beetle. Meanwhile in Great Britain, due to the poor corrosion properties of cast magnesium parts, manganese was added to magnesium alloys for the first time in 1926. The demand for magnesium in vehicles increased in 1928 due to a regulation that licensed vehicles based on weight, which led to the manufacturing of crank casings, gearboxes and axle shafts being switched to magnesium.

During WWII considerable amounts of magnesium metal were being produced in Germany, Italy, Great Britain and the U.S.A. for use in military vehicles and aircraft. The British company MEL (Magnesium Elektron – founded in 1934) initially used magnesite as the raw material for magnesium production, however as WWII loomed they switched to using magnesia from sea water, becoming the first company to do so in 1939. This year also saw the development of the Pidgeon process by Canadian Lloyd M. Pidgeon, for developing especially pure magnesium from dolomite. The Northrop XP-56, in 1940, was the first airplane designed to be almost completely constructed from magnesium.

In 1944 the global production of magnesium was approximately 210,000 tonnes. However, after the end of WWII the production dropped dramatically, in part due to the prohibition on Germany but also in Japan due to lack of resources. All 15 magnesium plants owned by the U.S.A. government were shut down by November 1945. Private factories were also closed,

leaving Dow's Freeport plant the only magnesium plant in the U.S.A. By 1947 no magnesium plants in Great Britain were producing magnesium.

Since much of the magnesium produced in the first half of the 20th century was used in wartime applications, after WWII the main use of magnesium was only in the Volkswagen Beetle. The demand for magnesium during peacetimes was so low that associations were developed in the UK and North America to think of new applications for the metal. Some applications included wrought magnesium for corrosion protection of hot water systems, hand trucks, chain saws and battery racks. Dow purchased a plant in Illinois to begin wrought magnesium production and throughout the 1950s produced a large amount of magnesium sheet that was used in rockets and aircrafts (including AZ31B in the Titan I rocket). Other uses for wrought magnesium included luggage, flooring and roof railings. However, with the increasing price of magnesium, many operations in magnesium plants were switched to aluminium. Interestingly, new ideas for the use of magnesium often came from outside of the magnesium industry. One in particular was the use of magnesium as an alloying element in aluminium as a result of the growing demand for aluminium beverage cans and also in aluminium auto-body sheet. Currently the die-cast magnesium industry is rapidly growing, primarily due to environmental demands in modern vehicles.

2.1.2 Properties and Uses of Magnesium and its Alloys

Magnesium and its alloys have a wide range of attractive properties. These include high specific strength and stiffness, low density, good fluidity, hot formability, easy machinability and good damping[1]. In particular the good fluidity of magnesium makes it easy to cast very complex and thin-walled (1.5 mm) shapes quickly and with less energy consumption used to cast other metals[1]. In comparison to aluminium (its greatest competitor) magnesium uses approximately 77% less energy to cast the same part using HPDC (high pressure die casting)[25]. In addition, unlike aluminium, magnesium does not solder to the die during casting and as a result the expensive die lasts longer[25]. The complex shapes formed find applications in automotive and aerospace applications. Current applications of magnesium alloys include aircraft frames[1], engines[1], transmission cases[1], missile skins and frames[1], ladders[27], electronic housings[1, 27], mobile phone casings[1], laptop cases[1, 27], cameras[1], hand luggage[1, 27] gravity conveyors[27], grain shovels[27] and power tools[1].

However, there are many non-structural applications of magnesium. As mentioned earlier, magnesium is often used as an alloying element in aluminium, lead and zinc alloys[27]. In addition, magnesium is used as an oxygen scavenger and desulfuriser[25] in the manufacture of nickel, copper, iron and steel[1]. Magnesium is also used as a reducing agent and is still used in pyrotechnics. Due to the high electronegativity of magnesium, it will corrode preferentially to most metals. As a result magnesium is often used as sacrificial anodes to protect other metals from corrosion. Other applications include dry cell, seawater and reserve cell batteries, and lithography.

Due to the attractive properties of magnesium it's surprising that only a small percentage (1% in 2007[1]) of automotive parts are currently manufactured from magnesium. However, this has been attributed to the relative high cost of magnesium, low wrought formability, making sheet manufacture more difficult than steel, low corrosion resistance and lack of experience in forming and design[1]. However, overwhelmingly the main obstacle for use of magnesium alloys is still cost[28]. Currently, within the auto industry magnesium alloys are used to manufacture car seat frames[1, 28], airbag housings[28], gear box manifolds[28], intake manifolds[28], door frames[1], instrument panels[1], consoles[1], engine blocks[1], steering wheels[1, 28], engine

cradles[1] and transmission cases[1]. Currently, Volkswagen cars contain approximately 25 kg of magnesium, however it has been suggested that in the future it is not unrealistic to consider this figure rising to around 80 kg[28]. However, these are all cast products and all located on the inside of the vehicles. When compared to aluminium, the costs for cast magnesium products are generally favourable. This is due to a number of factors, including:

1. Magnesium has a lower melting temperature than aluminium[29].
2. Aluminium will attack its steel die, whereas magnesium will not. This results in the magnesium tool life being over three times greater than for aluminium. As an example provided on magnesium.com[29], an aluminium tool may last 150,000 shots before requiring replacement or repair whereas a comparable magnesium tool will last approximately 500,000 shots.
3. Shorter casting cycle times. Magnesium has both high fluidity[1] and solidification rate, which means the magnesium is not only injected quicker (and with less pressure) than aluminium but its fast solidification means it can be ejected from the die faster. In addition, as the magnesium does not interact with the die steel (unlike aluminium) the cast item will not stick to the die and therefore the tool does not need to be lubricated as often[29].
4. Magnesium is significantly easier to machine than magnesium[1]. Due to its high heat dissipation and natural lubricity magnesium can be machined dry and with less tool wear. In addition, less machining is actually required on magnesium cast pieces as better tolerances can be achieved in cast magnesium over aluminium[29].

The specific strength of magnesium is equal to or greater than traditional aluminium auto alloys, meaning considerably greater weight reductions could be achieved if used as car panels[1]. Magnesium is also able to compete with polymers and composites due to having greater specific stiffness: again, this allows for greater weight reduction[1]. Whilst the formability of magnesium is generally quite low (due to the hexagonal crystal lattice), complex wrought shapes can still be produced at elevated temperatures. In addition, magnesium does not exhibit a ductile-to-brittle transition, allowing them to operate at low temperatures without compromising performance[1].

Extruded magnesium alloys find most of their applications in aerospace, luggage, nuclear industry, hand tools, bicycles and motorcycles. However, whilst many cast magnesium components are used in the automotive industry there are only proposed uses for wrought magnesium alloys in cars. Currently, the cost of magnesium alloys and the plastic anisotropy and tension-compression asymmetry limit the use of wrought magnesium alloys in cars[1].

As mentioned previously in 2.1.1, magnesium saw extensive use in the construction of aeroplanes and helicopters in the past (particularly WWII). Unlike the use of magnesium in automobiles, applications in aerospace generally saw the use of wrought magnesium products. Early airplane uses of wrought magnesium included fuel tanks and propellers. The list of applications throughout the first half of the 20th century grew to include wing frames, seat frames, body panels, tail cones and doors, among others[30]. However, its use declined as the poor corrosion properties (both atmospheric and galvanic) were discovered[30]. Currently, it is this poor corrosion resistance, particularly the galvanic aspect, which prevents its widespread use in aerospace. Currently, small components of magnesium are used in aeroplanes, including parts of wings and doors in the Boeing B707, B727, B737 and B747 and the nose canopy in the B29[30]. An interesting reason magnesium use on commercial airplanes is low is due to the fear of magnesium burning. In particular since the September 11 attacks on the U.S.A., aeroplanes have been designed to ensure that no components in the passenger cabin are constructed from

magnesium alloys, despite, for example, the joystick in the cockpit being manufactured from cast magnesium alloy[30]. Applications in space, however, see the widespread use of magnesium composites since corrosion does not pose an issue[30]. Unfortunately, lack of understanding of the corrosion of magnesium and magnesium alloys within industry as well as lack of knowledge in their mechanical properties and methods of processing often see them overlooked for aluminium alloys[30]. For example, in the U.S.A. military the view on magnesium is that it does and always will corrode[30]. F.H. Froes et al.[30] suggest that whilst the development of new magnesium alloys may see more exposure, of critical importance is the development of cheap and effective corrosion protection.

2.1.3 AZ Series

The AZ (magnesium-aluminium-zinc) class of magnesium alloys are the most common alloy family[2] and are very versatile, used in both casting and wrought applications. The microstructure is comprised of two main phases: the solid solution α phase matrix and the $Mg_{17}Al_{12}$ β phase, which form a network along the grain boundaries[2]. The β phase forms along the basal plane of the α phase as coarse laths and are not very responsive to age hardening. Al-Mn precipitates are also found in the microstructure. The stoichiometry of these Al-Mn particles can vary, including Al_2Mn , Al_3Mn , Al_4Mn , $Al_{11}Mn_4$, Al_8Mn_5 , $Al_{19}Mn_4$ and $Al_{10}Mn_3$ [31].

The addition of aluminium allows solid-solution strengthening, precipitate hardening and improves the castability of magnesium[2]. Zinc acts as a weak grain refiner in magnesium but also allows precipitation hardening and, like aluminium, it improves the castability of the alloy[2]. In particular, the alloy AZ91 (containing 9 wt% Al, 1 wt% Zn) can be used in a number of casting methods and is used in the automotive industry for a number of parts (as AZ91D and AZ91E) including brake brackets, clutch brackets, gearbox housing, intake manifolds, airbag housing, wheels and manual transmission cases among others[1]. Whilst the addition of aluminium to magnesium as an alloying element increases the tensile strength, the ductility is lowered and parts cannot be exposed to temperatures $> 125^\circ\text{C}$ due to poor creep resistance (due to the β phase). However, simply lowering the aluminium content does not eliminate the creep problems and hence AZ class alloys are not currently used in high temperature applications such as engine blocks within cars[1].

2.1.3.1 AZ31

With its low Al content, AZ31 is a wrought alloy. The main fabrication methods include extrusion, rolling and press forging at elevated temperatures in the range of $300\text{-}500^\circ\text{C}$ [26]. There are few magnesium sheet alloys available commercially, the most common is AZ31B. AZ31 is often extruded and common components include rods, bars, tubes and plate[32]. AZ31 is a cheap magnesium alloy and if an application requires a lightweight alloy with moderate strength, AZ31 is often chosen[27], however it is not used in applications where the temperature may exceed 148°C [32]. AZ31B is used in cathodic protection and AZ31C (the less pure version) is used in lightweight structural applications where corrosion performance is not a primary concern[27]. Even so, the poor corrosion performance and cost of producing sheet from AZ31 and other magnesium alloys prevent its use in other possible applications, particularly as auto body sheet. AZ31 alloy is only used in wrought conditions as it shows good formability but lacks the aluminium content for casting (e.g. vs. AZ91 – ≈ 9 wt% Al). The lower content of aluminium also reduces the amount of β phase in the alloy and subsequently the corrosion properties of the alloy (see section 2.2). The commercial composition of AZ31 is listed below in Table 2.1.

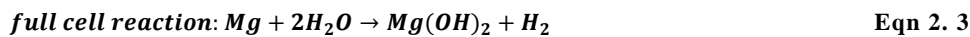
Table 2. 1 – Commercial composition of AZ31B alloy[33].

Element	Al	Zn	Cu	Mn	Si	Ni	Mg
wt%	2.50-3.50	0.60-1.40	<0.05	>0.20	<0.1	<0.005	97.0

2.2 Corrosion of Mg and AZ Alloys

Under regular environmental conditions, the corrosion of magnesium is comparable or superior to mild steel. However, the perception that magnesium corrodes rapidly persists[26]. This is in part due to misuse of the material in wet and polluted environments (e.g. near the ocean with Cl⁻ ions) and poor design resulting in unfavourable galvanic coupling[26].

Magnesium is very active thermodynamically, such that it will spontaneously and rapidly oxidise in environments containing oxygen or water[3]. In a neutral or basic aqueous environment magnesium will corrode by the formation of magnesium hydroxide (Mg(OH)₂), through the following:



In acidic solutions magnesium will oxidise to Mg²⁺ accompanied by the cathodic evolution of hydrogen gas (H₂)[3]. Magnesium is only thermodynamically stable as a metal at very low potentials and the Mg(OH)₂ surface film is only stable in highly alkaline solutions (pH > 11.5). Unfortunately, these conditions are rare and more often than not working conditions will be closer to neutral and the potential of the magnesium surface will be at its equilibrium potential and in many cases the open circuit potential (OCP) in solutions will be higher than the equilibrium potential[3]. As such, the potential of magnesium often sits in the corrosion region of the Pourbaix diagram. In addition, the passive region is not always true to its name. With the addition of corrosive ions, e.g. chloride ions (Cl⁻), magnesium will never be passive[3]. The formation of Mg(OH)₂ on the surface is primarily due to surface alkalisiation.

Magnesium, like aluminium, has a high affinity to oxygen and can form a resistant surface film. In aqueous solutions the surface film on magnesium will be comprised primarily of Mg(OH)₂ as opposed to magnesium oxide (MgO) as it is more thermodynamically stable. However, in dry air the opposite is true and the surface film will be primarily composed of MgO[3]. Also, the presence of moisture in the air will cause the oxide to react with water to form Mg(OH)₂, which results in both species present on the surface[3, 4]. In addition, carbon dioxide (CO₂) in the air can also react with the surface to form magnesium carbonate, which is commonly found on surfaces of magnesium exposed to the natural environment[3]. Industrial pollutants in the air, e.g. SO₂, can also react to form magnesium sulphate compounds. Magnesium alloys have a good resistance to atmospheric corrosion as the surface film forms in a similar manner to aluminium. Therefore, when atmospheric corrosion does occur, it is due to the breakdown of the surface film. With increasing relative humidity (R.H.) the corrosion of magnesium alloys will increase and when pollutants are present (e.g. Cl⁻ in marine conditions and industrial pollutant such as SO₂) surface protection is required for prolonged exposure[26]. Even so, unprotected magnesium alloys are still moderately resistant to corrosion in industrial and mild marine environments[26]. Problems will only really occur if there are recesses or areas on the magnesium piece which can retain water and hence form galvanic couples[26].

Due to the hexagonal unit cell of magnesium, mismatching exists between the metal and the structure of hydroxide and oxide films[5]. The passive layer also possesses a greater molar volume than the metal[6] which, alongside the mismatching, results in the passive layer being under compressive stress which leads to rupture and cracking[5-7]. With cracks present in the passive layer ingress of electrolytes can occur, which leads to further corrosion. Additionally, the Pilling-Bedworth ratio (P-B ratio) – which describes the coverage of the metal by its native film (where total coverage is 1) – for magnesium with a layer of mostly MgO is 0.81[3, 5], which indicates the MgO is formed under tension[34]. When the film is thin, MgO is ductile enough to cover the entire surface. It's when the oxide gets too thick and cracking occurs (due to the low P-B ratio) that MgO is not protective[3].

On the other hand, Mg(OH)₂ has a P-B ratio of 1.77[34], yet the corrosion properties in aqueous solutions are poor[3]. Mg(OH)₂ is not completely stable in aqueous solutions, particularly if they're not considerably alkaline, as such (to a certain extent) it will dissolve into solution[3]. In addition, Mg(OH)₂ is also reactive with numerous species in an aqueous environment including Cl⁻, SO₃²⁻, SO₄²⁻, NO₃⁻, PO₄³⁻, CO₃²⁻[5]. These reactions result in the formation of magnesium salts, which readily dissociate in the aqueous media leading to the passive film being dissolved[5]. These reactions are not limited to full immersion. These pollutants perform the same role in an atmospheric setting, where the compounds produced by their reaction can be washed away by rain[26]. In addition to breaking down the hydroxide surface film, SO₂ can promote pitting on magnesium alloys[26]. The formation of magnesium carbonate (MgCO₃) species in the air can be beneficial for atmospheric corrosion as it forms a hydroxyl-carbonate film. The deposition of this film is not influenced by the microstructure and it works to suppress both the anodic and cathodic reactions[26].

When fully immersed in water magnesium will form a surface film of Mg(OH)₂. When the impurities listed above come into contact with the surface film, the breakdown of the film will be accompanied by pitting of the magnesium alloy. As the temperature is increased the extent of corrosion increases (this is also true for atmospheric corrosion)[26]. Unlike aluminium, the corrosion of magnesium in water is unaffected by the concentration of oxygen. In stagnant water the corrosion rate of magnesium and its alloys will be low as the solubility limit of Mg(OH)₂ near the surface will be reached and the local pH will increase near the surface, stabilising Mg(OH)₂[26]. Hence, agitation will increase corrosion.

There are a number of factors which can alter the corrosion properties of a magnesium alloy:

1. Alloying additions.

The number and distribution of intermetallic phases is crucial to the corrosion properties of a magnesium alloy[35]. As mentioned in section 2.1.3, the microstructure of AZ magnesium alloys consists of the α matrix phase and the aluminium rich β phase (Mg₁₇Al₁₂). Aluminium is more electropositive than magnesium, as a result the β phase is more noble than the α phase. However, the effect this has on the corrosion properties depends on the content of β phase. When the aluminium content is low (e.g. 3 wt%) the β phase acts as local cathodes, resulting in microgalvanic corrosion of the α phase. However, when the content of aluminium is increased (e.g. 6-9 wt%) the β phase will act as anodic inhibitors and subsequently reduce corrosion[36]. This inhibition behaviour is due to the relative inertness of the β phase in corrosive aqueous media[37]. Song *et. al*[37, 38] suggest a number of possible reasons: 1) with more β phase in the microstructure there is less active area in the microstructure to corrode, which leads to an overall reduction in the corrosion; 2) the β phase forms along the grain boundaries in the microstructure. If the alloy has a low Al content the β phase will be discontinuous. The

corrosion of the α phase occurs through the lateral spreading of shallow pits adjacent to cathodic particles/phases. Therefore, it is proposed that a more continuous β phase (with alloys with more Al content) may prevent the spreading of the pits to adjacent grains; 3) if the α phase grains are sufficiently small, as the α phase is corroded (and undermined) the majority of the microstructure will eventually become the β phase and corrosion will slow.

It has also been suggested that the corrosion inhibition with higher Al content occurs due to the formation of an Al enriched surface film (Al_2O_3), which is more resistant to corrosion than the $\text{Mg}(\text{OH})_2$ native film of magnesium alloys[4]. Of the three layers that constitute the surface film on Mg-Al alloys, the enrichment of aluminium occurs in the innermost layer[35]. By increasing the stability of the oxide, the corrosion susceptibility is reduced.

A number of studies have been performed investigating the effect of new alloying additions to long-standing AZ magnesium alloys. These elements include calcium (Ca)[35], yttrium, neodymium (Nd)[39] and other rare-earth metals. The addition of 1 and 2% Ca to AZ91D resulted in a lamellar phase around the grain boundaries of the α phase. The composition of the lamellae was determined to be Al_2Ca . The authors concluded that the addition of Ca improved the corrosion resistance of AZ91D[35]. Similarly, with the addition of 1 wt% of Nd the β phase is affected and an additional phase is formed (Al_2Nd)[39]. The microgalvanic corrosion is not only the result of the β phase. Potential profiles of the different phases in as-cast AZ91D revealed that there are potential differences between the α phase and the Al-Mn particles of over 200 mV[31]. This is compared to the difference with the β phase, which is typically lower (200 mV or below[4]). Hence, the α /Al-Mn galvanic interaction should be stronger than that of α / β [31].

2. Microstructure.

For AZ magnesium alloys, if the grain size of the α phase is fine, the β phase is able to form a continuous network along the grain boundaries. This network acts as a barrier to corrosion and hence the corrosion resistance is increased[38, 39]. For large α grains the β phase becomes discontinuous and they act as cathodes in the microstructure to increase corrosion[38, 39]. Due to the relatively low content of Al in AZ31, the β phase is discontinuous along the grain boundaries and act as strong cathodes.

In general, new methods of producing magnesium alloys are being intensely investigated due to the effect of microstructure on corrosion. These processes include rheocasting, rapid solidification, ion implantation and vapour deposition. These methods often produce a more corrosion resistant alloy through a combination of a homogenous microstructure and increased solid solubility limits for alloying additions (hence reducing the amount of cathodic phases and intermetallics present)[26].

As magnesium alloys are more anodic than other engineering metals, bimetallic galvanic corrosion can be a serious issue[40]. To try to overcome this, substantial consideration into the design of the components must be made. These can include: the use of high purity magnesium alloys, better electrically insulating layers, choice of more suitable coupling alloy (based on the difference in position on the electrochemical series) and processing of the alloy to produce a more homogeneous microstructure.[40]

2.2.1 AZ31 Corrosion

In small amounts, both aluminium and zinc do little to improve the corrosion resistance of AZ31 versus pure magnesium. Without the addition of manganese extensive corrosion can occur in wet and moist conditions, as manganese works to precipitate dissolved Fe from the matrix[2]. The dissolved Fe will act as localised cathodes in the microstructure and hence cause extensive corrosion damage to the α phase when an electrolyte is present. The minor alloying additions (Cu, Si and Ni) all work to greatly decrease the corrosion resistance of the alloy[2] due to their highly cathodic nature in comparison with magnesium and therefore their content in the alloy must be controlled[41].

Studies have shown that the aluminium content in solid solution can work to significantly increase the corrosion resistance of these alloys[4]. The corrosion properties are improved as aluminium oxide (Al_2O_3) is incorporated into the surface film. Al_2O_3 is far more stable than MgO and $\text{Mg}(\text{OH})_2$, which improves the overall corrosion resistance of the alloy. However, at only 3 wt% Al (in AZ31) not enough aluminium is incorporated into the surface film and the aluminium is actually detrimental as it acts as cathodes in the microstructure. Song and Atrens[41] suggest that the β phase plays a dual role in serving as a corrosive galvanic cathode when low volume fractions are present (e.g. AZ31), but can also act as an anodic inhibitor if the volume fraction is high. Despite this, most Mg-Al alloys in marine conditions will undergo localised corrosion around the β phase. Studies by Pardo *et al.*[4] have shown an aluminium enrichment in the magnesium surface film during corrosion, which is believed to allow better passivation due to the formation of alumina. Consequently, higher aluminium containing AZ91 and AZ80 alloys show better corrosion properties than AZ31[4]. Despite the lower Al content, $\text{Mg}_6\text{Al}_2(\text{OH})_{16}\text{CO}_3 \cdot 4\text{H}_2\text{O}$ has been identified in the surface film on AZ31B[3].

2.3 Corrosion Protection for Mg Alloys

There are a considerable number of industry methods for the corrosion protection of magnesium alloys as well as others being researched, primarily to replace chromate containing methods. Some of these methods include: vapour deposition (physical and chemical), conversion coatings, anodising, electroplating/deposition, electroless plating, sol-gel coatings and organic coatings.

Due to the cathodic nature of many intermetallic particles and second phases, many other researchers are also investigating alloy design to reduce the effect of microgalvanic corrosion of Mg alloys. However, in the case of both micro- and macro-galvanic corrosion, coating design is required.

While the chromate conversion layer treatments are often highlighted for being hazardous, other corrosion protection methods, such as anodising, have also used this compound. In addition, as environmental regulations get harsher, the use of other compounds will also require phasing out (e.g. fluorides and phosphates). As these compounds are typically also the best at forming protective films this means that considerable research is required to find environmentally conscious replacements. This problem becomes increasingly complex/difficult as even if chromates or other hazardous chemicals are not used in the coating itself, they are often used in surface preparation. Whilst most of the corrosion protection on Mg alloys will be afforded by

the organic coating, pre-treatments such as conversion coatings and anodising are regularly used to improve adhesion and the overall protection of the alloy.

This section hopes to highlight popular techniques for minimising the corrosion of Mg alloys that are being currently used in industry or being researched. This section also aims to highlight the current problems with these systems and why there is still need for research into finding a solution to the problem of Mg alloy corrosion.

2.3.1 Surface Preparation: Cleaning & Acid Pickling

Prior to the application of any pre-treatment or coating, adequate surface cleaning is required. One of the main causes of increased magnesium corrosion is the presence of impurities in the microstructure. Even if the specific alloying additions of an alloy are controlled to ensure low levels of damaging impurities (e.g. iron), processing of magnesium alloys can often lead to surface impurities above the tolerance limit for an alloy[42]. Therefore, prior to the application of a surface coating, anodising, etc. the magnesium alloy must be cleaned. Cleaning can involve either mechanical or chemical processes. Mechanical processes involve grinding and polishing, abrasive blast cleaning or brushing[42]. Chemical methods typically include vapour degreasing, solvent cleaning, emulsion cleaning, alkaline cleaning and acid cleaning[42].

Acids often used for cleaning include phosphoric (H_3PO_4)[42, 43], nitric (HNO_3)[42-44], acetic (CH_3COOH)[43], hydrofluoric (HF)[43, 44], sulphuric (H_2SO_4)[42], chromic (CrO_3) and hydrochloric (HCl)[44, 45] acid. Recently there has been a push away from the use of chromic acid due to the carcinogenic nature of the hexavalent chromate ions (Cr(VI)), however hydrofluoric acid is also particularly hazardous.

Acid cleaning is capable of removing the natural oxide, embedded sand, iron and burned in lubricants. These impurities may not be soluble in solvents (such as water, ethanol or acetone) or in alkaline solutions[43]. The benefit of acid cleaning, as opposed to other chemical cleaning methods (and indeed, mechanical cleaning methods), is that it can result in the formation of protective layers through the reaction of magnesium with the acid[42, 43]. In particular, reaction with phosphoric and hydrofluoric acids produce thin, protective layers of magnesium phosphate and magnesium fluoride respectively. Due to increased surface roughening after acid pickling this process also results in increased adhesion of coatings[43]. For coating techniques that require the use of an electrical current (such as anodising and electroplating) the homogenisation greatly improves the quality of the coatings.

Care must be taken when acid pickling to avoid the formation of 'smut' layers, which consist of corrosion product from the dissolved substrate as this may implement subsequent coating steps[9]. The presence of smut layers can often be identified visually as it will often result in darkening or a dull or matte surface appearance[9].

2.3.2 Conversion Coatings

Conversion coatings are popular methods of corrosion protection because they are easy and cheap to apply and provide an adhesive base to subsequent organic coatings[46, 47]. As conversion coatings are electroless cost is kept low through simple processing technique, which typically involves immersing the metal in the conversion coating bath for a fixed time. When immersed in the conversion coating bath the native oxide is stripped and replaced with the metal oxides of the metal cation(s) in the compounds used in the coating bath[48]. These can include such oxides as CrO_3 and CeO_2 [46] among others. These oxides act as a more effective barrier to corrosion than the original native film, thereby decreasing the corrosion rate.

2.3.2.1 Chromate Conversion Coatings

For low level corrosion protection magnesium alloys are often immersed in acidic or near-neutral solutions containing chromium VI ions (Cr(VI)). These ions have a high passivating quality with most metals and spontaneously (that is, without the application of external currents or potentials) form a surface layer on magnesium alloys, which is more protective than the original native surface film[9, 49]. This film is termed a 'conversion coating' as the solution chemically reacts with the surface to create the film[8]. A conversion bath will typically contain oxidants, promoters, corrosion inhibitors, wetting agents and pH buffers[8]. The oxidants will accelerate the cathodic reaction by consuming a lot of H^+ and producing OH^- . They accelerate the dissolution of magnesium and the formation of the conversion film. Promoters deposit onto the magnesium surface to act as nucleation points for the conversion layer. The corrosion inhibitors absorb onto the magnesium to slow dissolution. They will also form complexes with magnesium, which stabilises the solution and controls the rate of the conversion layer growth. The wetting agents decrease the surface tension of the magnesium surface, allowing easier the formation of the conversion layer due to better contact between the surface and the conversion solution. Finally, the pH buffers regulate the solution pH, which affects both the speed at which the conversion layer forms and also the quality of the film[8].

These films are typically 1-5 μ m thick[5]. The coating thickness, as well as colour and corrosion resistance, will depend on the immersion time, temperature, solution composition, method of application and the metal substrate[9]. The formation of a conversion layer is an anodic reaction and begins with the formation of a hydrated oxide film of $MgO_x(OH)_y$ [5]. This film is then partially dissolved by the conversion electrolyte and pores are formed which quickly join to form cylindrical cell colonies[5]. Charge and ion exchange occurs through this layer and elements from the conversion electrolyte are incorporated into the $MgO_x(OH)_y$ matrix to form the conversion layer. For chromate conversion layers, the solution consists of H_2CrO_4 or $H_2Cr_2O_7$ with activator ions such as sulphates, chlorides, phosphates, fluorides, nitrates, acetates and cyanates[8, 9]. The solution pH is typically 1.2-3 to ensure the chromate exists in the dichromate state ($Cr_2O_7^{2-}$)[9]. Below the porous section ($Cr(OH)_3$ [50]) of the film a thin (approx. 5nm) barrier layer (Mg(II) and Cr(III) hydroxides[50]) exists[5]. Trace amounts of the ions of the conversion electrolyte exist in the pores (Cr(VI) ions in this case), which allow the 'self-healing effect' when the oxide is damaged[5, 9]. Chromate conversion layers can form within 30-60 seconds at room temperature[8]. These treatments are suitable for working conditions of normal atmospheric exposure for relatively short periods. This is because the films formed using these methods are typically porous and hence allow ingress of electrolyte[49]. Significant electrochemical activity occurs within the first 30 seconds of immersion in the chromate solution and the coating weight and thickness increase rapidly[9]. After 30 seconds the electrochemical activity diminishes but coating weight continues to increase whereas thickening slows or stops[9]. Prior to the application of a conversion coating the metal substrate will typically undergo chemical cleaning and acid deoxidation[9]. The conversion coatings formed on magnesium alloys are often used as a base prior to application of organic coatings.

Cr(VI) ions were used very often to form protective conversion layers on magnesium alloys. However, this compound has since been found to be highly toxic and carcinogenic[8, 9]. Environmental concern and regulations has led to the need for and development of other, alternative, environmentally friendly solutions[9]. Evaluating the replacement technologies is difficult due to the number and varying processing requirements and corrosion performances required in different sections of industry[9]. A number of alternatives are available which perform well when used as a pre-treatment prior to organic paint coatings, but there has been

far less success in working conditions that involve good corrosion performance without paints[9].

2.3.2.2 Alternative Conversion Coatings

Common replacements of chromates are phosphate and phosphate permanganate compounds. However, other solutions have been developed using compounds of V, Zr, Mo, W, Ti and Co[8]. Rare earth compounds, based on cerium, lanthanum, neodymium and praseodymium, and organic based systems can also be used to form conversion layers[8]. Unfortunately, most of these systems do not benefit from the self-healing ability that the chromate conversion layers possess. Only those formed from V or Mo compounds exhibit this behaviour[8].

2.3.2.2.1 Phosphate and Phosphate/Permanganate Conversion Coatings

Phosphate compounds have been greatly researched for the replacement of the chromate conversion coating due to their success on steels and aluminium[51]. The solutions typically consist of KMnO_4 , MnHPO_4 , K_2HPO_4 and H_3PO_4 [8]. The formation of a phosphate-permanganate conversion coating occurs in the same way as with chromate. The conversion layer composition consists of magnesium phosphate, oxidation products from the alloy (including Al_2O_3 when an Mg-Al alloy) and reduction products from the electrolyte[5]. While the corrosion protection afforded by phosphate-permanganate conversion layers is comparable to chromate[52], the phosphate-permanganate solution decomposes at a high rate (by forming magnesium dioxide), which greatly limits prospects of industrial application[5]. Also, due to this decomposition it is more difficult to produce conversion layers of consistent quality on different components[5]. The addition of vanadates, molybdenum and wolframate anions in a trademark process called MAGPASS-COAT can stabilise the electrolyte allowing consistency and greater ease of coating formation. However, like chromate conversion coatings, sealing is still required in order to prevent corrosion. Suitable sealants include wax, lacquers and hydrosilicon combinations based on sol-gels.

2.3.2.2.2 Rare-Earth Conversion Coatings

Rare-earth conversion coatings were investigated on Mg alloys after success with aluminium, zinc and steels[53]. Rare-earth (RE) conversion coatings are often formed using cerium (Ce)[46, 47, 54, 55], lanthanum (La)[46, 55], neodymium (Nd) and praseodymium (Pr)[55] with nitrate (NO_3^-)[46, 47], sulphate (SO_4^{2-})[54] and chloride (Cl^-)[56]. These compounds are considered to be environmentally friendly and, due to their simple chemistry, recyclable[56].

Currently, the main issue with rare-earth conversion coatings is the formation of cracks in the film[46, 54, 57], which can dramatically reduce the adhesion of the film to the substrate[56] in addition to the corrosion resistance. Lin *et. al*[56] investigated the evolution of a RE conversion coating on AZ31 in a solution of cerium nitrate ($\text{Ce}(\text{NO}_3)_3$). After one minute of immersion in the solution, micro cracks were present in the film, which grew in size with continued film growth. The cracks formed upon drying due to film shrinkage with the evaporation of water. Delamination of the films also occurred, which the authors concluded to be indicative of poor initial substrate adhesion[56]. Li *et. al*[47] investigated a Ce conversion coating (formed from $\text{Ce}(\text{NO}_3)_3$) on AZ31 and found that it had a two layered structure. The outer layer had poor adhesion to the inner layer and could easily be removed, either from stripping with tape or in 0.5 M NaCl. The authors concluded that the adhesion of the outer layer was crucial for the overall protectiveness of the coating.

Precipitation of the RE conversion layers (in the form of RE-oxides/hydroxides) occur at areas of alkalinity[55]. The level of corrosion afforded by RE conversion coatings is on par with

chromate conversion coatings[46, 55] and an anodic shift of E_{corr} by a couple hundred millivolts[57].

2.3.2.2.3 Other Conversion Coatings

Molybdenum (Mo) is often used in conjunction with phosphate[58], permanganate[59] and rare earth metals[48, 60, 61] to make composite conversion coatings. As with the RE conversion coatings, Mo conversion coatings also exhibit cracks[59, 61]. Yang *et. al* [61] compared the corrosion performance of AZ31B (blank) against Mo conversion coatings (using Na_2MoO_4), formed in a bath with and without the addition of La (from LaNO_3), in 3.5 wt% NaCl solution. With Mo alone, the corrosion current was reduced by approximately half an order of magnitude. Mo with the addition of La reduced the corrosion current by over an order of magnitude[61]. The reduction in the corrosion with La is likely due to the change in the morphology of the conversion coating. Similar behaviour was also found by Yong *et. al* with the Mo/phosphate system. With the addition of the phosphate the morphology of the coating was altered to remove the network of cracks[58].

Organic conversion coatings result from the formation of covalent bonds with the Mg substrate[62]. As a result the compounds used will have active functional groups that can readily react with the surface[63]. Organic conversion coatings are considered to provide very adhesive bases for organic paint coatings[62, 64]. Unfortunately, organic conversion coatings also suffer from cracking[63, 64].

2.3.3 Sol-Gel Coatings

Sol-gel coatings are those which are the result of gelation of a colloidal suspension, or sol[65]. The sol-gel coatings form a polymeric or ceramic like barrier layer which stops the ingress of water and other damaging species from getting to the substrate[66]. A large degree of control over the sol-gel process, including chemical structure, composition, rate and conditions of the hydrolysis or condensation reactions, curing temperature and time, and the inclusion of additives (e.g. dyes or inhibitors) results in a versatile method for forming protective coatings on magnesium alloys[66] (and indeed, other reactive metals). The sol-gel coating process involves four stages[65]: (1) hydrolysis, (2) condensation and polymerisation of initial molecules into polymer chains, (3) growth of the particles and (4) gelation (or agglomeration) of the polymer chains by the formation of polymer networks. The advantages of the sol-gel process include generally low processing temperatures and ease of coating of complex shapes[65]. Due to the absence of hazardous compounds and lack of waste product from this process, it is considered a 'green' coating method[43, 65]. This makes these films a promising alternative to the use of chromate conversion layers[43].

Research into sol-gel coatings has become considerably extensive due to their ability to form highly protective and adherent coatings on magnesium alloys[66]. Classical inorganic sol-gel coatings involve the formation of metal oxide films on the surface of magnesium alloys, including SiO_2 , ZrO_2 , Al_2O_3 , TiO_2 and CeO_2 [65]. These metal oxides provide enhanced chemical stability over the magnesium substrate and its native oxides and hence the corrosion performance is improved. However, these oxide films are brittle, coatings thicker than 1 μm are difficult to achieve due to cracking during drying and densification[67], porosity of the coatings does not adequately prevent ingress of water (and other detrimental species) and considerably high temperatures are required to cure the coatings (400-800°C)[65].

Inorganic-organic hybrid sol-gel coatings have been developed, which allow for the formation of thicker films (in the micrometre scale) without cracks and curing can be conducted at lower

temperatures[65]. As the protective capabilities of these coatings relies on a uniform defect free layer, the ability to include inhibitors in the hybrid sol-gel results in improved corrosion properties[65].

Deposition of sol-gel coatings is achieved through dipping, spinning or spraying of the magnesium substrate. Due to the formation of covalent bonds with the magnesium substrate sol-gel coatings provide excellent adhesion both to the substrate and subsequent coatings[66]. Therefore they are often used as precursors to organic paint coatings or as a sealant for anodised layers[43]. After reaction of the molecular precursors to form covalent bonds with the metal surface, the polymer network undergoes a heat-treatment for densification of the film[43]. This heat treatment can also stabilise the gel, remove unreacted organic molecules or crystallise the film[65].

Whilst successfully stable sol-gel coatings have been developed for aluminium, forming stable sol-gel coatings on magnesium alloys is still problematic[66]. In addition, characterisation of the performance of sol-gel coatings is often done so through hydrogen evolution[43], which does not adequately evaluate the corrosion processes of the substrate and hence the effectiveness of the coating[66]. Currently, poor stability of these coatings in alkaline environments is the main obstacle with this technique[65].

2.3.4 Plating and Electroplating

The idea of electroplating magnesium alloys is to replace the highly anodic and corrosion prone magnesium substrate with a more noble metal, which does not readily corrode. Hence, it is easy to imagine the benefits to corrosion protection from this method. However, this means that the coating is cathodic. This differs to the method of galvanising steel where Zn metal is coated onto the steel substrate and works as an anodic coating. Due to the cathodic nature of the coating, in the case of magnesium, it is very important that the coating is pore and defect-free. If not, in the presence of an electrolyte a situation of high cathode-to-anode area will arise and the corrosion of the magnesium substrate will be dramatically accelerated[68]. The majority of research into electroless plating and electroplating of magnesium alloys is focused on Ni, Ni-P and Cu based coatings[69, 70]. In particular, Ni-P alloy deposition is able to form a coating that has high corrosion resistance and hardness[53]. However, current Ni plating baths are considered to be generally unstable, such that alternative solutions are currently being researched[71].

Both electroless and electroplating processes require an acid pickling step to electrochemically homogenise the magnesium surface[53]. Issues in plating of magnesium alloys (both electro- and electroless) can also arise due to the high reactivity in the acid and alkaline plating baths. As a result pre-treatments are required in order to form an adequate coating. One process developed in industry by Dow Chemicals involves a number of steps which precede plating, which include alkaline cleaning, acid pickling, activation, zinc immersion, cyanide plating of copper and finally the plating[53, 68]. The pickling acid used is typically a mixture of nitric and chromic acids, the latter of which is toxic and carcinogenic and activation requires the use of the hazardous hydrofluoric acid HF. Also, the cyanide solution used to deposit Cu is also harmful, however in the case of Ni-P plating, without this step the life-time of the Ni-P coating bath is reduced due to decomposition from the Zn layer in the previous step[53]. Altogether, this results in a process which is time consuming and can be extremely harmful, not only to the workers/operators, but also the environment. Hence there is a need for the development of a more environmentally appropriate process. A possible solution has been proposed by Huang *et. al*, wherein galvanostatic etching was used to form a uniform, activated, surface in copper sulphate, without

the use of chromates or HF[70], whilst other authors propose “direct electrochemical plating”, wherein no steps prior to the plating are used[72].

Not surprisingly, when immersed in corrosive NaCl solution E_{corr} is shifted to noble values associated with the electroplated metal. This shift can be anywhere from two hundred[73] to over a thousand millivolts.

2.3.5 Anodising

2.3.5.1 Formation and Composition of Anodised Coatings

Anodising is one of the most popular industrial processes for corrosion protection of magnesium alloys[74]. The technique involves making the work-piece of interest the anode in an electrochemical cell. An anodic current or voltage is then applied to the work-piece to force oxide formation on the surface[74]. Solutions used for anodising are mainly aqueous solutions of inorganic substances, used either in mixtures or alone. Typical solutions are chromic acid, hydrofluoric acid, boric acid and/or their corresponding salts. Strong bases (KOH, NaOH, NH_3) are also added to ensure a large supply of OH^- ions. However, only a few solutions produce an anodic conversion layer, which supplies good corrosion resistance without the aid of sealing. Unlike aluminium, MgO does not provide full coverage (PB ratio of 0.81) over the metal[3, 5]. As a result anodising magnesium is more difficult[5], and the processes which occur during anodising are more complex[74]. Hence, anodising processes for magnesium differ considerably to those on aluminium[74]. Some of these differences include the use of higher voltages on magnesium, lack of sparking processes on aluminium, different electrolytes and an irregular porous structure on magnesium in comparison to a uniform film on aluminium[74]. In addition, the sparking process which occurs in anodising of magnesium results in extremely high temperatures on the surface, which in turn causes precipitation on the surface of species from the electrolyte[74]. The anodised films formed are rough, highly porous and irregular, and ceramic-like in composition[74].

During anodising, magnesium is oxidised and an oxide film is deposited on the surface[5]. The identity of the anodised film depends on the cut-off potential as MgO will only start to form (in place of $\text{Mg}(\text{OH})_2$) at potentials above 20 V[74]. The oxide film grows 50% into the magnesium substrate and 50% above the original surface height[74]. The thickness of the coating is dependent on anodising currents or potentials applied during formation. There is effectively a linear relationship between the final film thickness and the final anodising potential. The films formed will comprise mostly of magnesium and oxygen. However, specific composition varies with the anodising bath used, as components of the electrolyte will also be incorporated into the film. For Mg-Al alloys, aluminium enrichment is often observed in anodised coatings[74], which often result in the formation of MgAl_2O_4 spinels[5].

Plasma anodising is a technique of anodising for magnesium alloys that involves the use of very high voltages and/or currents, which sets it apart from traditional anodising techniques in that it purposefully causes sparking discharges. Plasma anodising covers techniques termed anodic spark deposition (ASD), anodic spark discharge, microarc oxidation (MO), electrical breakdown and plasmachemical oxidation. The sparking on the surface occurs due to the voltage exceeding the dielectric breakdown of the anodised coating[74]. Initially the sparks formed are small and are quickly extinguished but as the potential continues to increase the sparks become larger[74]. Sparking for many magnesium alloys begins around 50 V, but continues to considerably higher potentials. The film changes throughout these stages and as such the film is effectively continually undergoing breakdown and repair processes[74]. This anodising process forms a crystalline oxide-ceramic coating on the magnesium. The coatings provide both great wear and

corrosion properties. Unlike chemical vapour deposition (CVD) and plasma vapour deposition (PVD) no vacuum is required and it is cheaper. Unlike other anodic processes, plasma anodising is able to achieve coating thicknesses up to 150 μm . In addition, the corrosion resistance is high without the need for sealing.

Voltages greater than 100 V are used with AC, DC, three-phased and pulse current systems suitable. A considerable benefit of this method is that oddly shaped items can be consistently coated. Aqueous solutions are used and include anions of phosphate, fluoride, borate, silicate and aluminate. Application of the ceramic layer does not alter the bulk mechanical properties of the magnesium metal. However, due to the high voltages used, the electrolyte gets very hot and must be constantly cooled. Initially only a small current flows with the formation of a 1 μm passive layer. With voltages > 100 V applied a sudden increase in current occurs and sparks occur, which are the plasma discharges. The discharge causes partial damage to the passive layer and charge exchange begins to occur between the metal/oxygen/electrolyte contact point. The sudden release of energy melts the magnesium surface and causes it to react immediately with the ionised oxygen. This forms crystalline oxides and components of the electrolyte are also incorporated. This process continues until every localised point on the magnesium surface is oxidised, bit by bit. Increasing the voltage leads to this process occurring again. If the applied voltage is too high, however, the layer is destroyed.

During anodising to potentials of 50 V an amorphous, relatively smooth, finely porous film is formed. Above 50 V, dielectric breakdown results in a coarse morphology (plasma anodising discussed above). Anodised coatings often have a number of layers, typically with a very thin inner barrier layer and an outer porous layer(s) [74]. The distribution and structure of these pores depends on electrolyte composition and the potentials, current densities and temperatures the anodising is performed under [74]. In particular the anodising current has been associated with the microstructure of the final anodised coating. Phosphate in anodising baths contributes to colour, opacity and uniformity of the coating [74]. Phosphate was also found to increase the corrosion resistance of the inner barrier layer of anodised films [74]. Finally, low temperatures, near or below room temperature, are used due to the heat generated during dielectric breakdown and sparking [74]. Hence all of these characteristics affect the corrosion resistance of the films (discussed in 2.4.2).

Like with the native oxide formed on Mg-Al alloys in the air, with increasing content of aluminium in the alloy more aluminium is present in the anodised film [74]. In addition, with increasing aluminium content the dielectric breakdown of the films are increased. Also, the anodised coating formed on the β is often more porous than that formed over the α phase [74].

The anodising process can be grouped into four stages [74]: I: Linear growth (potential increases quickly and linearly with time), II: Gas evolving (potential increases but the rate decreases more with time, corresponding to increasing gas evolution with time), III: Uniform sparking (potential increases linearly with time with random sparking over the surface. Sparking and gas evolution increase with increasing time), and IV: Localised sparking (sparking is less random and occurs in more localised areas. These sparks are more intense and more intense gas evolution is experienced at the sparking areas. The rate of potential increase decreases with time). Often modes III and IV occur together. Stage I is very quick and short lived, and hence is often overlooked [74].

Oxygen evolution during anodising is typically small at low potentials (stage II) but increases with increasing potential. When sparking processes occur (associated with stages III and IV) the evolution of oxygen is far more aggressive, such that prior to sparking, O_2 evolution is

considered insignificant[74]. The oxygen evolution results from the electrochemical breakdown of water, which results in O₂ evolution at the anode, and H₂ evolution at the cathode. If sparking occurs thermal decomposition of water also results in the evolution of O₂[74]. Shi *et al*[75] measured the O₂ evolution as a function of cell potential during anodising of Mg alloy AZ91D at a constant charge of 18 C/cm². At potentials < 350 V, the evolution of O₂ is less than 0.5 mL/cm², whereas at potentials > 350 V the evolution dramatically increases to 3.5 mL/cm² at potentials just over 400 V, due to sparking behaviour.

A number of commercial anodising coatings for magnesium alloys have been developed. However in many cases the anodising bath solutions contain toxic, carcinogenic and harmful compounds, which not only pose a risk to workers but to the environment during waste disposal. Processes such as DOW 17, HAE, Tagnite and Magoxid-Coat contain fluoride containing compounds and in the case of DOW 17, chromate compounds. Tagnite and Keronite processes also involve the use of very high voltages[74]. These processes have been described in more detail elsewhere[5, 74].

2.3.5.2 Corrosion Properties of Anodised Coatings

Anodising is a very powerful technique for the production of protective coatings on magnesium alloys. The microstructure of the alloy, including composition and volume fraction of second phases (e.g. β phase), can directly influence the corrosion performance on an anodised coating on magnesium alloys[76]. Shi *et al* conclude that the corrosion resistance of an anodised coating relies upon the corrosion resistance of the alloy[76]. That is, if AZ91 and AZ31 were to both be anodised under the same conditions, AZ91 would still perform better in corrosive conditions. As the morphology of the anodised coating can be directly related to its corrosion performance, parameters such as anodising current and temperature can also alter the corrosion performance of the coating[75].

Both the industrial HAE and DOW17 anodising methods, when applied to magnesium alloy AZ91D, decrease the corrosion rate by a factor of approximately 25 in 3.5wt% NaCl solution[77]. Zhang *et. al*[77] developed an anodising technique which was able to decrease the corrosion current by a factor of approximately 200. This technique involved the use of potassium hydroxide, sodium carbonate, sodium silicate and sodium borate. Hence the anodising bath composition does not contain any hazardous substances. However, in order to achieve such a protective anodised film the cut-off potential for the treatment was 150 V (as opposed to 70-90 V for HAE and DOW17)[77]. In many cases, alternative anodising techniques to HAE and DOW17, which exhibit improved corrosion resistance, require anodising at much higher potentials[74, 77-79].

Due to the porous structure of the anodised coating, sealing is often considered to be the most important step in the process. This is done to avoid diffusion of aggressive species to the Mg metal interface through the pores (or cracks) in the anodised film[80]. Sealing of anodised coatings typically involves dipping in phosphate, silicate or borates solutions[80]. The dramatic impact of this step has been shown by Song, who demonstrated that sealing an anodised layer on ZE41 decreased the corrosion current by almost four orders of magnitude in 5wt% NaCl solution[80].

2.3.6 Organic and Polymer Coatings

The use of organic coatings, e.g. paints, allow for moderate corrosion protection. Other methods may include oiling or greasing the magnesium alloy to repel water. These are all temporary measures as they always need to be reapplied after a certain timescale. Paint is not

typically applied directly to the base alloy, and hence a pre-treatment, such as a conversion or anodised layer, is applied prior to painting. This is due to a couple of factors. Firstly, surface contaminants may be present on the magnesium alloy surface, by applying a pre-treatment they are removed. Secondly, the $Mg(OH)_2$ film which forms in moist air is alkaline, which is detrimental to the life of the paint coating (especially oil-based paints)[49]. Often, before the application of the top-coat of paint a primer containing Cr(VI) is applied to provide superior protection[49]. Organic coatings typically consist of three main components: the binder, pigments and additives. Additives can include dryers, hardening agents, stabilising agents, surface activating compounds, dispersion agents and (to a lesser extent) corrosion inhibitors[65]. Organic coatings protect by providing a barrier between the corrosive environment and the magnesium substrate. Hence, their performance relies heavily on high uniformity, good adhesion and absence of pores[65]. The incorporation of inhibitor additives or anodic particles into the coating can give these coatings self-healing properties if pores or cracks should be present[65].

Due to the alkaline environment of magnesium corrosion, paint selection for magnesium alloys should involve the selection of a primer which is an alkali-resistant resin, such as polyvinyl butyral, acrylic, polyurethane, vinyl epoxy or phenolic[65]. Additives such as chromate and titanium dioxide are also added to improve the corrosion resistance through self-healing[65].

Epoxy resin coatings have been used to provide superior corrosion protection on magnesium alloys. Epoxy resin is tough, impermeable to water and is excellently adhesive, making it a desirable choice for corrosion protection[49]. In addition, it can withstand repeated immersion in marine conditions, allowing magnesium alloys to be used in severe conditions. However, to form a resistant coating care must be taken in applying the resin (the magnesium piece must be heated when dipped in the resin) to prevent detrimental defects in the coating[49].

Another method which provides excellent corrosion protection is through a method called electrophoretic coating/deposition (E-coat/ EPD). This process uses an applied electrical field to influence charged particles to migrate to the metal surface of interest[8, 65]. This can be done either anodically or cathodically. In the anodic case, the workpiece is polarised at an anodic potential, which influences negatively charged particles to migrate to and deposit on the surface. Similarly, the cathodic process does this using a cathodic potential bias to influence positively charged ions[8]. This process forms highly uniform films with very low porosity and can be used to coat complicated shapes. In addition, the process is environmentally friendly due to lack of VOCs (volatile organic compounds)[8]. Prior to coating a surface pre-treatment must be performed. These can include surface cleaning, conversion coatings and anodised layers. At a minimum surface cleaning must be performed in order to remove surface contaminants, which would otherwise compromise the adhesion of the coating[8]. However, the application of a conversion layer prior to treatment is the most common pre-treatment[8].

2.3.7 Summary

There are many different alternative corrosion protection methods proposed to replace chromates, not all of which were covered above. Each technique currently has its disadvantages, either in difficulty, time or cost. For anodising, especially high voltage anodising (plasma anodising/microarc oxidation etc...), the use of high voltages leads to high operational (electricity) and equipment costs. For sol-gel coatings, the difficulty arises in forming a stable coating, whereas electroless and electroplating of noble metals/composites suffer not only from long pre-treatment steps, but from the use of toxic and harmful chemicals. Conversion coatings suffer from cracking, which not only affects the adhesion of the film but also the corrosion

protection. Hence, there is a need to develop a technique which does not involve the use of harmful chemicals, is cheap, easy to apply and reproducible and capable of forming a protective, adhesive and stable film on an Mg alloy surface.

2.4 Ionic Liquids

2.4.1 General Overview of Ionic Liquids

Ionic liquids (ILs) are salts which contain very large or unsymmetrical organic and inorganic anions and cations. The size and unsymmetrical nature of these molecules restrict their capability to order into a solid phase and hence, by definition, exhibit a melting temperature below 100°C[11, 12, 81]. Room temperature ionic liquids (RTILs) are ILs which are liquid at room temperature and hence exhibit considerably low melting temperatures. The fact that these materials are liquid at room temperature means they can behave as an electrolyte (due to the charged anion and cation molecules) without the need of a solvent (such as water). This lends these materials exclusive properties over other, 'classical', liquid electrolytes. These include negligible vapour pressure[10, 82] (they do not evaporate, even under high vacuum), high thermal[83] and electrochemical stability[10, 11, 84] and a high density of reactive species.

Due to the vast number of possible anion and cation combinations the physical and chemical properties of IL materials can be tailored to suit specific applications[83]. The popularity of ILs has risen in the past decade largely in part due to their high electrochemical window and non-volatile nature. They have been used to replace such volatile solvents, wherein they can be used as a 'green' solvent due to their recyclability[85, 86]. In addition, the size of their electrochemical windows, which can be as large as 5 V, has seen these materials gain interest for the use of electrodepositing alloys[10, 87]. The non-volatility, thermal and electrochemical stability, in addition with the conductivity afforded by the charged ions, has also seen ILs researched extensively for electrolytes in batteries and solar cells[88-90]. Ashassi-Sorkhabi also demonstrated that ILs can be used as corrosion inhibitors in acidic solutions[91].

2.4.2 Ionic Liquids and Corrosion

The corrosive properties of ILs is important to consider as the materials used for storage and transportation of ILs need to appropriately contain the material[92]. In addition, particular operation conditions can see ILs in contact with pipes and containers, which may or may not have an adverse reaction with the IL[92].

One of the main issues with assessing the effect of corrosion of alloys in ILs is that depending on the specific IL the corrosion properties may vary dramatically[19]. The literature on the corrosion properties of ILs is fairly scarce, but even with the current literature we get a sense that ILs will need to be individually evaluated with the alloy of interest. To complicate things further, as ILs are non-aqueous the standard knowledge on the corrosion behaviour of certain metals and alloys do not hold in an IL corrosive environment, particularly if the ability to form a passive oxide/hydroxide film is impeded by the low water and oxygen concentrations in many ILs[92, 93]. In a study on the corrosion behaviour of carbon steel (in addition to 304 stainless steel and Ti) in aluminium chloride-1-ethyl-3-methylimidazolium chloride ($[AlCl_3][EMIC]$), Tseng *et al* observed transpassive behaviour in the IL which was not present in a standard aqueous NaCl solution[93]. In addition, once the potential was forced out of this passive region the current of the anodic reaction resulted in unabated Fe dissolution directly into the IL, as no corrosion product was forming to act as a resistive barrier[93]. The authors found that the carbon steel and 304 stainless steel both experienced less corrosion in the IL as opposed to

aqueous NaCl solution but Ti, which is very passive in aqueous NaCl, corroded severely[93].

Since ILs are non-aqueous solvents, the amount of dissolved water in the IL can significantly alter the corrosion behaviour of ILs. Shkurankov *et al.* [10] studied the effect of water content in 1-butyl-3-methyl-imidazolium trifluoromethylsulfonate ([BMIm][CF₃SO₃]) on the corrosion of magnesium alloy AZ91D. The authors found that in the dry IL the corrosion rate of AZ91D was very slow. With the addition of a small amount of water (103 ppm) the corrosion rate increased by an order of magnitude. The addition of more water was shown to further increase the corrosion rate of AZ91D in the IL[10]. A similar trend was observed with aluminium exposed to 1-butyl-3-methyl imidazolium tetrafluoroborate ([BMIm][BF₄]), where increasing water content led to increased corrosion[89].

The first extensive study on the corrosion properties of ILs with commercial alloys was undertaken by Uerdingen *et al.*[19]. This study involved a range of materials including carbon steel, Hastelloy C22 (Ni-base), stainless steel, brass, copper, and aluminium (AlMg₃), which were exposed to a range of imidazolium and quaternary ammonium based ILs at 90°C under flow conditions. The authors found that depending on the IL and the amount of water in the system the corrosion rates of the various alloys could change dramatically[19]. The authors found that the ILs were generally non-corrosive but that the corrosive effect was controlled by the anion of the IL[19]. In dry IL, even the reactive aluminium alloy experienced low corrosion rates[19]. Poor corrosion behaviour in many of the wet ILs was concluded to be due to hydrolysis of the anions, which could then form acidic compounds, such as sulphuric and phosphoric acids[19].

In similar work by Bardi *et al.*[94] and Tolstoguzov *et al.*[12], the interaction of a similar range of industrial alloys (Ni alloy Inconel 600, Naval Brass, AISI 1018 carbon steel) with imidazolium based ILs was investigated. The alloys were immersed in IL at 225°C for 20 days and an inhomogeneous dark-brown coloured layer was found on the surface of all three alloys after immersion. The thickness and roughness of this layer was alloy-dependent and was more prominent on the Ni-based alloy, which was approximately twice the thickness as the other two alloys. The change in colour was attributed to the break-down of the IL and Ni was concluded to have acted as a catalyst[12, 94]. Perissi *et al.* studied the effect of varying temperatures on the corrosion of a range of metals and alloys in [BMIm][Tf₂N][95]. At room temperature the corrosion rate was low, however with increasing temperature the dissolution of metal increased, particularly for Cu, which crumbled against its Teflon support at 150°C[95].

A study on the effect of IL on magnesium alloy AZ91D was conducted by Caporali *et al.*[20]. The authors found that the rate of corrosion in AZ91D in this IL was slow, particularly at room temperature. X-ray Photoelectron Spectroscopy (XPS) analysis of the AZ91D surface after exposure to [BMIm][Tf₂N] IL at 200°C ranging from 1 to 30 days revealed breakdown products of the IL anion ([Tf₂N]) on the AZ91D surface[20]. In addition to this, Howlett *et al.*[13, 14], in studies of lithium batteries using an IL, found a passive solid electrolyte interphase formed on the lithium electrode from the reduction products of the IL anion during cycling.

In general it appears as though reactive metals, including magnesium, lithium and aluminium, passivate in ILs and that the anion of the IL appears to dictate corrosive or passive behaviour[13, 14, 19, 20]. This general passive effect in the literature is in part due to the popularity of the fluorine containing anion [Tf₂N], which reacts with the metal surface to form insoluble Me-F compounds[13, 20, 88].

2.4.3 Formation of Protective Coatings on Mg with Ionic Liquids

After it was established that a film formed on lithium metal[13, 14], interest in the use of ionic liquids to mitigate corrosion on magnesium alloys emerged. One of the most beneficial properties regarding ILs and their potential for dealing with reactive metals for corrosion purposes is that they are non-aqueous. In a pure IL the water content is negligible and thus it would be expected that the standard aqueous based corrosion reactions will not occur in well dried ILs.

The study of the film formed on Li batteries in $[P_{13}][Tf_2N]$ IL by Howlett *et al* revealed a layer comprised of two parts: an inner compact layer of LiF and an outer diffuse layer of breakdown products of the anion (e.g. Li_2O_4 , LiF, $LiSO_3CF_3$, Li_2SO_3 , Li_2S , Li_2O and LiOH)[13]. Therefore, it was hypothesised that the breakdown products from the IL tri(hexyl)tetradecyl phosphonium bis(trifluoromethanesulfonyl)amide ($[P_{6,6,6,14}][Tf_2N]$) may lead to the formation of corrosion resistant MgF_2 . The initial investigation was conducted on magnesium alloy AZ31 in $([P_{6,6,6,14}][Tf_2N])$ IL[21]. The authors found that treating AZ31 in the IL for 17 hours led to a reduction of the corrosion current by 50 times compared to an untreated alloy in a 0.1M NaCl solution. The surface also exhibited self-healing behaviour. In addition, specimens treated for 24 hours and exposed to 100% humidity for 30 days or 3 weeks maintained a relatively non-corroded surface in comparison with the control specimens[21]. EDS data from AZ31 exposed to the IL for 118 hours revealed F, C, P and S – all components of the anion. This is consistent with the studies mentioned previously on the role of the anion in corrosion/passivation.

A study by Sun *et al* investigated the corrosion performance of ZE41 with films formed after 1 hour immersion in a number of ILs containing the tetradecyltriethylphosphonium ($[P_{6,6,6,14}]$) cation[11].The authors found that most of the IL films improved the corrosion performance in 3.5wt% NaCl as opposed to the control ZE41 surface[11]. Using an ionic liquid with the same cation, Howlett *et al.* [96] also found that the IL tetradecyltriethylphosphonium bis(2,4,4-trimethylpentyl)phosphinate ($[P_{6,6,6,14}][C_8)_2PO_2]$) could passivate magnesium alloy AZ31. In addition, the authors found that films formed in the wet condition (5.8 wt% water) in comparison to the dry condition (0.9 wt% water) bestowed increased corrosion resistance when immersed in 0.01 M NaCl. The authors concluded that high cathodic stability of the IL cation (e.g. phosphonium) led to a surface film formed with chemistry controlled by the IL anion. The role of water concluded in this study differs from another, which found that corrosion is accelerated on Mg in water containing ILs[10]. This reinforces the comment made earlier that the specific corrosion properties between an IL and an alloy can vary with each system. In addition to the effect of water on film forming, it has been found that control of the immersion time is crucial. In a study with IL $[P_{6,6,6,14}][Tf_2N]$, Birbilis *et al.*[22] found that overexposure of the IL to highly pure (99.99%) Mg led to a more defective film, which performed worse in corrosion conditions. The defects were concluded to arise due to reaction of the Mg with residual water in the IL. The authors found the best film formed after 1 hour immersion in IL, with a film thickness of 87 nm[21]. This film was found to protect the Mg metal for up to 8 hours in a highly aggressive 0.1 M NaCl solution[22].

2.4.3.1 Effect of an Applied Voltage Bias on Film Formation

Generally, electroless deposition is used to form the IL films on Mg alloys. Hence, the ability for the film to form and grow depends considerably on the reactivity of the IL with the substrate.

More recently, the use of a small potential bias to the working electrode (i.e. magnesium alloy) during film formation was investigated[97].

In a study by Howlett *et al* [23] using trihexyl(tetradecyl)phosphonium bis(2,4,4-trimethylpentyl)phosphinate $[P_{6,6,6,14}][(\text{C}_8)_2\text{PO}_2]$, ZE41 and AZ31 magnesium alloys were polarised during immersion with the IL. AZ31 was polarised to -0.1 and 0.1 V vs. OCP (open circuit potential) and ZE41 was polarised to potentials up to 0.5 V vs. Ag/AgCl. In both cases an anodic potential led to either increased in-situ surface resistance (AZ31) or increased resistance in a 0.1 M NaCl solution (ZE41), as measured by EIS. XPS analysis of ZE41 treated with $[P_{6,6,6,14}][(\text{C}_8)_2\text{PO}_2]$ at 0.25 V vs. Ag/AgCl for an hour found evidence of phosphate species, magnesium hydroxide and magnesium oxide. The authors concluded the film formed on the surface was a composite between the oxide and hydroxides and the IL anion[23]. Following this, Efthimiadis *et al* [24] studied the effect of a potential bias on ZE41 with trihexyl(tetradecyl)phosphonium diphenylphosphate ($[P_{6,6,6,14}][\text{DPP}])$ IL. Two-dimensional Time of Flight Secondary Ion Mass Spectroscopy (ToF-SIMS) mapping revealed that the application of a -0.2 V vs. OCP bias provided a more uniform film deposition than a film formed on ZE41 with this IL at OCP. Hence, the authors concluded that a negative bias led to the formation of the most resistive film[24]. In comparison, Howlett *et al* reported that a small positive bias led to the best behaviour[23].

As the cations used in these two studies are identical, and both investigate magnesium alloy ZE41, this difference suggests that the properties of the anion dictate the polarisation of the preferential bias due to the reactions which promote the formation of a more resistive film (e.g. oxidation vs. reduction of the anion). These studies show that a potential bias can indeed influence the formation of the IL film on a magnesium alloy. In addition, with only relatively small potential perturbations of a couple hundred millivolts the film forming process can be either improved or hindered.

2.6 Summary

As outlined in this literature review, the main limitation for the use of magnesium alloys is due to the poor corrosion properties. This includes corrosion as the result of exposure to harsh environments, such as marine conditions and pollutants, but the galvanic properties are also a major drawback in use of magnesium alloys. Due to the highly anodic nature of magnesium, when used in conjunction with other metals and alloys, special design considerations are required to prevent severe galvanic dissolution of magnesium parts. The microstructure, including alloying additions, grain size, etc., can greatly dictate the corrosion behaviour of magnesium alloys in many environments by altering the effect of microgalvanic processes. However, changes to the microstructure do little to affect galvanic corrosion between magnesium and other alloys. Therefore, there is a need for the development protective coatings for magnesium alloys which are cheap, easy to apply, provide good corrosion resistance in aqueous media in addition to acting as a barrier for metal-on-metal contact. Currently the coatings and protective methods which fulfil these requirements often involve the use of the hexavalent chromate ion (Cr(VI)), which due to its toxicity and carcinogenic nature, are being phased out of use and, in some cases, banned. Due to chromate's excellent ability to form corrosion protective films it has been extensively used in a number of industrial corrosion protective processes. These include conversion layers, anodising, surface activation (prior to electroless and electro-plating) and pigments in paints (to provide self-healing protection at defects). By removing this compound from use, alternative compounds and coating techniques need to be developed to provide adequate replacements. This has provided a considerable

challenge to the research community as any alternative method must not pose a risk to the health of either the employees which are to apply the coating or to the environment due to waste or emissions. In addition, for magnesium to be a viable material for selection over aluminium, the coating techniques need to be economical. However, despite the significant amount of negative attention chromate has received, fluoride containing compounds, which have been used to form resistive MgF_2 films, are also highly detrimental to the environment. The risk is even greater when the source of the fluoride comes from the use of hydrofluoric acid. Due to the fantastic physical properties of magnesium and its alloys, considerable research is ongoing in the pursuit of this goal. However, protecting magnesium from corrosion is no easy task.

ILs present a unique range of properties (no solvent, high thermal and electrochemical stabilities) as well as the ability to tailor the chemical structure (and hence the specific properties of the material, e.g. reactions with the metal surface, as well as the cost of the compound). The ionic liquid investigated in this work contains few elements (mostly alkyl chains) and is thus, if it were to be produced on a large scale, expected to be cheap. The non-volatility of the material also removes environmental issues related to air pollution (due to evaporation). The few studies investigating the corrosion properties of IL films in corrosive NaCl solutions show promise for further development; in particular, the use of electrochemical techniques to influence the formation of the films. However, as traditional electrolytes are aqueous solutions, insight into the behaviour of an electrolyte which does not contain the typical solvent-solute makeup is crucial in determining the successful use of these materials in formation of resistive films. Primarily, as outlined in the previous chapter, the research presented aims to gain an improved understanding of the influence of electrochemical techniques on film formation process on Mg alloy AZ31 in an IL.

Chapter 3

Experimental Methodology

3.1 Materials

3.1.1 AZ31 Magnesium Alloy and Glassy Carbon (GC)

AZ31 magnesium alloy was obtained from a direct strip cast (DSC) cylinder. Specimens were taken from the edge of the cylinder for use in experiments. No heat treatments were performed on the ingot after being received. The microstructure, shown in Figure 3.1, of the alloy consists of the α matrix phase, the Al rich β phase ($Mg_{17}Al_{12}$) as well as Mn rich intermetallics.

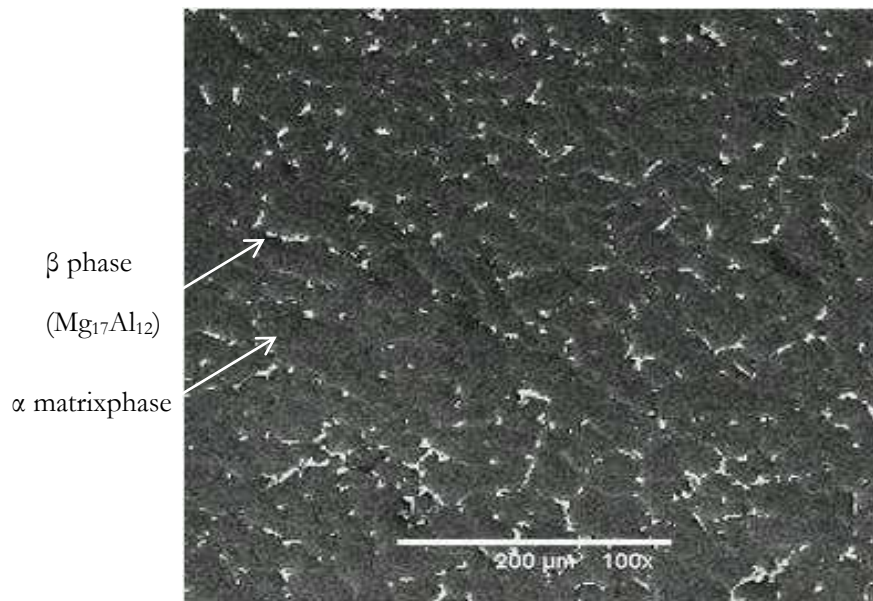


Figure 3.1 - SEM image of AZ31 from both the edge of the DSC cylinder. Image courtesy of Steven Lin.

The composition of commercial AZ31 is listed in Table 3.1 below.

Table 3.1 - Elemental composition of commercial AZ31[33].

Element	Al	Zn	Cu	Mn	Si	Ni	Mg
wt%	2.40-3.60	0.50-1.50	<0.1	>0.15	<0.1	<0.03	97.0

Mounted specimens were prepared by attaching an electrical wire to the metal using adhesive Cu conducting tape. Struers Epo-Fix cold-mounting epoxy resin was used to encapsulate the 0.5 x 0.5 cm specimens.

AZ31 specimens were ground to a P4000 grit surface finish on SiC papers under running deionised water. Surfaces were rinsed with acetone between papers and finally rinsed with acetone and dried under a nitrogen gas stream following grinding. All AZ31 surfaces were incubated in a desiccator at room temperature for one hour prior to use.

SIGRADUR® G glassy carbon (GC) from HTW Germany was used as a nonreactive reference for AZ31. GC was polished on fibre pads using 0.05 µm alumina powder with deionised water. The surfaces were rinsed with deionised water thoroughly after polishing and dried under a N₂ stream.

Mixed Oxide Coated Ti ribbon mesh was obtained from Savcor ART.

3.1.2 [P_{6,6,6,14}][ⁱ(C₈)₂PO₂] Ionic Liquid

Ionic liquid trihexyl(tetradecyl)phosphonium bis(2,4,4-trimethylpentyl) phosphinate ([P_{6,6,6,14}][ⁱ(C₈)₂PO₂]) was purchased from both Sigma-Aldrich and io-li tech with a purity of ≥ 95%. Purification of the IL was achieved by first dissolving in high purity liquid chromatography (HPLC) grade acetone and passing through a column containing coarse sand (SiO₂), activated charcoal, basic activated alumina and filter agent (fine SiO₂). The solution was then passed through µm filter paper and a µm hydrophilic syringe filter. Excess acetone and water was evaporated on a vacuum line until the water levels were between 700-1500 ppm (as measured by a Metrohm KF830 Coulometer).

Additional water was added to IL solution to make up the 6wt% H₂O solutions.

ICP analysis of both the ‘as received’ IL and the purified IL are given in Appendix G. ICP analysis returned values for the impurities of Fe, Ar, Zn, Pb, Cd, Cu, Mn, F, Si and excess P as below 2 µg/L.

The structure of trihexyl(tetradecyl)phosphonium bis(2,4,4-trimethylpentyl) phosphinate ([P_{6,6,6,14}][ⁱ(C₈)₂PO₂]) is shown in Figure 3.2.

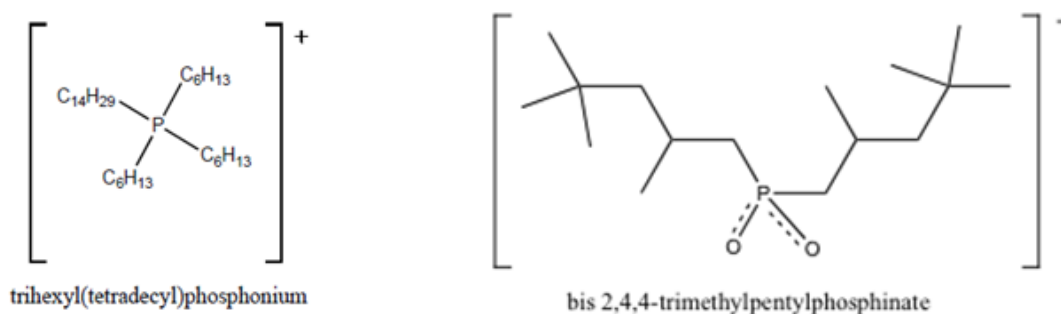


Figure 3.2 - Structure of trihexyl(tetradecyl)phosphonium bis(2,4,4-trimethylpentyl) phosphinate ([P_{6,6,6,14}][ⁱ(C₈)₂PO₂]) IL.

3.1.3 Dilute Solutions

A list of the various dilute solutions made using the IL are shown below in Table 3.2. HPLC acetonitrile was used to dissolve the compounds. Lithium triflate or lithium trifluoromethanesulfonate (LiCF₃SO₃) was obtained from Sigma Aldrich at 96% purity.

Table 3.2 – Compositions of dilute IL solutions prepared.

Solution	Solvent	Concentration of IL	Concentration of LiCF ₃ SO ₃	Name in Text
1	Acetonitrile	0.1 M	-	ILAN
2	Acetonitrile	0.01 M	-	Dilute ILAN
3	Acetonitrile	-	0.1 M	ANSO

3.2 Pipette Cells

Photos of the pipette cell set-up are shown in Figure 3.3. The inner area of the pipette (and therefore working electrode (W.E.) area) is $50.272 \pm 6 \text{ mm}^2$. The clamp (Figure 3.3 a) was used to make a seal on the working electrode to prevent leaking (through deformation of the base of the polyethylene pipette). The cell was comprised of the polyethylene pipette in conjunction with a Pt-wire pseudo reference and a mixed-oxide coated Ti-mesh counter electrode (Figure 3.3 b). In the first year of this PhD a Pt wire counter electrode was also used but later replaced with Ti mesh (commonly used in concrete and soil applications) to achieve better counter electrode geometry and exposed surface area.

A second cell was designed specifically for use within an argon glove box (early experiments, later experiments used the pipette cell as shown in Figure 3.3), and is shown in Figure 3.4. A steel plate with brass screws was used to compress the pipette on the AZ31 and glassy carbon surfaces. The body of the cell was made from polycarbonate.

The benefit of using the pipette cell was that its size allowed the use of very small volumes of IL (approximately 0.25 mL) with each test.

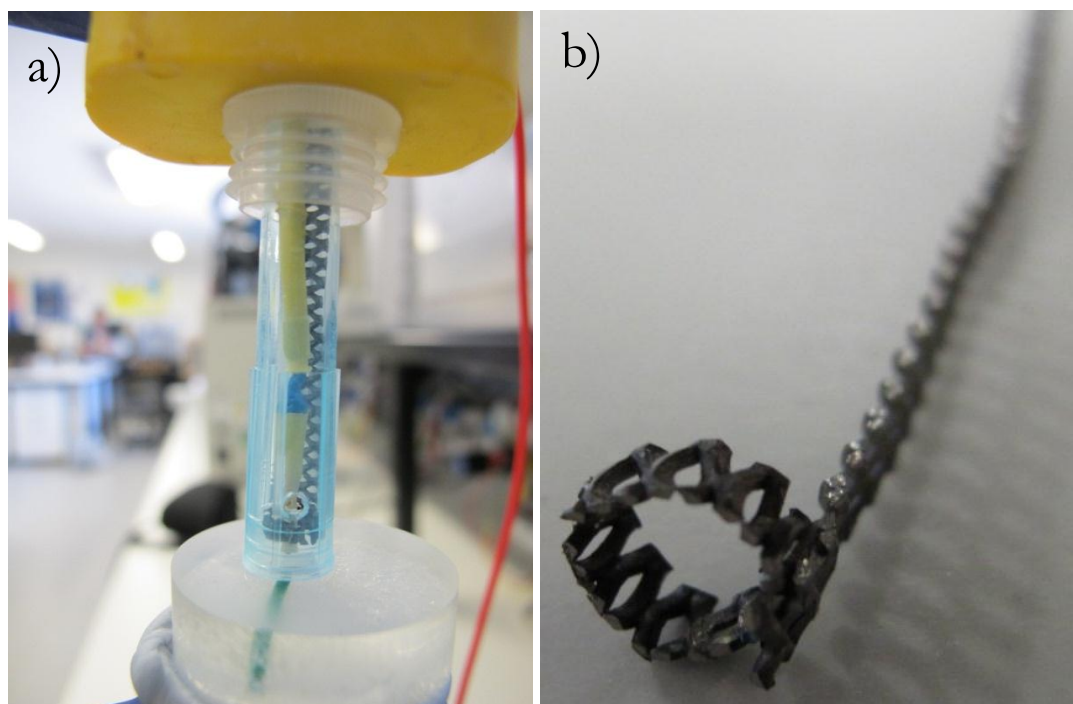


Figure 3.3 – Photos of a) pipette cell set-up (incl. PE pipette, Pt wire pseudo metal reference, mixed oxide Ti-mesh counter electrode); b) mixed oxide Ti-mesh counter electrode.

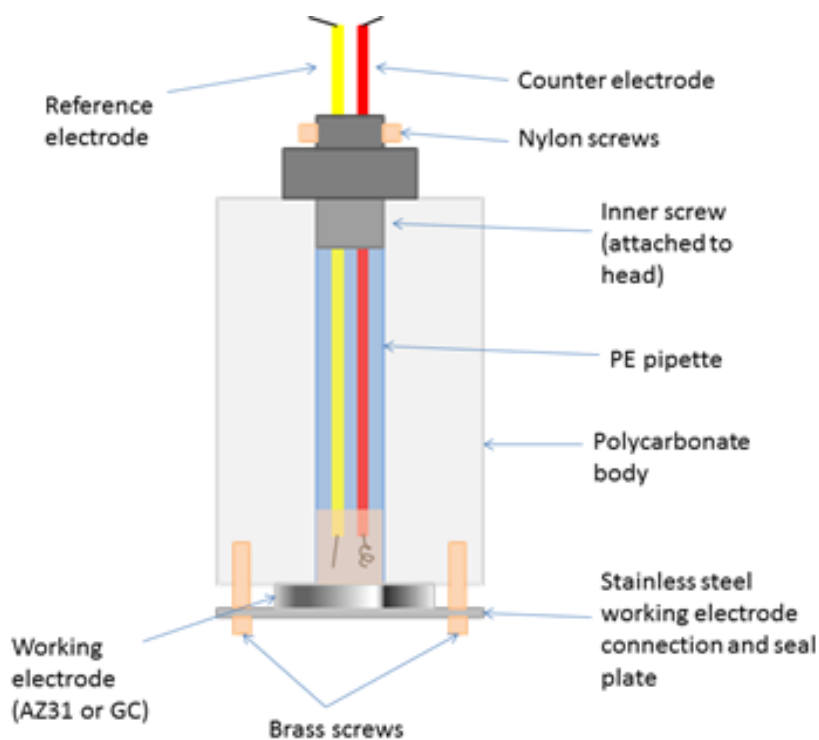


Figure 3.4 – Schematic of special pipette cell for use in an argon glovebox.

3.3 Cyclic Voltammetry (CV)

Cyclic voltammetry of AZ31 and GC in pure IL (both dry and wet) were performed on Princeton Applied Research VMP2/Z and Biologic VMP3 potentiostats. Experiments performed to exclude the influence of oxygen and ambient water in the atmosphere were performed in an argon glovebox, where both water and oxygen levels were maintained below 100 ppm. CVs were conducted at scan rates of 1, 10 and 100 mV/s, controlled by Biologic EC-Lab versions 8-10 software, inside a Faraday cage. Table 3.3 lists the different parameters used in these experiments.

Table 3.3 – Scan bounds used for evaluating electrochemical behaviour of AZ31 and GC. All scans were repeated 3 times (total of 4 cycles).

Scan Label	Scan Rate (mV/s)	Scan Bounds
1	1, 10 & 100	OCP ↔ 3 V
2	1, 10 & 100	OCP ↔ -3 V
3	1	OCP → 3 V ↔ -3 V
4	10	OCP → 0, 1.5, 2.5, 3, 4 V

CVs conducted in acetonitrile solutions (section 3.1.3 and Table 3.2) were conducted inside a Faraday cage using a Biologic VMP3 multi-channel potentiostat controlled by Biologic EC-Lab version 10.11 software. Scans 1, 2 and 4 (Table 3.3) were performed on both GC and AZ31 at 10 mV/s only.

CVs performed to produce films on AZ31 for corrosion protection were formed in IL at 1 mV/s to varying final voltages of 1 V and 3 V vs. Pt for a total of 10 cycles unless otherwise stated.

3.4 Film Formation

For cyclic voltammetry film formation see Section 3.3.

3.4.1 Constant Current/Galvanostatic Anodising

Anodising was conducted in the pipette cell (Figure 3.3) using a Biologic VMP3 multi-channel potentiostat, controlled by Biologic EC-Lab version 10.11 software. All experiments were conducted inside a Faraday cage on laboratory benches with full exposure to laboratory air.

Current densities of 0.005, 0.01, 0.05, 0.1 and 0.5 mA/cm² were applied in neat IL to a cut-off potential of 18 V. In some cases the final potential was maintained for an additional period of time ranging from 5 minutes to 1 hour. Surfaces anodised in ILAN were done so at current densities of 0.05, 0.5, 1, 2, 3, 5 and 10 mAcm⁻² to a cut-off potential of 18 V.

After treatment, surfaces were washed of excess IL using ethanol and deionised water and finally dried under a N₂ stream.

3.4.2 Constant Potential/Potentiostatic Anodising

Anodising was conducted in the pipette cell using either a Princeton Applied Research VMP2/Z or Biologic VMP3 multi-channel potentiostat. Biologic EC-Lab version 10.11 software was used to gather and interpret data.

The voltage was increased at a rate of 1 or 100 mV/s to the final potential and maintained for times between 1 and 96 hours. The current and potential was recorded throughout the entire experiment. When removed surfaces were washed of excess IL using ethanol and deionised water and finally dried under a N₂ stream. Potentials of 0, 1 and 3 V vs. Pt and ± 0.2 , ± 0.1 , -0.4 , 1.5 and 2.5 V vs. OCP were applied.

Elevated temperature experiments were performed using a copper hotplate at the base of the cell (between the AZ31 specimen and the base of the clamp containing the pipette cell) connected to a temperature control unit to maintain a stable temperature of 50°C. Measurements were controlled using EC-Lab version 10.11 with a Biologic VMP3 multi-channel potentiostat. Surfaces were polarised to 3 V vs. Pt for 24, 48 or 96 hours.

3.5 Electrochemical Impedance Spectroscopy (EIS) and Potentiodynamic Polarisation (PP)

PP and EIS were conducted in 400 mL, neutral pH (6.5-7.5) 0.01 M NaCl in a 3-electrode electrochemical cell (Figure 3.5) using a saturated calomel reference electrode (SCE) and a mixed-oxide Ti mesh counter electrode. All experiments were conducted in a Faraday cage open to the laboratory air.

EIS was conducted between 200 kHz and 50 mHz with a 10 mV amplitude, immediately after immersion and approximately every 12-15 minutes after immersion for a total time of 1 hour. PP was conducted at a rate of 0.167 mV/s (as per ASTM standard G61-86(2009)) between -0.2 V and $+0.5$ V vs. OCP approximately 1 hour after immersion.

Data was collected using a Biologic VMP3 multi-channel potentiostat with biologic EC-Lab version 10.11.



Figure 3.5 – 3 electrode electrochemical cell, 1: saturated calomel electrode (SCE) and luggin attachment, 2: Working electrode holder, 3: mixed-oxide Ti mesh counter electrode.

3.6 Surface Characterisation

Optical microscopy was performed on a Motic BA300Pol and Leica MZ6 Optical microscope.

Scanning Electron Microscopy (SEM)

Three SEM machines were used to collect the images presented in this thesis. Hence, they will be listed based on the data acquired using them.

Field Crystallised Surfaces:

Secondary scanning electron microscopy (SEM) with energy dispersive x-ray spectroscopy (EDS) was performed on a JEOL 840A SEM using Oxford Instruments INCA software at the Monash Centre for Electron Microscopy (MCEM). An accelerating voltage of 15 keV and a working distance of 39 mm were used in all cases unless otherwise stated.

Defects at Constant Current, Pickled and Etched Surfaces and Inhibitor Surfaces:

JEOL Neoscope JCM-5000 benchtop SEM, using a 5 keV accelerating voltage with JCM-5000, version 1.2.3 software.

Some images and EDS for the defects on the constant current surfaces in addition to the pickled and etched microstructures were obtained on a Phillips XL20 SEM at an accelerating voltage of 5 keV with an Oxford Instruments X-Max EDS attachment. Phillips Microscope Control XL and Oxford Instruments Aztec (version 1.0) software were used.

Focused Ion Beam – Scanning Electron Microscopy (FIB-SEM) was used to measure the film thicknesses formed from ILAN and IL using a FEI Quanta 3D FEG FIB-SEM instrument. Gallium ions were used to section the surfaces with a 3 nA current, prior to imaging using secondary electron SEM at an accelerating voltage of 5 keV. A platinum layer was deposited on

the surfaces prior to the milling and imaging to minimise shadowing effects from the rounded edge of the milled sectioning. The platinum was deposited from the compound (Trimethyl)methylcyclopentadienylplatinum(IV) at an accelerating voltage of 30 kV and a current of 6 pA μm^{-2} .

Au layers were sputtered for 180 seconds.

X-Ray Diffraction (XRD) was performed on a Philips 1140/90 powder diffractometer with a 1° divergence slit and .2° receiving slit using Cu k- α radiation. Experiments were performed at 2°/min with a 0.02° step size using GBC Traces version 6.6.1 software.

X-Ray Photoelectron Spectroscopy (XPS) was performed on the soft X-ray beam line at the Australian Synchrotron and on a Kratos AXIS Ultra DLD (Kratos Analytical Ltd, Manchester, UK) laboratory XPS, with a monochromated Al K α x-ray source, at LaTrobe University with assistance from Anthony Somers and Robert Jones.

Attenuated Total Reflectance-Fourier Transform Infra-Red (ATR-FTIR) and transmission Fourier Transform Infra-Red (FTIR) were performed on Varian 3100 Excalibur series instrument with a resolution of 2 cm⁻¹ using Varian Resolutions Pro version 4.1.0.101 software. The chamber was purged with N₂ gas for 3-5 minutes prior to each data acquisition.

Optical profilometry was conducted on Veeco ContourGT using Vision 64 software. Roughness values Sa and Sz were calculated using this software using Eqn. 3.1 and 3.2. The mean roughness (Sa) measures the overall texture of the surface but is insensitive to differentiating between peaks and valleys. The Ten Point Height (Sz) is a measure of the average difference between the five highest peaks and five lowest valleys, where a peak or valley is distinguished as any point that is above all eight nearest neighbours or below eight nearest neighbours respectively.

$$Sa = \iint_a |Z(x,y)| dx dy \quad \text{Eqn. 3. 1}$$

$$Sz = \frac{\sum_1^5 |PeakHeights| + \sum_1^5 |ValleyDepths|}{5} \quad \text{Eqn. 3. 2}$$

Time of Flight Secondary Ion Mass Spectroscopy (ToF-SIMS) was performed at La Trobe University on a Munster ION-TOF ToF-SIMS IV using a Bi³⁺ ion gun over a 500 × 500 μm area with the assistance of Anthony Somers and Robert Jones.

3.7 Electrochemical Technique Theory

3.7.1 Cyclic Voltammetry

Cyclic voltammetry (CV) involves ramping applied potential to the working electrode at a constant, set rate (v) between two pre-set potentials, E_i and E_f . The potential is then reversed and taken back to the initial potential (and can be cycled)[98]. This reversal of potential is what separates CV from linear sweep voltammetry[99]. The current is recorded, with respect to potential and time, throughout the experiment, which allows for the identification of potential-dependent reactions occurring in the system. Figure 3.6 shows a comparison of the potential application between linear sweep and cyclic voltammetry.

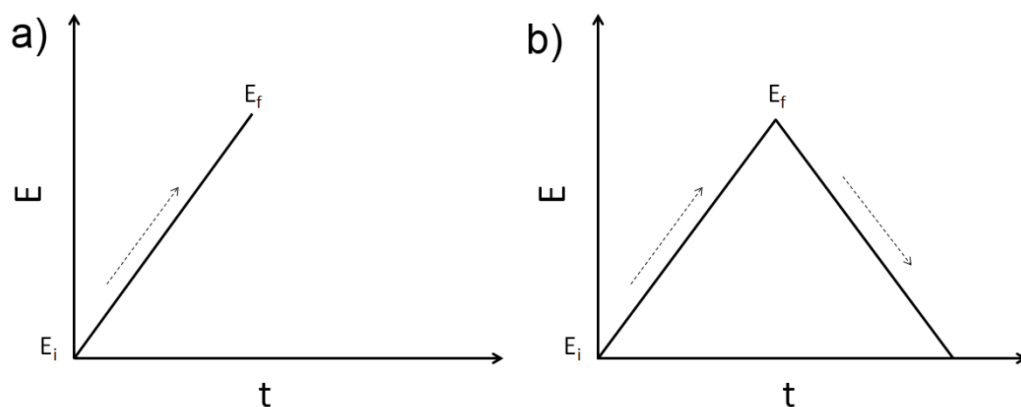


Figure 3.6 – Schematic representation of potential response in a) linear sweep voltammetry and b) cyclic voltammetry. E_i is the initial pre-set potential and E_f is the final pre-set potential.

An increase in positive current is associated with oxidation of a reactive species, whereas a negative current is reduction. The potential at which this initial current increase occurs is termed the *take-off voltage*. The current increase is due to Faradaic electron transfer as species are either oxidised or reduced[98, 99]. When the potential reaches a value appropriate for the oxidation or reduction of an electroactive species, the concentration at the working electrode will decrease with respect to the bulk solution as the species is reacted[98]. This establishes a concentration gradient between the electrode and the bulk and, from Fick's first law, a current will begin to flow[98]. As the potential is continued to scan, the concentration gradient will increase as more of the electroactive species is oxidised/reduced[98] and in order to continue oxidising/reducing reactive species must diffuse through the bulk electrolyte to the working electrode. However, the surface concentration will eventually approach zero, which leads to the formation of a peak current[98, 99]. At this point the concentration gradient can no longer increase with further potential scanning. In fact, due to the increased size of the diffusion layer throughout this process, the gradient relaxes and the current decreases with it[98]. The current plateaus at a new equilibrium current level as the reaction is rate limited by the diffusion of the reactive species[99]. When the current is reversed the process occurs again but with the other electroactive species. E.g. if the initial, forward, reaction involved $\text{Ox} \rightarrow \text{Red}$ (i.e. reduction of species Ox to species Red), when the potential sweep is reversed we will have $\text{Red} \rightarrow \text{Ox}$ (species Red oxidising to Ox). The shape of the current response with varying applied scan rates ($v - \text{V/s}$) allows identification of chemical complications such as adsorption or homogeneous reactions which occur with the electron transfer process[98]. Solutions must be left unstirred during cyclic voltammetry to ensure mass transfer properties are not disturbed[98].

As CVs are often performed in both the anodic and cathodic potential ranges, oxidation (positive current) and reduction (negative current) reactions can be identified. In addition, this can inform us as to whether a reaction is reversible, quasi-reversible or irreversible.

Upon reversing of the potential scan (after the initial peak) another peak will appear of opposite sign (reduction for initial oxidation and vice versa) and of the same magnitude if the system is reversible. Reversible systems are those that maintain equilibrium levels of oxidative and reductive species as satisfied by the Nernst equation[100], and as a result can be referred to as Nernstian processes[98]. Reversible systems are those in which the rate of the electron transfer is greater than the rate of mass transport[98]. Reversible systems present peaks whose peak-to-peak separation is equal to $59/n \text{ mV}$ (where n is the number of electrons passed in the reaction

per molecule) and the ratio of the forward and reverse peak currents are equal to 1[99, 100]. In addition, variation of scan rate does not lead to peak shift and the magnitude of the peak currents is proportional to the square root of the scan rate[100].

Irreversible systems are defined as those in which the reactions (electron transfer) are slow relative to the scan/mass transfer rates[98, 100]. As a result the reduction/oxidation of the electron transfer process can occur at more cathodic potentials than the formal electrode potential of this couple[98]. Hence, in irreversible systems the peak separation is no longer independent of the scan rate, and will move further from the standard potential (E°) with increasing scan rate[98]. Generally, the more irreversible the system, the greater the peak-to-peak separation[100]. Often the peak separation can be so large such that the reverse peak is undetected[98]. In addition, products can be produced by initial reactions, which then react differently as the system is cycled.

Finally, quasi-reversible systems are those which behave reversibly at low scan rates and irreversibly at high scan rates[98]. Hence, the rate of the electron transfer process is of the same magnitude as the mass transport[98]. The spacing between the forward and reverse peaks in a quasi-reversible system is greater than reversible systems[98]. Like with irreversible systems, the forward peak potential shifts to potentials further from E° with increasing scan rate[98]. In quasi-reversible systems the relationship of i_{pf}/\sqrt{v} increases with increasing scan rate[98].

Zanello demonstrates that the reversible, irreversible and quasi-reversible systems can be explained by reorganisation of the electroactive species involved in the transfer processes[98]. For reversible systems electron transfer results in no significant reorganisation of the molecule, whilst irreversible processes result in framework destroying reorganisations. As quasi-reversible systems lie between these two processes Zanello concludes that electrochemically quasi-reversible systems must undergo significant structural reorganisation of the molecule without fragmentation of the molecular framework[98].

In addition to the electron transfer processes, the current response obtained in CVs can be complicated by chemical reactions which involve the electroactive species. These chemical reactions can either precede (CE processes) or follow (EC and ECE (where ECE is a chemical reaction between two electron transfer processes)) the electron transfer and can also be reversible or irreversible reactions themselves. The specific effect of these reactions on the electron transfer process is also dependent on whether the electron process is reversible, irreversible or quasi-reversible. In general these reactions result in shifting the position of the peak positions and changes to the relationships i_{pf}/\sqrt{v} and i_{pf}/i_{pr} . For CE processes the current and potential of the forward peak (i_{pf} and E_{pf}) will be affected, whilst EC processes affect the current and potential of the reverse peak (i_{pr} and E_{pr})[98]. A large number of conditions can hence arise, and are explained in detail elsewhere[98].

Adsorption processes can also complicate the current response[101], the extent of which depends on the strength of the adsorption process. For weak adsorption, the current associated with the adsorbed reactant will increase significantly. That is, if the oxidant species is adsorbed the Ox \rightarrow Red peak will significantly increase in current and vice versa for Red[98]. The current response will increase linearly with scan rate such that the ratio i_{pf}/v remains constant. If the adsorption process is strong pre- and post-peaks will occur. If the adsorbed species is Red pre-peaks will occur whilst post-peaks will occur if Ox is adsorbed[98].

3.7.2 Electrochemical Impedance Spectroscopy

Electrochemical impedance spectroscopy (EIS) measures the conductivity of a surface by applying an AC potential and measuring the current response. EIS is a very powerful technique for the evaluation of corrosion properties of coatings on metals. This is partly due to the speed of measurement and evaluation of inhibitor and coating behaviour as well as the ability to estimate corrosion rates in low conductivity media.

This technique involves applying a small sinusoidal potential of a set value (usually less than 50 mV) to the working electrode over a range of frequencies and measuring the resultant current response. The frequencies applied are typically over the range of 1 mHz to 100 kHz. The measurement of impedance comes from a transfer function relating the Laplace (or Fourier) transform of a current response to the Laplace (or Fourier) transform of the perturbation potential[102, 103]. This becomes impedance when the conditions of causality (the response being a result *only* of the perturbation), linearity (the response due to the perturbation is independent of its magnitude), stability (the system returns to its starting state after perturbation) and finite valued (the impedance must be finite at all frequencies and as the frequencies approach both 0 and ∞) are fulfilled[102]. This time dependent current response $I(t)$ as a result of the applied sinusoidal potential $V(t)$ can be represented as an angular frequency, ω , dependent impedance $Z(\omega)$, such that[104]:

$$\mathbf{Z}(\boldsymbol{\omega}) = \frac{V(t)}{I(t)} = \frac{V_0 \sin(\boldsymbol{\omega}t)}{I_0 \sin(\boldsymbol{\omega}t + \boldsymbol{\varphi})} \quad \text{Eqn. 3.3}$$

Where ω is the angular frequency and φ is the phase angle between $V(t)$ and $I(t)$.

Different processes at the electrode surface absorb electrical current and this results in a time lag between the applied potential $V(t)$ and the recorded current response $I(t)$ (they go out of phase) and a measureable phase angle[104]. The impedance $Z(\omega)$ can be represented by real ($Z'(\omega)$) and imaginary ($Z''(\omega)$) components such that:

$$\mathbf{Z}(\boldsymbol{\omega}) = \mathbf{Z}'(\boldsymbol{\omega}) + \mathbf{Z}''(\boldsymbol{\omega}) \quad \text{Eqn. 3.4}$$

These components can be plotted as $Z''(\omega)$ as a function of $Z'(\omega)$ to form the Nyquist plot. Alternatively, Bode plots can be constructed of $\log|Z|$ and φ as a function of frequency, f , in Hertz, where $\omega = 2\pi f$ [104].

Schematic representations for a simple charge transfer process are represented in a Nyquist and Bode plot in Figure 3.7 a) and b) respectively. At high frequency the imaginary component of the impedance disappears and the impedance response consists only of the solution resistance R_s . When the frequency is sufficiently low the imaginary component will disappear again and the impedance response will consist of the solution resistance and the polarisation resistance R_p [104]. The parameter R_p is inversely proportional to the corrosion rate, and can thus be determined to estimate the corrosion of the metal[104]. The Bode plot gives much of the same information as the Nyquist plot; however the phase angle is commonly used to determine the intactness of coatings on a metal, where -90° is an ideal coating[105].

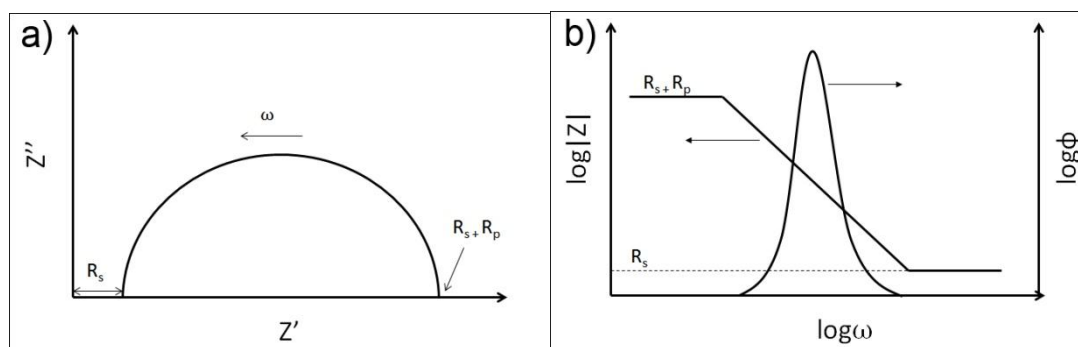


Figure 3.7 – Schematic EIS responses of a simple charge transfer process in a) Nyquist form and b) Bode form.

The advantage of using EIS as opposed to other electrochemical corrosion testing techniques (e.g. PP) is that the system is only perturbed by a small voltage, which means the surface is never polarised significantly from steady-state corrosion[9].

3.7.2.1 Modelling of EIS data

Modelling of EIS spectra is done through the use of a number of electrical components, including the resistor (R), capacitor (C) and inductor (L) (among others). The appropriate arrangement of these components into an equivalent circuit allows capacitance and resistance (etc.) values to be calculated and directly associated with physical corrosion processes[102]. If the voltage and current remain in-phase the response will be pure resistance. If the current and voltage go out of phase a capacitor or inductor will be in the circuit[106]. For coatings which have a capacitor and resistor in parallel, the coating is considered capacitive when the resistance and/or capacitance of the coating is high, and the phase angle (representative of the magnitude out-of-phase) will be near -90° . If the coating is resistive the resistance and/or capacitance is low and the phase angle will be near 0° [106]. Barrier coatings will have high capacitance, and hence phase angles near -90° . Coatings which leach into solution (or are simply soluble) will present resistive behaviour with phase angles closer to 0° [106].

When modelling EIS spectra, care must be taken not to include more electrical components than there are physical components to describe[102]. This can be a trap as obtaining a good correlation between the fit of the model with the experimental data is easier when more components are introduced into the circuit. However, this does not make the circuit a correct representation of the surface and the corrosion processes occurring. To avoid this, the simplest circuit that can fit the data is typically the correct circuit[102]. There are many mathematically equivalent circuits and hence care must be taken such that the choice of model is based on the physical processes of the system and not merely on the ability to get the best fit. This is especially important for unique circuits and if there are any components which cannot be easily explained[102].

In cases where there is a diffusion controlled process another element called Warburg impedance (W) is used. This component is incorporated into one of the most basic equivalent circuits, known as the Randles circuit. Figure 3.8 a) shows this circuit as well as the appearance of low frequency pseudo-inductive behaviour in Figure 3.8 b).

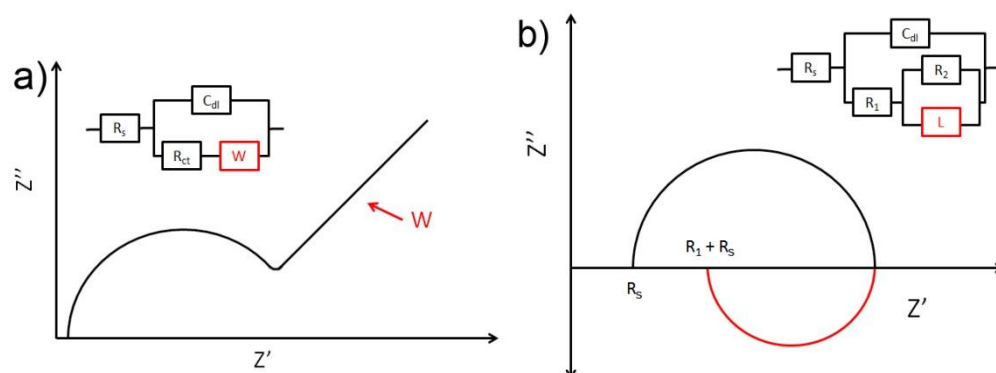


Figure 3.8 – a) Randles circuit for diffusion processes, where R_s = solution resistance, C_{dl} = double layer capacitance, R_{ct} = charge transfer resistance, W = Warburg impedance; b) low frequency pseudo-inductance behaviour, where R_s = solution resistance, C = double layer capacitance, R_1 = charge transfer resistance, L = inductance.

Inductive behaviour in EIS is a controversial topic. Physically, an inductor is an electrical component that stores electrical energy in its magnetic field. However, this definition of an inductor cannot be directly applied to corrosion systems. In a Nyquist plot this behaviour can be identified by the impedance entering the fourth quadrant (Figure 3.8 b), and in a Bode plot the impedance will decrease at low frequency and a negative phase angle will appear[102]. The difficulty with inductance arises from the ability for this behaviour to be due to things other than corrosion phenomena. One possible cause is nonlinearity of the response to the potential perturbation due to desorption or adsorption of an inhibitor (or other species) near the free corrosion potential[102, 107]. In the case of magnesium alloys, the adsorption process has been attributed to accumulation of $Mg(OH)^+$ and $Mg(OH)_2$ on the surface[107] and to film thinning with chloride (Cl^-) adsorption[108]. Another explanation for this behaviour with magnesium alloys commonly accepted in the literature is that the low frequency inductance occurs due to the initiation of localised corrosion in the form of pitting[42, 109-111]. However, these may indeed be the same process. Isa *et. al*[112] observed low frequency inductance behaviour with an Al-Zn-Sn alloy. They state that the inductive behaviour is typically interpreted as adsorption-relaxation phenomena, which is associated with oxidation processes and surface activity (i.e. corrosion) at the metal-electrolyte interface[112]. In addition, in a study of the corrosion of Al-Zn-Mg alloys, Cabot *et. al*[113] also attributes a low frequency inductive loop with adsorption of Cl^- ions associated with pitting corrosion.

3.7.3 Potentiodynamic Polarisation and Tafel Curves

Potentiodynamic polarisation (PP) involves scanning of the working electrode between two set potentials at a set rate (scan rate) and measuring the resultant current. This method can be used to evaluate the rate of corrosion of a metal surface in a range of corrosive solutions. It is important that the scan rate used is sufficiently low to satisfy ‘steady-state’ conditions in order to gain corrosion behaviour close to operating behaviour. A slow scan rate of 0.167 mV/s is a standard scan rate, as per ASTM standard G61-86(2009). The applied scan rate can be important as some features identified through PP curves are dependent on the scan rate. For example, with increasing scan rate the pitting potential, E_p , will increase to more anodic, noble potentials[102].

The shape of the polarisation curve can be explained by the Mixed Potential Theory[104]. This theory states that the sum of the cathodic reduction currents must equal to the sum of the anodic oxidation currents. Hence the rate of the anodic and cathodic reactions are equal[104]. The corrosion potential, E_{corr} , can also be referred to as the mixed potential as it is a combination of both the anodic and cathodic half-cell reactions[104].

The polarisation response can be broken down into two types: activation and concentration polarisation. Activation polarisation exists when the electron flow is controlled by a half-cell reaction. The Tafel relationships can be represented by[104]:

$$\eta_a = \beta_a \log \frac{i_a}{i_0} \quad \text{Eqn. 3.5}$$

$$\eta_c = \beta_c \log \frac{i_c}{i_0} \quad \text{Eqn. 3.6}$$

Where β is the Tafel slope, i is the current of the reaction (anodic or cathodic), i_0 is the exchange current and η is the potential change $E - e$, where e is the equilibrium half-cell potential. Equation 2.6 represents the anodic parameters whilst equation 3.6 represents the cathodic parameters. For cathodic polarisation, η_c , the excess of electrons to the electrode results in a negative shift of E with respect to e [104]. With anodic polarisation, η_a , electrons are removed from the surface This results in a positive shift of E with respect to e . Based on reactions 3.5 and 3.6 we can see these give linear curves. Concentration polarisation occurs when depletion of the reactive species occurs adjacent to the electrode. Concentration polarisation can be represented by[104]:

$$\eta_{conc} = \frac{2.3RT}{nF} \log \left[1 - \frac{i_c}{i_L} \right] \quad \text{Eqn. 3.7}$$

Where R is the gas constant, F is Faraday's constant, T is temperature, n is the number of electrons in the reaction, i_c is the current of the cathodic reaction and i_L is the limiting current (that cannot be exceeded due to the limited diffusion of the reacting species)[104]. The limiting current can be described by:

$$i_L = \frac{D_Z n F C_B}{\delta} \quad \text{Eqn. 3.8}$$

Where D_Z is the diffusion coefficient of the reacting species Z , and C_B is solution concentration.

Hence these relationships can be combined to form:

$$\eta_{T,c} = \beta_c \log \frac{i_c}{i_0} + \frac{2.3RT}{nF} \log \left[1 - \frac{i_c}{i_L} \right] \quad \text{Eqn. 3.9}$$

As the anodic reaction is dissolution of the metal electrode, only the cathodic reaction is complicated by concentration polarisation[104].

As both anodic and cathodic reactions continue their half-cell electrode potentials change according to equations 3.5 and 3.9 until the potentials are equal at the corrosion potential E_{corr} . At E_{corr} the rates of the anodic and cathodic reactions are equal such that $i_c = i_a = i_{corr}$ (the corrosion current).

Polarisation curves are typically plotted with $\log J$ (where J is current density – mAcm⁻²) as a function of potential, E . The corrosion potential E_{corr} and corrosion current i_{corr} can be calculated graphically by extrapolating the linear sections of the polarisation curve such that the anodic and cathodic reactions intersect. Along with being able to calculate corrosion currents and potentials, the currents of the anodic and cathodic reactions themselves can be used to understand corrosion processes on an electrode. For example, a lower anodic current means less metal dissolution as a function of potential. This can also lead to determination of passive behaviour, which can be found in some alloys wherein the current becomes independent of the potential for a specific potential window.



Chapter 4



Results and Discussion

Summary

This chapter presents an investigation which attempts to understand the film forming process when AZ31 is anodically treated in $[P_{6,6,6,14}][C_8]_2PO_2$ IL. The focus of this chapter begins with the electrochemistry of the IL. The research established prior to this work used both anodic and cathodic biases to alter the IL films formed on the magnesium alloy surfaces. However, lack of understanding of the behaviour of the IL in both anodic and cathodic conditions presented a need for further investigation. The electrochemistry reported here revealed that, in this particular IL, anodically grown passivating films could be formed. Two main methods of film formation were employed: constant potential and constant current (galvanostatic) anodising. The focus shifted primarily to the galvanostatic process as greater control over film growth was realised. Films formed using both methods consisted primarily of Mg and O (mostly in the form of $Mg(OH)_2$ and small components of the IL (C and P elements). The films preferentially deposited over the α phase, which led to a decrease in the anodic reaction on AZ31 in aqueous 0.01 M NaCl. However, forming high quality, protective films was difficult. A surface pre-treatment in the form of acid pickling prior to film deposition provided a measurable improvement in corrosion performance. With the acid pre-treatment the IL films were able to reduce the cathodic reaction as well as the anodic reaction, which suggests greater coverage of the IL film.

4.1 Electrochemistry of $[P_{6,6,6,14}][C_8]_2PO_2$ IL on AZ31 and Glassy Carbon

4.1.1 Section Overview

Previous studies involving the potential biasing of magnesium alloys (both AZ31 and ZE41) in ILs only cover a relatively small potential range.

In order to understand the reactions which occur on AZ31 in IL, it is important to have an inert comparison. This comparison allows reactions as a result of AZ31 to be separated from the purely IL-based reactions. This will facilitate further understanding of the formation of an IL based protective surface film.

This section focuses on determining the behaviour of the IL system over a reasonably large voltage range, in order to determine any limitations for potentiostatic treatments and also on understanding the effect of water and potential bias, as well as the influence of scanning rates, on the electrochemical processes which occur on the alloy in comparison with an inert glassy carbon (GC) electrode. The kinetics and reactions of the systems were evaluated using a

dynamic electrochemical technique, *cyclic voltammetry* (CV). Detailed theory on this technique has been described in Section 2.5.1.

4.1.2 Reactions in IL on AZ31 and GC: A Comparison

AZ31 and GC were cycled from OCP to +3 V vs. Pt and OCP to -3 V vs. Pt at 1, 10 and 100 mV/s. Karl Fischer analysis of the IL gave water levels of approximately 1000 ppm, however, due to the water absorbing nature of the IL (even in a desiccator) this may have increased to values as high as 1500 ppm during storage between experiments. Despite this, the water levels are still significantly low in comparison to the water levels investigated later in section 4.1.4 (as per the effect of water on CVs).

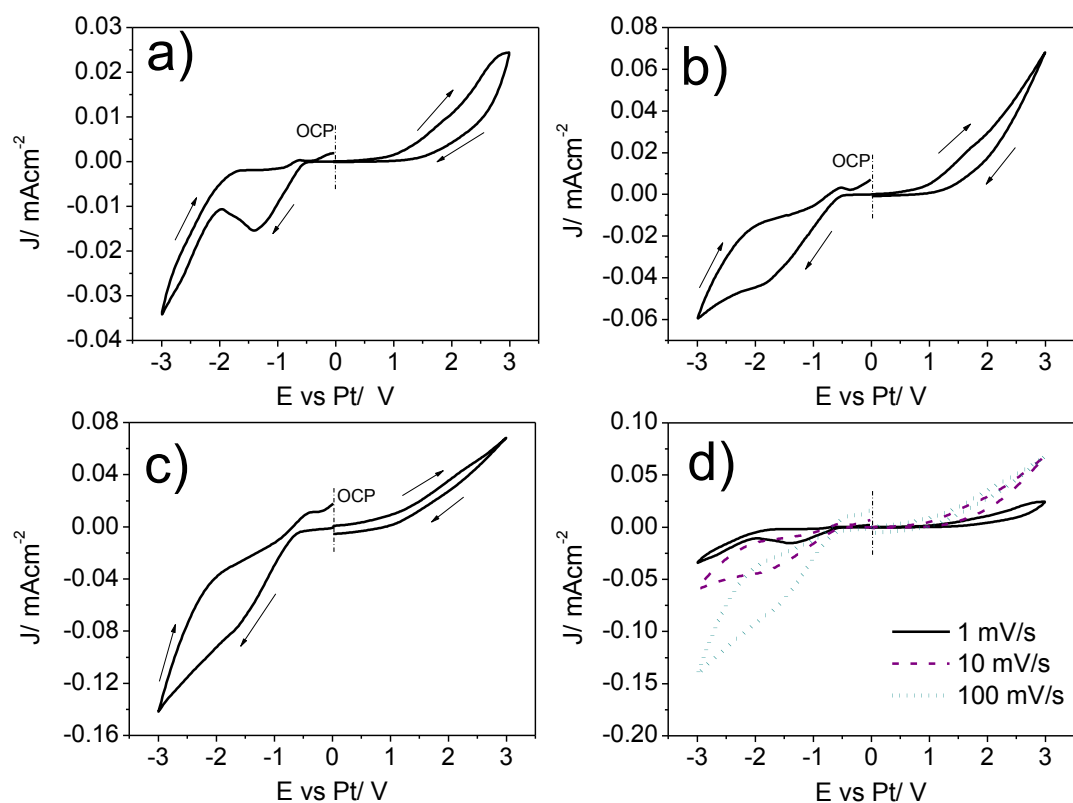


Figure 4.1 – Cyclic voltammograms of Glassy Carbon (GC) in $[P_{6,6,6,14}][(i)C_8)_2PO_2]$ IL between OCP and 3 V vs. Pt and OCP to -3 V vs. Pt at a) 1 mV/s, b) 10 mV/s, c) 100 mV/s and d) 1, 10 and 100 mV/s. Arrows indicate the scan direction.

Scans at 1, 10 and 100 mV/s on GC are shown in Figure 4.1. Scans in the positive direction show a partly obscured single limiting oxidation reaction at approximately 1.5 to 1.7 V vs. Pt. This reaction is followed by oxidation of the IL at 3 V vs. Pt. Similarly, the negative scan shows a reduction reaction at approximately -1.5 V vs. Pt followed by reduction of the IL at -3 V vs. Pt. The reverse scan in the cathodic direction also shows an oxidation peak at approximately -0.5 V vs. Pt. The positions of these two cathodic reaction peaks remain fairly constant with scan rate, which suggests the reaction at -1.5 V is reversible[98]. Since GC is inert, only the IL, oxygen and water will react. The peaks at approx. ± 1.5 V and -0.5 V have hence been attributed to oxidation and reduction of water, as apart from the IL it is the only reactive species in the system. In addition, the peak current increases with increasing water content (see Figure A.1, Appendix A). If a reaction is reversible, the positions between the peaks should equal $59/n$ mV, where n is the number of electrons involved in the reaction[98]. The reduction of water involves

two electrons, and thus would suggest the spacing to be 118 mV, which is not the case in this system. Instead, the reverse peak is less negative (more anodic) than it should be in addition to having a lower peak current than expected (for reversible reactions the relationship $i_{pr}/i_{pf} = 1$ should stand[98], where i_{pr} is the reverse peak current and i_{pf} is the forward peak current). These two characteristics suggest that the reaction is still reversible but that a chemical reaction follows the forward water reduction peak and affects the reverse peak, known as an ECE process[98]. An ECE process describes a system wherein the electrochemical reaction is followed by a chemical reaction. This chemical reaction involves the chemical conversion of all or some of the products of the preceding electrochemical reaction and can be irreversible or reversible. In the case of an irreversible chemical reaction the current of i_{pr} may be reduced (partially or completely depending on the speed of the reaction with respect to the timescale of the scans), whereas a reversible chemical reaction will have no obvious effect on the CV[98]. The identifying characteristics of these processes include the cathodic shift of the forward peak $30/n$ mV for every 10 fold increase in scan rate[98]. This should therefore correspond to a shift of 15 mV of the peak of each of the scans above. However, this does not entirely hold for the scans above as for the scan rates of 1, 10 and 100 mV/s the peak potentials are -1.412, -1.736 and -1.704 respectively. The increase from 1 to 10 is over 300 mV and then the potential decreases by 32 mV; therefore the data here does not follow a consistent trend. Unlike aqueous and organic solvents, and even many ILs, the viscosity of the IL used in this study is considerably high (806 mPas[83], which is approximately 800x the viscosity of water). The high viscosity translates to low mobility of the ionic components of the IL, which leads to an uncompensated iR drop. Typically an iR drop also exhibits a shift of the reaction peaks away from OCP[114], and the effect of the iR drop increases with increasing scan rate[115, 116]. The effect of the iR drop can be identified by the water peaks on the cathodic scans. This may explain the larger than expected shift of more than 15 mV with every 10-fold increase in scan rate (ν).

With increasing scan rate, the current of the reverse peak increases at a greater rate than the forward peak. As a result the relationship of i_{pr}/i_{pf} increases with increasing scan rate. In addition, the relationship $i_{pf}/\sqrt{\nu}$ decreases with increasing scan rate (ν) (see Table 4.1). Therefore, it is likely that the chemical reaction taking place during this process is irreversible.

Table 4.1 – Relationships calculated from Figure 4.1.

ν (mV/s)	i_{pf} (mAcm ⁻²)	$i_{pf} \nu^{-1/2}$	i_{pr} (mAcm ⁻²)	i_{pr}/i_{pf}
1	0.015	0.015	0.00057	0.038
10	0.042	0.013	0.0037	0.088
100	0.079	0.0079	0.012	0.15

Conversely, the anodic scan does not show any indication of reversible behaviour with a complete absence of a reverse peak. The forward peak is also barely resolved in this case, with the majority of current behaviour associated with the oxidation of the IL at 1.5 V vs. Pt.

In comparison, Figure 4.2 shows the behaviour on AZ31 to be significantly different. In the anodic direction the current density immediately begins to increase from the OCP of AZ31 (approximately -1.5 V vs. Pt) to a limiting current at approximately -0.6 V vs. Pt (Figure 4.2 a). This reaction is irreversible, as there is no reverse peak. With increasing scan rate the anodic peak shifts to more passive potentials, leading to the limiting peak also existing at approximately 0.5 V and 0.8 V vs. Pt at 10 and 100 mV/s respectively (solid lines in Figure 4.2). Interestingly,

instead of the current density reducing after the initial reaction to form a peak it continues to increase at a slower rate until oxidation of the IL at 3 V vs. Pt.

In the cathodic scan no reaction peaks are present. Instead the current increases as the IL is reduced at -3 V vs. Pt. Furthermore, there are no water reaction peaks visible in either the anodic or cathodic scans. Since the current densities of the reactions on AZ31 are lower than the water reactions on GC it is unlikely that the AZ31 reactions are masking the water reactions. Magnesium (and hence AZ31) is highly reactive with water and thus it is likely that the water in solution immediately reacted with AZ31 when immersed to form $\text{Mg}(\text{OH})_2$ and hence eliminating the water peaks from the CVs.

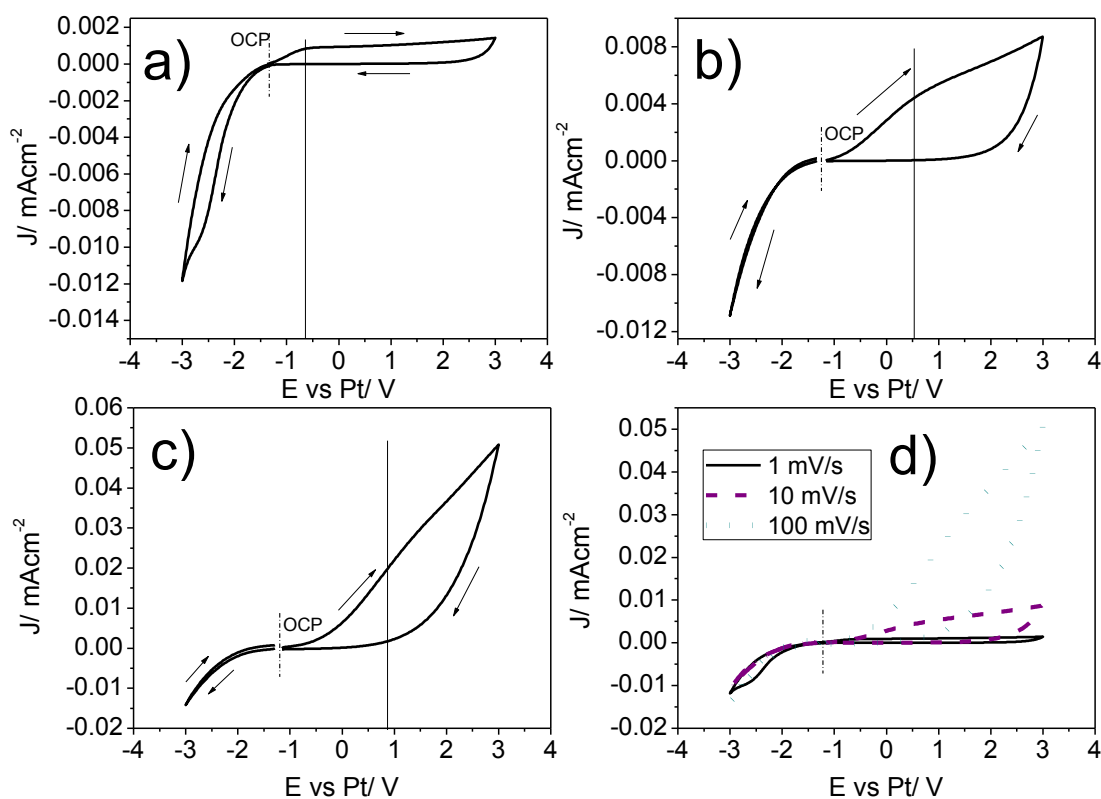


Figure 4.2 – Cyclic voltammograms of AZ31 in $[\text{P}_{6,6,6,14}][(\text{C}_8)_2\text{PO}_2]$ IL between OCP and 3 V vs. Pt and OCP to -3 V vs. Pt at a) 1 mV/s, b) 10 mV/s, c) 100 mV/s and d) 1, 10 and 100 mV/s. Arrows indicate the scan direction.

As shown in the next section (4.1.3), a progressive reduction in current with continued anodic cycling on AZ31 is observed (Figure 4.3 a). Thus it is expected that some amount of adsorption/film forming process must be occurring on the surface. With an adsorption process, the relationship i_{pf}/\sqrt{v} increases with increasing scan rate, which the above scans follow. However the relationship of i_p/v , which should remain constant, also increases. When strong adsorption processes occur involving the adsorption of an oxidised species a ‘post peak’ will be observed in the CV. On the other hand, when weak adsorption processes involving an oxidised species occurs the current of i_{pf} will increase[98]. Hence, if adsorption processes are occurring during these CVs they are likely to be weak.

4.1.3 Passivation and Film Formation with Cyclic Voltammetry

4.1.3.1 Anodic Behaviour of AZ31 in Neat IL and Dilute IL

Due to their unique physical properties, ILs are unlike other solvent systems. Therefore the interaction of an IL with a reactive metal may differ to a similar condition in a traditional salt electrolyte. Therefore, in order to understand the specific role of the IL on film formation a dilute solution was prepared as a comparison. Since $[P_{6,6,6,14}][C_8)_2PO_2]$ is a hydrophobic IL, to ensure no erroneous results from agglomerates of the IL due to immiscibility, the IL was diluted into acetonitrile. Two solutions were prepared at 0.1 and 0.01 M IL in acetonitrile. Acetonitrile was selected as this IL is readily soluble in organic solvents and acetonitrile is effectively benign and accessible.

Figure 4.3 a) compares the effect of dilution of the IL into a solvent. Both systems were cycled from OCP to 3 V vs. Pt in neat IL and also in two diluted systems. To make the dilute systems, IL was dissolved to concentrations of 0.1 and 0.01 M in acetonitrile. Henceforth, these solutions will be referred to as ILAN and dilute ILAN (0.1 and 0.01 M respectively) in the text.

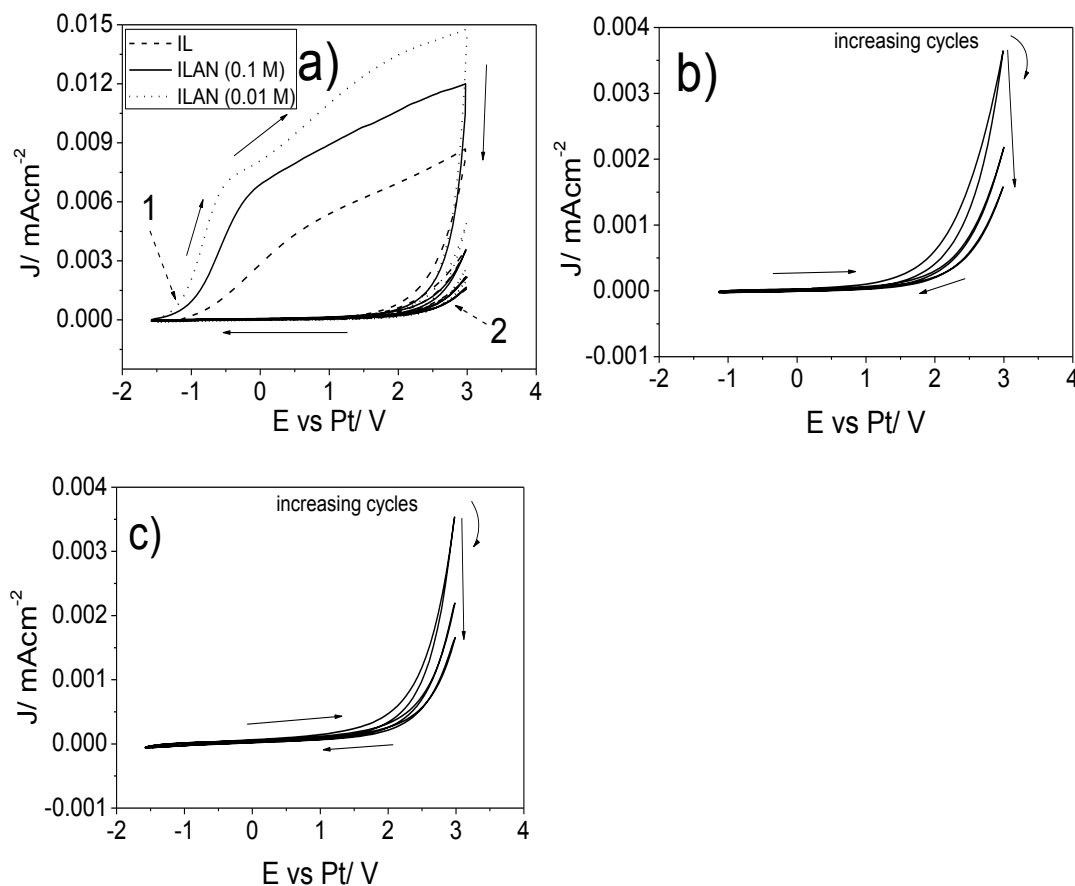
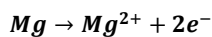


Figure 4.3 – Cyclic voltammograms from OCP to 3 V vs. Pt at 10 mV/s for a) initial scan of AZ31 in dry neat IL and ILAN (0.1 M and 0.01 M IL in acetonitrile solutions) and repeat cycles b) $[P_{6,6,6,14}][C_8)_2PO_2]$ IL and c) 0.1 M ILAN solution.

As mentioned previously, when AZ31 is anodically polarised the current density begins to increase immediately from OCP (approximately -1.5 V vs. Pt). This behaviour remains unchanged in both dilutions. In the cases of the two ILAN solutions and neat IL the first part of the initial reaction occur at the same rate (i.e. the gradient of the curves are essentially the

same). After approximately -1.0 V vs. Pt, the gradients of each curve increase (indicated by dashed arrow 1). This increase in current at -1 V vs. Pt can be attributed to oxidation of magnesium, as per Eqn. 1. The rate of magnesium oxidation is greater for the dilute IL solutions than in the neat IL solution. The increase in oxidation rate in the dilute systems is most likely due to the decrease in viscosity, and subsequent increase in the conductivity and ion mobility. The decrease in IL concentration, and therefore its influence on the dissolution of magnesium (i.e. due to fewer IL species to passivate AZ31), could also lead to increased oxidation currents.



Eqn. 4.1

At potentials of -0.5, -0.2 and 0.5 V vs. Pt (for dilute ILAN, ILAN and neat IL respectively) the slope of the curves are significantly reduced. The current density in this stage continues to increase, but at a reduced rate. If the AZ31 surface is repeatedly cycled the measured current density is considerably lower than the initial scan until approximately 2 V. The dashed arrow (point 2) in Figure 4.3 a) displays the difference between the current densities of the initial scans to the repeat cycles, which shows a significant reduction in the reactivity of the system. In addition, as the current does not rise until 2 V vs. Pt the initial oxidation reaction does not occur. This behaviour suggests the passivation of the metal electrode. Therefore, the region between approximately -0.5, -0.2 and 0.5 V vs. Pt (for dilute ILAN, ILAN and neat IL respectively) and 3 V must correspond to film growth on AZ31. Figure 4.3 b) and c) show in more detail the repeat cycles from neat IL and ILAN respectively. Here it can be seen that with increasing cycles the maximum current density recorded at 3 V is further reduced. However, of more import is that the repeat cycles from neat IL and ILAN are almost identical in electrochemical behaviour. In Figure 4.3 a) the recorded current densities for the dilute solutions were considerably higher than the neat IL. However, since the repeat current densities are essentially the same the passive film being formed in neat IL and ILAN must also be essentially the same. This supports the hypothesis that the change in viscosity is responsible for the different electrochemical behaviour in the first cycle. Collectively, Figure 4.3 also shows that the acetonitrile solvent molecules have no observable effect on the ability for the IL to form a passive film. Since the basic shape of the CVs is unchanged, the acetonitrile does not appear to interact with the IL nor AZ31 under these conditions.

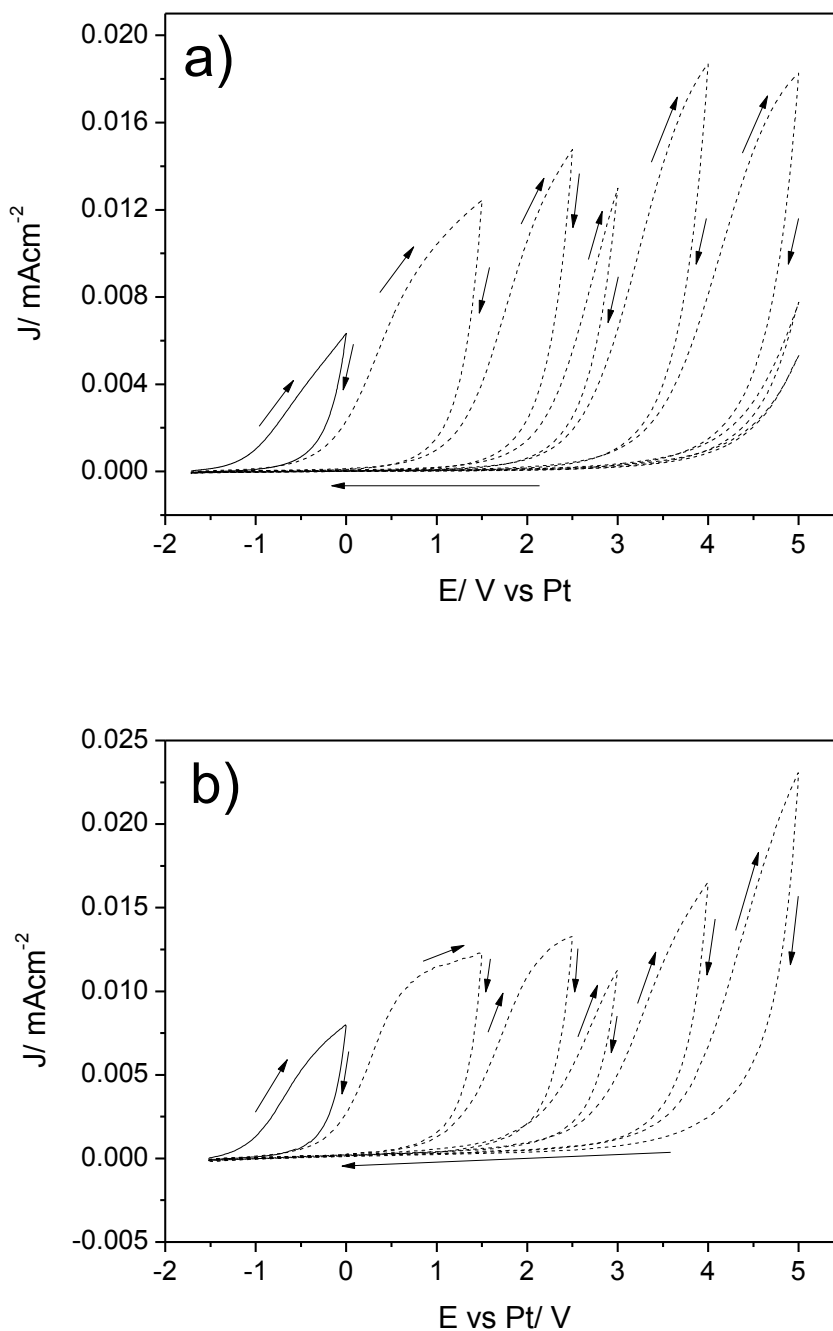


Figure 4.4 – Potential switching of AZ31 in a) $[P_{6,6,6,14}][(\overset{+}{C}_8)_2PO_2]$ IL and b) ILAN. Scans were performed progressively from OCP to potentials of 0, 1.5, 2.5, 3, 4 and 5 V at 10 mV/s. Two consecutive scans between OCP and 5 V were performed in neat IL after the initial scan to 5 V vs. Pt.

Figure 4.4 shows the effect of potential on the film forming process on AZ31. In this figure the potential on AZ31 in neat IL (Figure 4.4 a) and ILAN (Figure 4.4 b) is continually switched between OCP and six final potentials of 0, 1.5, 2.5, 3, 4 and 5 V vs. Pt (in that order). Figure 4.3 showed that the recorded current densities of the repeat cycles were suppressed until approximately 2 V vs. Pt. The rise of this current at 2 V followed the same general line of the return curve of the initial cycle. That is, there was no overlap of the repeat curves with the initial curve. Similarly, in Figure 4.3 b) and c), the third cycle does not overlap with the second nor the

fourth with the third. The same behaviour is seen in Figure 4.4. Within the potential range of the previous switch the curves do not overlap, and they behave in the same manner as the repeat cycles in Figure 4.3. However, once outside the potential range of the previous switch the current density continues to rise and the shape of the response is the same as the response in the previous potential bracket. This behaviour is continued with continued potential switching to higher potentials. In addition, Figure 4.4 a) (of this behaviour in neat IL) also includes two cycles repeated to 5 V vs. Pt. The behaviour of these repeat cycles is consistent with that observed in Figure 4.3. Figure 4.4 b) shows the potential switching behaviour of AZ31 in ILAN. The profile of the potential switching in ILAN is the same as in neat IL. Also, with dilution there is still no overlap between any of the potential switches. Again, the action of the IL in both pure and dilute systems appears to be the same. Figure 4.4 shows that the passivation of AZ31 in the neat IL and the dilute IL solutions are potential dependent. Thus, when anodically polarised to 0 V vs. Pt an anodic film is grown and this growth is terminated when the potential is forced to reverse (by the controlled electrochemical technique). Thus, when the potential is increased above 0 V vs. Pt this film growth is resumed (and etc. for the remaining potential switches). The lack of curve cross-over during this process is indicative of no chemical dissolution of the film during the experiment [117, 118]. That is, the film which is being grown is stable in this system.

Figure 4.5 shows the effect of growing a film through immersion in IL prior to the electrochemical film formation. If the AZ31 surface is held at OCP before being polarised (Figure 4.5 a), the formation of an adsorbed IL film does not disrupt the oxidation behaviour when the surface is polarised. Figure 4.11 b) shows a CV on AZ31 from OCP to 3 V vs. Pt at 1 mV/s *after* being held at OCP for 100 hours. The change in the OCP with time shows the surface becoming nobler (potential becoming more positive) with increasing immersion time in the IL. This behaviour can be associated with the formation/adsorption of an IL film on AZ31. Due to the initial holding time the peak for the oxidation reaction of magnesium, which was not visible in any previous experiments, appears just shy of 0 V vs. Pt. The current density of this peak is approximately half the magnitude of the analogous point when polarised immediately. Therefore, the degree of oxidation of magnesium in the IL has been reduced by the 100 hour immersion. This behaviour suggests that, despite the extended period of immersion, the application of an anodic bias still results in film thickening. This also suggests that the film thickness from simple immersion is either thinner compared to when AZ31 is polarised to 3 V vs. Pt or does not cover as much of the surface.

Interestingly, whilst the repeat cycles in Figure 4.3 show a continual decrease in the recorded current densities on AZ31, the repeat cycles in Figure 4.5 b) do not significantly change. The decreasing currents in Figure 4.3 suggest some continued minor growth of the film. However, the insignificant current decrease in the repeat scans in Figure 4.5 suggests the thickness of the film formed from the initial scan cannot be significantly increased until application of a greater potential. This is likely due to the combined thickness of the film from both immersion and anodic polarisation. The same behaviour presented in Figure 4.5 b) can be replicated by long on-going cycling between OCP and 3 V vs. Pt (not shown).

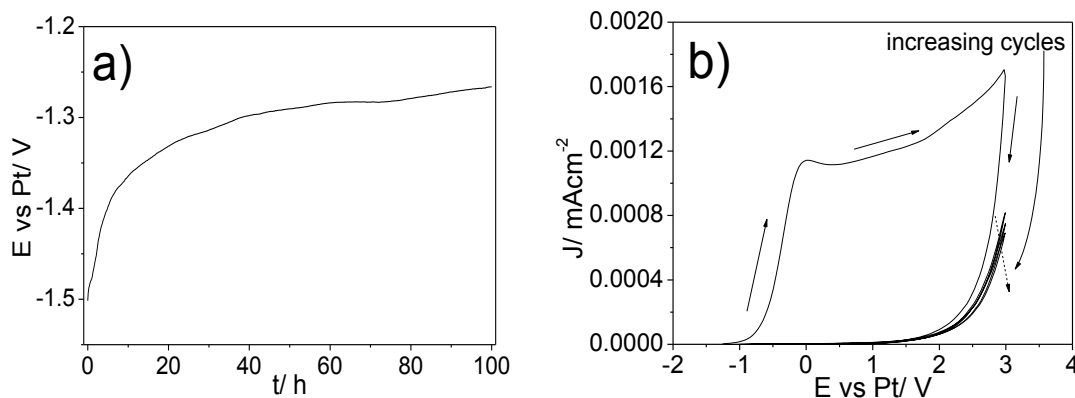


Figure 4.5 – a) 100 hour long OCP of AZ31 in IL; b) cyclic voltammogram of AZ31 in IL cycled between OCP to 3 V vs. Pt at 1 mV/s after being held at OCP for 100 hours.

Initially the current will decrease significantly with each cycle until it reaches a point where the current is essentially unchanged, or decreases very slightly with ongoing cycling. The fact that current is still measured (in both cases) suggests some degree of ongoing magnesium dissolution. This suggests that the films are either porous or do not cover the entire surface uniformly.

Characteristic Shape of the CVs in neat IL and ILAN

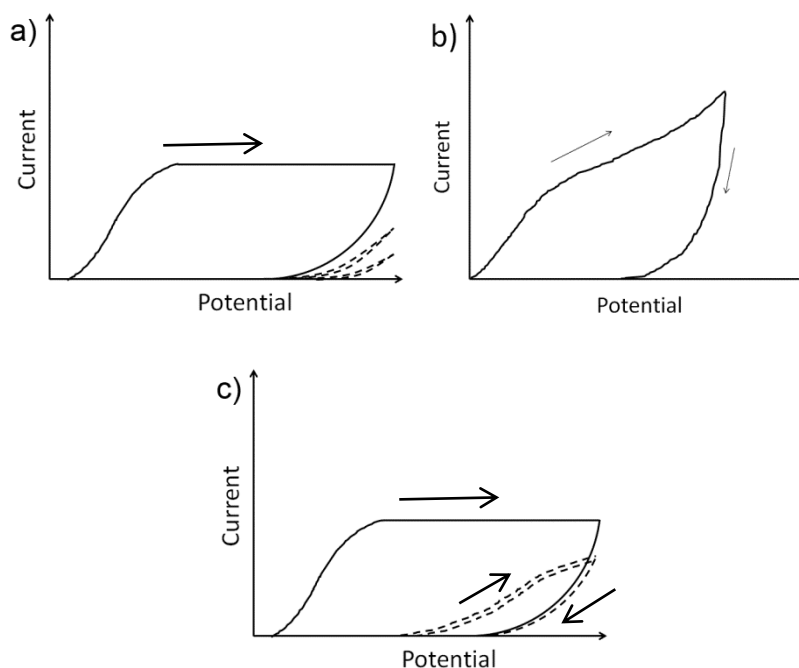


Figure 4.6 – Schematics of simulated CV responses of valve metals when a) no dissolution and perfect anodic film growth; b) effect of adsorption on anodic film growth. The incorporation of a compound from the anodising bath changes the potential distribution of the film and promotes dissolution, hence non-plateau behaviour; c) dissolution behaviour of the subsequent cycles – overlapping of the initial curve. Schematic images adapted from data presented in [119] and [118].

Curves with similar behaviour to those of the anodic curves on AZ31 in Figures 4.2 and 4.3 have been observed in a number of metal systems, including Al, Ta, Sn, Bi and Mg[117-121]. In a study on the anodic oxide formation on Bi in sodium hydroxide (NaOH), Williams *et. al*[120] found the current density would increase sharply with anodic polarisation and between one and three peaks were observed. These peaks were followed by a section where the current density

was effectively plateaued (like in Figure 4.6 a). The peaks were determined to be indicative of nucleation of an anodic film and the plateau the thickening of the film over the surface[120]. The authors have proposed that the plateau was indicative of galvanostatic anodising behaviour, wherein a constant current density results in increasing potential, corresponding to film thickening (following Ohm's law)[120]. Similar behaviour was also reported in the cyclic voltammetry of Sn in borate solutions[117]. The authors observed two peaks which they proposed represented the oxidation of Sn and the formation of tin oxide/hydroxide[117]. In the anodic cycling of Bi in disodium hydrogen phosphate (Na_2HPO_4), Perez *et. al* did not find a distinct peak for the anodic oxidation of Bi to Bi^{3+} [118]. Instead they found the progression of metal oxidation to the stable film forming stage to be similar in appearance to the data presented here for AZ31.

The response seen in the CVs of Figure 4.2 and 4.3 (and the mode of film growth) can be explained through growth by the "high-field" mechanism. The high-field mechanism predicts decreasing current density proportional to increasing passivation time[122]. The growth of film through this process involves the migration of ions to and from the surface through the passive film due to the formation of an electric field within the film[118, 122]. The occurrence of a steady-state current density plateau (which the CVs in Figure 4.2 and 4.3 deviate from) is typical behaviour of a valve metal when anodically polarised[118]. Valve metals, by definition, oppose current flow when used as an anode and allow current flow when used as a cathode during oxidation. These metals are also characterised by their film forming capabilities, and include Al, Bi, Sn, Ti, Nb, Zr, W, Hf and Mg metals and alloys.

The behaviour of the repeat curves in Figure 4.3 (b and c) and Figure 4.4 can also be explained using the high-field mechanism[118]. Perez *et. al* explain that once a certain thickness of oxide is grown no appreciable growth can continue until the potential is increased to values that correspond to the high field mechanism[118]. With repeating cycles the film will continue to thicken, although not by much, which is why the current is not zero in the repeat cycles but continues to decrease with continued cycling to the same potential. Therefore, metals which follow the high field mechanism form potential dependent films. While the current density will continue to decrease with increasing cycles within a particular potential range, if the potential is increased to a higher maximum potential the current density will increase in the same fashion as in the initial scan. Moreover, if a line connecting the tops of the separate scans were to be drawn the shape would resemble a singular scan if taken directly to that final potential[118]. This shows that the surface is passivated within the potential range that it has been scanned in but will begin, and will continue, to react when the potential is increased to continue film growth. This is not particularly surprising as traditional galvanostatic anodising shows a relationship between potential and film thickness[74]. Thus, by forcing the potential to increase the system will react to form a thicker film.

Possible Explanations for Non "Plateau" Behaviour

Unlike the situations explained above, the current density does not plateau for AZ31 polarised in this phosphinate IL. Perfect anodic film growth is represented in Figure 4.6 a) by the flat current plateau. Hence the shape of the CVs of AZ31 in IL is not typical of perfect anodic film growth. Instead, with potential the current density steadily increases such that it is potential dependent as opposed to becoming independent and forming a plateau. Interestingly, the shape of the first curves from the CVs of AZ31 in neat IL and ILAN are similar in appearance to Al in a 0.5 M sulphate solution (Figure 4.6 b), investigated by Lee *et. al*[119]. The authors suggested that the increasing current with increasing potential was due to adsorption or incorporation of

the sulphate into the oxide at the oxide/electrolyte interface. They suggested that the introduction of the sulphate changed the potential distribution across the oxide. As a result, cation transfer through the film into solution was promoted and oxide dissolution occurred.

In the study of Al in the sulphate solution investigated by Lee *et. al*, the 2nd, 3rd, etc. cycles intersected with the first curve and each other [119] (such as in Figure 4.6 c), which is indicative of a poor film as the film must continually replace itself. Lee *et. al* [119] also presented a CV for Al in 0.5 M borate solution, which showed similar behaviour of the repeat cycles (Figure 4.6 a) as our data. The authors explain that this behaviour was similar to the cycling behaviour of Al in a chromate solution, which we know forms protective films on Al. Unlike the sulphate solution with Al, dissolution does not accompany every cycle with AZ31 in IL. In the presence of the IL the change in slope of the first cycle shows that film growth is occurring alongside adsorption of the IL and dissolution of the film. However, in the subsequent scans the current profiles do not show dissolution behaviour. Instead the magnitude of the current progressively reduces and the repeat cycles do not overlap. After the initial cycle, the AZ31-IL system behaves in the same manner as Figure 4.6 a), which corresponds to perfect film growth (as with chromate).

4.1.3.2 Anodic Behaviour of AZ31 in a Lithium Triflate Solution

A third dilute solution in acetonitrile was prepared using the compound lithium triflate (0.1 M $LiCF_3SO_3$ - termed ANSO for convenience). Figure 4.7 shows the electrochemical behaviour of this solution on AZ31 when cycled anodically. As with the behaviour in neat IL and ILAN, in this system the current density also increases immediately from OCP (see Figure 4.7 a) inset). Until approximately -1.1 to -1.0 V vs. Pt the gradient of this is relatively low, however, once the potential passes -1.0 V vs. Pt the gradient of the increases rapidly, at a significantly greater rate than the ILAN solutions (a gradient of approximately 11.5 vs. 0.0077 mAcm⁻²V⁻¹ for ANSO and ILAN respectively). Therefore, there is considerable magnesium oxidation, and hence dissolution, in ANSO.

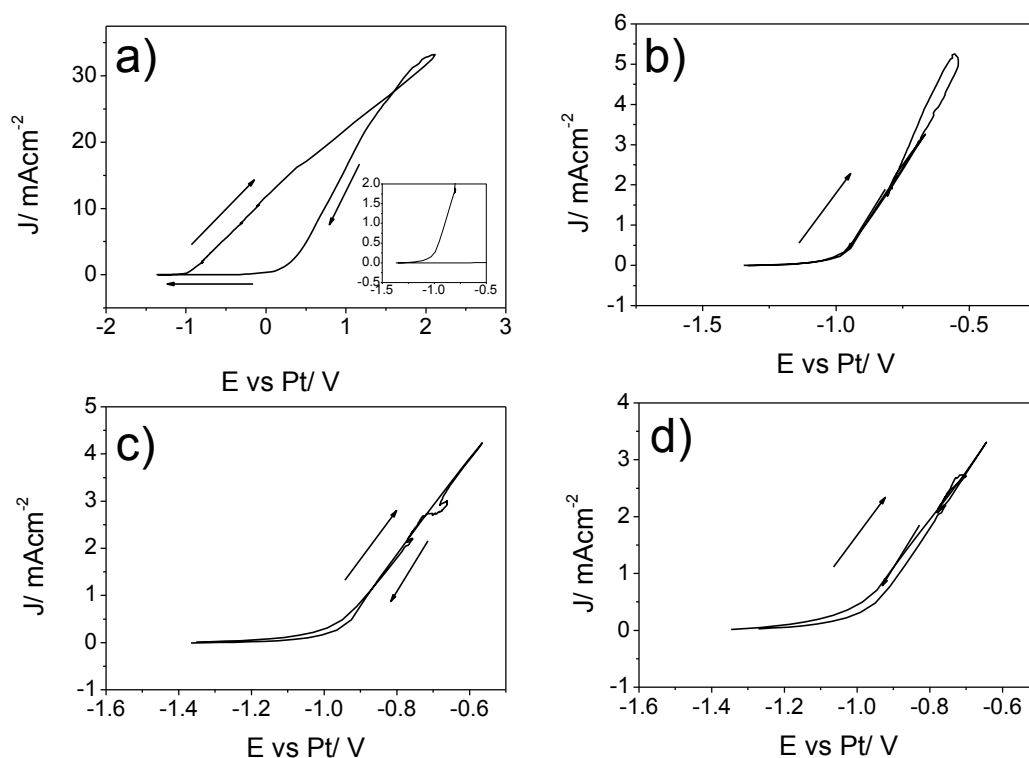


Figure 4.7 – Cyclic voltammograms of AZ31 polarised from OCP to 3 V vs. Pt in ANSO solution, a) cycle 1, b) cycle 2, c) cycle 3, d) cycle 4. The final potential was not achieved in any cycles due to the build-up of white precipitate on the Ti counter electrode.

The current density continues to increase until it peaks at approximately 34 mAcm^{-2} , over 3000 times greater than the current densities of the other systems. Thus, the magnesium oxidation appears to continue unabated in ANSO. This suggests that the triflate compound may attack the AZ31 surface as opposed to the formation of a resistive film on the surface of AZ31 when the phosphinate IL is present.

Figure 4.7 b)-d) compare the three scans following the initial scan in Figure 4.7 a). What is notable from these curves, including the initial scan in Figure 4.7 a), is that despite the final voltage being set for 3 V vs. Pt, the counter electrode was unable to polarise to this in any of the scans: with increasing scans the voltage range decreases from approximately 4 V to only 0.8 V.

This behaviour suggests that something is impeding the action of the counter electrode, as the counter electrode applies the potential difference to polarise the working electrode. It also shows that with increased cycling, the issue gets increasingly worse. When the pipette cell was disassembled a white deposit was observed on the counter electrode (Figure 4.8 a). At this stage we believe that this deposit is the likely cause of the decreasing maximum potential as passing charge would have become increasingly difficult given that the deposit would decrease the active surface area of the counter electrode. Figure 4.9 is a comparative scan in ANSO on GC. When scanning GC in ANSO, the final voltage of 3 V vs. Pt was achieved in all scans and no deposit was formed on the Ti counter electrode. Therefore it is expected that the deposit on the Ti counter electrode is a magnesium compound. In addition, when the cell was disassembled there was a distinct “rotten egg” smell associated with sulphide compounds. Therefore, during cycling with AZ31 the LiCF_3SO_3 has been decomposed (reduced) at the counter electrode. Figure 4.8 b) shows the degree of damage sustained by AZ31 in this solution. The presence of sulphides in solution would accelerate the dissolution of AZ31, which may be responsible (in part) for the

severe pitting on the surface. After cycling in ANSO on GC the solution remained pristinely clear. In addition, there was no scent of sulphides.

Figure 4.8 c) compares the pH of ANSO after cycling on GC and AZ31 using litmus paper. The pH of ANSO with GC was found to be neutral (pH 6-7). However, the pH for ANSO cycled with AZ31 was expected to be acidic, due to the pungent smell, which is often associated with H_2S . Instead the solution was actually basic (pH 10-11). Figure 4.8 d) shows the appearance of the ANSO solution after cycling on AZ31. The basic pH measurement in Figure 4.8 c) may be due to the formation of lithium hydroxide (LiOH) from the hydrolysis of the triflate compound.

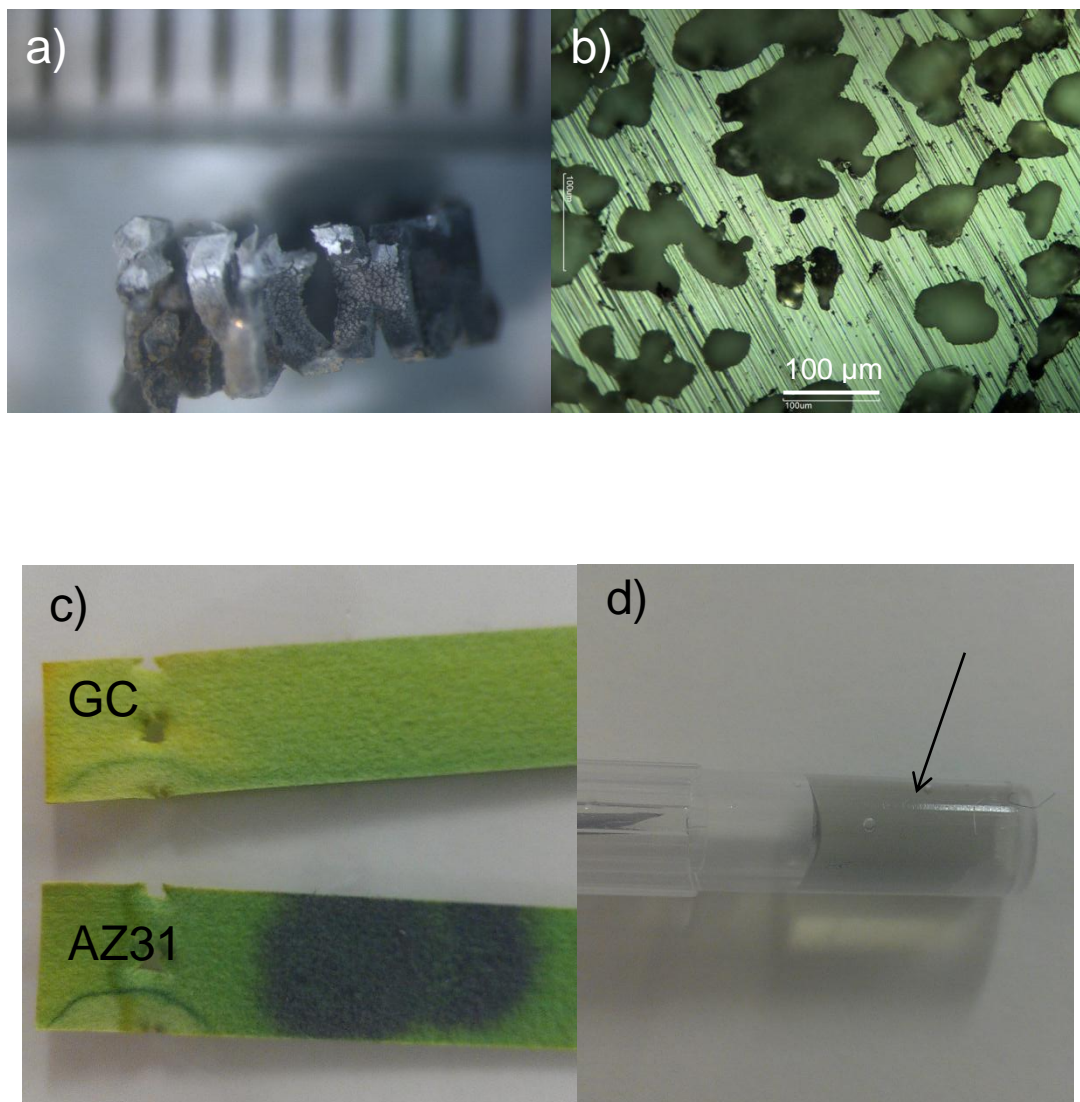


Figure 4.8 - a) Photograph of white deposit (circled) formed on the Ti counter electrode after polarising AZ31 in ANSO solution (vertical lines at top of image correspond to 1 mm increments); b) Optical micrograph of AZ31 after cycling in ANSO; c) pH indication on litmus paper of ANSO after cycling with GC and AZ31; d) optical appearance of ANSO after cycling with AZ31.

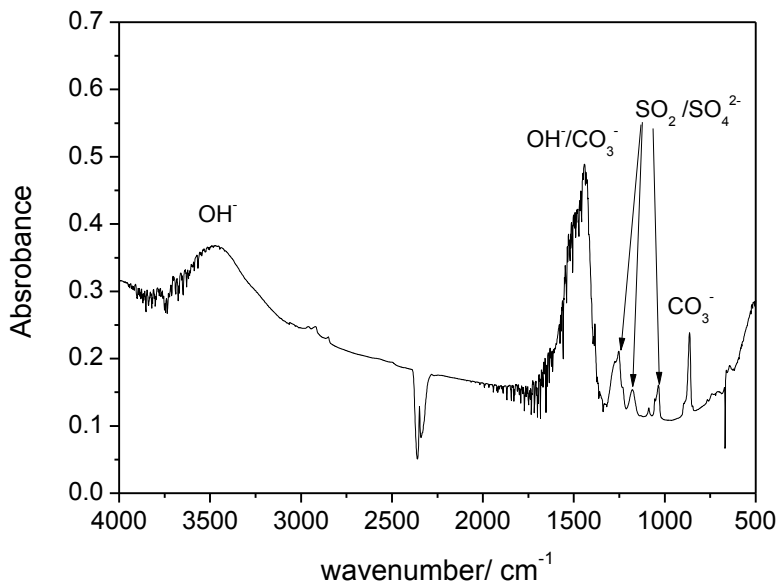


Figure 4.9 – FTIR spectrum of deposit scraped from the counter electrode formed into a KBr disc.

The deposit from the counter electrode was scraped off using a scalpel and collected and pressed into a KBr disc. Transmission FTIR of the disc returned the spectrum in Figure 4.9. The main peaks have been identified as CO_3^- , OH^- , SO_2 and SO_4^{2-} [123]. Electrochemically, LiCF_3SO_3 is stable as no reaction peak is present on glassy carbon except for what is likely the oxidation of water (there being approximately 1000-1500 or so ppm in solution) at approximately 2.5 V vs. Pt (Figure 4.10). Therefore, the chemical reaction occurs exclusively when Mg^{2+} ions are present. It appears the Mg ions dissolved into the solution at the anode have reacted with the breakdown products of the triflate ion to deposit some or all of the species identified on the counter electrode. The OH^- present may also be due to the deposition of LiOH from breakdown of the triflate anion.

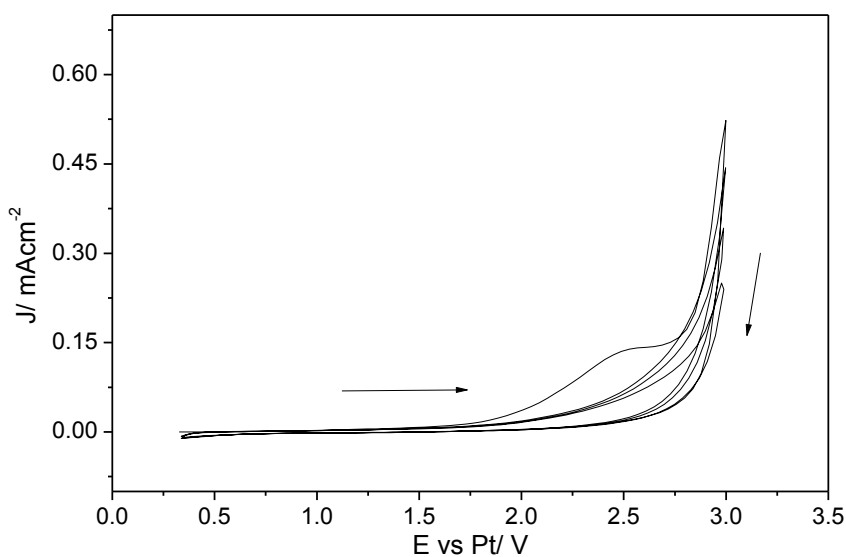


Figure 4.10 – Cyclic voltammogram of GC cycled between OCP and 3 V vs. Pt in ANSO (4 cycles in total).

4.1.3.3 Cathodic Behaviour of AZ31 in Neat IL

Figure 4.11 shows the electrochemical response of AZ31 when cycled cathodically in neat IL. When AZ31 is polarised cathodically in IL the current density for the electrolyte reduction increases with increasing cycles, which may be the result of hydrogen reduction on the AZ31 surface[120]. Thus, Figure 4.11 shows that the passive behaviour is not observed when AZ31 is polarised cathodically.

Figure 4.12 shows the effect of polarising cathodically after anodic film formation. The anodic film is formed in the same manner as previously shown; however the potential is then scanned to -3 V vs. Pt. When the potential becomes anodic once more the scan resembles the repeat cycles in Figure 4.3 b). Therefore, the cathodic cycling does not alter the anodic film or its continued growth. It was mentioned earlier that the anodic reaction on AZ31 is irreversible. Therefore it appears that if AZ31 is cycled between 3 and -3 V vs. Pt, the cathodic scan does not strip the anodically formed film. Thus, even with significant cathodic polarisation the film that is formed is stable in the IL environment. However, it also suggests that charge is still able to freely pass between the electrode (AZ31) surface and the electrolyte (IL), which suggests the film formed either a) does not fully cover the surface, b) is porous or c) allows for cathodic ion migration.

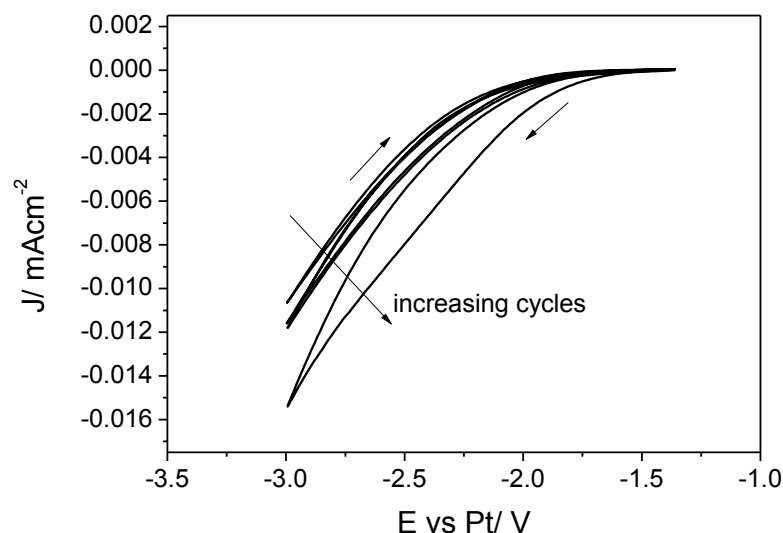


Figure 4.11 – CV of AZ31 in $[P_{6,6,6,14}][(C_8)_2PO_2]$ scanning between OCP and -3 V vs. Pt at 1 mV/s.

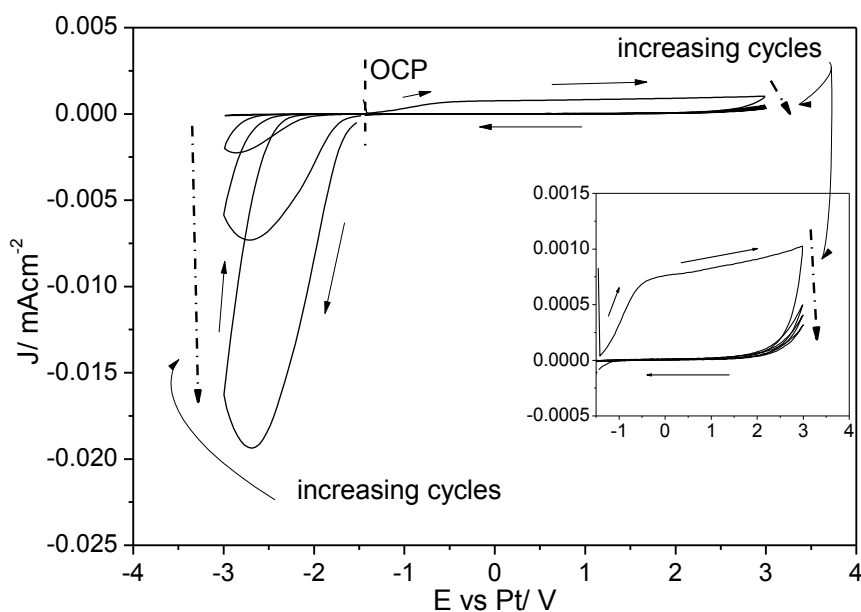


Figure 4.12 – AZ31 polarised from OCP to 3 V vs. Pt and cycled between 3 V and -3 V vs. Pt at 1 mV/s in $[P_{6,6,6,14}][(\text{C}_8)_2\text{PO}_2]$ IL. Inset shows the zoomed in anodic side of the scans.

4.1.4 Effect of Air and Water

Previous work on film formation in $[P_{6,6,6,14}][(\text{C}_8)_2\text{PO}_2]$ IL found that with the addition of 6 wt% water the film formed was more protective than when dry (see Section 2.). These studies were conducted at the free corrosion potential of AZ31, and therefore the behaviour when polarised is expected to be different. In addition, the influence of oxygen on the reactions must be taken into consideration. To analyse the effect of air, oxygen and water both wet (6 wt% H_2O [approx. 60,000 ppm]) and dry (1000-1500 ppm H_2O) solutions of IL were prepared. Both solutions were analysed in the two following conditions:

1. On a bench open to the laboratory air.
2. In an argon glovebox (no air, atmosphere water levels < 100 ppm).

Both conditions were performed on AZ31. Responses on GC can be found in Appendix A.

4.1.4.1 Condition 1 – Open-to-Air in Laboratory (wet IL)

Experiments involving dry IL on AZ31 were presented previously in section 4.1.1 (Figures 4.1-4.4 etc.); therefore this section will cover the use of the wet IL ($\approx 60,000$ ppm) on AZ31 with references to section 4.1.1 and 4.1.3.

Figure 4.13 a) shows the anodic response of AZ31 in wet IL cycled from OCP to 3 V vs. Pt at 1 mV/s. The repeat cycles are also shown in Figures 4.13 b-d). The first cycle (Figure 4.13 a) begins in the same manner as the dry condition: the current density increases immediately before the current density gradient is significantly reduced at approximately -1.1 V vs Pt. As with the dilution of IL in section 4.1.3, with the addition of water to the IL the change in the current density gradient occurs at a lower potential than in neat IL. In addition, the current density is also slightly larger. The second curve (red dots) in Figure 4.13 a) is a trace of the experiment performed in the dry IL, which shows comparatively that the current density in the wet condition is larger.

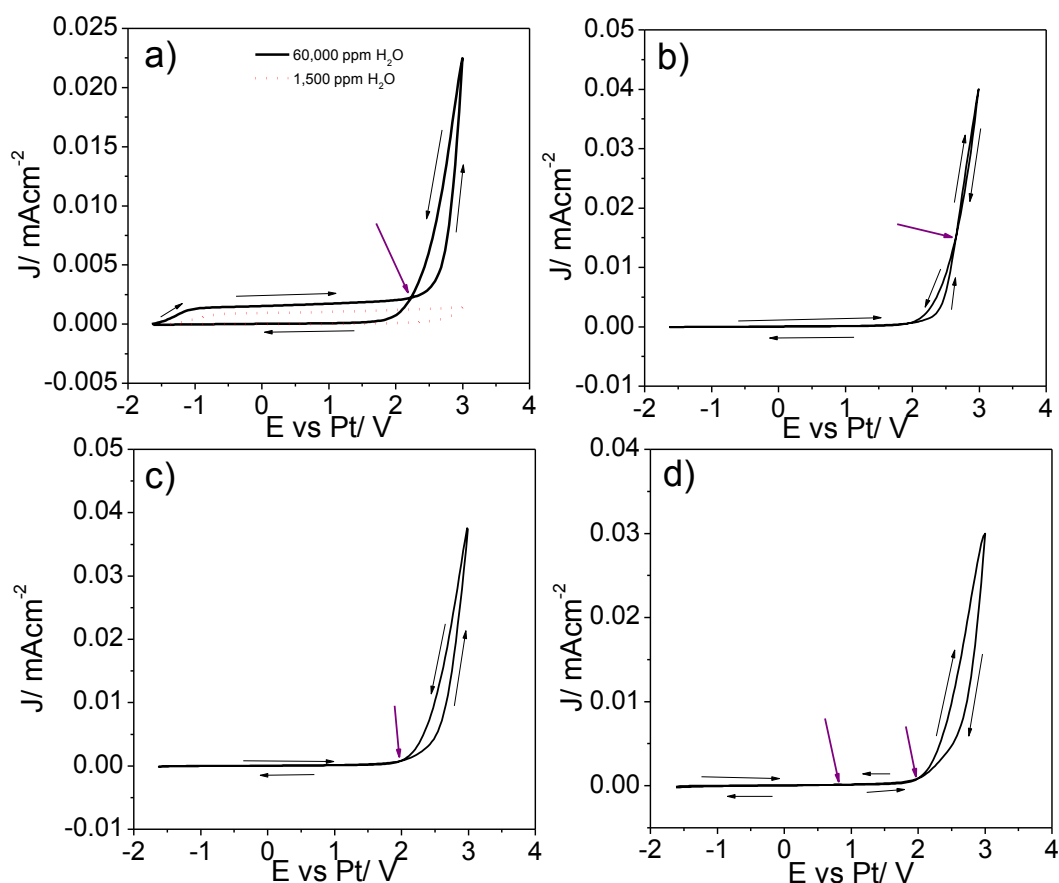


Figure 4.13 – CVs on AZ31 in IL with 6 wt% (60,000 ppm) H_2O between OCP and 3 V vs. Pt at 1 mV/s; a) initial cycle; b)-d) cycles 2-4. The purple arrows indicate the points of intersection between the forward and reverse scans.

This difference in current density is likely due to the same difference seen in the dilute system. With the addition of 6 wt% water, the viscosity of the solution decreases and we expect a similar increase in conductivity. As with the dilute ILAN system, the gradient over the bulk of the potential range in the wet condition is approximately the same as in the dry condition; this suggests that a passive film is forming under the anodic conditions. However, above 2.0 V vs. Pt, the current density starts to rapidly increase. Williams *et. al* observed similar behaviour with Bi[120]. When the anodic potential was greater than a critical value, the current rapidly increased. They associated this behaviour with dissolution of the metal through pitting[120]. Similar behaviour has also been witnessed with pitting on Al[124].

Furthermore, instead of the return curve passing at a higher potential, the curve crosses over itself (indicated by the arrow). This intersection is associated with surface modification of the working electrode and can also represent adsorption of species onto the working electrode. Therefore, it appears as though the introduction of water makes the solution more reactive and less able to passivate at higher potentials. However, we know a film has deposited as the current densities of the repeat cycles at potentials < 2.0 V are significantly reduced. Figure 4.14 shows an optical micrograph of AZ31 after the cycling conditions in Figure 4.13. When the AZ31 specimen was cycled and removed from the pipette cell after four cycles between OCP and 3 V vs. Pt, the treated area was a distinct yellow-orange colour. This colour change suggests that possible pitting of the surface may also be accompanied by adsorption of the IL onto the surface. Alternatively, this could mean that no pitting occurs and all the current is involved in the reaction of the IL (hydrolysis). The surface of AZ31 after the cycling does not show obvious

pitting, which suggests that the IL is likely responsible for the current behaviour as opposed to pitting of the surface.

Figure 4.14 shows selective deposition of this film over the α -phase. The light uncovered areas over the surface correspond to the β -phase in the microstructure (arrow), whilst the entire coloured region is the α -phase. Hence, the film being formed during cyclic voltammetry forms mainly over the α phase. This preferential deposition is likely due to anodic film formation only forming over the β phase at potentials greater than 80 V[74].

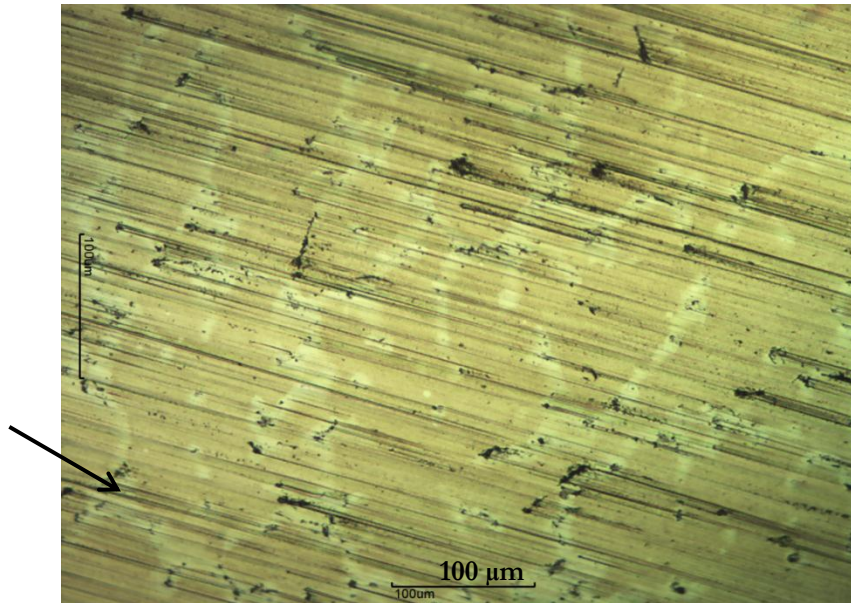


Figure 4.14 – An optical micrograph of AZ31 cycled four times between OCP and 3 V vs Pt in IL containing 6 wt% (60,000 ppm) water. Arrow points to uncovered β -phase (light area). The dark area is the covered α -phase. The small black dots on the surface are due to grinding, not from pitting.

Figure 4.15 presents the effect of cathodic cycling on the anodic behaviour of AZ31 in wet IL. In section 4.1.3, Figure 4.12 showed that polarising cathodically after polarising anodically did not disrupt the passive anodic behaviour (in addition, the anodic polarisation does not disrupt the cathodic polarisation). As with the example in Figure 4.11 the anodic cycles maintain the same general behaviour. However, in cycle 3 and 4 the cross over during anodic polarisation no longer occurs. Once again it appears that cathodic polarisation is *not* beneficial to passive film formation in this IL.

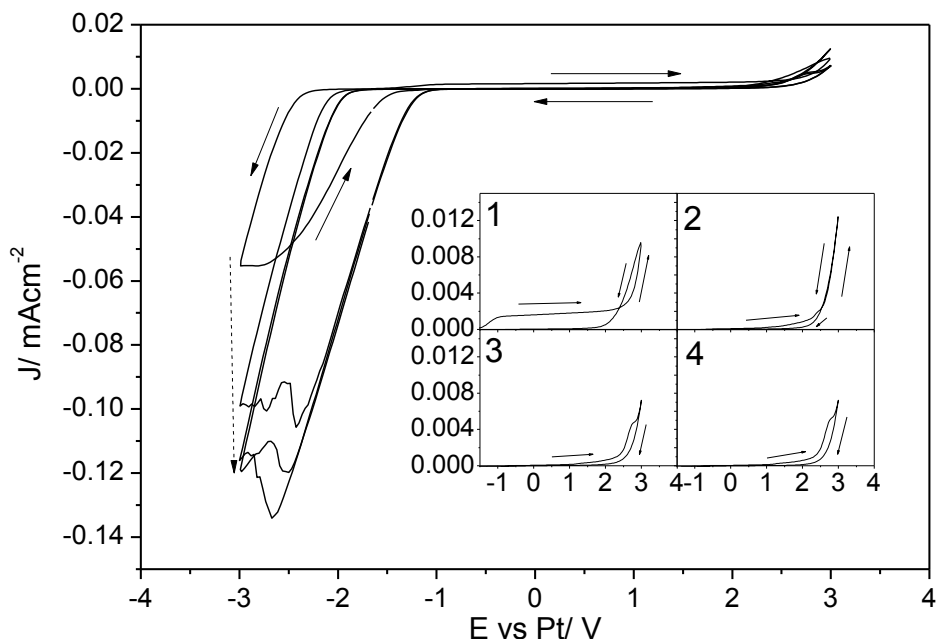


Figure 4.15 – Cyclic voltammogram of AZ31 in IL with 6 wt% (60,000 ppm) water. AZ31 was cycled at 1 mV/s from OCP and cycled between 3 V and -3 V vs. Pt. The inset show cycles 1-4 of the anodic portion of the scans (OCP to 3 V vs. Pt). Solid arrows indicate the direction of the scan, the dashed arrow indicates the progressive cathodic cycles.

4.1.4.2 Condition 2 – Argon Glovebox

The purpose of repeating the experiments in the argon glovebox is to determine the influence of oxygen on the reactions on the surface (it also prevents H₂O adsorption from the atmosphere), in particular its influence on the water reaction, which occurs in condition 1.

Figure 4.16 is a CV on AZ31 between OCP and -3 V vs. Pt at 1 mV/s. Unlike the reactions occurring in the IL-glassy carbon system, the reactions in the IL-AZ31 system have been dominated by the reaction of AZ31 as opposed to water. When polarised cathodically on the laboratory bench, the only reaction which occurred was the reduction of the IL at -2 V vs. Pt (Figure 4.2). As seen in Figure 4.16, when the same experiment is conducted in the argon glovebox, nothing is significantly changed. In fact, the current densities are not significantly different from the experiments conducted on laboratory benches. On the laboratory bench (Figure 4.2) the current density increases from approximately 0.011 mAcm⁻² in the first cycle to 0.016 mAcm⁻² in the final fourth cycle. As can be seen in Figure 4.16, the current densities within the glovebox remain between 0.01 and 0.011 mAcm⁻². In addition, there is no significant change in the following cycles, and the subsequent curves overlap each other considerably, suggesting no change in the reduction process of the IL in the absence of oxygen.

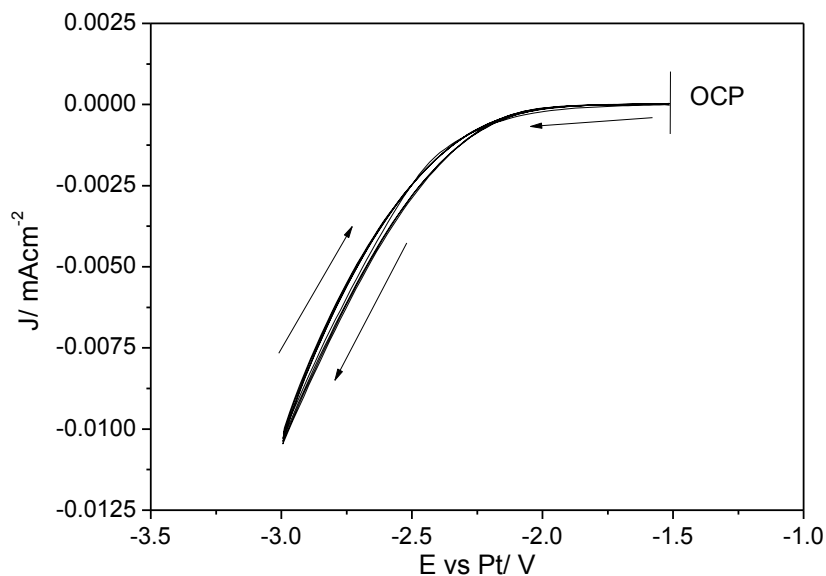


Figure 4.16 – Cyclic voltammogram of AZ31 in IL cycled between OCP and -3 V vs. Pt at 1 mV/s in an argon glovebox. Water content of IL used was approximately 1000 ppm. All four cycles are shown in the graph, however the deviations in maximum current density in the repeats differ less than $10 \mu\text{A}/\text{cm}^2$, and in no particular direction.

Figure 4.17 shows the anodic behaviour of AZ31 cycled between OCP and 3 V vs. Pt at 1 mV/s. The most important aspect of this curve is that, along with Figure 4.2, 4.3 & 4.13, it shows that regardless of the environment the polarisation is performed in, the basic characteristic shape is always present when polarised anodically in the IL. As with the other conditions, the current density takes off immediately and there is an abrupt gradient change at approximately 0 V vs. Pt. The main difference between the curve obtained in the glovebox to that on the laboratory bench is that at approximately 1.5 V vs. Pt the gradient increases. From the behaviour on GC (Appendix A, Figure A.2) this change in gradient is likely the oxidation of the IL species taking place. Therefore, the absence of oxygen and moisture in the atmosphere does not change the initial oxidation of magnesium, but appears to alter the formation of the passive film. When air has access to the cell, the oxidation of the IL appears to be suppressed when anodically polarised with AZ31 (the current density increases, but at a continually slow rate). When using the dry IL (1000-1500 ppm) on the laboratory bench the current densities do not exceed 0.002 mAcm^{-2} (Figure 4.2 a). However, in the argon glovebox the current densities are slightly higher. Figure 4.2 shows that the passivity of the system is increased when air is allowed to freely access the cell. This is good news in a practical sense as this suggests films do not need to be formed under expensive atmospheres to achieve the best performance.

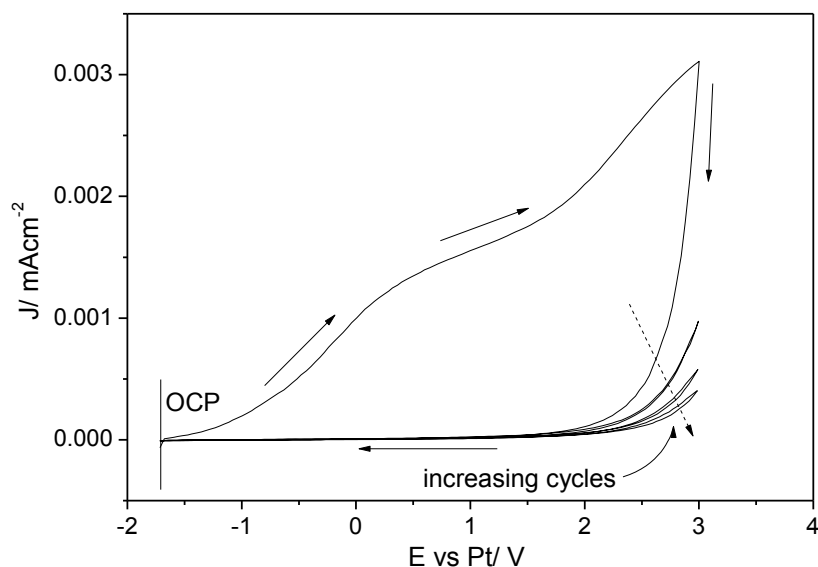


Figure 4.17 - Cyclic voltammogram of AZ31 in IL cycled between OCP and 3 V vs. Pt at 1 mV/s in an argon glovebox. Water content of IL used was approximately 1000 ppm.

4.1.5 Section Key Points

From the results presented in this section, the following key points can be made:

- Passive film formation occurs on AZ31 during anodic polarisation through the high field mechanism of growth, consistent with valve metal behaviour.
- The formation of the passive film is potential dependent.
- Adsorption of the IL occurs during anodic film growth.
- The passive film formation is an irreversible electrochemical process.
- Dilution of IL into acetonitrile does not affect the film forming capabilities of the IL.
- Polarising anodically in wet IL leads to significant surface modification, likely due to adsorption of oxidised IL.
- Dissolved air and moisture contribute to the film formation process.
- Cathodic polarisation in the IL does not passivate the AZ31 surface.
- Cathodic polarisation does not affect the ability of the system to form a passivating anodic film.

4.2 Electrochemical Film Formation in $[P_{6,6,6,14}][(^iC_8)_2PO_2]$

4.2.1 Section Overview

As outlined in the introduction and literature review of this thesis, the earliest work in forming films on magnesium alloys in ILs involved simple immersion of the alloy coupon in an IL. More recently, techniques by Howlett *et. al*[23] and Efthimiadis *et. al*[24], employing the use of electrochemical bias for film formation involved the application of a constant potential for a fixed time. In most cases the potential was maintained for a number of hours and the potential used was within a few hundred millivolts of the alloy's OCP. The following work not only covers a greater potential range but the galvanostatic (constant current) method of forming films is also addressed. This section details the effect of different treatment parameters on the formation of these films and discusses the formation of film defects.

4.2.2 Constant Potential

The intention behind applying a constant potential bias in this case is to influence the migration of the IL ions to or from the surface of the working electrode (AZ31). By positively polarising the AZ31 electrode, the negative anion of the IL will be influenced to migrate to the surface to be oxidised. In previous work by Forsyth *et. al*[21], the composition of the IL film formed on AZ31 when in contact with the IL $[P_{6,6,6,14}][NTf_2]$ at OCP for several hours was comprised significantly of the components of the anion. Further work by Birbilis *et. al*[22] on commercially pure magnesium also showed that the film was comprised of components of the anion. These authors formed the conclusion that the anion plays a major role in the film formation in these systems. Hence, when polarising the surface it would seem appropriate to apply a positive bias to lure the anion to the AZ31 electrode. Therefore, the magnitude of this potential is important as it should influence the behaviour of both the substrate (AZ31) and the anion and cation in the IL.

Figure 4.18 shows typical current vs. time behaviour of AZ31 in IL when a relatively low constant potential is applied (0 and 1 V vs. Pt (approx. 1.5 and 2.5 V vs. OCP respectively)) for 3 hours. When the constant potential is applied the current immediately decays at a rapid rate and then levels out. This behaviour has been attributed to amorphous film growth[125]. Consequently, when the cell is disassembled the film is not optically visible. Figure 4.18 a) shows the difference between the application of two different bias potentials of 0 and 1 V vs. Pt. The behaviour of both potentials is essentially the same, however, both the initial and final (stabilised) current density for the surface biased at 1 V is larger than for 0 V. For example, when 0 V is applied to the substrate the current density at the beginning of the curve is 0.04 mAcm⁻², as opposed to 0.07 mAcm⁻² for a 1 V bias. Figure 4.18 b) shows the current density transient for AZ31 held at 1 V vs. Pt for 96 hours, and indicates that even when held for such a substantial amount of time, the response changes only very slightly after the initial current drop. However, the 'stabilised' current density continues to decrease for the entire 96 hour period.

The magnitude of the stabilised current density alone is not indicative of one film being more passive than another. This is because the current densities will always be greater when a higher potential is being applied. The difference between the current density at the beginning compared with the stabilised current density may be indicative of a thicker film (due to change in

resistance, R), and therefore, the film formed at 1 V vs. Pt would be expected to be more resistive to that at 0 V vs. Pt.

As the current density appears to decrease indefinitely (at least in this 96 hour period) these current transients do not indicate whether there is an optimum treatment time. Obviously, a three hour treatment would be much more desirable than a 96 hour treatment.

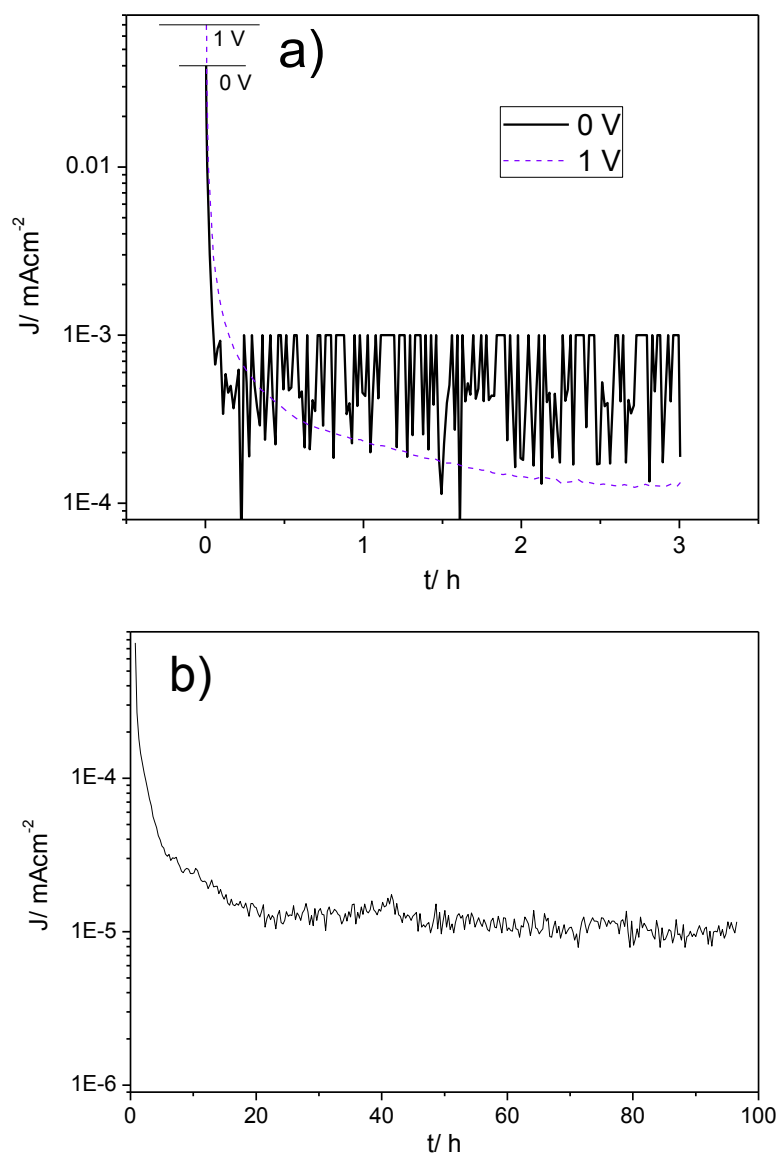


Figure 4.18 - Current density vs. time for AZ31 in $[P_{6,6,6,14}][(C_8)_2PO_2]$ held at a) 1 and 0 V vs. Pt for 3 hours; b) 1 V vs. Pt for 96 hours. The noise in a) is not indicative of the actual behaviour on the electrode, it is more likely poor choice of current range on the equipment.

Figure 4.19 a) shows a cross section using FIB-SEM of AZ31 anodised at 2.5 V vs. OCP (approx. 1 V vs. Pt) for 4 hours. A thin layer of gold (Au) was deposited onto the surface prior to ion milling to distinguish the top of the film. Unfortunately, this Au layer itself (based on predictions from the sputterer) was expected to be in the range of 50 nm thick. Keeping this in mind, with the application of a relatively low potential this FIB-SEM image shows the film formed is considerably thick (400-500 nm). It is uncertain by looking at Figure 4.19 a) exactly

where the Au layer is (i.e. part of the top white section or the darker line below). Discussion into the issues of imaging thin films from FIB-SEM is presented in section 4.2.3.

Figures 4.19 b)-d) show the EDS spectra corresponding to points 1-3 respectively. EDS was used to confirm the presence of the Au film and thereby set it apart from the film formed in IL. The EDS spectrum from the film and the AZ31 alloy below are shown in Figure 4.19 c) and d) respectively (for points 2 and 3 respectively). However, even using EDS (due to the area of interaction) it was difficult to conclusively determine where the Au layer stops and the IL film begins. In addition, the composition of the film could not be accurately measured. As shown in Figure 4.19 c), the elemental counts are very similar to the AZ31 base alloy (Figure 4.19 d). In addition, no counts for P were observed. Unfortunately, even if P was detected on the surface its peak exists at the same energy as Au, hence separation of the two would not be possible. In addition, it appears as though the film may be multi-levelled.

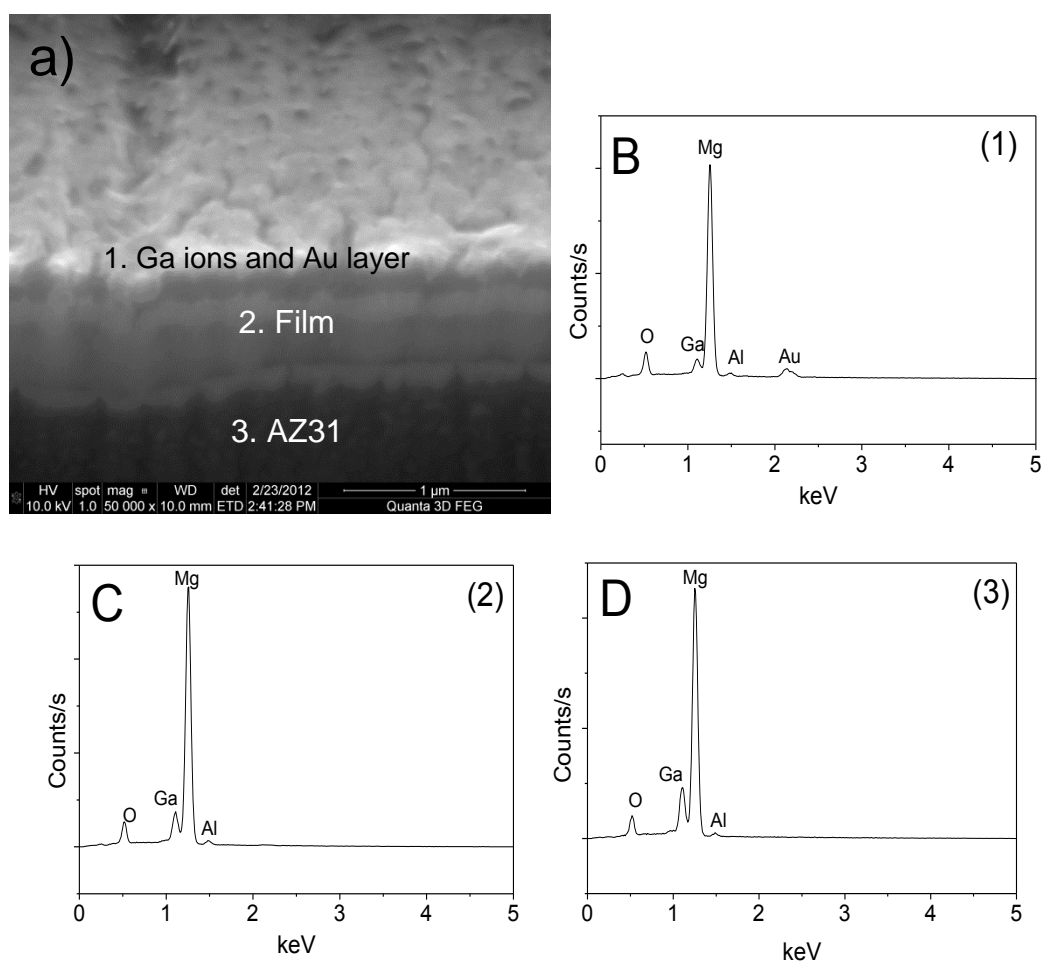


Figure 4.19 – FIB-SEM cross section of AZ31 anodised at a constant potential of 2.5 V vs. OCP (approx. 1 V vs. Pt) for 4 hours. b)-d) are EDS of parts 1-3 in a) respectively.

4.2.1.1 Using EIS as a Diagnostic Tool

One of the initial methods used to characterise the films being formed was through in-situ EIS measurements, which were previously used by Howlett *et al.* [23] and Efthimiadis *et al.* [24] to characterise IL/Mg alloy interactions.

Figure 4.20 a) shows a Bode plot of the evolution of impedance with time of AZ31 biased at -0.2 V vs. OCP. What we see is promising: with increasing treatment time the impedance is increasing, which would correspond to the thickening of the IL film on the surface. Figure 4.19 b) plots the resistance at 139 mHz against time for a number of different potential biases on AZ31. This allows us to get a better view of the evolution of the impedance with time, and hence the film thickening with time. In this case, peak impedances are realised in the 24 hour treatment time for both 3.5 and -0.1 V vs. OCP. Therefore, based on this data one would expect the optimum treatment times for 3.5 and -0.1 V vs. OCP would be approximately 2.5 and 0.5 hours respectively. On the other hand, the treatments of -0.2 and 0.1 V vs. OCP continue to increase for the entire 24 hour duration.

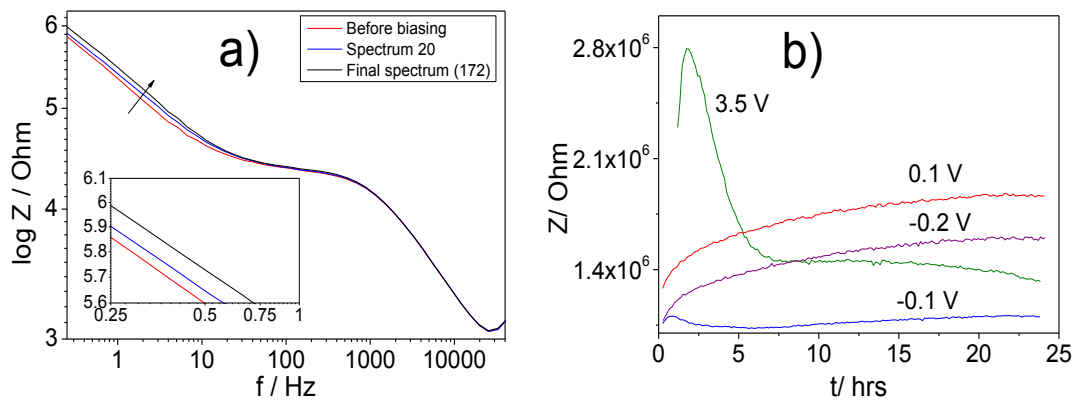


Figure 4.20 – a) Bode plot of AZ31 treated in $[P_{6,6,6,14}][C_8]_2PO_2$ at a potential bias of -0.2 V. An EIS spectrum was taken every 8 minutes; b) Z vs. t of AZ31 in IL biased at -0.2, -0.1, 0.1 and 3.5 V vs. OCP plotted at 139 mHz.

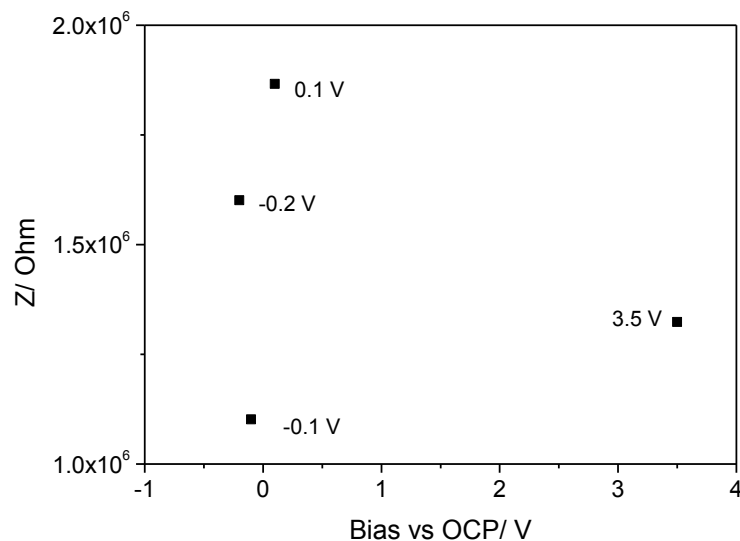


Figure 4.21 – Impedance values at 24 hours in IL for AZ31 biased at -0.2, -0.1, 0.1 and 3.5 V vs. OCP. Taken at 139 mHz.

Figure 4.21 is a plot of impedance values at a frequency of 139 Hz at 24 hours taken from AZ31 treated in IL at -0.2, -0.1, 0.1 and 3.5 V vs. OCP. If the biases are ordered based on this for their predicted protective qualities the order would be $0.1 > -0.2 > 3.5 > -0.1$ V vs. OCP. Figure 4.21 shows the impedance measurements taken of these surfaces 30 minutes after immersion in 0.01 M NaCl. Once placed in the corrosive environment the order changes to $-0.2 > 3.5 > -0.1 > 0.1$ V vs. OCP. In addition, the impedance of the -0.2 V vs. OCP bias was the only treatment with a higher resistance than the control. Although, as these resistance measurements were taken at 30 minutes after immersion (and not immediately) the resistance values may be skewed by the presence of corrosion product on the surface. Taking this into account, the difference between the impedance values for the surfaces treated at 0.1 and -0.2 V vs. OCP suggests one of these films is more defective than the other (e.g. high impedance of the -0.2 V treatment may be due to the formation of corrosion product and not the IL film or due to a more resistive IL film; the data here does not allow us to distinguish between these).

Nevertheless, Figure 4.21 & 4.22 we can conclude the use of EIS during film formation cannot be used to predict the protective ability of the film.

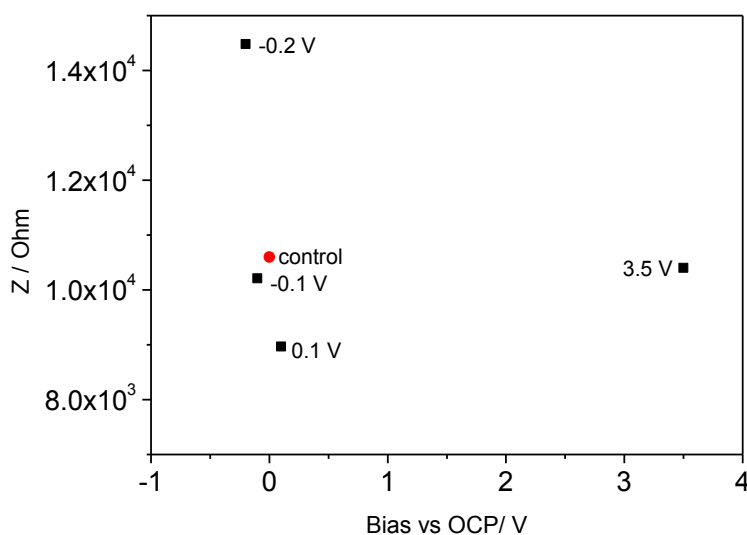


Figure 4.22 - Impedance values at 30 minutes in 0.01 M NaCl for AZ31 biased at -0.2, -0.1, 0.1 and 3.5 V vs. OCP in IL for 24 hours. Taken at 1.8 Hz (due to erratic behaviour at lower frequencies).

4.2.1.2 Higher Potentials and Field Crystallisation

4.2.1.2.1 Field Crystallisation at Room Temperature

Figure 4.23 shows the behaviour of AZ31 in IL exposed to a constant potential of 3 V vs. Pt for 96 hours. It was expected that the current density would behave in a similar manner as the lower bias potential profiles shown in Figure 4.18. However, the measured current in Figure 4.23 deviates dramatically from the stable behaviour in Figure 4.18.

Initially the behaviour in Figure 4.23 is similar to Figure 4.18 in that the current decays rapidly and then remains constant. However, after approximately 5 hours (arrow) the current density in Figure 4.23 begins to increase. Therefore, we suggest that initially an amorphous film grows at this potential, as in Figure 4.18, but after 5 hours a second process begins. This behaviour can be explained by a phenomenon known as *field crystallisation*. The literature on this phenomenon explains a process wherein the amorphous film on a metal undergoes crystallisation due to the

influence of an applied electric field. This process was first explained by Vermilyea[126, 127] and is represented graphically in Figure 4.24. The electric field is supplied by the constant potential applied across the IL from the counter electrode to the AZ31 substrate. As the amorphous film grows and thickens, the electric field within the film will increase until small electrical discharges occur. These discharges result in localised heating in the film and the nucleation of crystals. When crystals begin to nucleate the current begins to increase[125]. The current continues to increase as crystals grow and more nucleate. Once these crystals impinge on one another the current will peak and decay to the leakage current through the new crystallised film[126].

After the peak in current and subsequent decay in Figure 4.23 the current takes off again and behaves much more erratically shortly after. Figure 4.25 shows the corresponding surface from this experiment taken with an optical microscope. What is obvious from Figure 4.25 is that the film is highly non-uniform. Based on these images and the erratic current behaviour which occurs from approximately 45 to 96 hours, the AZ31 substrate must continue to react. Therefore, this crystallisation process is not particularly stable for the AZ31 surface. Figure 4.26 shows the optical appearance of the crystallised film if the experiment is terminated after the initial peak in current and subsequent decay (approx. 48 hours). However, in this case the film is not as dense as those formed in Figure 4.25. In addition, in Figure 4.26 b), it appears that there is some preferential deposition/crystallisation over the α phase as opposed to the β phase. Since the crystals nucleate within the amorphous film, this suggests the initial amorphous film growth must occur only over the α phase. Literature on anodising of magnesium alloys states that the α phase will react immediately in anodic conditions, however the β phase will not react to form a film until potentials exceeding 80 V are reached[74]. This is consistent with the observations here.

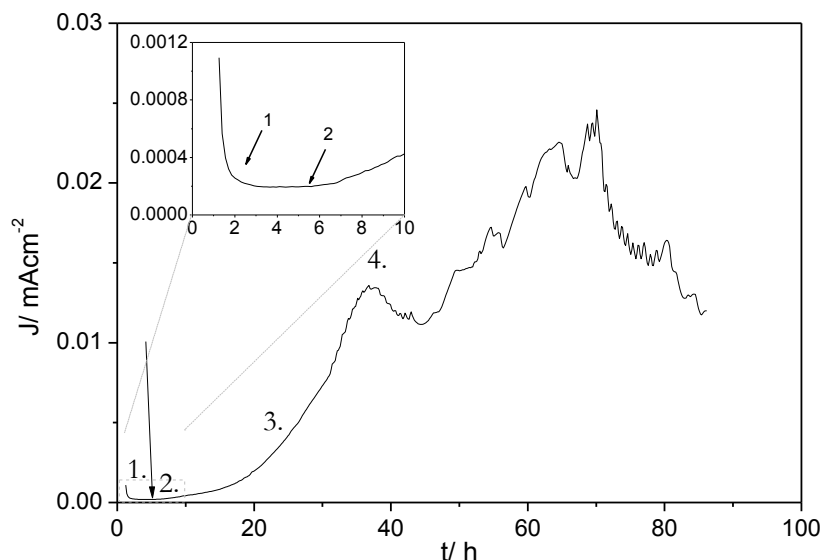


Figure 4.23 – Current density vs. time for AZ31 held at 3 V vs. Pt for 96 hours in $[P_{6,6,6,14}][(C_8)_2PO_2]$. Inset is magnified current response between 0 and 10 hours.

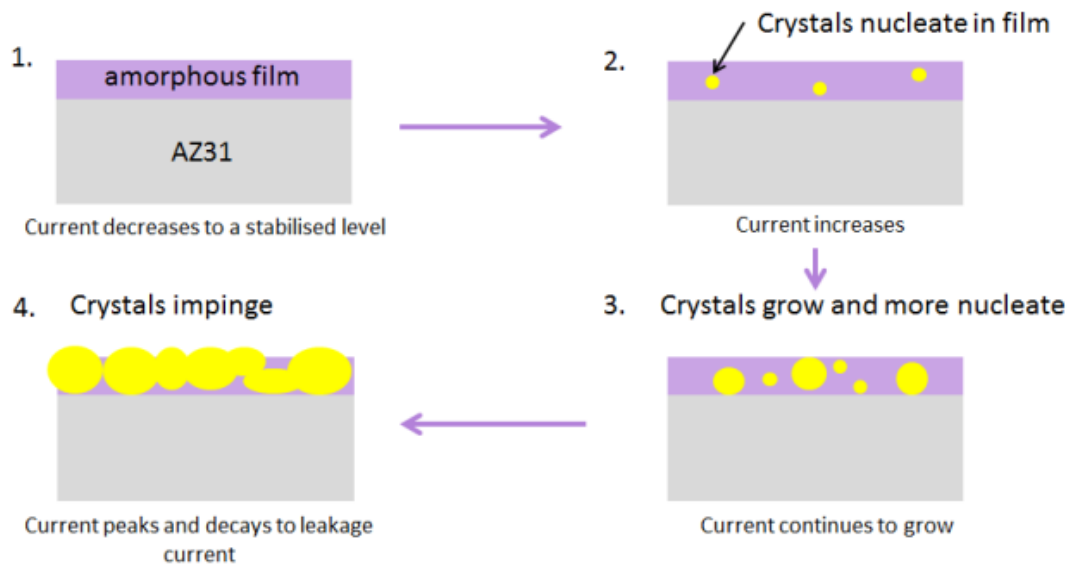


Figure 4.24- Schematic representation of the field crystallisation process. Numbered steps correspond to the numbers in Figure 4.24.

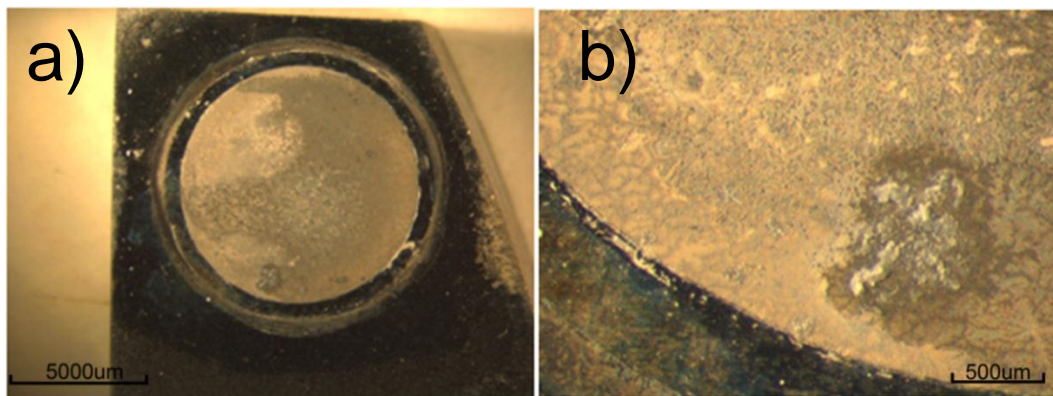


Figure 4.25 – Optical micrographs of AZ31 treated at 3 V vs. Pt in $[P_{6,6,6,14}][[(C_8)_2PO_2]$ for 96 hours at room temperature (approx. 22°C).

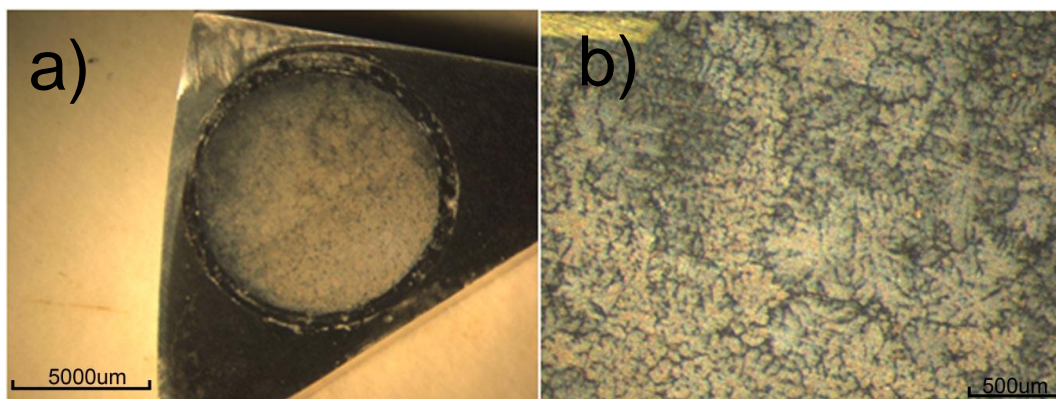


Figure 4.26 - Optical micrographs of AZ31 treated at 3 V vs. Pt in $[P_{6,6,6,14}][[(C_8)_2PO_2]$ for 48 hours at room temperature (approx. 22°C).

4.2.1.2.2 Field Crystallisation at Elevated Temperature

Figure 4.27 shows current profiles for AZ31 treated at 3 V vs. Pt for 48 and 96 hours at an elevated temperature of 50°C. The elevated temperature appears to remove some of the erratic behaviour observed in Figure 4.22. Due to the elevated temperatures during treatment there is significantly more noise than in the room temperature treatments, which may, in turn, conceal the erratic behaviour in Figure 4.23. Not surprisingly, the elevated temperatures lead to higher current densities than the profiles at room temperature. However, unlike the behaviour seen in [127], the increased temperature does not noticeably expedite the onset of the crystallisation process.

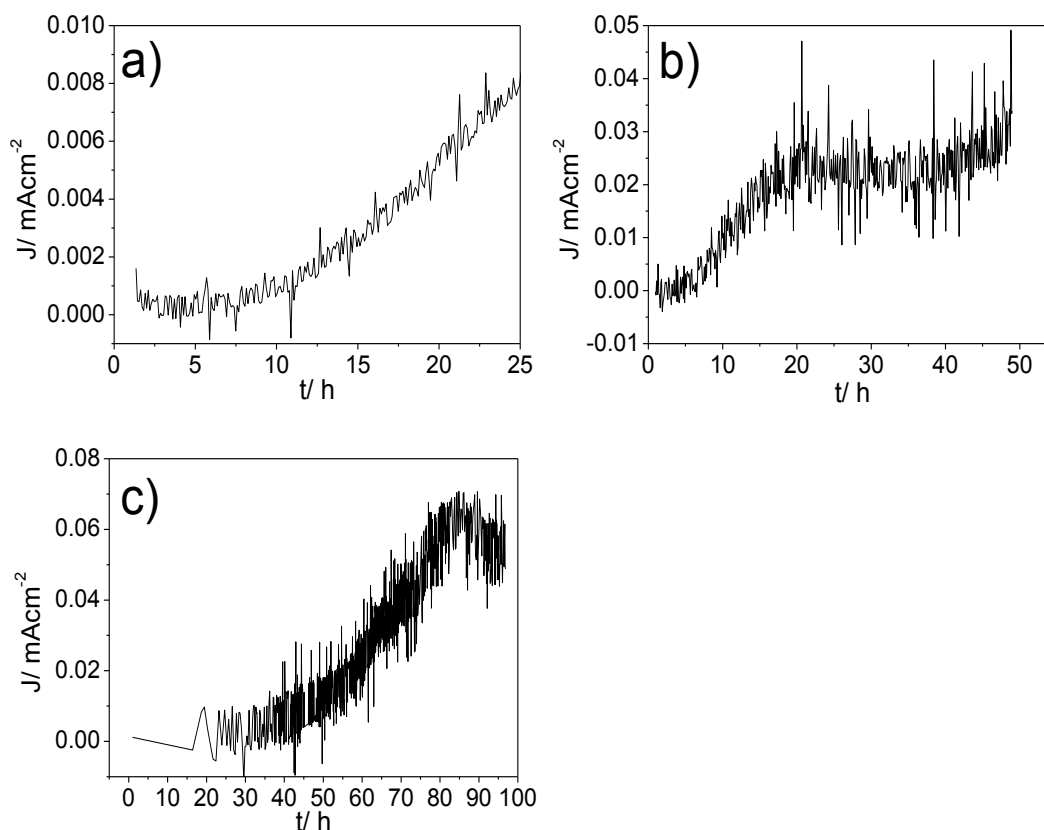


Figure 4.27 – Behaviour of current density with time of AZ31 treated at 3 V vs. Pt and 50°C in $[P_{6,6,6,14}][(C_8)_2PO_2]$ at a) 24 hours, b) 48 hours and c) 96 hours.

Figure 4.28 show the corresponding optical micrographs. As with the micrographs for the crystallised films formed at room temperature, there is a distinct preference for deposition over the α phase. Accelerating the crystallising process with the elevated temperature appears to lead to greater densification of the film. Unlike the film formed at room temperature, even after 96 hours only localised areas of severe crystallisation are present and the film formed at 48 hours is very uniform. The density of the film is also increased following a longer (96 hours) holding time. This suggests that crystals continue to nucleate and grow over a longer time frame at the higher temperature. If we consider Figure 4.27 c), we can see that the current does not peak until approximately 85 hours. Hence, film growth continues for almost an extra 40 hours compared to the same conditions as at room temperature. In comparison to Figure 4.28, the amount of coverage doesn't appear to actually change but the uniformity and density of the film is far superior. Therefore the elevated temperature may assist the formation of nucleation and growth over the Mg alloy surface.

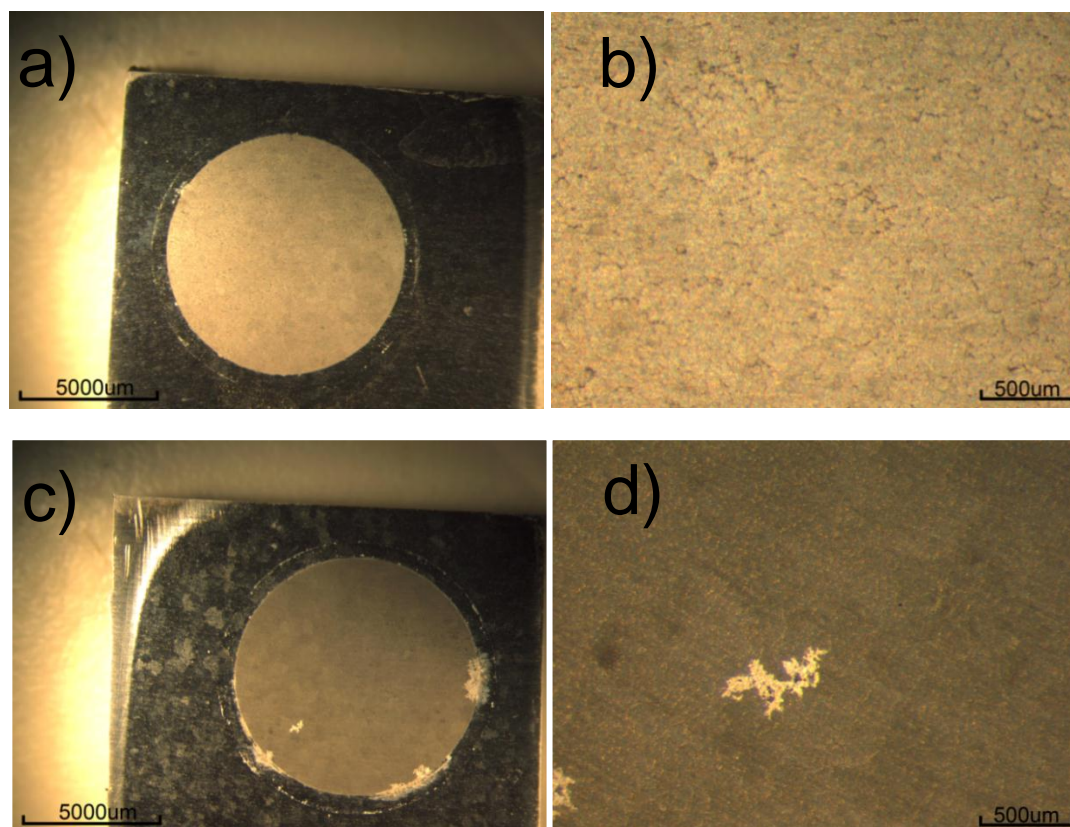


Figure 4.28 - Optical micrographs of AZ31 treated at 3 V vs. Pt in IL at 50°C for a)&b) 48 hours, c)&d) 96 hours.

Figure 4.29 presents optical profilometry images of AZ31 treated at 3 V vs. Pt and 50°C at three progressive times: 24 hours, 48 hours and 96 hours (a, b and c respectively). Figure 4.29 is a comparison of 'as-polished' AZ31 (ground to a P4000 grit finish). The main features on the surface are the marks from the grinding. Neither α nor β phase is identifiable on this image. However, as with the optical images, after field crystallisation, the β phase and α phase can be differentiated on the profile images in Figure 4.29. In all three cases (24, 48 and 96 hours) the β phase can be identified as the lower *smooth* areas surrounded by the rough, raised crystalline film over the α phase. With increasing exposure time, the density of the crystalline film increases. Although despite the increase in density (and hence surface coverage) the roughness is considerable in all three cases (see Table 4.2). Due to the way in which the crystals nucleate and grow the crystals form a morphology of 'small hills' on the surface[125]. Therefore, these films are highly porous in nature.

Table 4.2 – Surface roughness values for constant-voltage treated surfaces obtained from optical profilometry data over a 937.5 x 1249.7 μm area.

Treatments	Sa – Mean Roughness (μm)	Sz – Ten Point Height (μm)
Control	0.159	2.81
3 V 50°C 24 hrs	0.139	4.22
3 V 50°C 48 hrs	0.432	6.90
3 V 50°C 96 hrs	0.919	9.46

The surface roughness of the specimens (apart from the R.T. surfaces) was measured using the optical profilometer and are tabulated in Table 4.2.

The S_a and S_z values for a control (ground to a P4000 finish) are also included in Table 4.2 as a comparison. The average surface roughness (S_a) of the control specimen is fairly low ($0.159\mu\text{m}$), however due to the relatively coarse P4000 surface finish the S_z is quite large at $2.81\mu\text{m}$.

After 24 hours the average surface roughness is decreased and S_z is decreased, which is likely due to the small crystals effectively filling in the grooves caused by the P4000 grit finish. At this point the crystals are too small to significantly increase the film thickness (as seen in Figure 4.28 a). Thus the values of S_a and S_z appear to be less than the control despite the presence of nucleated crystals in the amorphous film. On the other hand, the roughness is almost three times greater than the control when treated for 48 hours and almost six times greater when treated for 96 hours. Not surprisingly, the difference between the valleys and the peaks is also significantly greater for the specimens treated for longer times, with $6.9\mu\text{m}$ for 48 hours and $9.5\mu\text{m}$ for 96 hours. This coincides with the visual data, which shows the surface roughness (which, given the porosity, is also an approximate measure of the oxide thickness) increasing with increasing treatment time.

Figure 4.31 is a current transient for AZ31 treated at 1 V vs. Pt for 48 hours. Apart from the high levels of noise due to the applied temperature, the transient is more or less the same as in Figure 4.18. The current decreases and stabilises at a lower value and maintains this for an extended period of time. Hence, the application of 50°C vs. room temperature does not change the ability for the amorphous film to crystallise. This is because for field crystallisation to occur the applied electric field must be sufficiently high. As with the curves in Figure 4.27 the elevated temperature resulted in a noisier curve but otherwise the increase in temperature does not affect the essential behaviour of the system regarding field crystallisation. Therefore, increasing the temperature only influences the crystallisation process in systems that would crystallise anyway (due to applied potential), regardless of temperature.

Unfortunately, due to the unpredictable nature of this crystallisation process, at least in this II, this method of film formation is not ideal. As it appears the temperature has a considerable effect on the uniformity of the film, general temperature fluctuations could destroy the reproducibility of these films. In addition, at least at 3 V vs. Pt, the time taken to form a thick uniform film (48 hours) is too long for any real practical value. The films also form preferentially over the α phase as opposed to the entire microstructure and when oxidised the porosity is high. Later, in section 4.3, we show that this porosity leads to poor corrosion performance. Therefore the remainder of this section focuses on the constant current treatments.

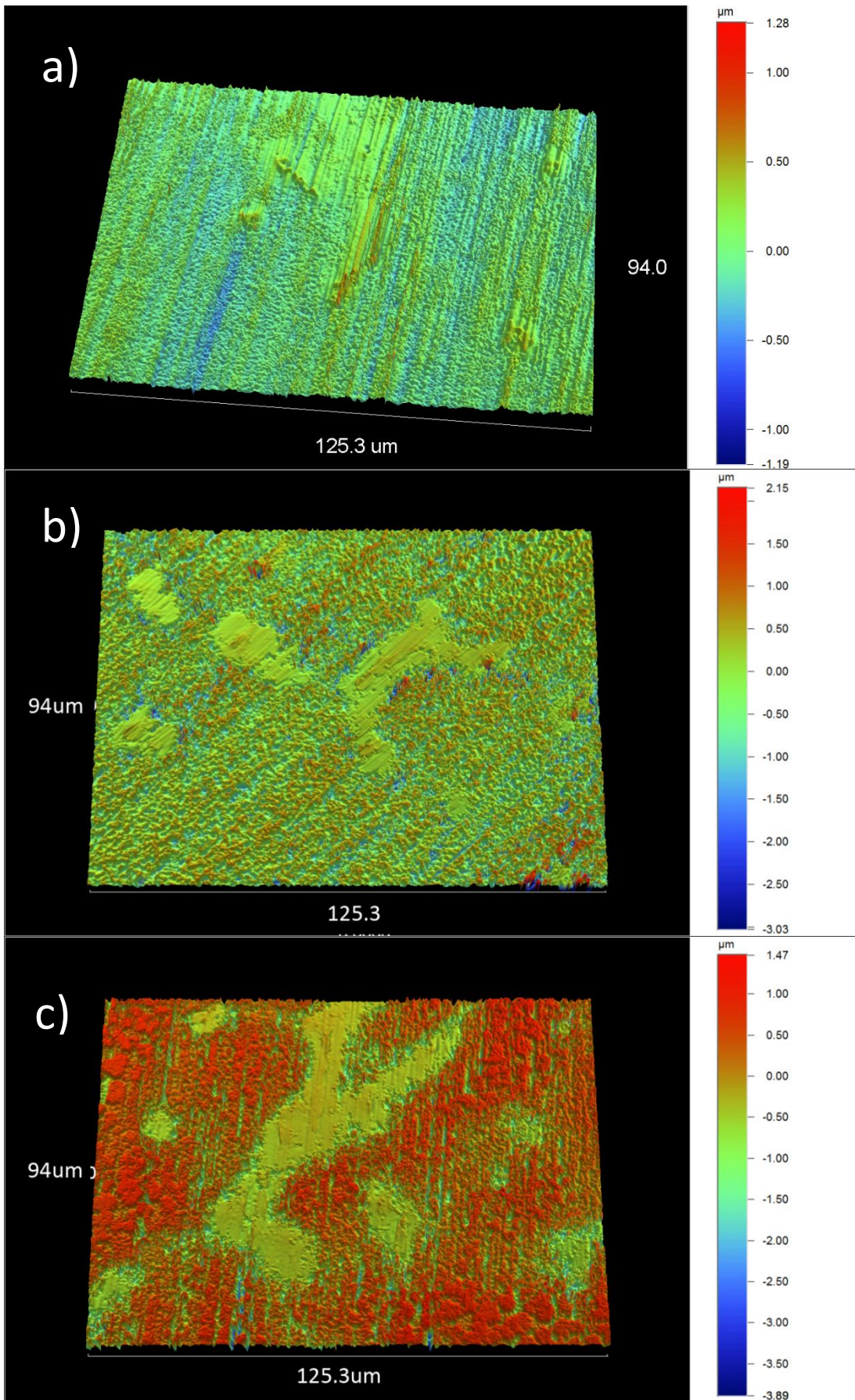


Figure 4.29 – Optical profilometry of AZ31 after treatment at 3 V vs. Pt and 50°C for a) 24 hours b) 48 hours and c) 96 hours.

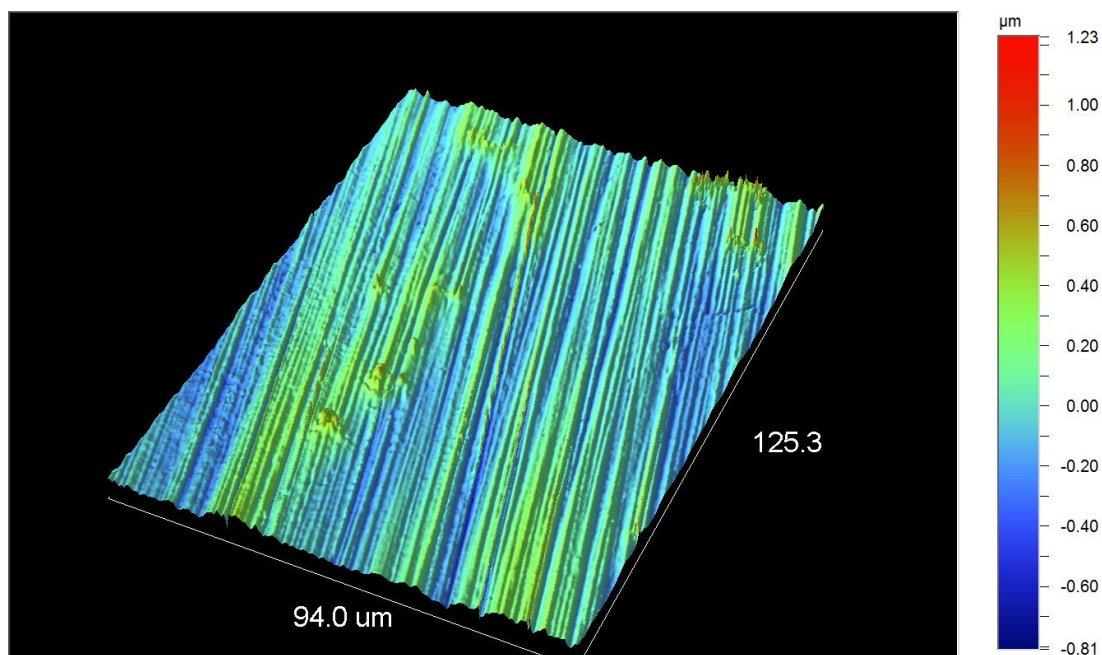


Figure 4. 30 – Optical profilometry of AZ31 ground to a P4000 grit finish.

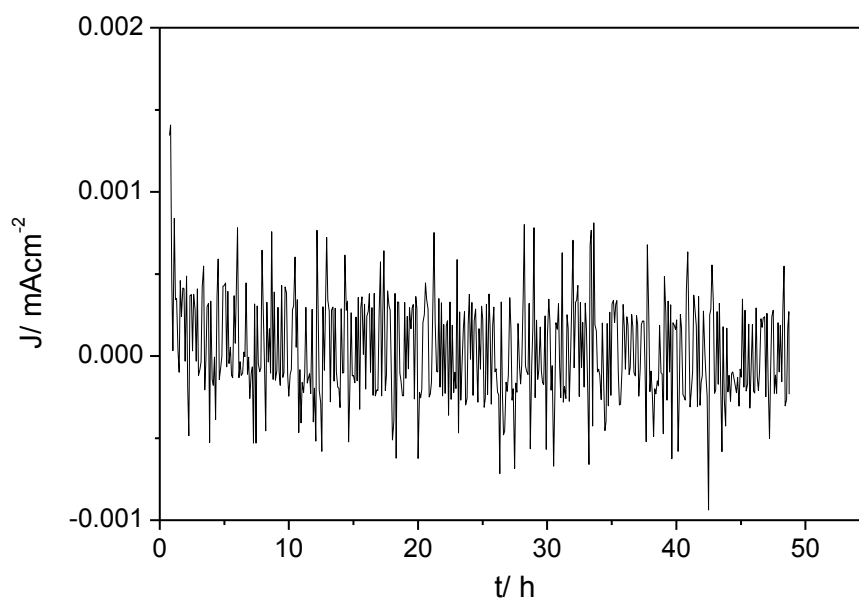


Figure 4. 31 – Current density behaviour over 48 hours of AZ31 treated at 1 V vs. Pt and 50°C.

4.2.3 Constant Current

A very popular method of forming a protective layer on magnesium alloys is through a technique called galvanostatic (constant current) anodising (theory in section 2.3.5). This technique involves applying a current density to the surface of interest in order to form a thick oxide, which can be used to protect the surface from corrosion.

The behaviour that was observed in section 4.1 showed the passivation of the AZ31 surface with continued anodic cycling. As seen in Figure 4.8, if the potential that AZ31 is cycled to is increased continually, AZ31 will continue to react within the new potential range. It is important to note that whilst the current density increases when the potential is increased, the current density within the range of the cycle preceding it is passive (as seen in the case of repeated cycling to the same potential). As mentioned earlier, this indicates that there is no chemical dissolution of the film during the experiment[117]. It also indicated that the formation of the film on the surface is highly dependent on the potential.

Figure 4.32 shows potential transients for AZ31 treated in IL at current densities of 0.005, 0.01, 0.05 and 0.1 mAcm^{-2} . Due to the limitations of the potentiostat being used (max voltage limit of 20 V), the final cell voltage of 18 V was set. A successful treatment was judged by the ability of the cell potential to reach 18 V. In all transients, the rate of potential increase decreases with anodising time, which suggests that the current being put into the system is being used by a process other than film growth. It has been suggested that gas evolution (typically of oxygen) can cause this[74]. In addition to this, the potential transients for the treatments at lower current densities (0.005 and 0.01 mAcm^{-2}) experience one or more distinct slope changes (indicated by arrows). For both the current densities of 0.005 and 0.01 mAcm^{-2} this initial sharp slope change occurs at approximately 5 V.

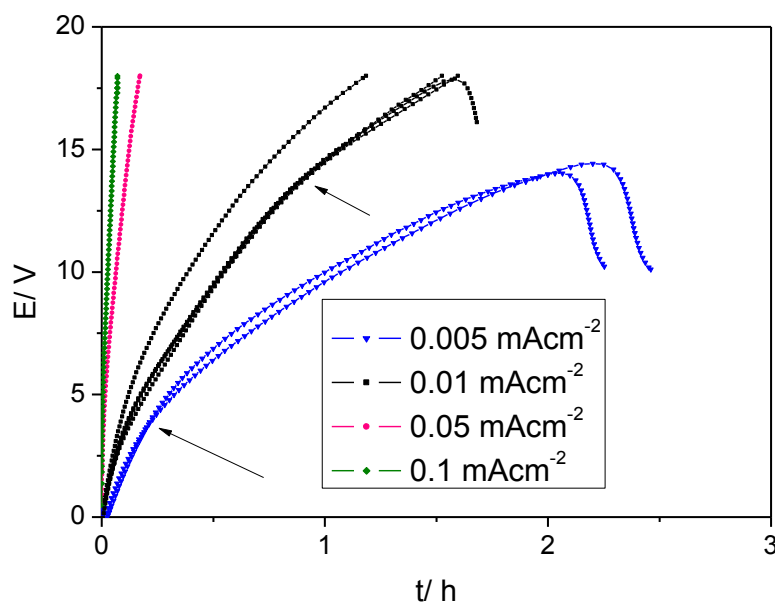


Figure 4.32 – Cell potential vs. time for treatment of AZ31 using current densities of 0.005, 0.01, 0.05 and 0.1 mAcm^{-2} . The final potential set was 18 V.

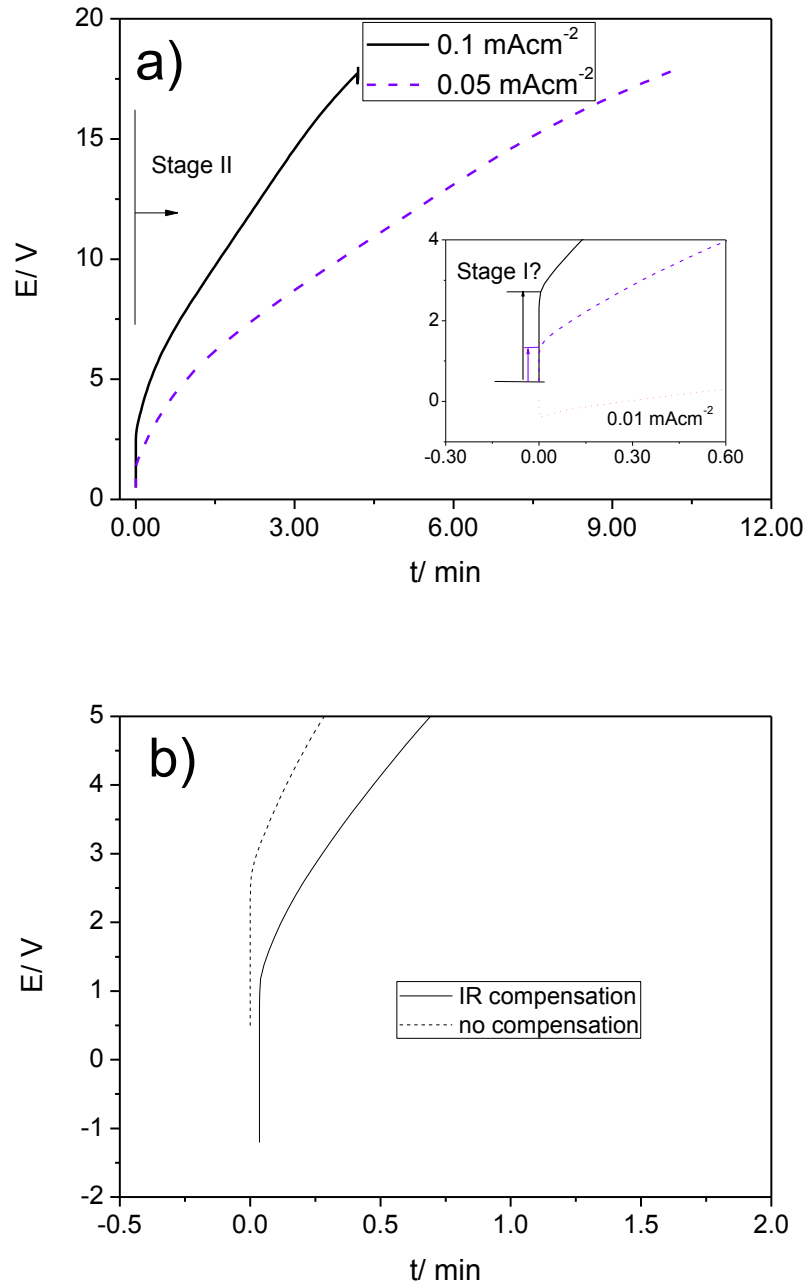


Figure 4.33 – a) Cell potential vs. time for treatment of AZ31 using current densities of 0.1 and 0.05 mAcm⁻²; b) comparison of potential “jump” between AZ31 anodised at 0.1 mAcm⁻² with and without iR compensation.

Figure 4.33 a) shows two potential transients of AZ31 anodised at 0.05 and 0.1 mAcm⁻². Unlike the transients for low current densities, those performed at higher current densities do not appear to show such a change in slope. The slopes at the higher current densities are much more linear; however, as seen in Figure 4.33, the slope actually changes very gradually with increasing potential. Figure 4.33 a) also shows a sudden increase in the potential when the current density is high enough, which appears to indicate an iR drop. This occurs due to the resistance of the solution (that is, the IL) interferes with the recorded cell potential.

Figure 4.33 b) shows the potentials transients for AZ31 anodised at 0.1 mAcm⁻², with and without internal iR compensation. However, even when the resistance is compensated for the system, the very sharp potential increase does not completely disappear, but is reduced.

Otherwise, this initial jump may be due to one of two things (perhaps even both): (1). the resistance of oxide already on the alloy surface[74] or (2). the first stage of anodising (see section 2.4 for more details)[74]. For magnesium alloys (as mentioned in section 2.4) there are four main stages during anodising. As a cut-off potential of 18 V was selected in these experiments only stages I and II will apply this system (as stages III-IV involve dielectric breakdown of the film). Hence the majority of the behaviour of these transients (Figure 4.32 and 4.33) exists in stage II.

The decrease in slope in Figure 4.33 not only indicates a decrease in anodising efficiency but also represents a higher electronic conductivity of the oxide film[128]. This decrease in efficiency can also be noted by the total treatment time between the different current densities in Figure 4.33. The time it takes for the cell potential to reach 18 V is not proportional to the applied current density at lower current densities. For example, treatment at 0.1 mAcm^{-2} takes approximately 4 minutes, which jumps up to 90 minutes when treated at 0.01 mAcm^{-2} . Decreasing the current by a factor of 10 does not make the treatment take 10 times as long. In fact, in the case of 0.1 vs. 0.01 mAcm^{-2} the lower current density results in a treatment time over 20 times longer. The slope change may be due to either a change in the structure or the composition (often cited as incorporation of the anion of the anodising bath[129]) of the anodic oxide[130] but can also be associated with breakdown of the film[128] through defects in the oxide[131]. This behaviour has been witnessed during anodising of Ti[129] where electron micrographs found breakdown sites increased in number and size with the progression of the decreasing slope. It was suggested that the formation of these sites increases the conductivity of the oxide, leading to the transient profile decreasing in dE/dt with ongoing anodising[129]. By allowing current flow through the defects, less current would be used to grow the film, resulting in lower anodising efficiency (that is, the slope decreases). In particular, like with AZ31 in IL, the transient for Ti incurred a distinct slope change at 5 V[129]. The CV data presented in 4.1 suggests adsorption of the IL during anodic cycling. Therefore, it is likely the non-linear slopes may also be due to adsorption of the IL.

A study on Zr oxides found that the use of lower current densities resulted in blistering of the oxide, which was worse with lower applied current densities[132]. The authors concluded that the blisters formed due to internal stresses in the oxide once the film reached a certain thickness. With increasing current density they suggest stress relaxation can occur within the oxide, which prevents the formation of defects[132]. The process of breakdown has also been suggested to be due to crystallisation of the amorphous film at defects[129]. High localised current flow through a defect will result in localised heating of the surrounding film, which can cause crystallisation.

Better oxide films are formed by metals such as Al, Ta, Nb and Ha. In the case of these metals the slope of the potential transient is steep and there is no change in slope with increasing potential[133]. Therefore, it should be possible to predict the quality of the film based on how linear the potential transient is during treatment. That is, a more linear potential transient likely corresponds to a better film.

4.2.3.1 Film Morphology of Constant Current Anodised Films

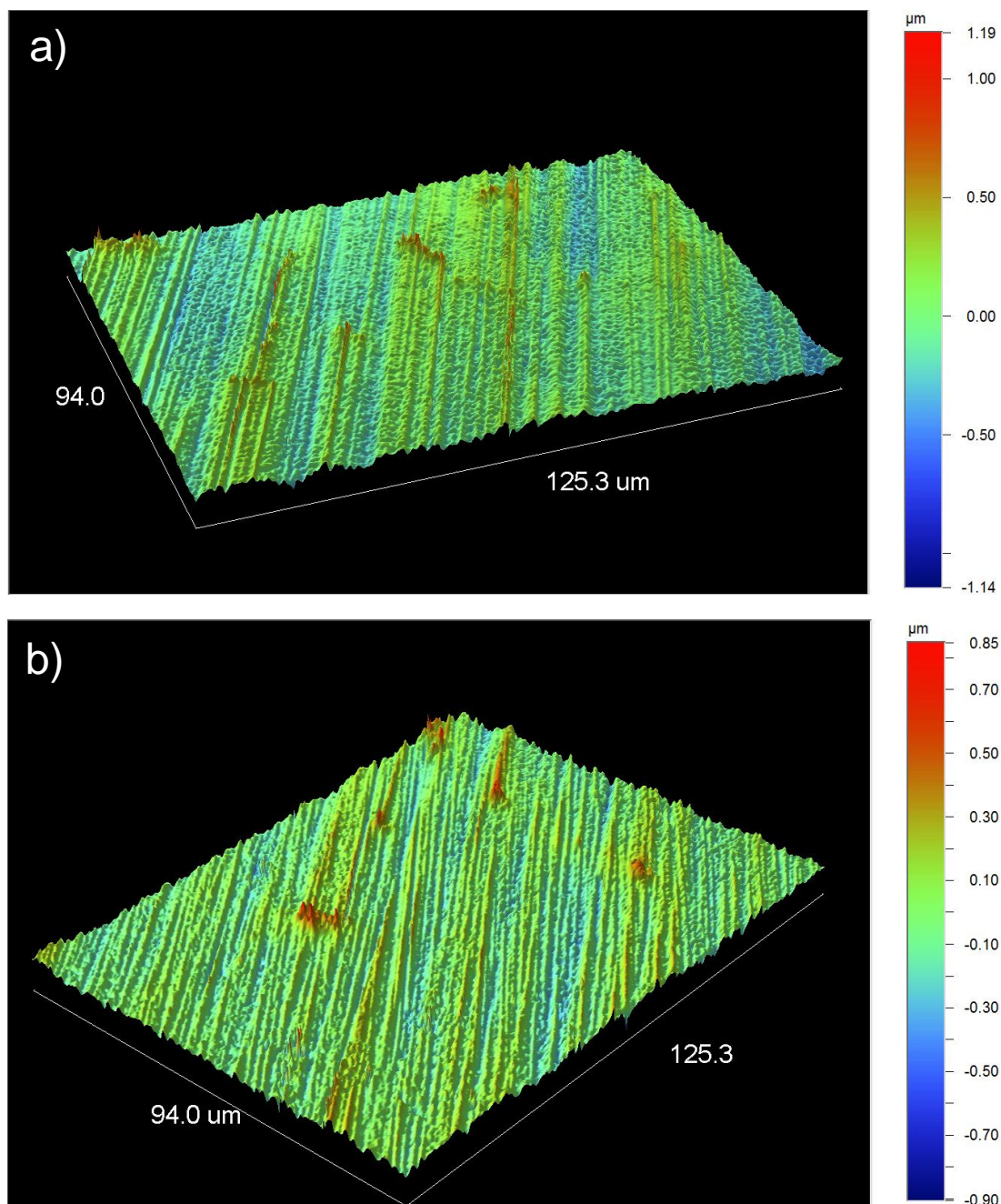


Figure 4.34 - Optical profilometry of constant current treated surfaces: a) 0.05 mAcm⁻² and b) 0.1 mAcm⁻².

Figure 4.34 a) and b) show high magnification optical profilometry of AZ31 anodised at 0.05 and 0.1 mAcm⁻² respectively. The thin films can be differentiated from the polishing marks when compared to Figure 4.29 (section 4.2.1) of the ground AZ31. The lines from grinding in Figure 4.30 are smooth, whilst the anodised surfaces in Figure 4.34 are dimpled in appearance. The presence of these lumps is appears to be fairly homogeneous over the surface. Table 4.3 tabulates the surface roughness values taken from these profilometry profiles. Both Sa and Sz were explained earlier in the methodology in Chapter 3. Unlike the 48 and 96 hour surfaces treated at constant voltage (Table 4.2), the average roughness for the constant current anodising specimens are very similar to, or even smaller, than values for the control.

However, S_z is considerably greater for both treated surfaces, which may be due to the irregular morphology of the films. Interestingly, both S_a and S_z are lower for the greater current density, which possibly suggests that a more uniform and/or denser film is deposited in this case.

Table 4.3 - Surface roughness values for constant-current treated surfaces obtained from optical profilometry data over a 94 x 125.3 μm area.

Current Treatments (mAcm^{-2})	S_a - Mean Roughness (μm)	S_z - Ten Point Height (μm)
Control	0.159	2.81
0.05	0.169	3.38
0.1	0.150	3.14

Figure 4.35 a) shows a top-down view of a trench (rectangular feature) milled into AZ31 anodised at 0.05 mAcm^{-2} using Ga ions in a technique called Focused Ion Beam Scanning Electron Microscopy (FIB-SEM). Figure 4.35 b) shows the same trench from a front-on angle. When imaging the films using this method difficulty lies in ensuring an accurate measurement of the film thickness, especially when dealing with very thin films. There are two main reasons an incorrect thickness can be taken:

1. If we look closely at Figure 4.35 a), we can see a lighter ‘halo’ around the trench. This lighter, patchy, area is caused by Ga ions deposited on the surface as a result of the ion milling. Figure 4.35 b) shows this Ga layer as a thin light band/film on top of the AZ31 (dark region) surface. If the films being analysed are very thin it may be possible to mistake the Ga layer as part of their film, which can lead to uncertainty in measurements (i.e. it is difficult to identify where the film of interest ends and the Ga begins).
2. Curvature of the edge of the milled area can also cause shadowing. This shadow, being a different shade to the area below it, may also be mistaken for a film. As a result, it can be difficult to say, beyond doubt, that the shift in contrast is the result of the film or simply curvature of the milled area.

Figure 4.36 a) shows a high magnification cross section of AZ31 anodised at 0.05 mAcm^{-2} . The lighter layer at the top of the image is a Pt layer deposited within the FIB-SEM instrument. Due to the issues mentioned previously, the deposition of this layer allows the identification of the thin surface film (dark layer below it) from the AZ31 surface (bottom section of image). The Pt layer has essentially sandwiched the film between the deposited Pt and AZ31. This deposition has hence eliminated the two factors above, allowing for accurate thicknesses to be measured. The thickness of the film was measured at approximately 80 nm.

Figure 4.36 b) shows the cross section of Pt deposited on bare ‘as-polished’ AZ31. This was done to quell speculation that may arise based on possible appearance of “shadows” at the interface of deposited Pt with the AZ31 surface. In this image the light colour of the Pt layer goes directly into the darker layer of the AZ31, without any intermittent change in between. This comparison conclusively demonstrates the presence of a film in Figure 4.36 a).

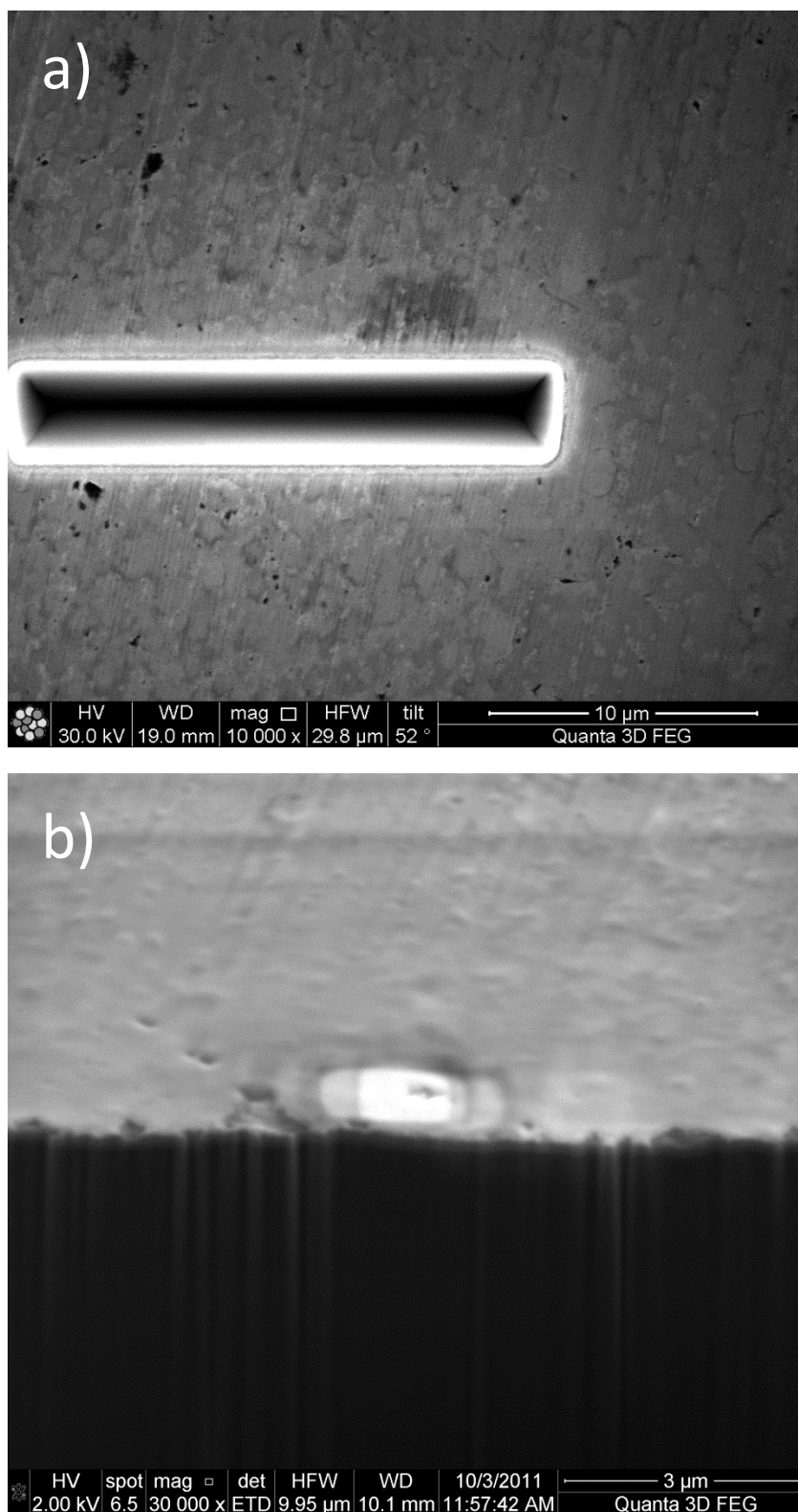


Figure 4. 35 – FIB-SEM image of Ga ions on surface due to milling, a) ring of Ga ions around the sputtered area and b) thin light layer of Ga ions on surface make it difficult to confidently distinguish film.

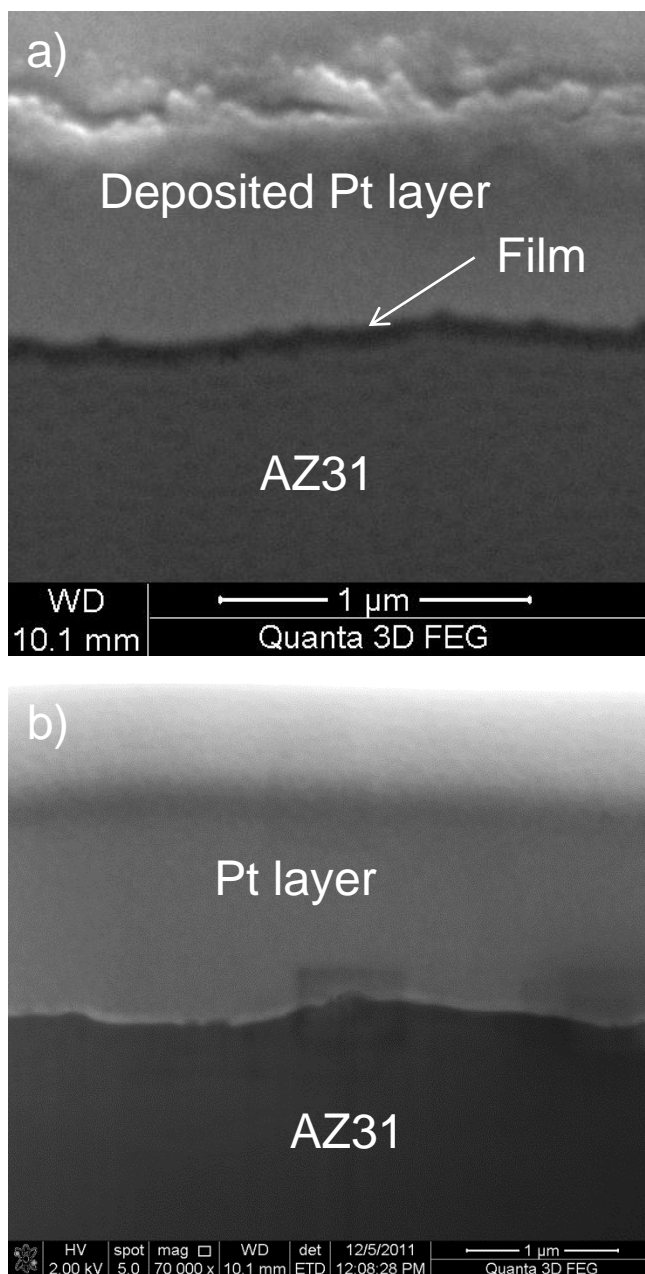


Figure 4.36 – FIB-SEM cross section of AZ31 a) treated in IL at 0.05 mAcm^{-2} between a layer of deposited Pt (upper light layer) and AZ31 (lower dark layer). Thickness is approx. 80nm. b) cross-section of ‘as-polished’ AZ31 with a deposited Pt layer.

The FIB-SEM presented isn't the first instance of the thickness of an IL film formed being measured on magnesium. After exposure to $[\text{P}_{6,6,6,14}][\text{NTf}_2]$ IL for one hour an 87 nm thick film was identified on 99.99% Mg[22]. Using this method of surface pre-treatment a film of analogous thickness could be formed in a quarter of the time, which, if ever used commercially, would result in greater turnover of product. However, 18 V is very low for this type of technique as stage III and IV of anodising are not achieved. Hence there is scope to expose AZ31 to considerably higher potentials and current densities, which will lead to considerably thicker and more resistive films. The need to provide a cut-off potential of 18 V (due to equipment total potential range of 20 V) is the greatest limitation in this work.

Mg-Al alloys are considered passive at potentials up to 3 V, above which dissolution occurs through the formation of pits[74]. Despite this point dissolution of our AZ31 alloy was experienced at much lower potentials. However, more interestingly Mg-Al becomes passive

again after 20 V due to the formation of MgO[74]. The maximum potentials used in this work fall short of this value, which may be in part responsible for insignificant change in corrosion properties, which will be covered in section 4.4.2. However, that being said the potentials used can vary greatly with different anodising baths as protective films have been formed on Mg alloys at 3 and 5 V[74]. Either way, higher potentials are clearly the next step of investigation in this work.

4.2.3.2 Film Breakdown

Many of the potential transients in Figure 4.32 do not reach the cut-off potential (18 V) and instead peak and decay. When a current density is applied to the surface the cell potential will begin to increase. If we consider Ohm's law we know $V \propto IR$. As I is constant and V is increasing, R must also increase. This increase in resistance corresponds to the film growth on the surface. Therefore, the greater the potential recorded, the thicker the deposited film should be. When V begins to decrease, the resistance of the film must be decreasing, which can be due to the formation of defects. Thus when the potential actually declines none of the current applied to the system is going into film formation: the film has catastrophically broken down.

Current densities $\geq 0.05 \text{ mAcm}^{-2}$ were able to reach the final potential without this significant breakdown occurring, however current densities of 0.01 mAcm^{-2} often failed before reaching 18 V and those treated at 0.005 mAcm^{-2} all resulted in breakdown. This behaviour suggests that a critical current density near 0.01 mAcm^{-2} is required to form a uniform film in this IL.

Table 4.4 – Charge densities passed during anodising.

Current Density (mA/cm ²)	Charge Density(C/cm ²)
0.005*	0.041 ± 0.003
0.01	0.054 ± 0.006
0.05	0.028 ± 0.003
0.1	0.019 ± 0.005
Failed 0.01*	0.056 ± 0.001

**The charge was calculated from $Q=It$ until the peak in the potential (i.e. point of breakdown), the charge following is not considered.*

Table 4.5 lists the charge densities passed for each of the applied current densities. It is possible that the amount of charge passed is crucial in whether or not breakdown occurs with a treatment. With increasing current density the charge passed to reach the final cell potential, or point of breakdown, typically decreases. The only exception is that films formed using 0.005 mAcm^{-2} breakdown at charges lower than those at 0.01 mAcm^{-2} . It has been suggested that breakdown in anodic oxide films occurs when a certain level of charge is passed[129]. However, this has been suggested to be more related to the thickness of the film that corresponds to the charge passed, as opposed to the charge itself. This is based on the premise that once a certain thickness of film is reached internal compressive stresses form, which lead to cracking. Based on the values in Table 4.4 the critical charge appears to vary between 0.041-0.054 C/cm².

Figure 4.37 presents six separate potential transients for AZ31 anodised in IL at 0.01 mAcm^{-2} . What is interesting about the data here is that despite the same current density used the points of breakdown (and hence charge passed) are different for each transient. In addition, one of the transients actually managed to maintain film growth to the 18 V cut-off potential. The variation in the calculated charge passed (gathered from Figure 4.37) at which breakdown occurs is considerable, ranging from 0.008-0.049 C/cm² (note, these curves were not used to calculate the charges supplied in Table 4.4). Hence, this data shows that the charge does not dictate the breakdown process of these films. Similar behaviour has been reported in the literature[128]. In

a study on anodising zirconium (Zr) Overmeere *et al.*[128] found that, for the same amount of charge passed under the same anodising conditions, breakdown would also occur in some films and not in others. They concluded that internal stress within the oxide was the cause of breakdown in their films. The authors found that films which failed at lower levels of charge had significantly higher levels of internal compressive stress, regardless of total film thickness[128]. The authors found that they could alter the levels of internal film stress by controlling variables of applied anodising current density, solution concentration, and the batch of Zr metal used. The use of lower current densities was found to produce greater internal stresses in the oxide[128]. Earlier work by Archibald *et al.*[134] also found similar behaviour with Zr. With increasing film thickness the internal stresses increased and the magnitude of the stress was greater for the lower current densities. The origin of these increased internal stresses with current density is currently unclear; however the increase occurrence of breakdown at lower current densities is consistent with a more highly stressed film and hence more defects.

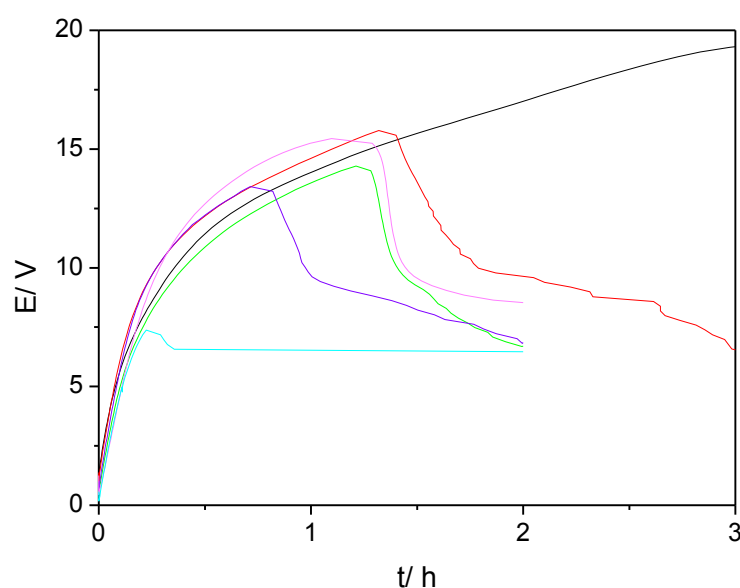


Figure 4.37 - Cell potential vs. time for treatment of AZ31 using a current density of 0.01 mAcm^{-2} .

4.2.3.3 Morphology of Film Breakdown

Figure 4.38 presents optical micrographs of AZ31 treated at a constant current density of 0.01 mAcm^{-2} . Figure 4.38 a) shows the appearance of a successfully formed film (no catastrophic breakdown) while Figure 4.38 b) shows the appearance of a film which has undergone catastrophic breakdown. Successfully formed films (such as that in Figure 4.38 a) are hard to image optically whereas broken down films are highly visible. Breakdown processes in anodising have been proposed to occur through high local current flow at cracks formed in the film, which causes localised heating and ultimately crystallisation[129]. Hence, the change in optical properties in Figure 4.38 is likely due to crystallisation of the majority of the film, corresponding to the change in slope behaviour explained previously (Figures 4.32 and 4.37).

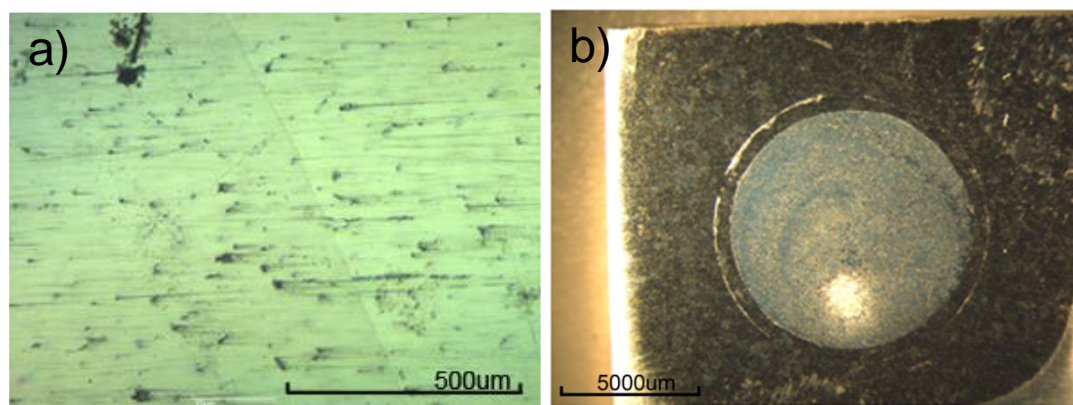


Figure 4.38 – Optical micrographs of AZ31 treated at 0.01 mA/cm^2 A) successfully formed film at 4.0x and B) film after breakdown at 0.63x.

Even without the catastrophic breakdown (where the cell potential decreases with time) films formed at the lower current densities (where the potential transient has a readily distinguishable slope change) are more visible on the AZ31 surface than those which form at higher current densities. Typically, the higher the current density applied, the less visible the film. However, catastrophic breakdown behaviour which results in the decrease of potential with a constant applied current density (corresponding to complete termination of film growth) is likely associated with a very large amount of current passing through a defect in the film. This will cause significant heating of the surrounding film and hence crystallisation. This severe crystallisation is likely the cause of the visible white ‘spot’ on the surface of the alloy (Figure 4.38 b).

Figure 4.39 a) shows the potential transient of AZ31 anodised in IL at 0.05 mAcm^{-2} wherein two considerable breakdown processes have occurred (indicated as 1 and 2). If the potential remains constant during the application of a constant current, film growth has been effectively terminated. When the potential decreases the film has been catastrophically damaged. Hence, the first breakdown in Figure 4.39 a) can be identified by the decrease in rate of film growth (dE/dt) near 9 V. However, the potential is not static and does actually continue to increase, albeit slowly, therefore, the film is continuing to grow. As anodising continues the rate of film growth begins to increase, which suggests the defects in the film, which resulted in the first breakdown, have been repaired. Shortly after this, a defect/s has formed in another section of the film which the system is unable to repair. This may be indicative of a larger defect in the film. As a result the potential peaks and begins to drastically decrease. The corresponding optical micrographs for these points of breakdown are shown in Figure 4.39 b)-d). Figure 4.39 b) shows the appearance of the surface corresponding to the first breakdown, whilst Figure 4.39 c) and d) indicate the appearance of the second breakdown.

Table 4.5 – Roughness values obtained through optical profilometry of sites of breakdown in Figure 4.35.

Current Treatments (mAcm^{-2})	Sa - Mean Roughness	Sz – Ten Point Height
	(μm)	(μm)
Control	0.159	2.81
Lesser breakdown	0.186	3.74
Catastrophic breakdown	0.220	4.37

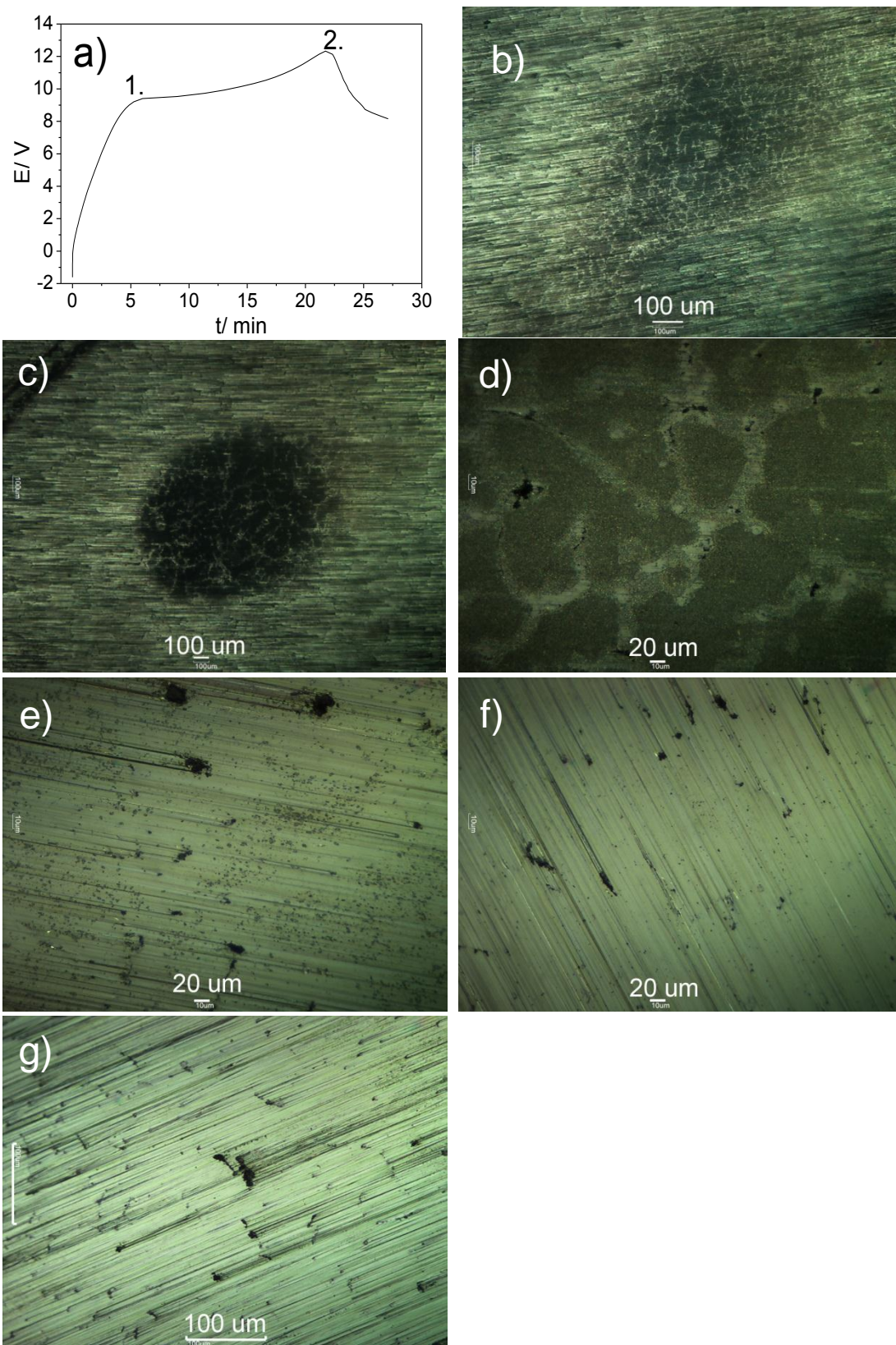


Figure 4.39 – Potential transient and optical micrographs of the three different breakdown processes on the surface of AZ31 anodised in IL at 0.05 mAcm^{-2} : a) Potential transient; b) minor breakdown spot (1); c) & d) catastrophic breakdown spot (2); e) small areas of breakdown over remaining surface; f) as polished AZ31; g) AZ31 anodised in IL at 0.5 mAcm^{-2} .

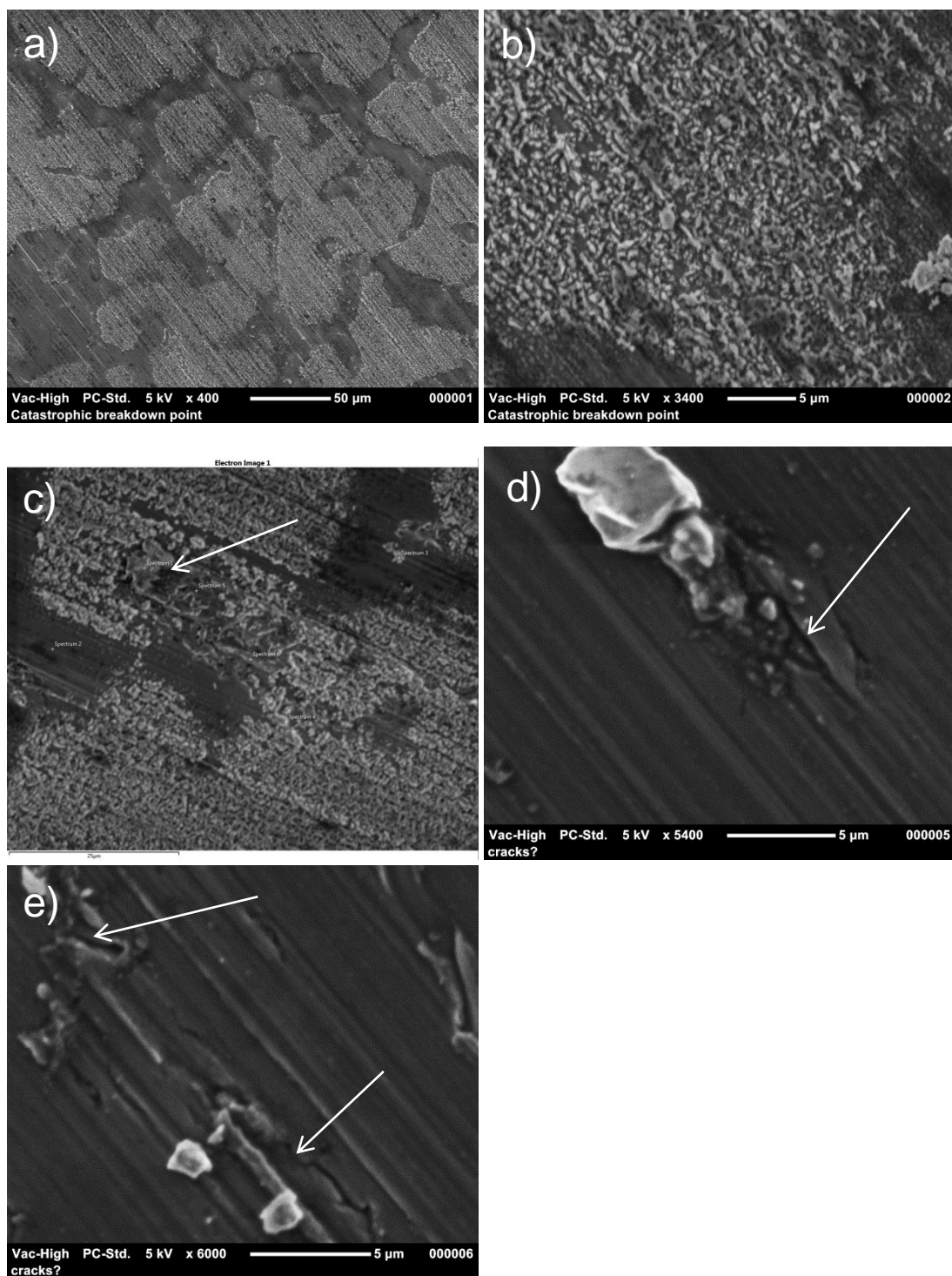


Figure 4.40 – Secondary electron micrographs at 5 keV of a)-b) catastrophic breakdown point; c) Possible rupture point which caused breakdown (arrow); d)-e) cracks (indicated by arrows) over the surface away from the large breakdown sites (corresponding to areas like that represented in Figure 4.39 e)).

Hence, it seems possible for films to repair and recover from breakdown processes. The formation of defects (associated with significant decrease in slope) does not stop the ongoing growth of the film. However, at least optically, no significant signs of the defects which caused these breakdowns could be identified. Outside of the localised breakdown the film is very transparent, as the grinding marks are visible, in contrast the point of serious breakdown can be clearly detected (Figure 4.39 c).

Table 4.5 presents the levels of roughness of these breakdown sites obtained from optical profilometry (not shown). Whilst the optical profilometry of these areas showed the surfaces to be very rough; however, there was no appreciable change in the Z height as opposed to the nearby β phase. As expected, the roughness is greatest at the larger, more severe, site of breakdown.

Figure 4.39 e is an optical image of the anodised surface away from the large breakdown points. In this image we can see a scattering of relatively large clusters over the surface, which likely correspond to small breakdown points. The formation of defects and cracks in the film is not isolated to the large breakdown processes indicated by points 1 and 2 (Figure 4.39 a). Figure 4.39 f) shows an optical image of 'as-polished' AZ31 (P4000 surface finish). Small spots can also be observed on as-polished AZ31; however these spots are much smaller and scarcer than those in Figure 4.39 e). Figure 4.39 g) is an optical image of AZ31 anodised in IL at 0.5 mAcm^{-2} where the film was formed without incident. Again only the small black spots present in the as-polished condition are still also visible here (upper right corner on Figure 4.39 g).

Figure 4.40 shows secondary electron images of the second breakdown region (Figure 4.40 a-c) and of defects over the film away from the large breakdown processes (Figure 4.40 d-e). SEM was performed as the morphology of the suspected defects could not be observed under optical illumination. Figure 4.40 a) and b) visually confirm the crystallisation of the film (due to breakdown) occurs over α phase and shows the morphology of these crystals as very small nodules (or 'hills'). Figure 4.40 c) shows a point in this region which looks like a rupture in the film, which may be the culprit of the catastrophic breakdown. EDS of these areas revealed large counts of both Mg and O, based on the proportion of these counts the crystals are likely MgO.

Figure 4.40 d) and e) show the appearance of scattered defects over the remaining surface. These images show quite clearly ruptures and cracks in the film. In addition, as with the crystallised areas in the severely broken down regions, MgO crystals (white deposits in electron images) were identified near these defects. These crystals likely correspond to the large spots imaged in Figure 4.40 e).

4.2.3.3.1 Summary of Film Defects

The visual information presented here suggests that the breakdown process of these films occurs due to cracks and defects formed in the film (due to internal stresses in the film), which lead to high localised current flow and crystallisation of the surrounding film [129, 131, 132]. The change in morphology of the film near the points of breakdown (and crystal nucleation) suggests crystallisation has occurred as a result of the defects. High magnification of the area of catastrophic breakdown shows a rough surface covering only the α phase. However, small defects are sustainable as the system is able to repair these sites with continued film growth.

4.2.3.4 Film Formation in Dilute IL Solution (ILAN)

Section 4.1.1 & 4.1.2 (Figure 4.3 & 4.9), presented CVs on AZ31 performed in a solution of IL diluted in acetonitrile. The behaviour was essentially the same over the 4.5 V electrochemical window as in the neat IL. In addition, the potential switching behaviour in Figure 4.8 also mimicked the behaviour in neat IL. Hence, it should be possible to form similar films using the IL in a dilute form. In addition, by using a dilute system, a higher current density can be applied, which may aid the formation of the film regarding the previously mentioned breakdown features.

Figure 4.41 shows a comparison between a surface treated at 0.05 mAcm^{-2} in neat IL and ILAN. Despite the significant dilution of the IL in acetonitrile (and hence large reduction in viscosity)

the time taken to reach 18 V in both cases is very similar. Based on these potential transients, the film formed in neat IL has undergone breakdown at approximately 5 V, which gets worse at approximately 15 V. On the other hand the potential transient for ILAN is considerably more linear. Since the concentration of each solution is the only real difference (granted, this affects the physical properties such as viscosity (lower) and conductivity (higher)) the observation of worse anodising properties for the neat IL may be due to the amount of active species available to react with the surface/ Mg^{2+} ions as it was mentioned previously that the incorporation of the anion results in a decreasing slope of the potential transient[133].

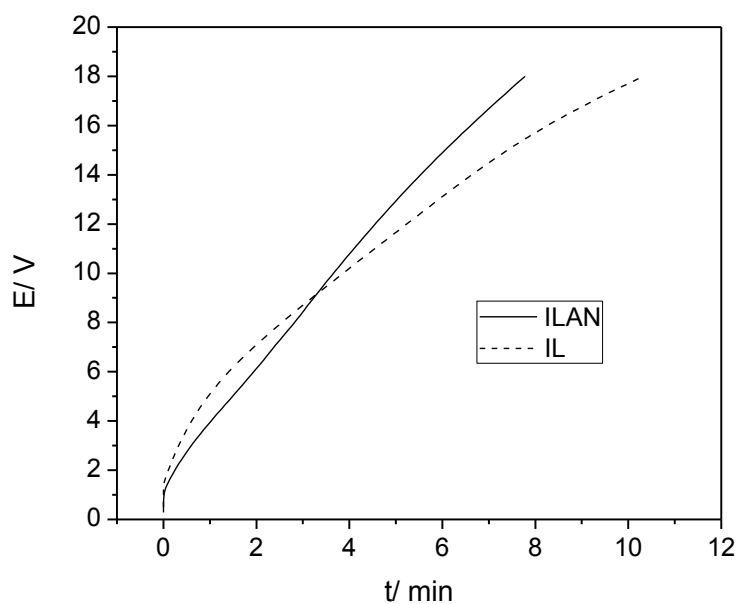


Figure 4.41 – Potential transients of AZ31 treated in $[P_{6,6,6,14}][C_8]_2PO_2$ and ILAN at 0.05 mAcm^{-2} to a final cell potential of 18 V.

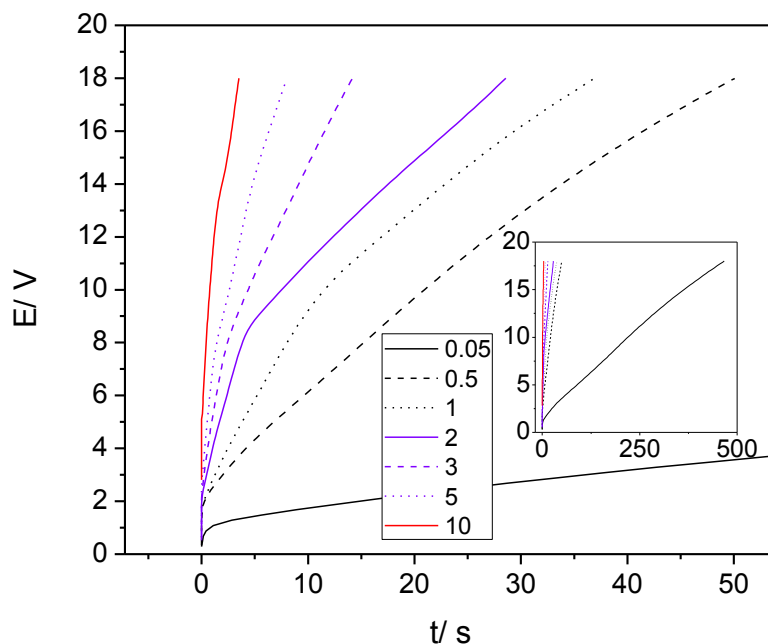


Figure 4.42 – Potential transients of AZ31 anodised to a final cell potential of 18 V in 0.1 M [P_{6,6,6,14}][(C₈)₂PO₂] in acetonitrile at various current densities. Inset is full view of the potential transient for 0.05 mAcm⁻² in comparison to the other applied current densities.

Figure 4.42 shows the potential transients from AZ31 anodised in ILAN at a range of different current densities between 0.05 and 10 mAcm⁻². Interestingly, the anodising efficiency for ILAN varies dramatically between low and high current densities. At 0.05 and 0.5 mAcm⁻² the potential transients are fairly linear. Strangely, as the current density is further increased the linear behaviour is disrupted. Poor behaviour (based on deviation from linearity of the potential transients) was recorded for current densities of 1-3 mAcm⁻², with only some slight improvement at 5 and 10 mAcm⁻². It may be possible that if the current density is too high current may be lost to side reactions such as oxygen generation[128]. However, it appears as though the best performance would come from the application of 0.05 or 0.5 mAcm⁻² (and possibly current densities in between).

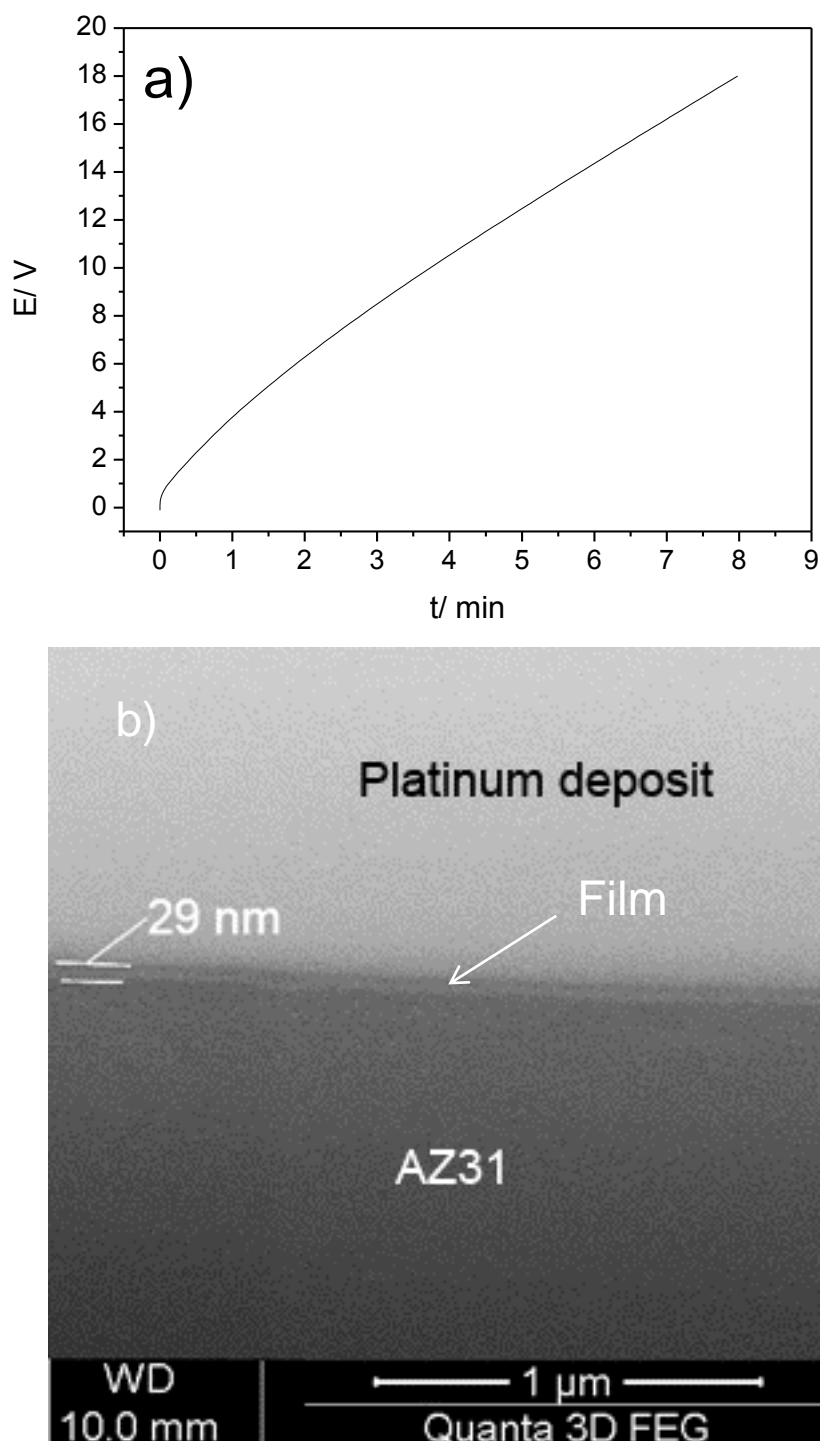


Figure 4.43 – a) Potential transient of AZ31 anodised at 0.07 mAcm⁻² to 18 V; b) FIB-SEM cross section of thin film (approx. 29 nm) formed in ILAN using a current density of 0.07 mAcm⁻². The film is less obvious than the film formed in neat IL. However it can be identified by the two thin dark lines above and below which signify interfaces between the Pt layer and the film, and the layer and the AZ31 alloy.

Figure 4.43 shows a FIB-SEM cross section on AZ31 anodised at 0.07 mAcm⁻². Typically the final cell potential corresponds to the final thickness of the film (assuming the increase in thickness is linear to increase in resistance). Hence, it is strange that the thickness of the film formed in ILAN under similar conditions to the neat IL formed film is considerably smaller than for neat IL. It may be that the films formed in the ILAN solution are more

compact/dense, allowing for comparable film resistance for a thinner film. This may be due to the effect of decreasing viscosity, which will result in increased conductivity and ion mobility in the solution.

4.2.3.5 Two-Step Process

A two-step, constant current – constant potential, anodising technique was also briefly investigated. Figure 4.44 shows the current vs. time curves of the four holding times after anodising at 0.05 mAcm^{-2} . These include 5, 15, 30 and 60 minutes at 18 V vs. Pt. In all cases the current density decays, however for shorter holding times the current density does not stabilise. The intention of this step is to have the current reduce to a value significantly lower than the current used to form the bulk of the film. By holding the final potential after constant current anodising step the thickness of the film should continue to grow as the current decay (at constant potential) is associated with anodic film growth.

Despite the current density decreasing the most for the longer exposure, the performance of the final film cannot be judged solely from these current profiles. This is especially so considering the rate of current decay in each test is not equal in each case. However, it is possible that this is due to batch differences. The surfaces held for 60 and 30 minutes were performed in a different IL batch than those at 15 and 5 minutes. Hence, potentiodynamic polarisation tests in 0.01 M NaCl solution were used to discriminate between the protection of these surface films (presented in section 4.4.2).

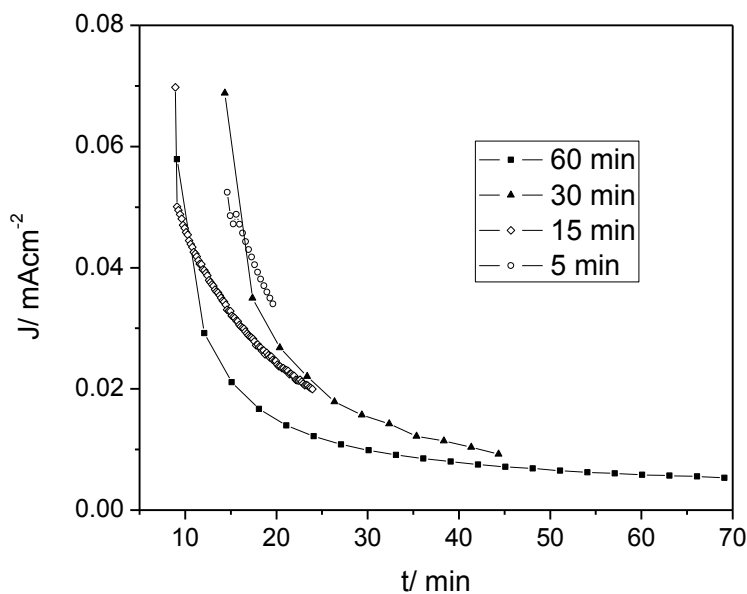


Figure 4.44 – Current decay during static application of 18 V after anodising at 0.05 mAcm^{-2} .

4.2.4 Section Key Points

From the results presented in this section, the following key points can be made:

- The IL film formed using a constant potential bias of 2.5 V vs. OCP for 4 hours led to a film 500 nm thick.
- The IL films formed using constant current densities to a final cell potential of 18 V were much thinner than the film formed at 2.5 V vs. OCP for 4 hours. The measured thicknesses were approximately 80 and 29 nm for films formed in neat IL and ILAN respectively.
- The application of higher constant potentials (3 V vs. Pt in this case) led to crystallisation of the film on AZ31.
- Field crystallisation at RT led to an inhomogeneous film whereas field crystallisation at 50°C led to a denser and more homogeneous film. Optical profilometry revealed these films to be highly porous.
- Anodic films formed in the potential range analysed deposited/grew only over the α phase of the microstructure.
- Films formed using constant current densities allowed for greater control over the films formed and films could be formed very quickly.
- The use of current densities of $\leq 0.01 \text{ mAcm}^{-2}$ resulted in frequent breakdown of the anodic film.
- Breakdown was attributed to the formation of cracks and ruptures in the anodic film, which may be the result of internal stresses in the films.
- The film surrounding defects appeared to crystallise, which is likely due to localised heating from increased current flow through these defects.
- Anodising to form an IL film was possible in a dilute solution of IL in acetonitrile (0.1 M –ILAN). Due to decreased viscosity, higher current densities could be used.

4.3 Corrosion Performance of Treated Specimens

4.3.1 Corrosion Performance of Field Crystallised Coatings on AZ31

Based on the surface profilometry presented in section 4.2.1.2.2, we know that the films are highly rough, porous and form preferentially over the α phase. Nevertheless, to test the corrosion performance a film formed at 3 V vs. Pt and 50°C for 48 hours along with a control surface (P4000 grit finish) were exposed to 5 μ L droplets of 0.01 M NaCl at 80% relative humidity (R.H) for 3 hours. Both surfaces were cleaned in a chromic acid solution prior to imaging to remove corrosion product.

The optical micrograph in Figure 4.45 presents the appearance of the treated surface after the 3 hour exposure. Immediately after exposure to the 0.01 M NaCl droplet the colouration of the film on the surface disappeared. The area to the right of the image has not been exposed to the droplet and hence the dark coloured film is still perfectly visible. However, the area to the left, which was exposed to the droplet, appears completely bare. This film appears to be permeable to the 0.01 M NaCl solution, which may be due to porosity (as shown previously), or that the film allows ion migration (e.g. it is conductive). As a result the film does not prevent migration of the corrosive Cl⁻ ions or water to the AZ31 surface, which leads to the same degree of corrosion as on the control surface.

The most severe corrosion appears to be localised near intermetallic particles in both the IL treated surface and the control. An example of this is shown in Figure 4.46. Through the aid of optical profilometry what initially appears to look like a pit in the optical micrograph is in fact a raised particle (Figure 4.46 b). These particles behave as cathodes in the microstructure, which results in microgalvanic corrosion and leads to dissolution of magnesium around the particle. This behaviour ultimately leads to undercutting of the particle, which eventually results in the formation of large pits like those in Figure 4.47 and 4.48 due to the particle falling out of the alloy. The particle in Figure 4.46 is likely a manganese (Mn) containing intermetallic particle (such as the one identified in Figure E.2 from EDS and SEM in Appendix E). Severe levels of corrosion occur outside of the cathodically protected area surrounding the particles. As seen from optical profilometry in Figure 4.46, the depth of this corrosion can be significant (6 μ m). The larger pits seen in Figure 4.47 and 4.48 are likely the result of undercutting of a similar particle.

In general, Mg-Al alloys do not corrode via the formation of deep pits. Instead shallow irregular pits nucleate in the α phase, which spread laterally and cover the whole surface[4, 41]. This effectively results in the formation of clusters of shallow pits over the surface. An example of this is shown in Figure 4.49 as well as optical profiles in Figure 4.50.

As expected given the observations of the nature of the field crystallised films in section 4.2.1.2, these surface films are not desirable for preventing corrosion on AZ31.

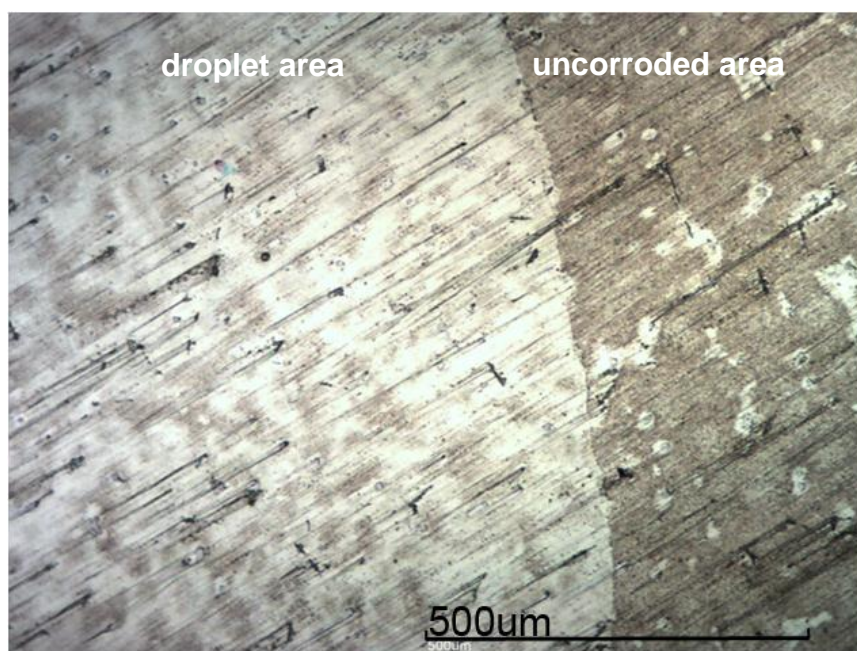


Figure 4.45 – Optical micrograph change in appearance of film formed at 3 V vs. Pt, 50°C for 48 hours on AZ31 after exposure to 5 μ L 0.01 M NaCl for 3 hours.

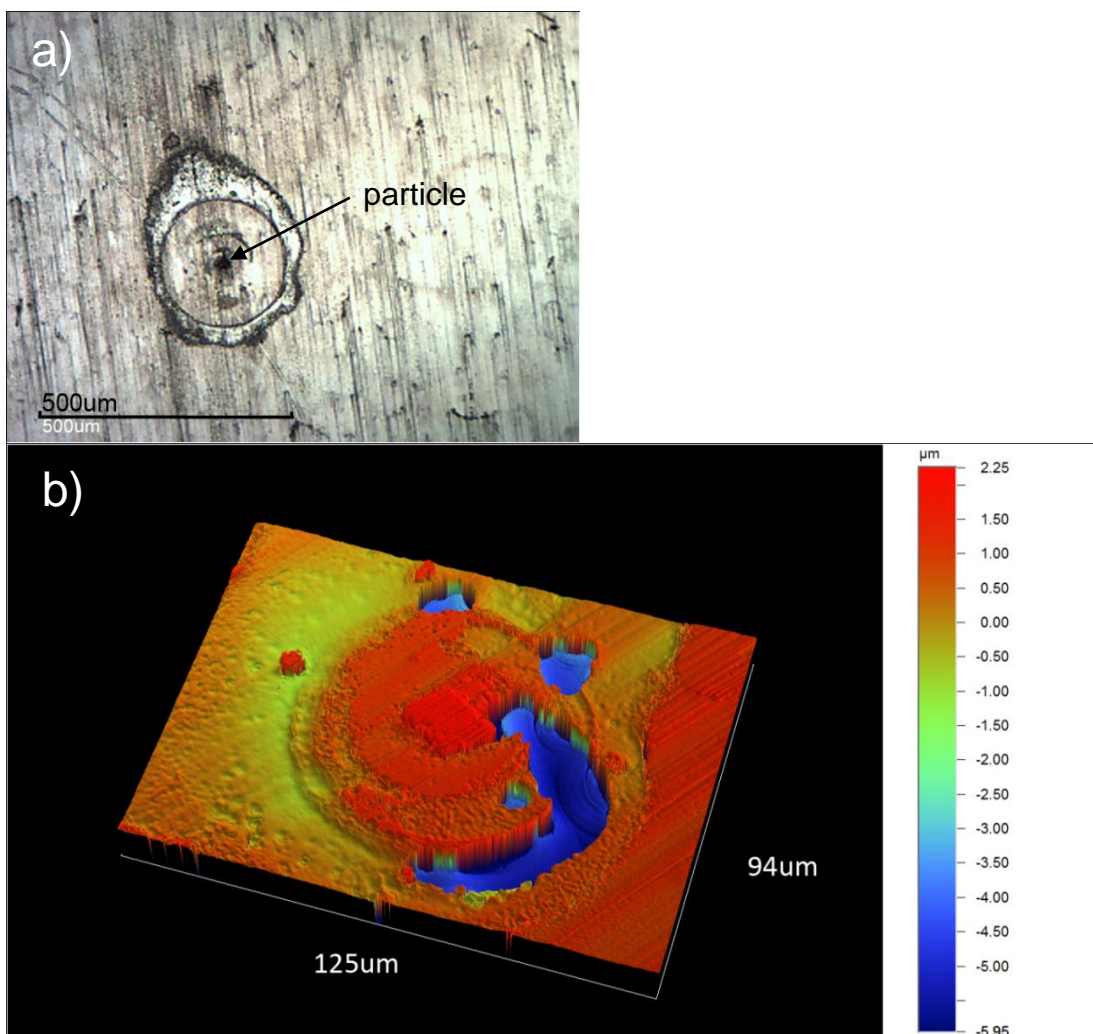


Figure 4.46 – Microgalvanic corrosion around a cathodic particle in the microstructure of AZ31 after exposure to 5 μL 0.01 M NaCl for 3 hours on a) AZ31 treated in IL at 3 V vs. Pt and 50°C for 48 hours: optical micrograph; b) AZ31 ground to a P4000 surface finish: optical profile.

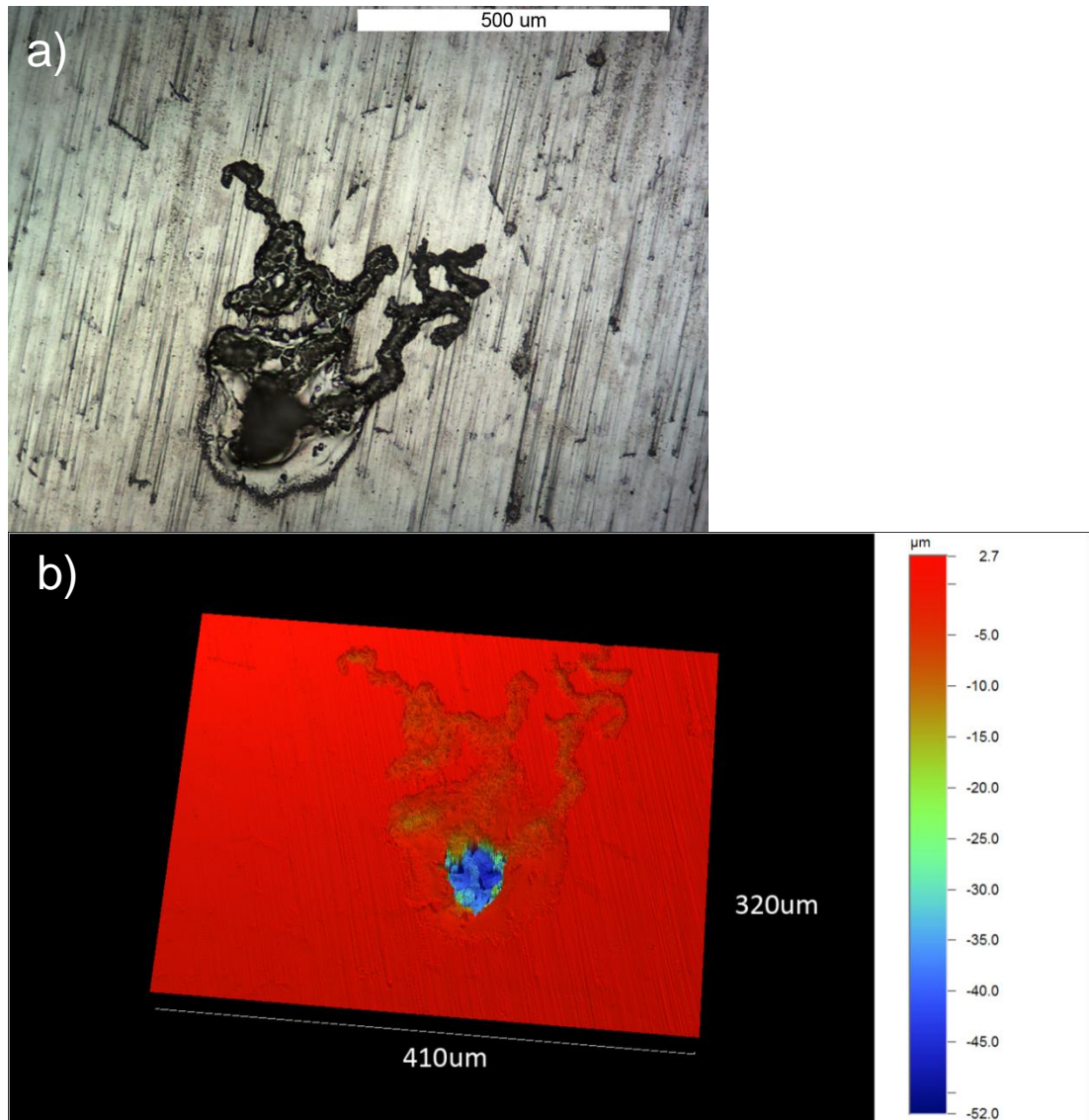


Figure 4.47 – Large pit likely formed from undercutting of a cathodic particle in the microstructure of AZ31 treated in IL at 3 V vs. Pt and 50°C for 48 hours, after exposure to 5 μL 0.01 M NaCl for 3 hours: a) optical micrograph; b) optical profile.

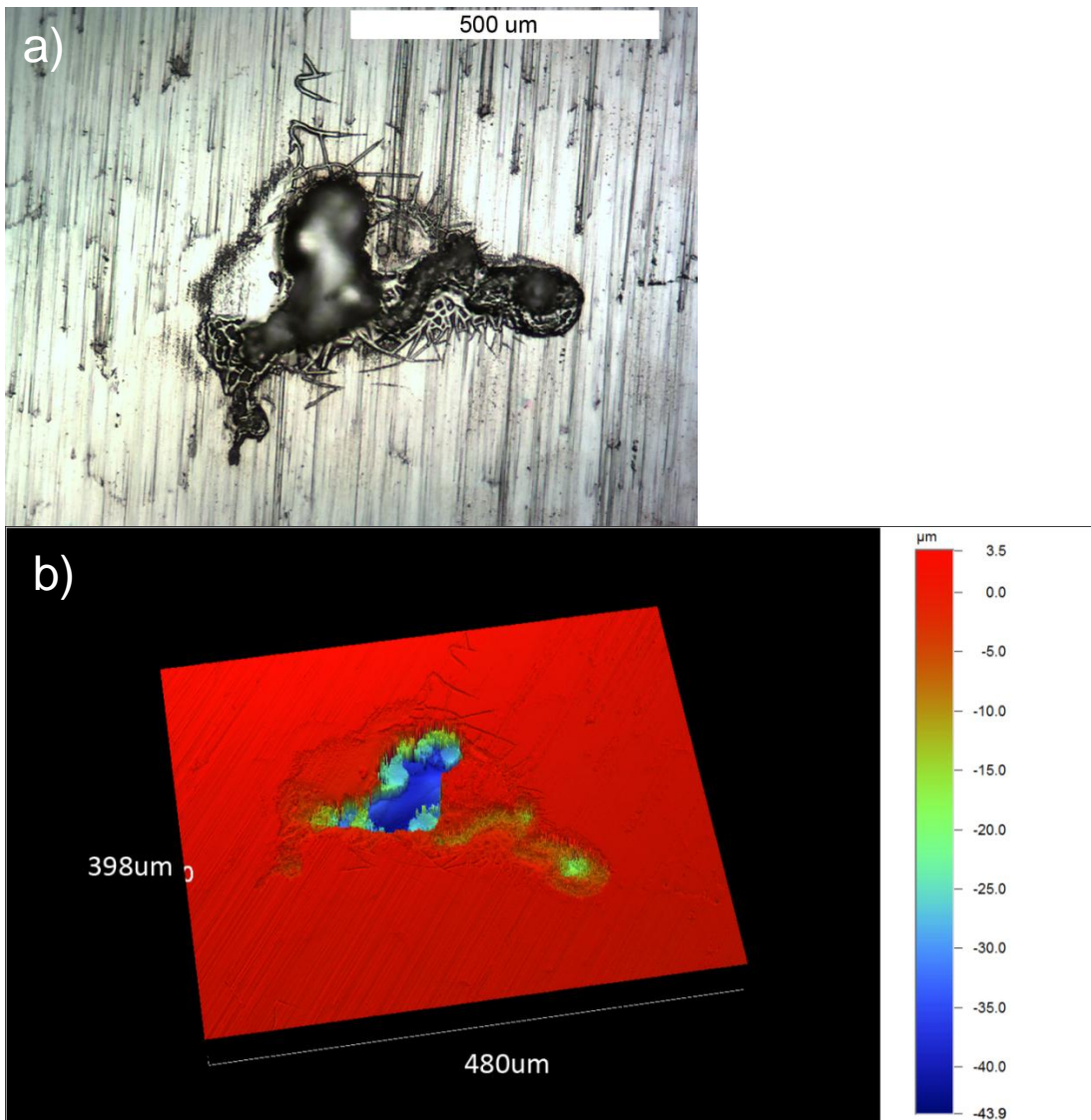


Figure 4.48 - Large pit likely formed from undercutting of a cathodic particle in the microstructure of AZ31 ground to a P4000 grit surface finish, after exposure to 5 μL 0.01 M NaCl for 3 hours: a) optical micrograph; b) optical profile.

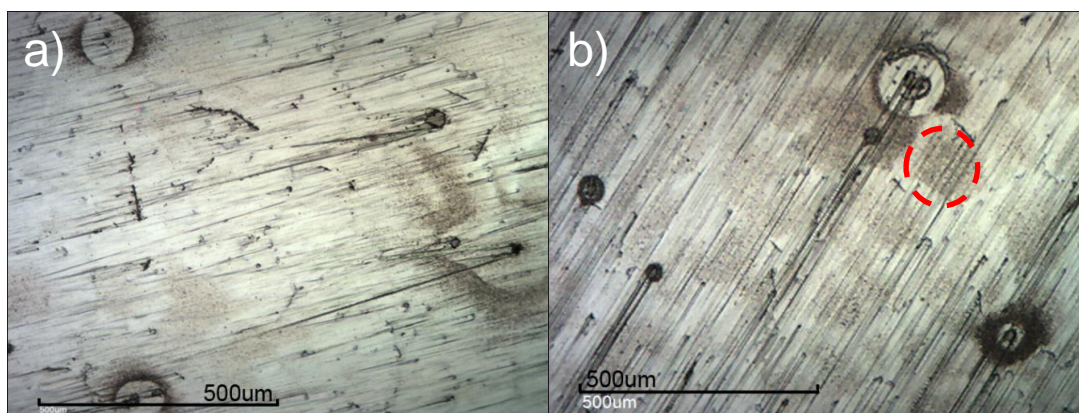


Figure 4.49 - Localised pitting corrosion over the α phase of AZ31 after exposure to 5 μL 0.01 M NaCl for 3 hours: a) AZ31 treated in IL at 3 V vs. Pt and 50°C for 48 hours; b) AZ31 ground to a P4000 grit surface finish. Pitting cluster on b) indicated by circle.

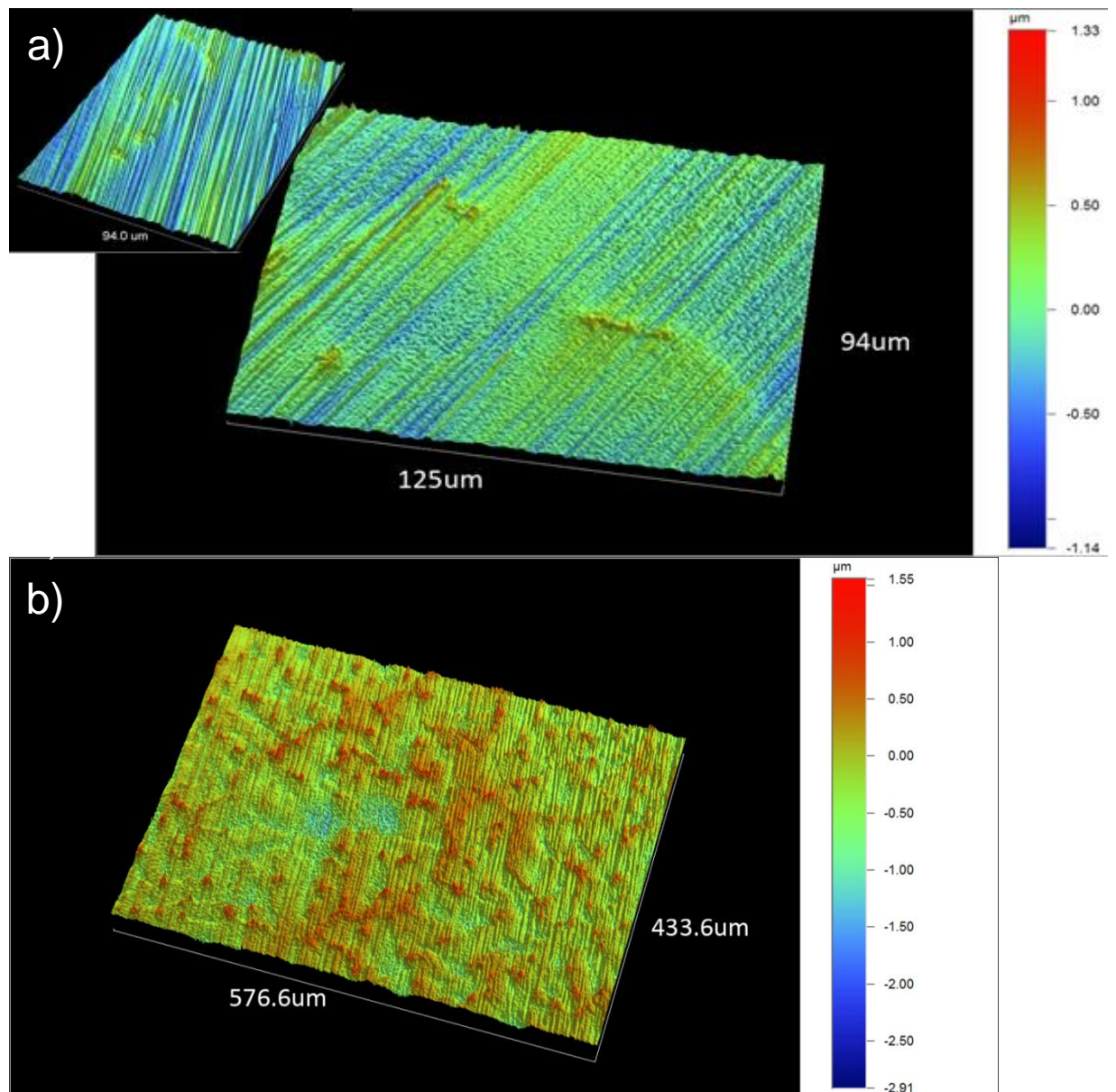


Figure 4.50 – Optical profilometry of Small surface pit clusters over α phase in a) control P4000 grit polished AZ31 exposed to 5 μL 0.01 M NaCl for 3 hours; b) AZ31 treated at 3 V vs. Pt and 50° C for 48 hours exposed to 5 μL 0.01 M NaCl for 3 hours. Inset in a) is ‘as-polished’ AZ31 (as seen in Figure 4.29) prior to corrosion: notice the lack of pitting ‘bumps’ over this surface.

4.3.2 Corrosion Behaviour of Films on Bare AZ31 via Potentiodynamic Polarisation

4.3.2.1 Potentiodynamic Polarisation

Potentiodynamic polarisation (PP) can be a powerful tool in differentiating the corrosion performance of different systems, particularly because it allows for the corrosion rate to be identified as well as any effects on the cathodic or anodic reactions. From the passivation behaviour observed with the cyclic voltammetry in section 4.1 and the uniform films observed from FIB-SEM in section 4.2 we expect that the application of the anodic film through constant potential or constant current will lead to improved corrosion performance of the AZ31 surfaces.

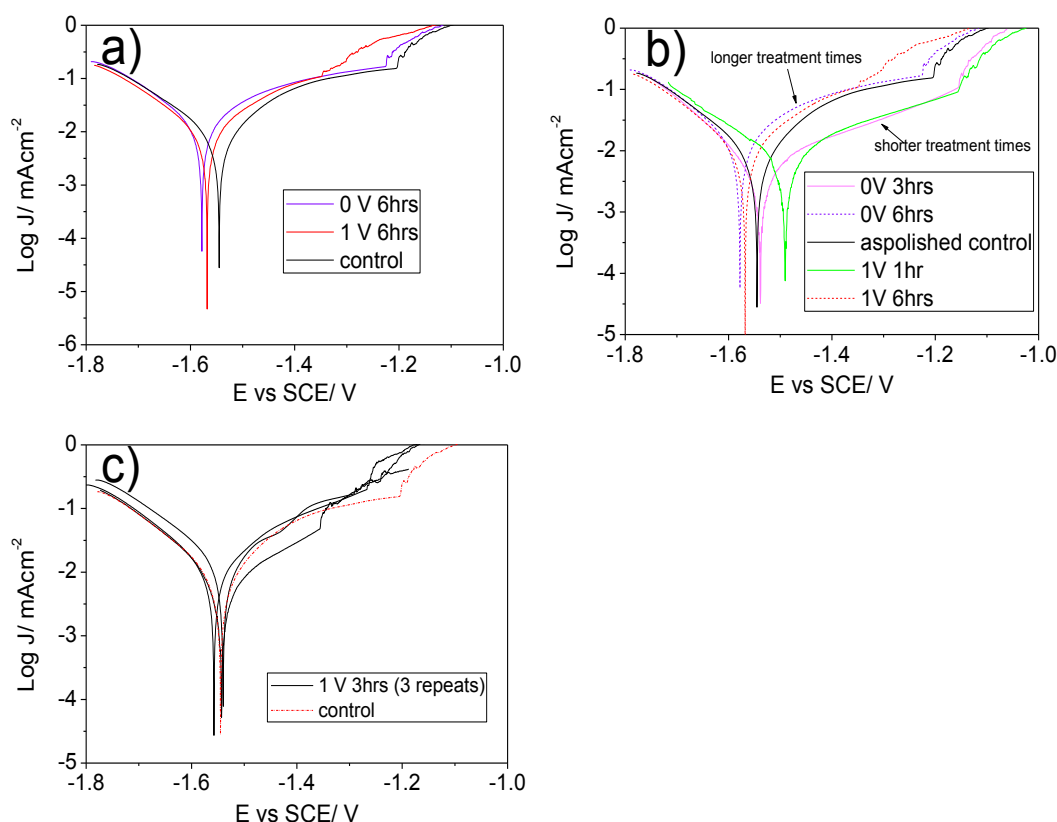


Figure 4.51 – PP curves obtained in 0.01 M NaCl for AZ31 treated at constant potentials of a) 0 V and 1 V vs. Pt for 6 hours; b) 0 V vs. Pt for 3 and 6 hours and 1 V vs. Pt for 1 and 6 hours; c) 1 V vs. Pt for 3 hours. The same control PP curve is used in a, b and c.

Figure 4.51 a) shows PP curves obtained from AZ31 treated for 6 hours at two potentials of 0 V (blue) and 1 V (red) vs. Pt in neutral 0.01 M NaCl. A curve from AZ31 ground to a P4000 grit surface finish is also included in black as a comparison. Firstly, it can be seen by the close positions of all three curves that the corrosion performance of AZ31 after coating is not noticeably improved. The application of a different potential appears to have no effect on the performance of the IL film. A previous study on IL film formation found that extended treatment times could lead to the formation of thick defective films[21], which may explain the similar corrosion performance to the control in Figure 4.51 a). Previously in section 4.2.2, Figure 4.19, the thickness of a film formed with a constant potential of 2.5 V vs. OCP (approx. 1V vs. Pt) for 4 hours was approximately 400-500 nm. This is very thick as previously measured IL film thicknesses have been ≤ 100 nm[11, 22]. Therefore shorter treatment times were also investigated.

Figure 4.51 b) shows PP curves obtained from AZ31 treated at 0 and 1 V vs. Pt for 3 and 1 hour respectively. In this figure the two treatments from 4.51 a) are also included (dashed red and purple lines). With the shorter treatment times the anodic reaction is reduced significantly and E_{corr} is shifted to more noble values, particularly for the 1 V, 1 hour treatment. In contrast, the cathodic reaction remains unchanged. Data presented previously (in section 4.2) showed preferential film deposition over the α phase as opposed to the β phase. Therefore, with the application of a good film we would expect the kinetics of the corrosion reaction involving the α phase (that is, Mg dissolution) to be reduced. In the case of the two shorter treatments the anodic reaction is reduced by more than half an order of magnitude. No change in the cathodic kinetics suggests that water is still able to migrate to cathodic sites, most likely due to the absence of film formation over the β phase and the apparent permeability of the film to water (Figure 4.45).

As with the two treatment potentials in Figure 4.51 a), the application of the two potentials at shorter times still resulted in very similar corrosion responses. Thus it appears that the duration of the application of the potential bias is more significant on the corrosion properties of the film (e.g. thickness and related internal stresses) than the specific potential itself. Whilst the anodic reaction in Figure 4.51 b) is reduced to the same amount for both of the shorter treatments, the significant anodic shift in E_{corr} is only witnessed for the shorter of the two treatments; that is, 1 hour rather than 3 hours (at 3 hours E_{corr} is the same as the control).

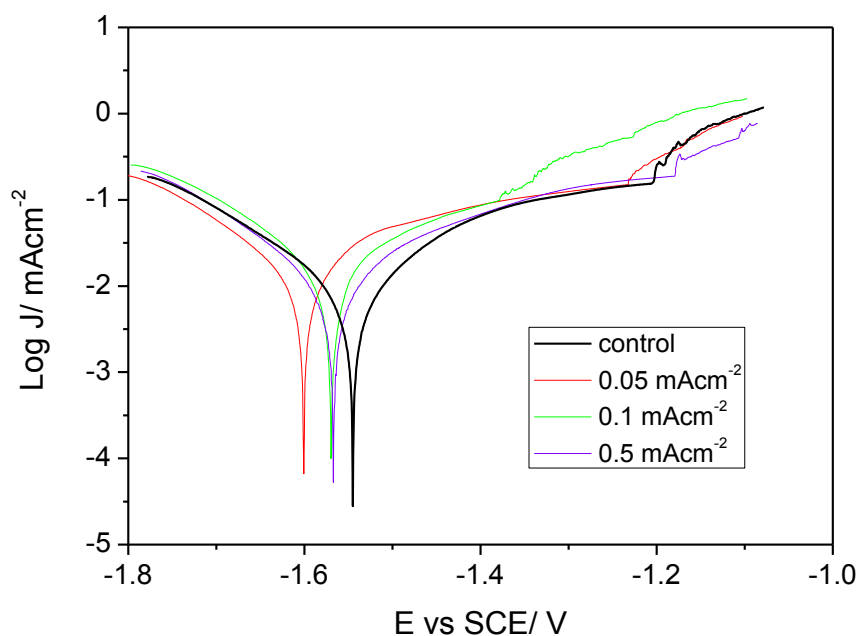


Figure 4.52 – PP curves obtained in 0.01 M NaCl for ‘as-polished’ AZ31 (P4000 grit finish) and AZ31 anodised in IL at 0.05, 0.1 and 0.5 mAcm⁻².

Figure 4.51 c) supports this notion. It presents three separate repeats of AZ31 in 0.01 M NaCl after treatment at 1 V vs. Pt for 3 hours (as the 1 V, 1 hour response is in Figure 4.51 b). Each repeat in Figure 4.51 c) shows an E_{corr} value either equal to or more cathodic than the control. One of the repeats displays the same action in reducing the anodic reaction on the AZ31 substrate, which shows a good film can still be formed up to 3 hours. However, even with the shorter treatment times of 3 hours and 1 hour it is difficult to form a consistently good film, as the scatter of results in Figure 4.51 suggests.

Figure 4.52 presents PP curves obtained in 0.01 M NaCl of AZ31 anodised in IL at current densities of 0.05, 0.1 and 0.5 mAcm^{-2} to a final cell potential of 18 V. Interestingly, with the application of a constant current density the corrosion performance appears to worsen in all cases. The degree of this effect increases with decreasing applied current density. It appears as though the longer the AZ31 surface is exposed to a potential bias or current, the film properties worsen. This is exhibited by the continual shift in E_{corr} to more cathodic values, increasing i_{corr} and increasing anodic reaction currents. We have shown the presence of a compact film of 80 nm thickness (Figure 4.36) formed at a current density of 0.05 mAcm^{-2} and we know passivation occurs on the AZ31 surface in the IL at anodic potentials (from CVs in section 4.1). However, rather than providing protection against the chloride solution the constant current method appears to have had the opposite effect. This may mean that (1) the film is not adherent in water (possible delamination), (2) has extensive porosity or (3) is permeable to water, possibly in a similar way to the field crystallised surface in section 4.3.1.

Whilst the longer treatment times at a constant potential can be related to ongoing thickening of the film (which may then crack from internal stress) the thickness of the films treated at constant current densities should be equal (due to the same cut-off potential). This change in performance between the different current densities may be due to the use of lower current densities resulting in film rupture due to the presence of greater internal film stresses[128, 132, 134].

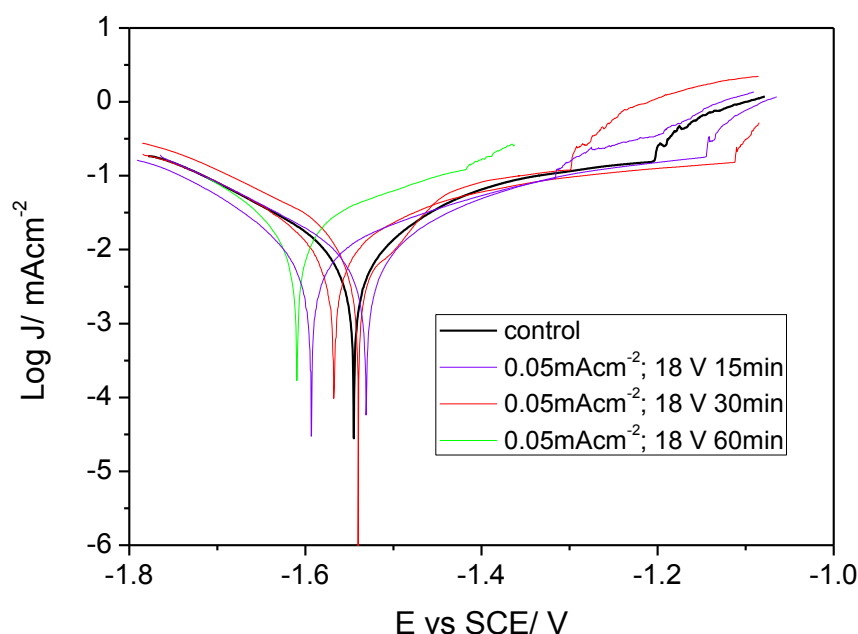


Figure 4.53 - PP curves obtained in 0.01 M NaCl for ‘as-polished’ AZ31 (P4000 grit finish) and AZ31 anodised in IL at 0.05 mAcm^{-2} followed by the static application of 18 V for 15, 30 and 60 minutes.

Figure 4.53 shows the PP curves obtained in 0.01 M NaCl of AZ31 anodised in IL at 0.05 mAcm^{-2} at three different static holding times of 18 V (15, 30 and 60 minutes). These holding steps were performed with the expectation to increase the thickness and resistivity of the film and hopefully the corrosion performance. With increasing holding time the performance of the film became worse. This again supports the idea that extensive exposure to bias potentials and currents is detrimental to the protectiveness of the film. In the case of Figure 4.53 the change in

performance to the holding time can be linked to the thickening of the film in the same manner as Figure 4.51. It is likely that the addition of a static holding time has increased the thickness and consequently ruptured or cracked the film due to increased internal stresses.

Figure 4.54 shows seven different current densities used to anodise AZ31 in the ILAN (0.1 M IL in acetonitrile) solution. Due to the low viscosity of the ILAN solution a greater range of current densities could be investigated, however the specific impact of these different current densities is not clear. These curves demonstrate that the formation of a consistently good film in this solution, with these conditions, is also difficult. Regardless of the different shifts in E_{corr} , the cathodic reaction is unchanged in all cases. On the other hand the anodic reaction deviates considerably. When the film is good the currents of the anodic reaction are reduced and when the film is defective the anodic currents are increased or equal to the control. This is consistent with the film forming over the α -phase.

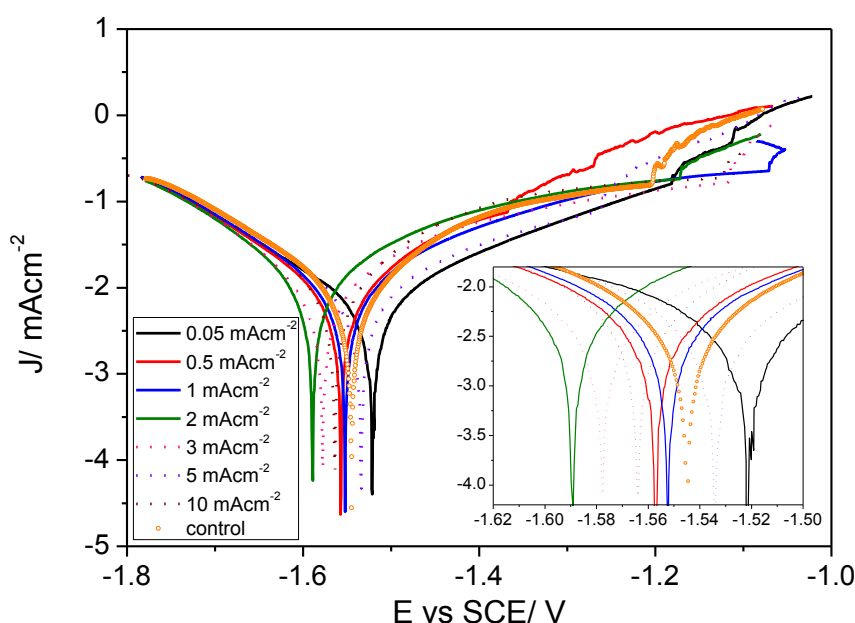


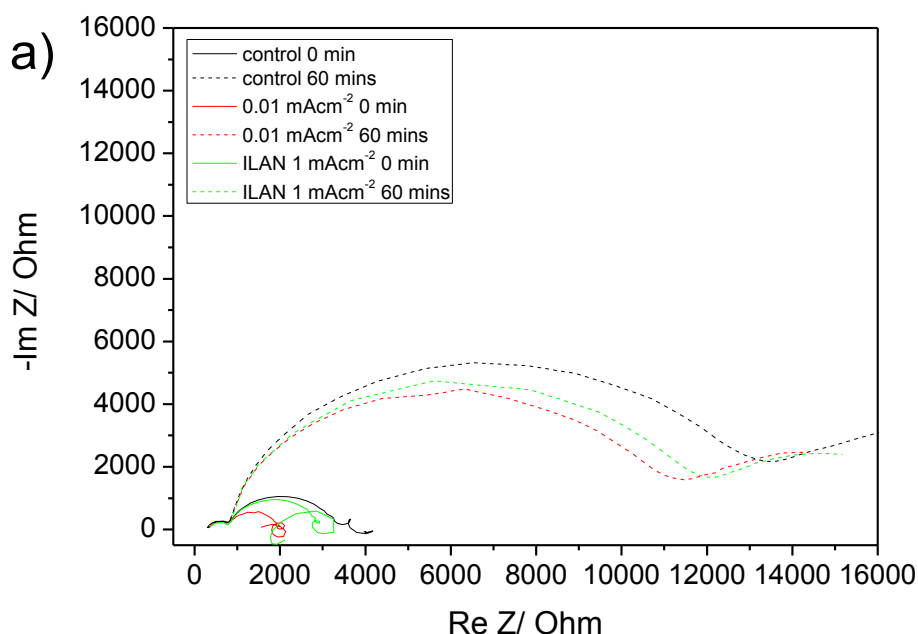
Figure 4.54 – PP curves obtained in 0.01 M NaCl for ‘as-polished’ AZ31 (P4000 grit finish) and AZ31 anodised in ILAN (0.1 M IL in acetonitrile) at 0.05, 0.5, 1, 2, 3, 5 and 10 mAcm⁻² to a final cell potential of 18 V.

4.3.2.2 EIS analysis of Film Behaviour of IL Films on As-Polished AZ31

Figure 4.55 a) shows Nyquist plots of the EIS behaviour of IL and ILAN films on ‘as-polished’ AZ31, whilst Figure 4.55 b) and c) show Bode plots of the EIS behaviour of the IL and ILAN films on ‘as-polished’ AZ31 of the impedance and phase angle respectively in corrosive 0.01 M NaCl solution. The response for all surfaces show one capacitive arc at high frequency, which is likely the response of the double layer, and another at mid-high frequency, which corresponds to charge transfer[135] at the substrate/solution interface through pores in the film. Hence this mid-frequency capacitive arc represents the corrosion behaviour of the surface film on the AZ31 surface[42]. At low frequency an inductance loop is also identified, which is typically associated with localised corrosion through defects in the film[136, 137].

Initially after immersion the resistance of the second capacitive arc is greater for the control than the two IL treated surfaces. This suggests that the film formed on the surface through anodising is less protective than the native film. This is supported by the phase angles in Figure 4.55 c). A greater phase angle corresponds to better film coverage or quality of a film, where -90° is a perfect, capacitive film[105]. The phase angles initially after immersion are -32.8° , -23.8° and -31.2° for the control, AZ31 anodised in IL at 0.1 mAcm^{-2} and AZ31 anodised in ILAN at 1 mAcm^{-2} respectively. They are low in all cases, but the values for the anodised films (particularly the 0.1 mAcm^{-2} anodised film) are lower than the control. Therefore the IL films on AZ31 either cover less of the surface than the native oxide film or the film leaches into (or is soluble in) the NaCl solution[106], which may explain the detrimental effect on corrosion observed in the PP curves (Figure 4.55).

After 60 minutes immersion the resistance of the film increases for all surfaces. This increase can be associated with the formation of a resistive layer of corrosion product on the surface. The deposition of the corrosion layer also results in improved surface coverage and hence the phase angles for the three surfaces also increase to -55.9° , -53.7° and 53.6° for the control, AZ31 anodised in IL at 0.1 mAcm^{-2} and AZ31 anodised in ILAN at 1 mAcm^{-2} respectively. In addition, the inductance loop is no longer present. Instead a 'tail' appears at low frequency, which looks similar to Warburg impedance. However, Warburg impedance has a 45° angle, which is greater than the angle of this tail and hence is likely another capacitive arc.



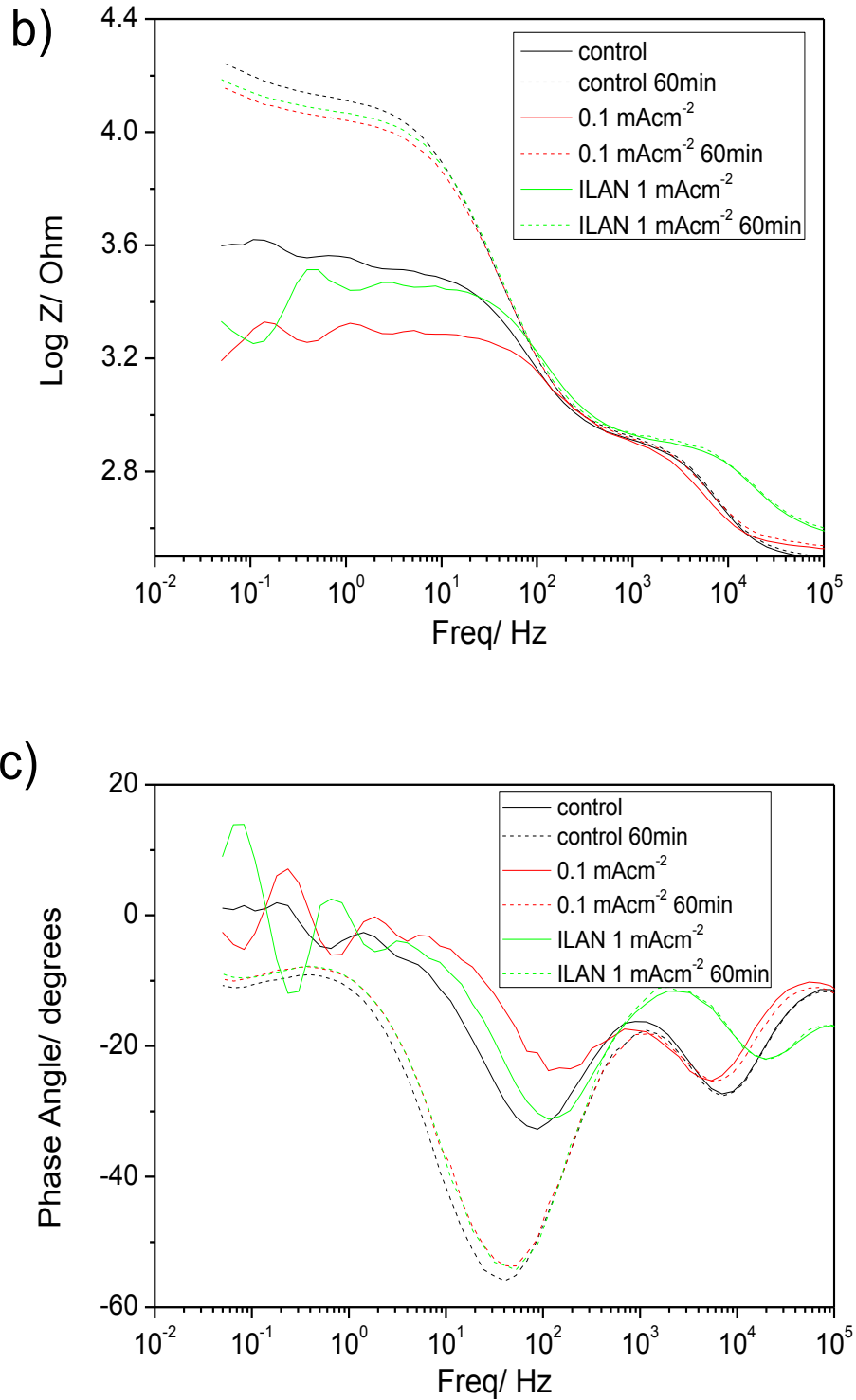


Figure 4.55 – EIS response of as-polished AZ31 (blank) and as-polished AZ31 after anodising in IL at 0.1 mAcm⁻² and ILAN at 1 mAcm⁻² in 0.01 M NaCl after 0 and 60 minutes immersion: a) Nyquist plot; b) Bode plot of impedance with frequency; c) Bode plot of phase angle with frequency.

4.3.3 The Effect of Surface Pre-Treatments on the Corrosion Behaviour of IL Treated AZ31 Surfaces

4.3.3.1 Surface Pre-treatment

Before metals are coated or anodised they often undergo a series of surface cleaning and etching/pickling steps[42]. This not only removes impurities from the surface (including the oxide/hydroxide film) but it can also form a precursor film that allows for greater adhesion of the coating/anodised layer to come. In all the work prior to this section the only step in surface preparation was through grinding of the AZ31 specimens to a P4000 grit finish followed by rinsing in acetone and drying under a nitrogen gas stream. From section 4.2 we know that the films formed using the IL (constant potential and current modes) result in preferential film growth over the α phase. The corrosion behaviour presented previously in section 4.3.2 showed that the films formed on bare AZ31 only affected the anodic reaction on the surface. In this section the electrochemical homogenisation of the surface by a pickling step to allow for greater deposition and coverage of the IL film is investigated.

Many of the solutions used to pickle magnesium alloys are not suitable. That is, they often contain chromates (which are toxic) or hydrofluoric acid (HF - which is extremely dangerous). Due to the preferential deposition over the α phase, finding a pickling solution which would be active on both phases was desired (as opposed to just the α phase). The acid mixture used was taken from Zhu *et. al*[138] and was used with and without an alkaline degreasing step in 1 M NaOH. The acid mixture of nitric (HNO₃) and phosphoric (H₃PO₄) acids were chosen as Zhu *et. al* reported the removal of the β phase as well as the α phase, leading to greater homogeneity of the surface[138]. It is hypothesised that the improved homogeneity will improve the formation of the IL film. In addition, the increased surface roughness due to the pickling attack should hopefully increase film adhesion.

Two pre-treatment techniques were trialled and are listed in Table 4.6.

Table 4.6 – solutions and technique used to pre-treat AZ31 prior to application of IL film formation processes.

Technique	Solutions	Procedure
1	30 mL/L HNO ₃ and 605 mL/L H ₃ PO ₄	60s immersion. Rinse with deionised water and dry under N ₂ stream.
2	1 M NaOH 30 mL/L HNO ₃ and 605 mL/L H ₃ PO ₄	30 s immersion in 1 M NaOH Rinse with deionised water and dry under N ₂ gas stream. 60s immersion in acid mixture. Rinse with deionised water and dry under N ₂ stream.

The degree of metal dissolution for the two pre-treatment techniques is shown via optical profilometry in Figure 4.56 a) and b) for technique 1 and 2, in Table 4.6, respectively. Depths of approximately 7.56 and 3.60 μm were removed from the AZ31 surfaces for technique 1 and 2 respectively. A 30 s immersion in NaOH (alone) increased the weight of the AZ31 substrate by 0.03%, the 60 s immersion in the acid mixture decreased the weight by 0.94% and the combined weight loss after both processes performed together was 0.90%. Nwaogu *et. al* found that a minimum depth of 5 μm of alloy should be removed after pickling to ensure sufficiently good corrosion performance by the appropriate removal of surface impurities[42]. The 60s acid pickle has reached this requirement, however the 30s immersion in NaOH limits the pickled depth to

only 3.6 μm , which means that longer immersion in the acid mixture is probably required. If the results of the study by Nwaogu *et. al* are consistent with these AZ31 surfaces we would expect that the corrosion performance would be made worse by the addition of this step.

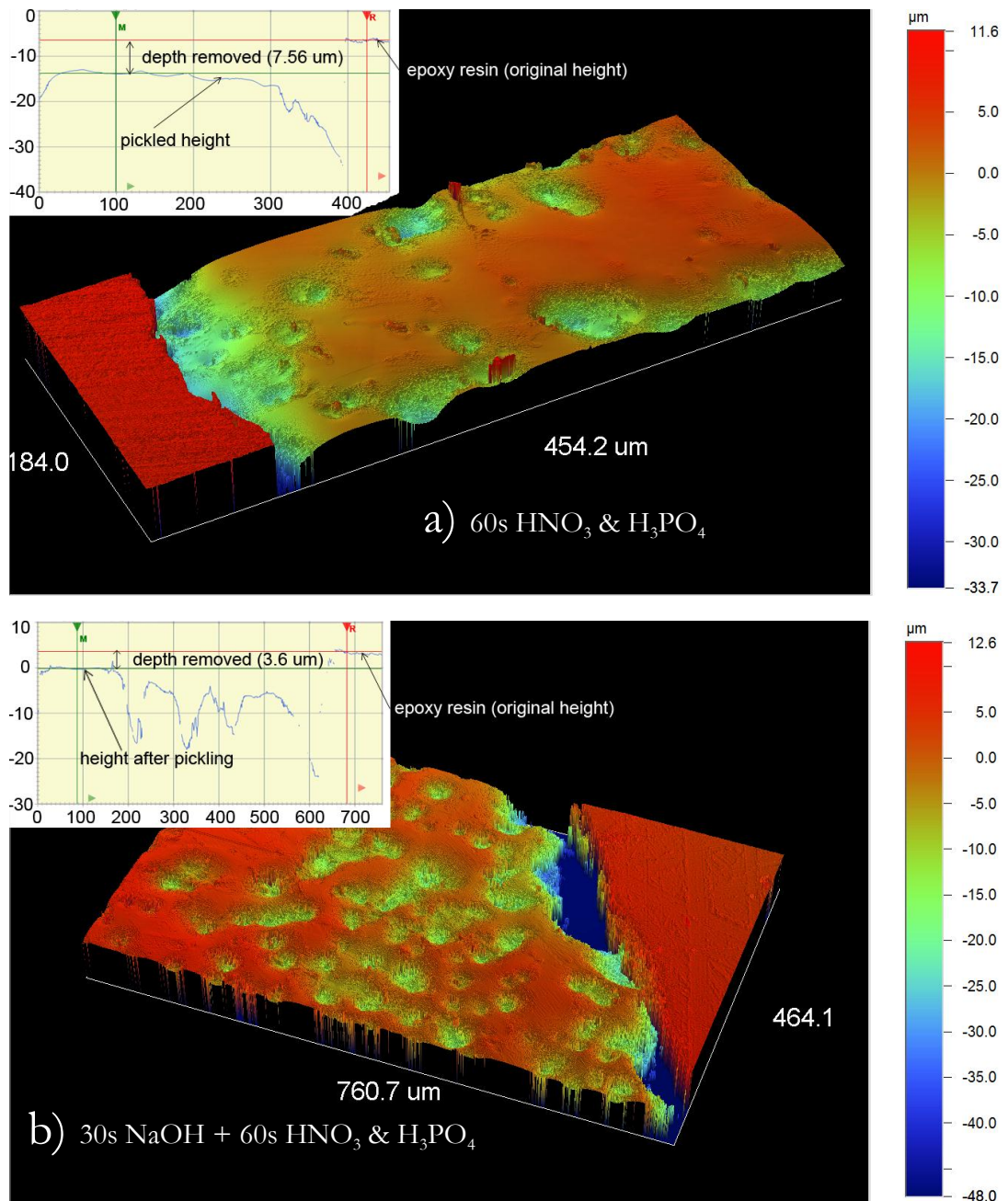


Figure 4.56 – Optical profilometry of AZ31 surfaces after immersion in a) HNO_3 & H_3PO_4 for 60s and b) NaOH for 30s followed by HNO_3 & H_3PO_4 for 60s. Units of the inset are μm .

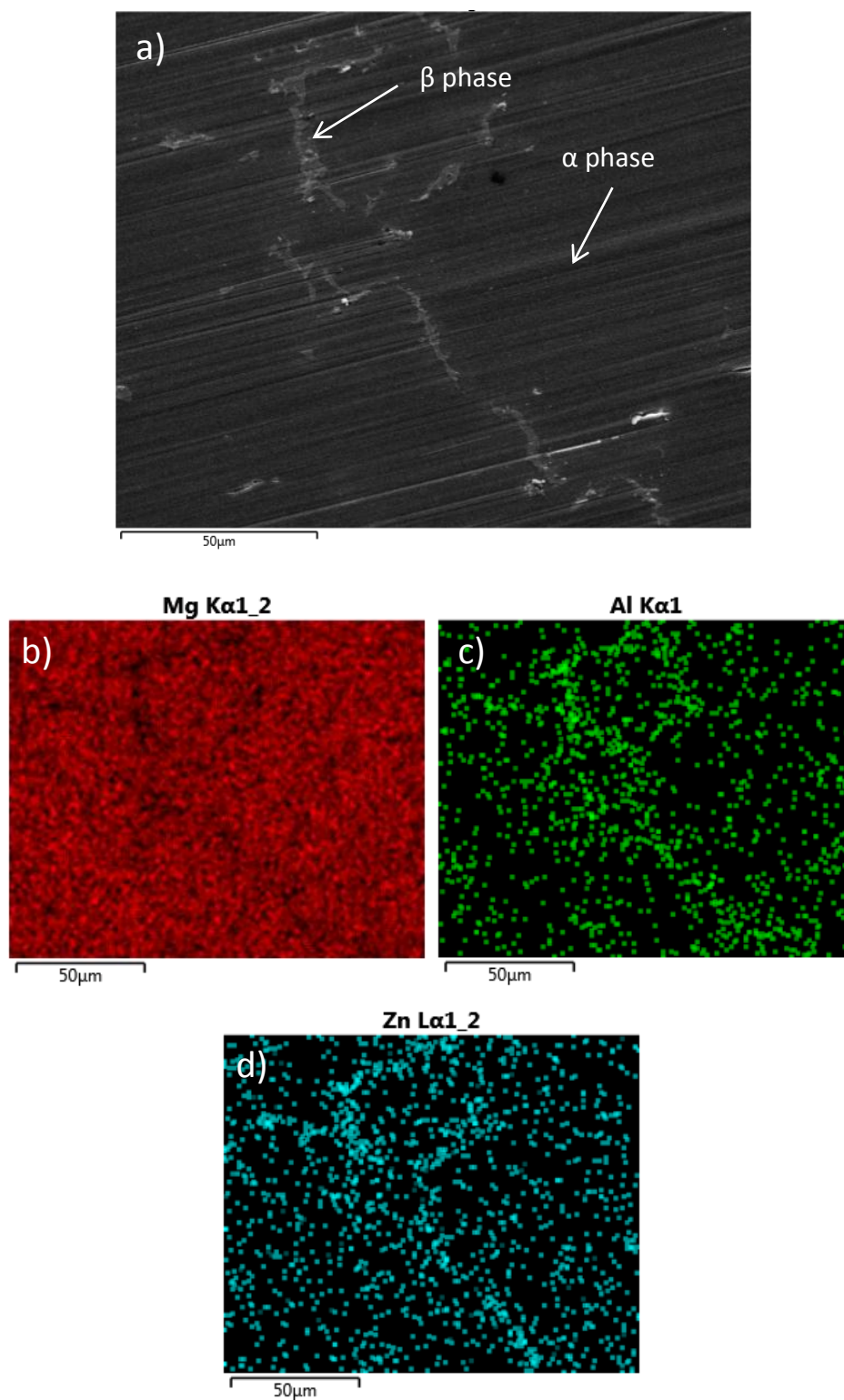


Figure 4.57 – AZ31 ‘as-polished’ to a P4000 grit surface finish a) SEM image; b) EDS map of Mg; c) EDS map of Al; d) EDS map of Zn. The EDS maps were obtained over the area shown in a).

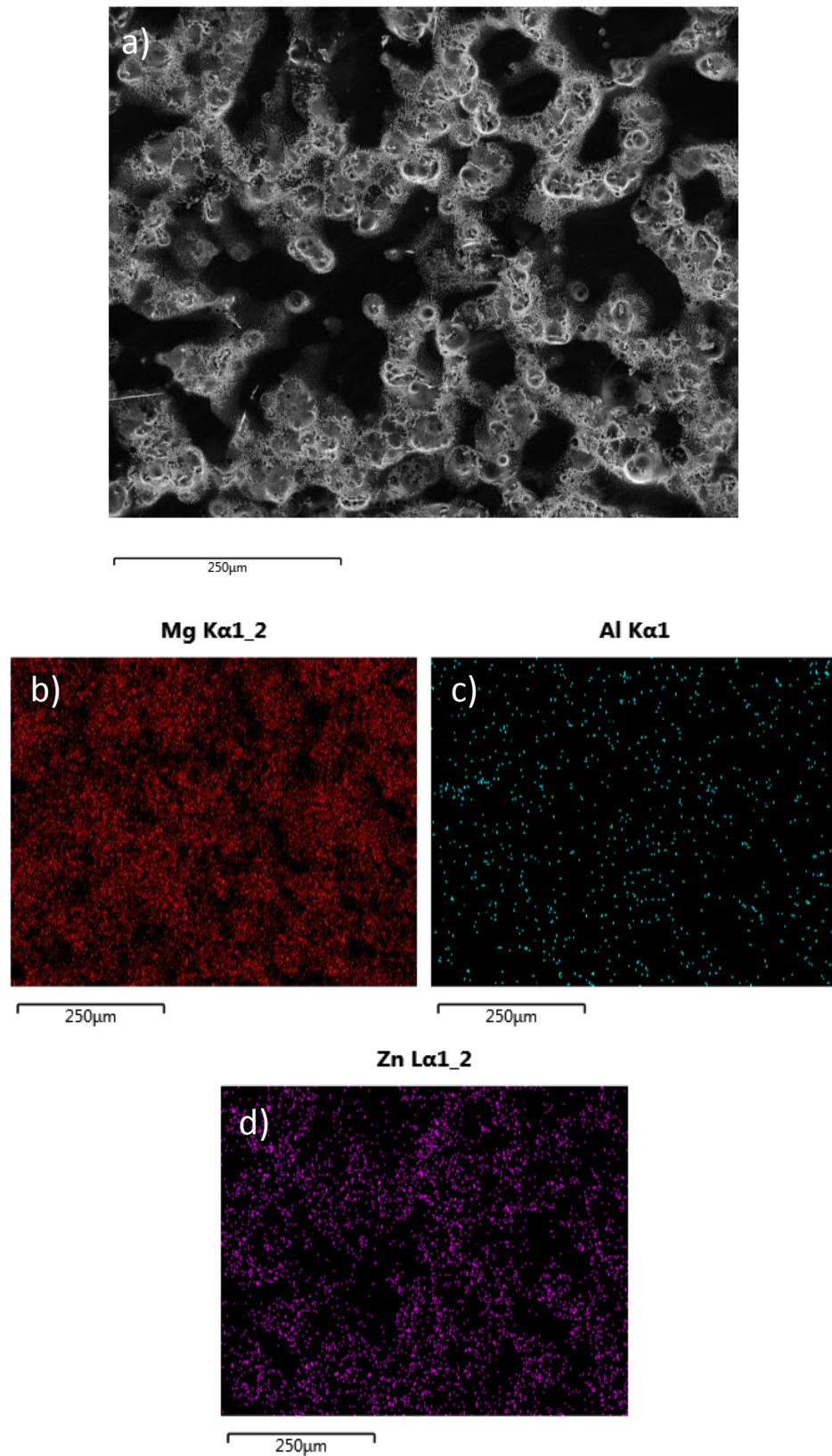


Figure 4.58 - AZ31 pickled in a mixture of HNO_3 and H_3PO_4 for 60 seconds a) SEM image; b) EDS map of Mg; c) EDS map of Al; d) EDS map of Zn. The EDS maps were obtained over the area shown in a).

Figures 4.57 and 4.58 compare the appearance of the surface and 2D elemental distribution before and after acid pickling of the surface for 60 seconds, using SEM (Scanning Electron Microscopy) and EDS (Energy Dispersive X-Ray Spectroscopy). Prior to pickling (Figure 4.57)

the microstructure is primarily comprised of the α matrix phase and the Al rich β phase at the grain boundaries. Al and Zn are also present in solid solution within the α phase. Prior to pickling, the Al content throughout the microstructure is high. Figure 4.58 shows the appearance of the surface after 60 seconds immersion in the acid mixture. The depressed area (or pitted area) is primarily Mg and the raised area is primarily Zn. In comparison to Figure 4.57 the Al content is significantly reduced after pickling and there is a significant redistribution of Zn particles uniformly over the microstructure.

Figure 4.59 compares the corrosion performance of the acid pickled surfaces with ‘as-polished’ AZ31. The pickling of the surface has dramatically shifted the potential of E_{corr} to more anodic and noble values, taking it from approximately -1557 mV to -1283 mV. This accounts for an anodic shift of almost 300 mV. In addition, the anodic current is significantly reduced (for the 60s acid pickle at least), by over an order of magnitude. On the other hand, the cathodic current is significantly increased by an order of magnitude for both pre-treatments. Therefore, the changes to the surface from the pickling process accelerate the cathodic reaction, but decrease the anodic reaction. Similar corrosion behaviour was reported by Orlov *et al.* [139] on magnesium alloy ZK60. They attributed this behaviour (increased cathodic reaction, decreased anodic reaction) with redistribution or re-solutionising of significant cathodic Zn particles. The Zn maps in Figure 4.57 and 4.58 show a considerable redistribution of the Zn particles after pickling. As Zn is a more cathodic element than Mg, the large presence of this element on the surface is likely responsible for the 300 mV shift in E_{corr} as well as the increased cathodic activity.

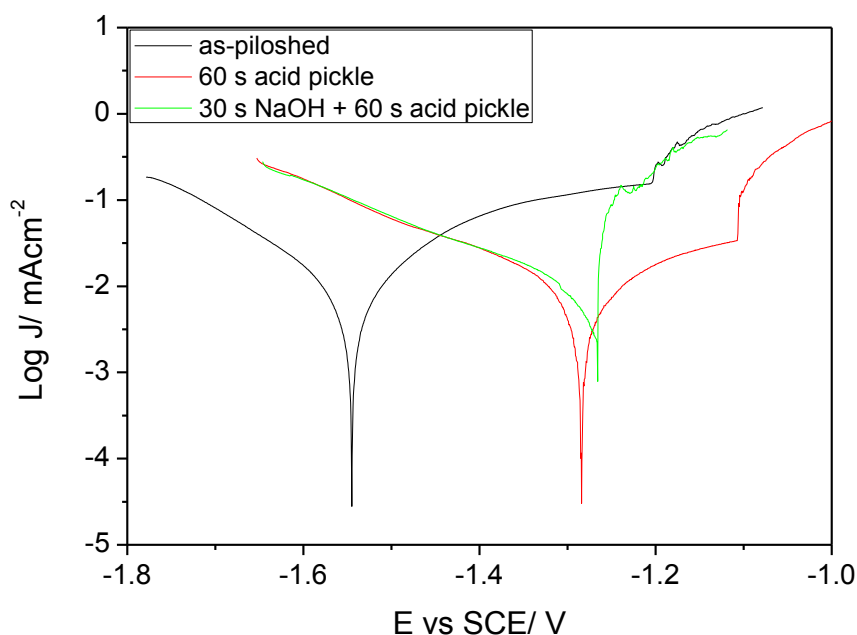


Figure 4.59 - PP curves obtained in 0.01 M NaCl for a) ‘as-polished’ AZ31 (P4000 grit finish) and AZ31 anodised in IL at 0.05 mAcm⁻²; 18V 15min, and 0.1 mAcm⁻²; b) AZ31 immersed in a mixture of HNO₃ and H₃PO₄ for 60s (technique 1 – Table 4.10) blank and anodised in IL at 0.05 mAcm⁻²; 18V 15min, and 0.1 mAcm⁻².

Interestingly, the corrosion performance of the pre-treatment including a 30s NaOH immersion is worse than without and also worse than the ‘as-polished’ AZ31 surface. The shift in E_{corr} is the same as with the acid pickle alone, however pitting is initialised immediately from E_{corr} . This suggests that whilst the surface modification is essentially the same, the phosphate film on the surface (due to reaction is phosphoric acid) may be defective.

Figure 4.60 compares the impedance responses for bare ‘as-polished’ AZ31 (black), acid pickled AZ31 (60s in HNO_3 & H_3PO_4 - red) and base- acid pre-treated AZ31 (30s NaOH + HNO_3 & H_3PO_4 – green) in 0.01 M NaCl at neutral pH. The response for all surfaces show one capacitive arc at high frequency, which corresponds to the double layer, and another at mid-high frequency, which corresponds to the surface film. For the acid and base-acid pre-treated surfaces a low frequency inductance loop is also identified, which is typically associated with localised corrosion through defects in the film[136, 137].

Immediately after immersion the impedance of second (mid freq.) capacitive arc of the three surfaces are almost equal. This suggests that the thin magnesium phosphate film which forms due to pickling[138] and the native oxide film on AZ31 are similarly resistive. After 60 minutes the resistance of the films on the three surfaces increase, with the greatest increase for ‘as-polished’ AZ31. This increase in resistance can be associated with the build-up of corrosion product on the surface ($\text{Mg}(\text{OH})_2$), which provides a resistive barrier to further corrosion[42]. Therefore while the films formed on the pre-treated surfaces are defective (based on inductance loop), they still manage to protect against corrosion better than a P4000 grit ‘as-polished’ surface finish, which is consistent with the PP data in Figure 4.59.

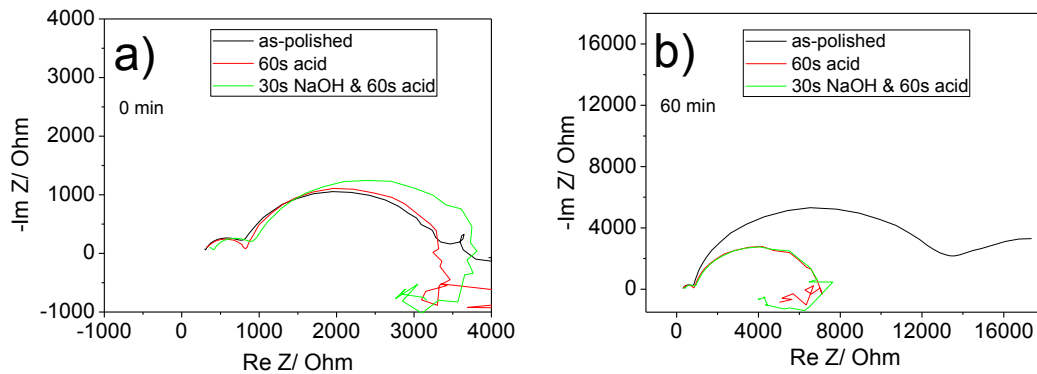


Figure 4.60 – Electrochemical impedance spectroscopy of as-polished AZ31, AZ31 after 60s immersion in a mixture of HNO_3 & H_3PO_4 and AZ31 after 30s immersion in NaOH and 60s in a mixture of HNO_3 & H_3PO_4 : a) 0 minutes after immersion in 0.01 M NaCl; b) 60 minutes after immersion in 0.01 M NaCl.

Figure 4.61 a) and b) show the equivalent circuits used to fit AZ31 in the ‘as-polished’ condition. Due to the noisy behaviour at low frequency at 0 minutes, Figure 4.58 a) was used to fit only the two high frequency arcs. Each capacitive arc can be represented by a constant phase element (CPE or Q) and resistor (R) in parallel, which are placed in series with each other. The solution resistance is expressed by R_s , the double layer resistance by R_{dl} and double layer capacitance by the constant phase element Q_{dl} . Similarly, the surface film/charge transfer resistance and capacitance are represented by R_t and Q_t respectively. Figure 4.61 b) was used to fit the ‘as-polished’ surface at 20-60 minutes due to the appearance on a third capacitive arc. This arc has been associated with pores in the corrosion product, where R_{pore} and Q_{pore} are the resistance and constant phase element of the pores respectively. Figure 4.61 c) shows the equivalent circuit for the acid pre-treated AZ31 surfaces. The equivalent circuit is effectively the same as the circuit in Figure 4.61 b) but with the addition an element, L, to account for the inductive behaviour. Inductive behaviour in an EIS response is characterised by the response entering the fourth quadrant when plotted in Nyquist form. The cause of inductive behaviour in EIS is a controversial topic. One possible cause is desorption or adsorption of a charged species near the free corrosion potential[102, 107]. In the case of magnesium alloys, the adsorption process has been attributed to accumulation of $\text{Mg}(\text{OH})^+$ and $\text{Mg}(\text{OH})_2$ on the

surface[107] and to film thinning with chloride (Cl^-) adsorption[108]. This adsorption can be linked to the initiation of localised corrosion in the form of pitting[42, 109-111]. Hence, the new components in this circuit include the inductance element (L) and the resistance through the defects (R_3).

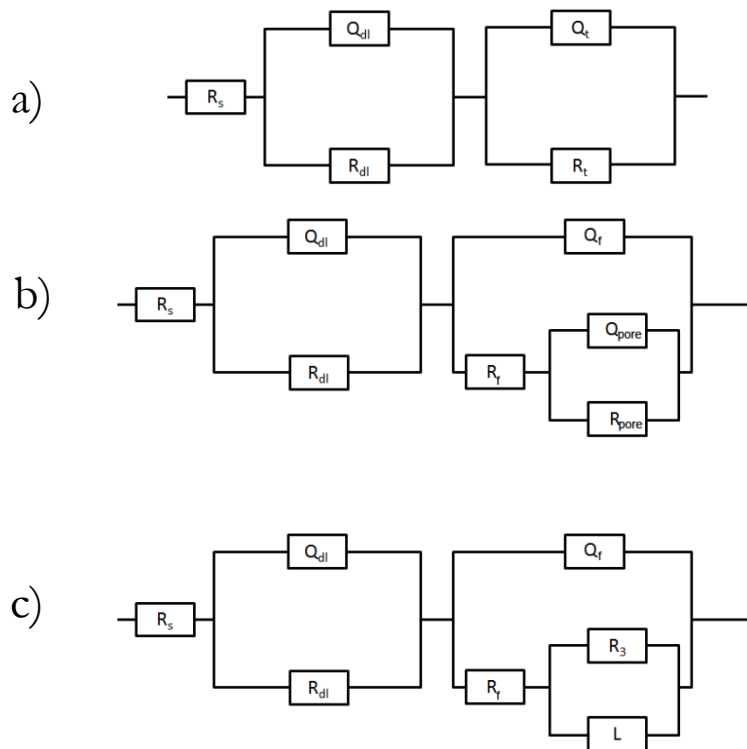


Figure 4.61 – Proposed equivalent circuits for a) as polished AZ31 immediately after immersion in 0.01 M NaCl; b) as polished AZ31 60 minutes after immersion in 0.01 M NaCl; c) acid and base treated AZ31 immersed in 0.01 M NaCl. R_s = solution resistance; Q_{dl} = double layer capacitance; R_{dl} = double layer resistance; Q_f/C_f = film capacitance; R_t = film resistance/charge transfer resistance; R_3 = resistance through film defects; L = inductance.

Table 4.7 – Film resistance and capacitance obtained from fitting of equivalent circuits. The qualities of the fits for these models are presented in Appendix D. Capacitance was calculated from resistance using an online calculator[140].

Surface type	Immersion time	$R_t (\Omega \cdot \text{cm}^2)$	$C_f (\mu\text{F} \cdot \text{cm}^{-2})$
As-polished	0 min	637	0.296
	20 min	1080	0.290
	40 min	2128	6.88
	60 min	2905	6.56
60s acid pickle	0 min	487	24.88
	20 min	781	20.0
	40 min	676	20.3
	60 min	905	22.3
30s NaOH + 60s acid pickle	0 min	280	20.8
	20 min	667	22.0
	40 min	471	24.2
	60min	877	25.5

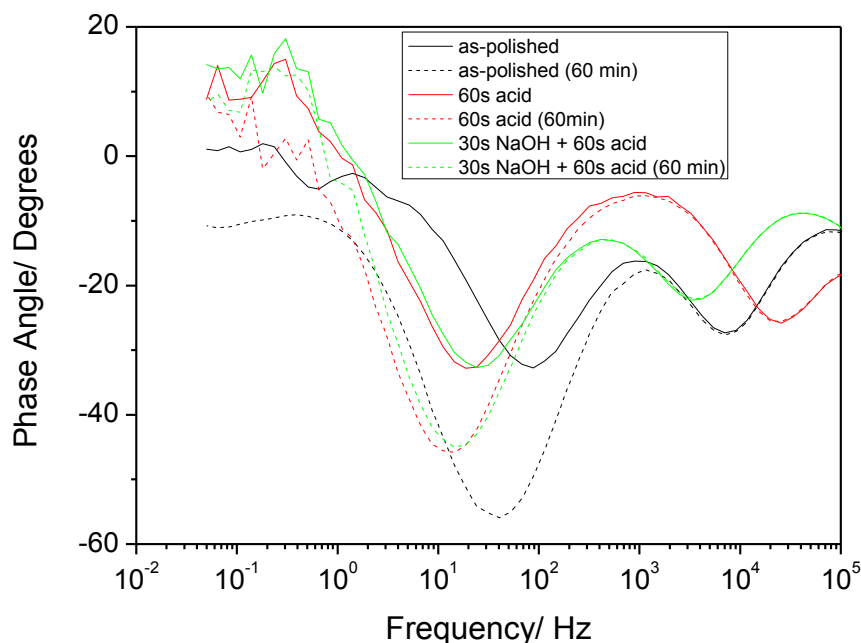


Figure 4.62 – Bode plot of phase angle against frequency of as-polished AZ31, AZ31 after 60s immersion in a mixture of HNO_3 & H_3PO_4 and AZ31 after 30s immersion in NaOH and 60s in a mixture of HNO_3 & H_3PO_4 0 and 60 minutes after immersion in 0.01 M NaCl.

Using these models values for the film resistance and capacitance were calculated and are tabulated in Table 4.7. The resistance values logged in Table 4.7 quantify the behaviour seen in Figure 4.62. The values for capacitance and resistance of the films in the pickled conditions are much more stable over the 60 minute immersion than the ‘as-polished’ AZ31 surface, suggesting considerably less corrosion of these surfaces. The capacitance of the pickled surfaces also shows that the magnesium phosphate films are very thin.

Figure 4.62 shows the corresponding phase angles of the films. The phase angle describes the quality of a film on a surface, where -90° implies perfect coverage[105]. The phase angle associated with the two capacitive arcs in Figure 4.60 is represented by the two minima in Figure 4.62. The minima at high frequency corresponds to the first capacitive arc (double layer) and the second, larger minima corresponds to the mid-frequency arc (film). Hence, it is the phase angle at this lower frequency that is of interest. Immediately after immersion the phase angles for the three surfaces are fairly equal at approximately -30° . After 60 minutes immersion the phase angle for the ‘as-polished’ AZ31 increases significantly to -56° , whereas the two acid/base pre-treated surfaces only increase to -46° . Therefore, whilst the pickling in acid for 60s results in the formation of a phosphate surface film, the coverage of this film is no better than the native oxide film formed on AZ31 after grinding to a P4000 grit finish. Despite this, the acid/base treated surfaces undergo less corrosion. This may be due to the modification to the surface (e.g. dissolving away β phase and intermetallics) or that the film, whilst not covering the entire surface, is more robust than the native film in the sodium chloride solution. As with the increase in resistance of the surface film with ‘as-polished’ AZ31, the larger increase in surface coverage must be due to the build-up of a layer of corrosion product on the surface.

4.3.3.2 Film Behaviour of IL Films on 60 s immersion HNO₃ & H₃PO₄ Acid Pickled AZ31

The two dashed lines in Figure 4.63 show the corrosion response of pickled AZ31 after anodising in IL at 0.1 mAcm⁻², to cut-off cell potential of 18 V, and 0.05 mAcm⁻² with a static 18 V hold for 15 minutes. With the application of the IL film there is a shift in E_{corr} to more anodic/noble potentials (as with the blank pickled surface). The application of the IL film appears to greatly affect the anodic corrosion reaction, which, in the 0.1 mAcm⁻² case, is significantly reduced by about half an order of magnitude in comparison to the ‘control’ pickled surface and about one and a half orders of magnitude in comparison to the ‘as-polished’ surface. In addition, the cathodic reaction is also reduced. Interestingly, the surface treated at 0.05 mAcm⁻² has a different effect. In comparison to the pickled control, the anodic reaction is only slightly reduced but the cathodic reaction is reduced by almost half an order of magnitude.

The reduction of both the anodic and cathodic reactions suggests the film must cover more of the surface with the acid pickle pre-treatment than without. In addition, it was possible to form more consistently good films on these surfaces than on ‘as-polished’ AZ31.

These curves were fit using Tafel extrapolation (EC-Lab software) and are tabulated in Table 4.8. These calculated values show that these films reduce the corrosion current of AZ31 by over a factor of 2 in comparison to pickling alone, and by over a factor of 3 in comparison to ‘as-polished’ AZ31.

Figure 4.64 compares the corrosion performance of AZ31 (both ‘as-polished’ and pickled) anodised at 1 mAcm⁻² in ILAN. This figure shows that the measurable improvement in corrosion properties on the pickled surfaces is not limited to neat IL formed films. Whilst the reduction in the corrosion current is not as significant as the IL anodised films, the corrosion current is still reduced 1.8 x (Table 4.8) over ‘as-polished’ AZ31. In addition, the ILAN film appears to suppress the anodic and cathodic reactions equally (as opposed to favouring one more than the other), which may suggest more uniform film deposition over the surface when the dilute solution treatment is used.

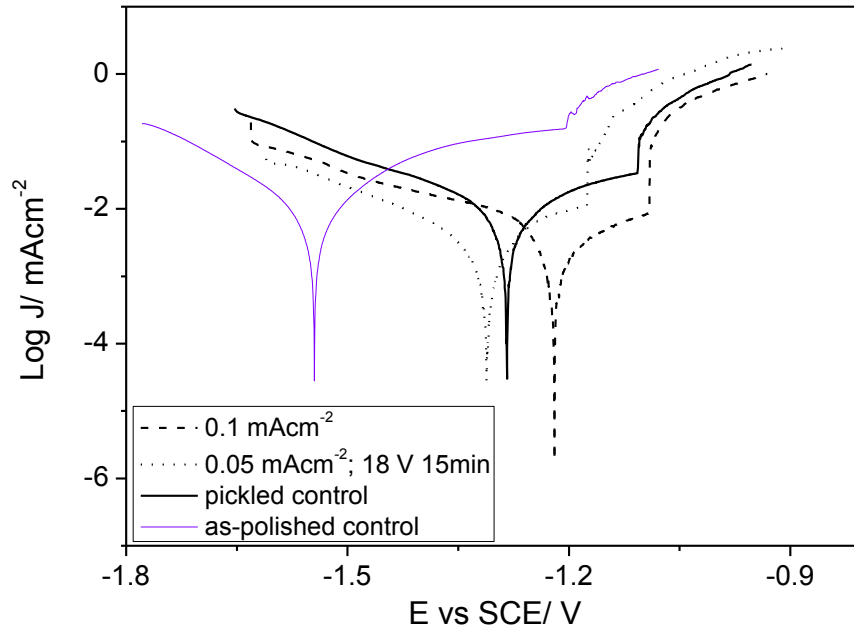


Figure 4.63 - PP curves obtained in 0.01 M NaCl for 'as-polished' AZ31 (P4000 grit finish) blank and AZ31 immersed in a mixture of HNO_3 and H_3PO_4 for 60s (technique 1 – Table 4.10) blank and anodised in IL at 0.1 mAcm^{-2} and 0.05 mAcm^{-2} with a static 18 V hold for 15 minutes.

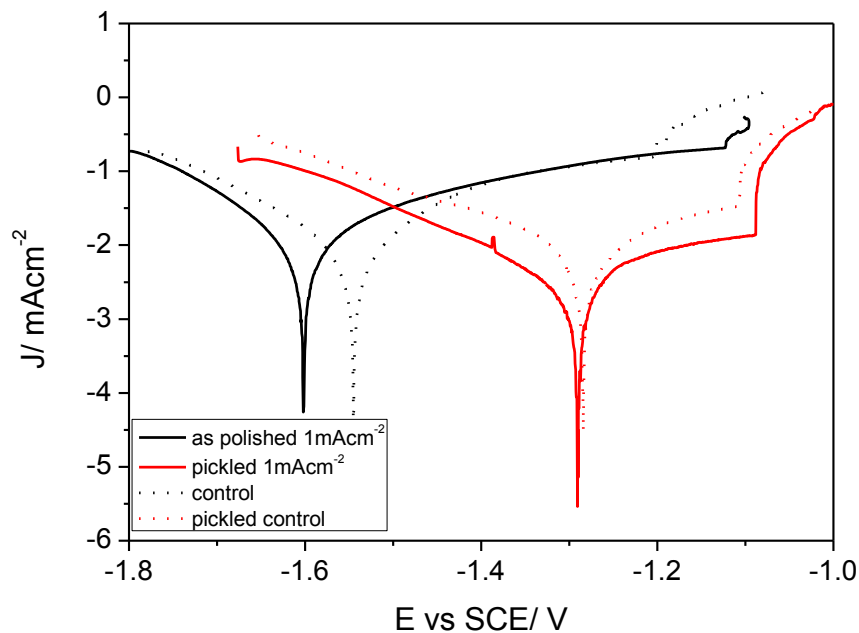


Figure 4.64 - PP curves obtained in 0.01 M NaCl for 'as-polished' AZ31 (P4000 grit finish) blank and anodised in ILAN at 1 mAcm^{-2} and AZ31 immersed in a mixture of HNO_3 and H_3PO_4 for 60s (technique 1 – Table 4.10) blank and anodised in ILAN at 1 mAcm^{-2} .

Figure 4.65 show the EIS responses for IL treated AZ31 surfaces after 60 s acid pickling. The IL treated films presented are the same as those shown in Figure 4.63 and 4.64. The profile of the Nyquist plots (not shown) are the same for the IL treated surfaces as the acid pickled control both immediately after immersion and 60 minutes after immersion. That is, there are

two capacitive arcs at high and medium frequency followed by an inductive arc at low frequency. Hence, these EIS responses can be described using the equivalent circuit presented in Figure 4.61 b).

Unlike the IL treated 'as-polished' AZ31 surfaces, the resistance of the IL films on the acid pickled surfaces are greater than the control surface (also pickled). As with the data already presented, with increased immersion time of 60 minutes the resistance of the films are increased. The initial resistance is greatest for the surface treated at $0.1 \text{ mAcm}^{-2} > \text{ILAN } 1 \text{ mAcm}^{-2} > 0.05 \text{ mAcm}^{-2}$; $18 \text{ V } 15\text{min} > \text{control}$. The fact that the film resistance is greater than the control (as opposed to equal to or less than) suggests that the magnesium phosphate surface film formed due to immersion in phosphoric acid has improved the formation or adhesion of the IL film. However, the IL films are still imperfect as they exhibit an inductive loop at low frequency. Between 0 and 60 minutes the resistance of the films increase, but only by a very small amount compared to the acid pickled control (which, from Figure 4.57 increased much less than the 'as-polished' control). In fact, the resistance for the IL film formed at 0.1 mAcm^{-2} actually decreases at 60 minutes.

Figure 4.65 b) compares the phase angle behaviour of these films. At 0 minutes the phase angle for the pickled control is -32.8° and the IL films are -51.3° , -50.5° and -49.8° for 0.1 mAcm^{-2} , ILAN 1 mAcm^{-2} and 0.05 mAcm^{-2} $18\text{V } 15 \text{ min}$ respectively. Hence the film formed at 0.1 mAcm^{-2} has the greatest surface coverage, which is likely the reason for the greater measured resistance. It also shows that the ILAN solution is capable of forming a well deposited film, despite IL dilution.

At 60 minutes the phase angles increase to -45.8° , -51.1° , -56.9° and -49.0° for the control, 0.1 mAcm^{-2} , ILAN 1 mAcm^{-2} and 0.05 mAcm^{-2} $18\text{V } 15 \text{ min}$ respectively. The phase angle for the control surface has increased significantly, which is due to a corrosion product layer covering the surface; however the phase angle for the IL films remain mostly unchanged. The angle for the film formed in ILAN does increase, which suggests this film may be less stable than the other two films. This may be due to difference in thickness between the films formed in ILAN and neat IL. On the other hand, the slight decrease in the phase angle for the IL anodised surfaces (and the resistance for 0.1 mAcm^{-2}) may be due to some slight breakdown of the film in the 0.01 M NaCl . However, this breakdown would be minor as high levels of corrosion would cause the resistance and phase angle to increase, as in other cases (such as 'as-polished' control).

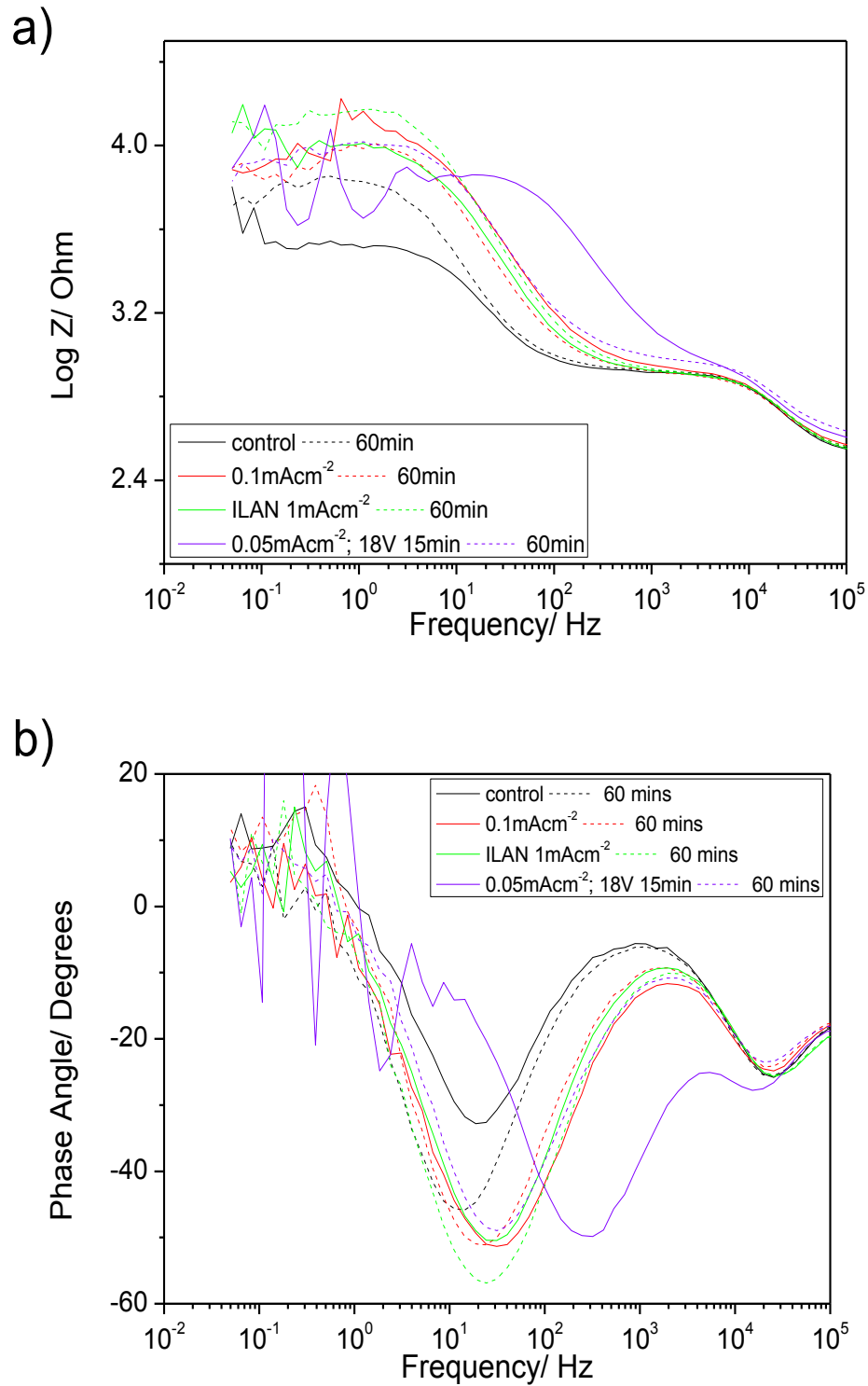


Figure 4.65 - EIS response of 60s acid pickled AZ31 (blank) and 60s acid pickled AZ31 after anodising in IL at 0.1 mAcm⁻² and 0.05 mAcm⁻² with a 15min 18V hold and ILAN at 1 mAcm⁻² in 0.01 M NaCl after 0 and 60 minutes immersion: a) Bode plot of impedance with frequency; b) Bode plot of phase angle with frequency.

4.3.3.3 Film Behaviour of IL Films on 30 s immersion NaOH and 60 s immersion HNO₃ & H₃PO₄ Pickled AZ31

Figure 4.66 shows the influence of the 30s NaOH immersion (prior to the acid immersion) on the corrosion properties of the IL films. In all repeats of the ‘control’ base/acid pre-treated surface, pitting would initiate immediately from E_{corr} . This suggests that the film formed is defective and that it is very difficult to form a consistently good film. Despite this, successfully formed films could still be deposited using IL treatments.

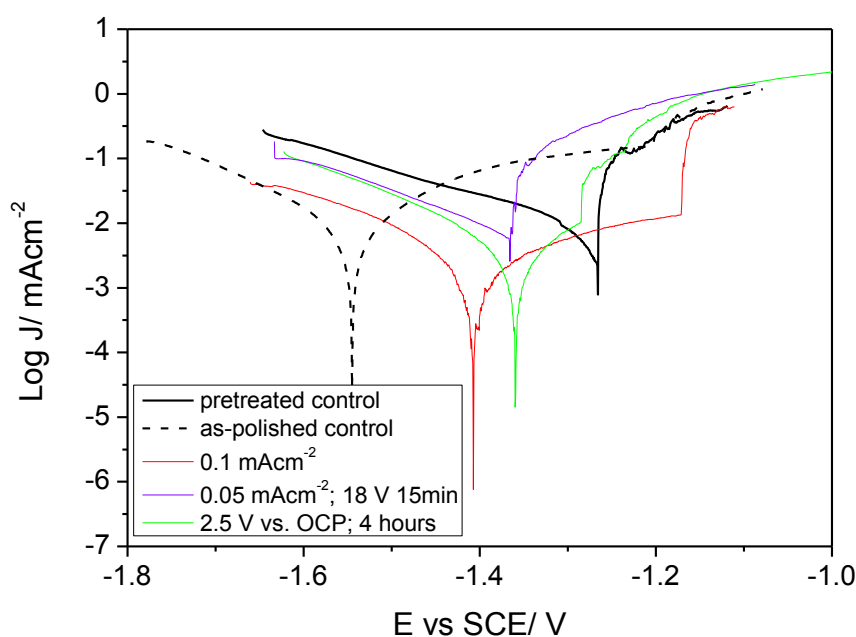


Figure 4.66 - PP curves obtained in 0.01 M NaCl for ‘as-polished’ AZ31 (P4000 grit finish) and AZ31 immersed for 30s in NaOH and 60s in a mixture of HNO₃ and H₃PO₄ (technique 2 – Table 4.10) blank and anodised in IL at 0.05 mAcm⁻²; 18V 15min, and 0.1 mAcm⁻² and a constant potential of 2.5 V vs. OCP for 4 hours.

The IL film formed at 0.1 mAcm⁻² (red) results in a positive shift in E_{corr} as well as a reduction in i_{corr} and the corrosion kinetics of the anodic reaction (Mg dissolution). In this case the anodic reaction is reduced by just over an order of magnitude in comparison to ‘as-polished’ AZ31, which is slightly less than the reduction observed for acid-only pickling with the 0.1 mAcm⁻² IL film. The most interesting aspect of this particular IL treatment is the significant reduction in the cathodic reaction. In the case of acid-only pickling, the cathodic reaction is slightly reduced with the application of an IL film. The cathodic reaction in Figure 4.63 for the IL film formed at 0.1 mAcm⁻² is over an order of magnitude less than the cathodic reaction of the pre-treated control. In fact, the cathodic reaction is back to the same levels as before the pre-treatments. Based on this, we would expect that the surface coverage and the resistance of this film will be significantly greater than the control-base/acid pre-treated surface.

Figure 4.67 shows the EIS response for IL treated AZ31 surfaces after 30 s immersion in NaOH followed by 60 s immersion in a mixture of HNO₃ & H₃PO₄.

The Nyquist plot of the responses (not shown) consists of two capacitive arcs at high and mid frequency and an inductance loop at low frequency. The reoccurrence of this inductance loop

shows that the 30s immersion in NaOH did not prevent the formation of defects in the IL films.

Immediately after immersion the greatest film resistance is recorded for the IL film formed at 0.1 mAcm^{-2} , which is what we expect based on the PP curves in Figure 4.63. Unlike the films formed on AZ31 with only acid pickling, the impedance response of the mid frequency arc increases significantly for the treated surfaces after 60 minutes, which suggests more corrosion is occurring on these surfaces. The change in resistance for the control is much less than the treated surfaces. However of the IL treated surfaces, the film formed using 0.05 mAcm^{-2} ; 18V 15min not only has one of the higher initial resistances, but appears to be the most stable over the 60 minute immersion time.

Figure 4.67 b) shows the phase angle response of these films in 0.01 M NaCl at 0 and 60 minutes after immersion. At 0 minutes the phase angles for these surfaces are -32.7° , -40.0° , -33.8° and 43.7° for the control, 0.1 mAcm^{-2} , 2.5 V vs. OCP 4 hours and 0.05 mAcm^{-2} 18V 15 min respectively. This shows that the IL films formed at 0.1 mAcm^{-2} and 0.05 mAcm^{-2} (+ 18V 15 min) effectively cover more of the AZ31 surface. After 60 minutes immersion the phase angles change to -45.0° , -59.1° , -53.3° and -53.4° for the control, 0.1 mAcm^{-2} , 2.5 V vs. OCP 4 hours and 0.05 mAcm^{-2} 18V 15 min respectively. This shows that after the surface was treated in IL the corrosion properties actually worsened, due to the formation of what appears to be highly defective films. The phase angle values around -56° correspond to the values of 'as-polished' AZ31. This suggests that a significant amount of corrosion product has deposited onto the surface to form a resistive surface layer. However, what is most interesting is that the defective behaviour implied by the EIS data is not consistent with the behaviour seen in the PP tests. The exact same surfaces, which appear highly defective in EIS have performed well in PP. The reason for this is unclear.

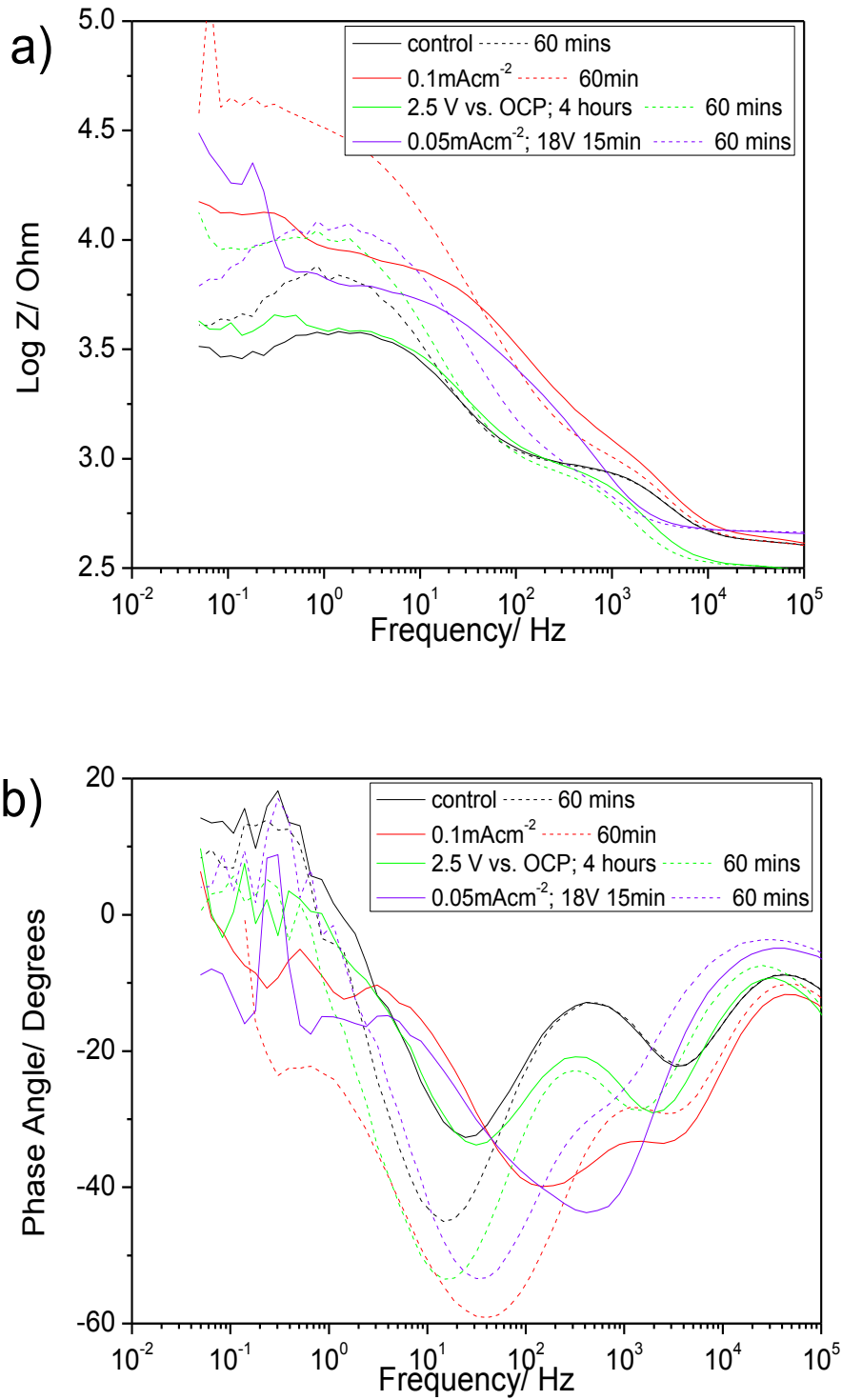


Figure 4.67 - EIS response of 30s NaOH immersion followed by 60s acid pickled AZ31, blank, and after anodising in IL at 0.1 mAc m^{-2} and 0.05 mAc m^{-2} with a 15min 18V hold and ILAN at 1 mAc m^{-2} in 0.01 M NaCl after 0 and 60 minutes immersion: a) Bode plot of impedance with frequency; b) Bode plot of phase angle with frequency.

4.3.4 Summary

Table 4.8 – Tafel extrapolations pre-treated AZ31 surfaces tested in 0.01 M NaCl solution. Measurements were made 20 mV either side of E_{corr} over 20 mV lengths.

Treatment		E_{corr} (mV)	i_{corr} (μAcm^{-2})
As-polished	Control	-1557 ± 10	3.6 ± 1.1
60s HNO ₃ & H ₃ PO ₄	Control	-1218 ± 82	2.4 ± 0.4
	0.1 mAc m^{-2}	-1295 ± 80	1.1 ± 0.3
	0.05 mAc m^{-2} ; 18 V 15min	-1312 ± 45	1.0 ± 0.3
	ILAN 1 mAc m^{-2}	-1280 ± 12	1.0
30s NaOH + 60s HNO ₃ & H ₃ PO ₄	Control	-1305 ± 56	7 ± 6
	0.1 mAc m^{-2}	-1397 ± 54	1.2 ± 0.6
	0.05 mAc m^{-2} ; 18 V 15min	-1380 ± 32	8 ± 3
	2.5 V vs. OCP; 4 hours	-1331 ± 38	1.33 ± 0.04

From Table 4.8 we can see that through a very quick, 60 second, immersion in a mixture of nitric and phosphoric acid the corrosion resistance of AZ31 is significantly increased. The pickling pre-treatment alone leads to a reduction in the corrosion current by a factor of 1.6. The surface modification caused by acid pickling led to a measurable change in corrosion properties with the application of the IL film. In fact, when anodised at 0.1 mAc m^{-2} the corrosion current reduced by a further factor of 2, resulting in an improvement over ‘as-polished’ AZ31 by 3.3 times.

Without surface modification by acid pickling, it was difficult to form consistently protective IL films. In addition, in some cases the corrosion properties of AZ31 were worsened by the application of the IL film. It appeared that with increased exposure to anodic bias potentials and currents led to worsened corrosion properties of the films and EIS showed that regardless of the presence of these films, both the resistance and the phase angle increased at the same rate and to almost identical magnitudes, as bare ‘as-polished’ AZ31. However, the successful IL films formed on ‘as-polished’ AZ31 showed that the IL film actively affects the anodic reaction on AZ31, with no change in the cathodic reaction. This effect can be associated with the preferential deposition of the IL film over the α phase as opposed to the β phase (see section 4.2).

Acid pickling was performed to eliminate the effect of the microstructure on the film deposition. The 60s acid pickle in nitric and phosphoric acid led to a significant anodic shift in E_{corr} and the currents of the anodic reaction were reduced, which can be associated with surface homogenisation from pickling.

When an IL film was deposited onto pickled AZ31, the anodic reaction was further reduced, which suggests the IL films actively slowed the dissolution of magnesium. The EIS data showed that these films were not only more resistive and had greater surface coverage (in comparison to the controls and the films on ‘as-polished’ AZ31), but were also much more stable in the 0.01 M NaCl solution. The resistance and phase angle of these films did not significantly change after 60 minutes immersion, which is indicative of the formation of less corrosion product and hence less corrosion. It was also much easier to consistently form protective films on pickled AZ31 than on ‘as-polished’ AZ31. The possible reasons for this may be that (1) the formation of the magnesium phosphate film from interaction with phosphoric acid[138] may coordinate with the

alkyl phosphinate and organophosphorus species in the IL to form a more adherent film, (2) electrochemical homogenisation of the surface through the removal of β phase and Mn-rich intermetallics allows for a more uniform current/potential distribution over the surface which leads to a more uniform film, (3) increased surface roughness due to material removal improves the adhesion of the IL film.

The EIS data highlighted the detrimental effects of the 30s NaOH step. In most cases the resistance and phase angle of the films increased with immersion time in the same manner as 'as-polished' AZ31. As mentioned previously in section 4.3.3.1 (Figure 4.55), due to the removal of less material from the surface, this effect may be due to insufficient removal of cathodic intermetallics and the β from the microstructure.

4.3.5 Section Key Points

From the results presented in this section, the following key points can be made:

- Field crystallised films are highly porous and do not prevent the ingress of aqueous 0.01 M NaCl solution.
- Successfully formed IL films on 'as-polished' AZ31 shift the corrosion potential to slightly more anodic values and reduce the currents of the anodic reaction by up to half an order of magnitude.
- Acid pickling in a mixture of HNO_3 and H_3PO_4 resulted in a significant anodic shift in E_{corr} , a reduction in i_{corr} , a significant decrease in the anodic reaction currents and a significant increase in the cathodic reaction currents. This behaviour can be attributed to the electrochemical homogenisation of the surface due to Zn redistribution[139] (Figures 4.57 and 4.58) and the formation of a magnesium phosphite film[138].
- The acid pickle either improves the adhesion (due to roughness) of the IL film or takes part directly in its formation on the surface, either from the magnesium phosphate film (which may improve bond adhesion) or through electrochemical homogenisation (which will allow for greater coverage of the film deposition).
- IL films formed on acid pickled AZ31 surfaces provide greater resistance and coverage of the surface and are significantly more robust/stable when exposed to 0.01 M NaCl.
- Films formed in ILAN are less stable over 60 minutes than films formed in neat IL, which may be due to the difference in film thickness.
- The corrosion current for AZ31 after acid pickling and anodising in IL at 0.1 mAcm^{-2} is reduced by a factor of 3.3 over an 'as-polished' AZ31 specimen.
- The IL films greatly reduce the anodic reaction, and also reduce the cathodic reaction (with respect to the increased level of bare pickled AZ31) in 0.01 M NaCl. However, in most cases the cathodic reaction of the pickle + IL film system is greater than on 'as-polished' AZ31.

4.4 Elemental Film Characterisation

4.4.1 Section Overview

This section investigates the composition of various films formed in the $[P_{6,6,6,14}][(\overset{i}{C}_8)_2PO_2]$ IL. The films include those investigated in the previous section using constant potential and constant current techniques. Methods of analysis include X-ray Photoelectron Spectroscopy (XPS), Energy Dispersive Spectroscopy (EDS), X-ray Diffraction (XRD) and Attenuated Total Reflectance Fourier-Transform Infra-red Spectroscopy (ATR-FTIR). XPS and ATR-FTIR provide information of the bonds and compounds present on the surface as well as structure (XPS) and functional groups (IR) whilst XRD provides crystallographic and phase information and EDS provides basic elemental information. Together these methods allow for insight into the nature of these films to be further understood.

4.4.2 XPS of IL Treated Surfaces

XPS of the neat IL is presented in Appendix B, for referencing with the data presented in this section.

This subsection will compare each region scan between the different films formed in IL (at both constant potential and constant current). The films formed under constant potential were analysed using the Sychrotron x-ray source whilst those formed using constant current densities were analysed using a standard XPS instrument. However, the focus will remain on spectra obtained using a 1486 eV x-ray source. Also, it must be noted that region scans were only performed on two of the films formed using constant potential (due to time constraints at the Synchrotron) but due to interesting results seen in the survey scans of this surface they are also included (but without peak fitting).

Figure 4.68 shows a typical survey spectrum of an IL film using an X-ray beam at 1486 eV. This survey shows the presence of O, C, P and Mg on the surface. In particular, the detection of P confirms the presence of an IL containing film. These survey spectra can be used to calculate an estimate of the film composition, which are presented in Tables 4.9 and 4.10.

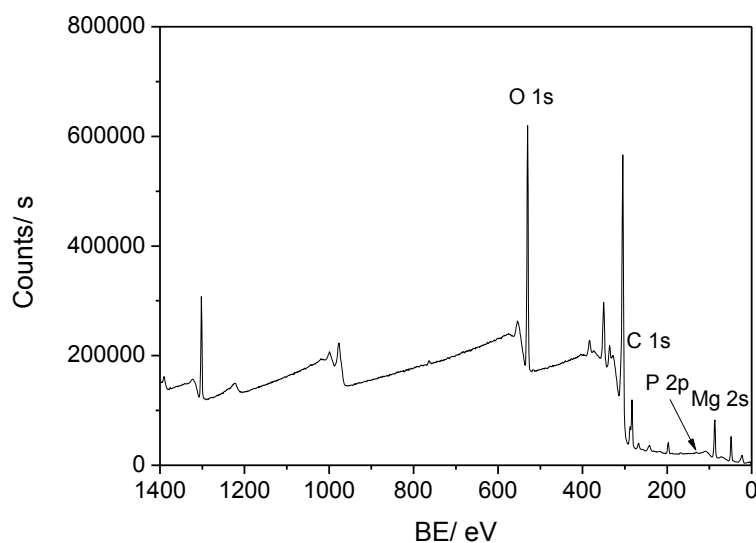


Figure 4.68 – Survey spectrum of AZ31 treated in $[P_{6,6,6,14}][(\overset{i}{C}_8)_2PO_2]$ at a constant current density of 0.1 mAcm^{-2} to 18 V.

Table 4.9 - at% of elements found in XPS survey for specimens anodised in IL at constant potentials (vs. OCP) for 4 hours.

Element	-0.4 V	1.5 V	2.5 V
Mg 2s	16.19	14.81	2.86
O 1s	36.35	32.15	9.93
C 1s	46.73	51.20	82.97
P 2p	0.73	1.83	4.24

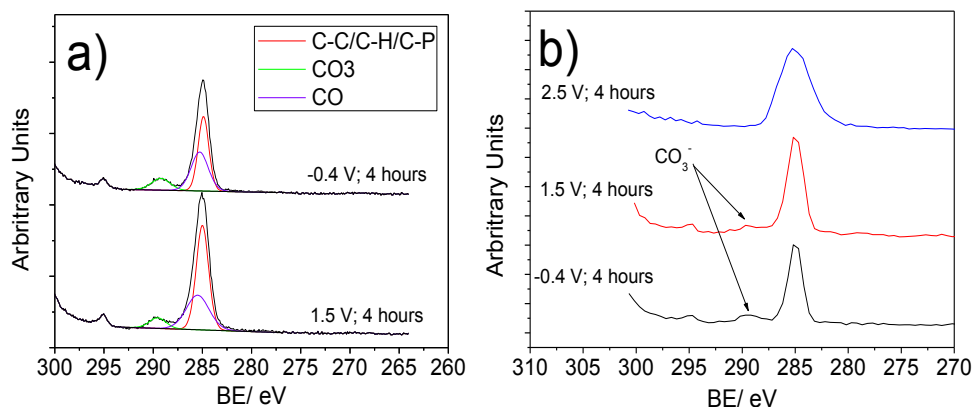
Table 4.10 - at% of elements found in XPS survey for specimens anodised in IL at constant current densities to a cut-off potential of 18 V.

Element	0.1 mAcm ⁻²	0.01 mAcm ⁻²	0.5 mAcm ⁻²	0.01 mAcm ⁻² ; 18V 1hr
Mg 2s	20.23	19.24	17.85	21.20
O 1s	47.88	48.69	45.64	50.55
C 1s	31.58	31.67	35.65	27.28
P 2p	0.31	0.20	0.44	0.13

Based on the calculations in Table 4.9, the composition of the cathodically biased surface (-0.4V) and the anodically biased surface (1.5V) are very similar. With the application of a more anodic bias (2.5 V vs. OCP) the film atomic percentage of P and C species increase significantly. This suggests more components of the IL constitute the film with the greater anodic bias.

Similarly, the values in Table 4.9 show greater levels of C and P in the films formed using higher current densities. Interestingly, holding a static constant potential after anodising (0.01 mAcm⁻²; 18V 1hr vs. 0.01 mAcm⁻²) leads to more Mg and O in the film.

4.4.2.1 C 1s Region Spectra

**Figure 4.69 – C 1s spectra obtained at 1486 eV of AZ31 treated at constant potentials of -0.4, 1.5 and 2.5 V vs. OCP for 4 hours: a) region spectra; b) survey spectra.**

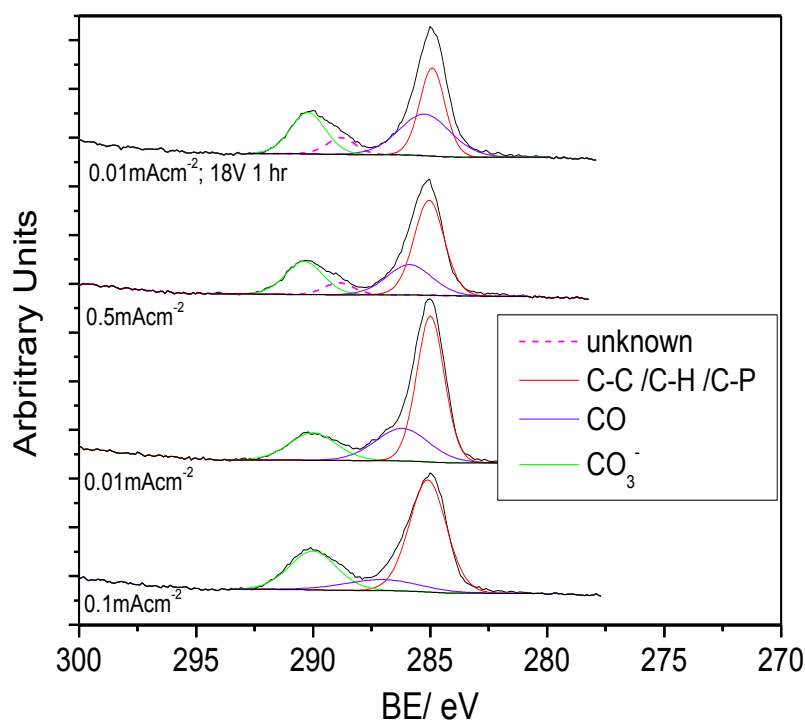


Figure 4.70 – C 1s spectra obtained at 1486 eV of AZ31 treated at current densities of 0.01, 0.1 and 0.5 mAcm⁻² to a final cell potential of 18 V. The broadness of some of the fits is likely due to the presence of additional species on the surface, which were not able to be accurately fit and identified.

Figure 4.69 and 4.70 shows the C 1s region spectra for AZ31 with IL films formed at constant potential and constant current density respectively. Despite the variety of treatment methods the composition of C species on the surface are essentially the same. Peaks exist at (approximately) 290, 287 and 285 eV, which have been attributed to carbonate (CO₃⁻)[141], C-O[142] and C-C/C-H/C-P[142, 143] alkyl bonds respectively.

All surfaces show a carbonate peak except for the surface treated at 2.5 V for 4 hours, which only shows the peak related to the alkyl bonds. In Figure 4.70 another peak has been identified at approximately 288 eV, the identity of which is currently unknown.

4.4.2.2 O 1s Spectra

Figures 4.71 and 4.72 show the O 1s region spectra obtained at 1486 eV for AZ31 with IL films formed at constant potential and constant current density respectively. Like with the C 1s region the species present on the surface using both methods are essentially the same. Peaks at (approximately) 529, 531.5 and 532.5 eV correspond to magnesium oxide (MgO)[142, 144], magnesium hydroxide (Mg(OH)₂)[144] and CO₃⁻ & phosphate [141, 142, 144] bonds respectively. However, if phosphate is on the surface this suggests the phosphinate anion has been oxidised or broken down during the treatment, which is unlikely. As phosphinate contains a PO₂ bond (which by itself is a phosphate), it is likely that the position of the phosphinate peak will be within the range commonly quoted for phosphates.

In general, the films formed using constant potential methods (including the static hold after anodising) have greater amounts of MgO than the other films. The films formed using constant

current densities appear to have greater levels of CO_3^- & phosphinate species than those formed using constant potential. However, these are small differences. The only film which significantly deviates from the others is the film formed at 2.5 V vs. OCP for 4 hours (Figure 4.71 b). In this case the intensity of the O 1s peak is dramatically reduced, however the shape of the peak appears the same and thus it is expected that the same species are still present on this surface.

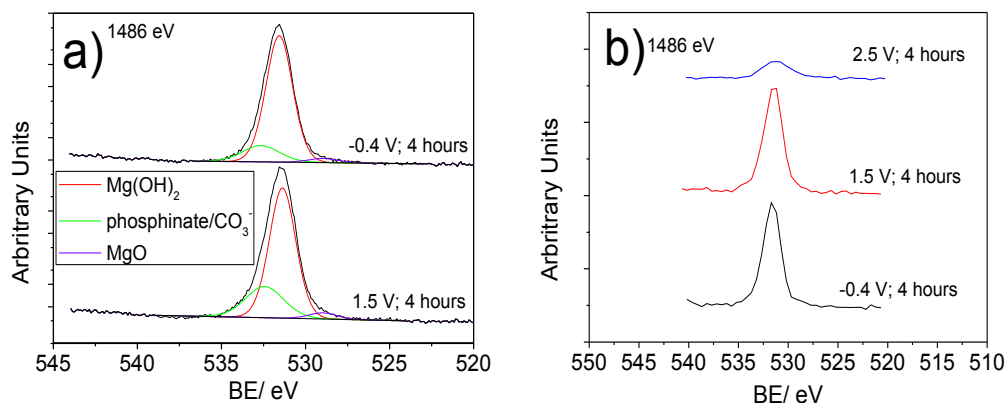


Figure 4.71 – O 1s spectra obtained at 1486 eV of surfaces treated at constant potentials of -0.4, 1.5 and 2.5 V vs. OCP for 4 hours. a) region scans and b) survey spectra.

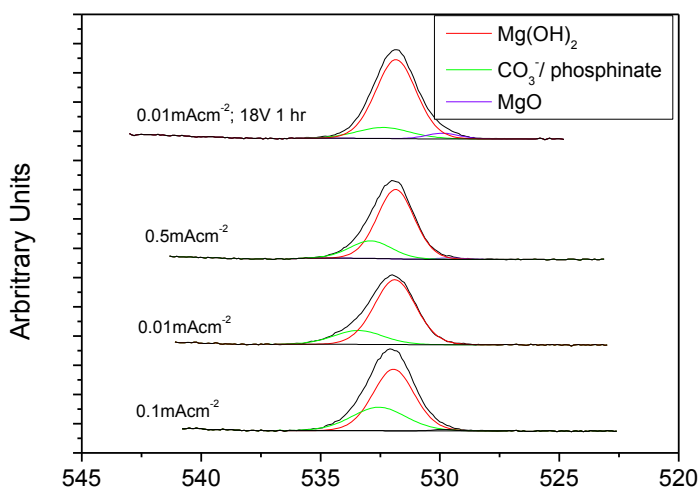


Figure 4.72 – O 1s spectra at 1486 eV of surfaces treated using constant current densities of 0.01, 0.1 and 0.5 mAcm^{-2} to a final cell potential of 18 V.

4.4.2.3 Mg 2p Spectra

Figures 4.73 and 4.74 show the Mg 2p spectra obtained at 1486 eV for films formed on AZ31 at constant potential and constant current density respectively. Three main peaks were identified in this region at (approximately) 48, 50 and 51 eV, which correspond to Mg metal[142], MgO & $\text{Mg}(\text{OH})_2$ [142, 144] and magnesium carbonate (MgCO_3) & magnesium phosphinate (due to similarity to phosphate, quoted in this energy range by [142, 144]).

Despite the C 1s and O 1s spectra confirming the presence of $\text{Mg}(\text{OH})_2$, MgO, MgCO_3 and magnesium phosphinate species, the Mg 2p peak is very symmetrical, which is why the energies for $\text{Mg}(\text{OH})_2$ & MgO, and MgCO_3 & magnesium phosphinate were grouped into two separate

peaks (due to close binding energies in the Mg region). However, even with this simplification the peaks were still hard to separate and fit consistently.

As with the O 1s peak presented in Figure 4.68 b), for the film formed at 2.5 V vs. OCP for 4 hours, the intensity of the Mg 2p peak is significantly reduced in comparison to the other treatments.

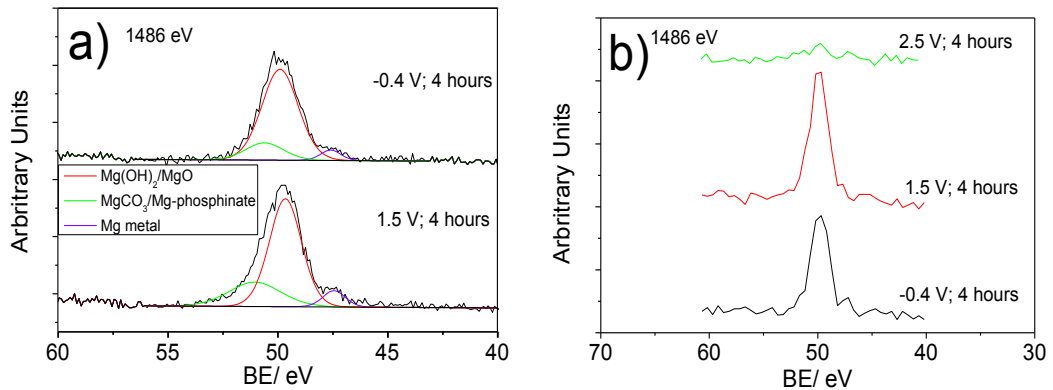


Figure 4.73 - Mg 2p spectra obtained at 1486 eV of AZ31 treated at constant potentials of -0.4, 1.5 and 2.5 V vs. OCP for 4 hours. a) region spectra; b) survey spectra.

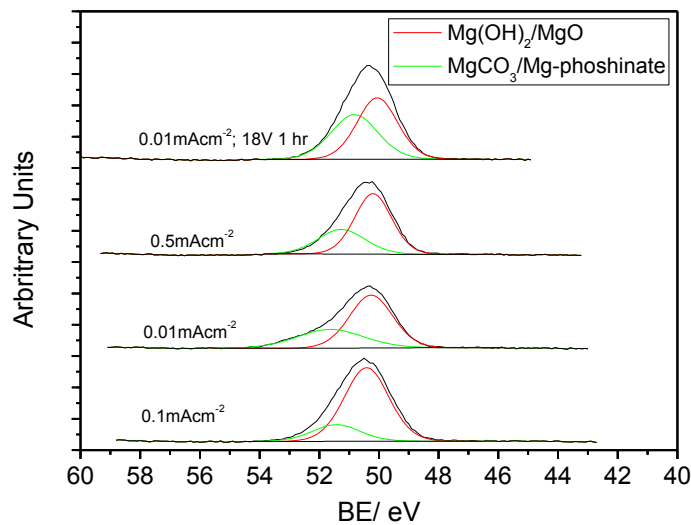


Figure 4.74 – Mg 2p spectra obtained at 1486 eV for AZ31 surfaces treated at constant current densities of 0.01, 0.1 and 0.5 mAcm⁻² to a final cell potential of 18 V. The larger intensity of the peak at high binding energies probably reflects a thinner film, resulting in greater contribution of the carbonate (see C 1s).

4.4.2.4 P 2p Spectra

Figure 4.75 and 4.76 shows the P 2p spectra at 1486 eV for films formed on AZ31 at constant potentials and constant current densities respectively.

Only two peaks were able to be fit under these curves, which account for the P 2p doublet as opposed to two different P related bonds (Figure 4.75). However, only one peak could be fit under the P 2p peak in Figure 4.76 due to the noise in the measurement. A shift from elemental P is such that the doublets are present at approximately 132.4 and 133.4 eV, which have been associated with phosphate in the literature[141, 142], but are likely phosphinate (from the anion)

in this case. All surfaces contain the phosphinate species regardless of the treatment conditions. However, the size of the peak fluctuates based on treatment conditions.

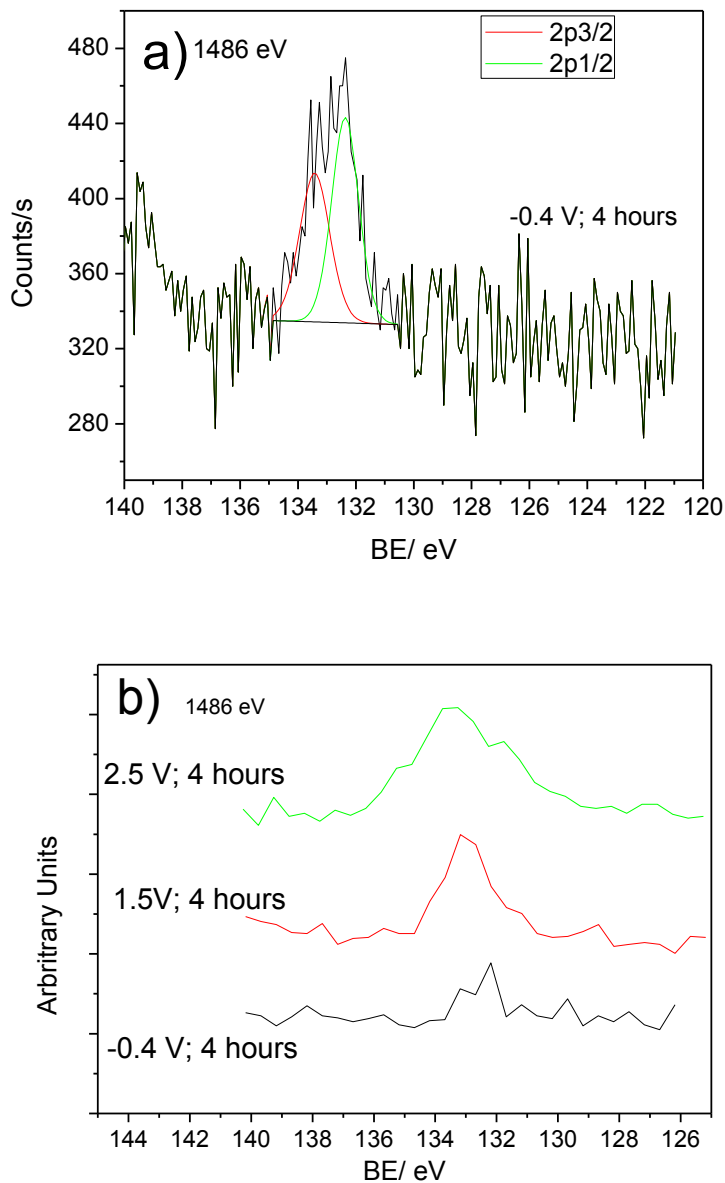


Figure 4.75 – P 2p spectra obtained at 1486 eV of a) region spectra of AZ31 treated at -0.4 V vs. OCP for 4 hours; b) survey spectra of AZ31 treated at constant potentials of -0.4, 1.5 and 2.5 V vs. OCP for 4 hours.

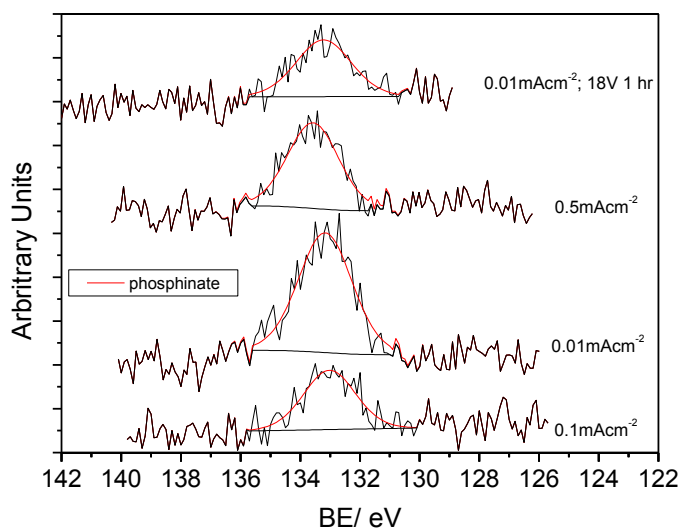


Figure 4.76 – P 2p region spectra obtained at 1486 eV for AZ31 treated at constant current densities of 0.01, 0.1 and 0.5 mAcm⁻² to a final cell potential of 18 V.

4.4.2.5 Summary

The spectra presented in this sections show that the compounds which compose the films on the surface of AZ31 are the same with different treatment types, but the amount of these species differ. The films appear to be comprised of alkyl chains, magnesium oxide, hydroxide, carbonate and phosphinate species.

The detection of the P 2p peak at binding energies associated with phosphinate in all of the films suggests that in all cases the anion is heavily involved in the formation of the film. No definitive indication, either in the C 1s or P 2p region, of the presence of the cation in the surface film was made. The close proximity of the C-P bond binding energy with C-C and C-H bonds meant it could not be said whether or not the C-P bond from the cation was on the surface. Indeed, P-C bonds also were not detected in the P 2p scans, which may be indicative of the cation either not interacting with the surface or due to a weak signal lost in noise (due to high levels of noise in these regions). From the XPS data in Appendix B, despite the anion to cation ratio being 1:1 in the IL, the intensity of the peak associated with the cation was significantly lower than the anion, regardless of incident beam energy. Therefore, considering the small size of the P 2p peaks obtained on the surface, the signal of the cation bonds may have been too weak to distinguish. Certainly, the inability to identify this peak does not tell us whether the cation is or is not on the surface. However, it must be noted that even if P-C bonds were detected on the surface this is not definitive of the presence of the cation as the anion also contains P-C bonds. In any case, as most of the films were formed using anodic methods, the polarisation of the AZ31 would be such that the migration of the anion of the IL would be promoted *towards* the surface and the cation *away*. Hence, we would expect the anion to dominate the IL interaction with the surface as opposed to the cation, which is what appears to occur.

The carbonate peak identified at 290 eV is not present in the neat IL (Appendix B), which suggests that the carbonate peak detected on the treated AZ31 surfaces is due to magnesium

carbonate formed through reaction of the substrate with CO₂ in the air. Hence, the native film which formed on the AZ31 surfaces prior to treatment is detected through the IL formed films.

In the case of the surfaces treated at constant current, the film formed using the lowest current density (0.01 mAcm⁻²) contained the highest levels (based on measured counts in the surveys) of phosphinate and C-H/C-C/C-P bonds, despite the at% of these species (presented in Table 4.10) being less in the overall film in comparison to the films formed at higher current densities (0.1 and 0.5 mAcm⁻²). These quantities suggest that the film formed at the lower current density is thicker than those at higher current density. With the extra one hour static 18 V hold, the film composition changes quite significantly. Not only does the overall composition of the film shift to less components of the IL, but the overall intensity of the C 1s and P 2p peaks decrease. This suggests that the film has actually thinned by comparison. Granted, the intensity of these peaks remains at a similar level with those from the films formed at a higher current density, including the ratio between the C-C/C-H/C-P peak and the carbonate peak. The intensity of the carbonate peak is greater after the 1 hour hold. As mentioned previously, the carbonate is part of the native oxide on the surface. This supports the idea that the 1 hour hold results in film thinning. Given that considerably thick films have been grown using constant potentials, it is interesting that this step results in what appears to be a thinner film. As magnesium is not passive at 18 V, it may be that the applied potential results in increased magnesium dissolution, or disruption of the film, as opposed to thickening.

Based on the influence of the bias potential on ion migration we would expect that a cathodic bias would lead to the cation dominating the interactions with the AZ31 surface. However, even when AZ31 was polarised cathodically at -0.4 V vs. OCP for 4 hours, phosphinate species were detected without any indication of P-C bonds (Figure 4.75). Hence the anion interaction dominates, even when cathodically polarised. This may be due, in part, to the relatively small cathodic bias, which may not significantly repel the anion to prevent interaction of the alkyl phosphinate. Figure 4.75 compares the relative intensities of the phosphinate peaks obtained from films formed at constant potentials. The intensity of the phosphinate peak is significantly reduced with the cathodic bias in comparison to the anodic biases, which confirms that whilst the anion is still interacting with the surface, the degree of interaction is decreased. If we now compare the intensity of the C 1s peak of the cathodic bias with the anodic biases (Figure 4.69) the amount of alkyl chain present is essentially equal regardless of the bias. From the chemical structure of the IL (Appendix B, Figure B.1) we know that the IL contains large alkyl chains. Hence, the alkyl chains detected via XPS are present from the interaction of the IL with the AZ31 surface. The fact that the intensity of the peak associated with the alkyl chains for the surface treated at -0.4 V is not reduced whereas the phosphinate peak is reduced suggests that some amount of the alkyl peak must be from the cation.

Alongside the incorporation of the IL, the film which is grown on the surface of AZ31 is overwhelmingly Mg(OH)₂, with only a small fraction of MgO detected (based on O 1s spectra – Figures 4.71 and 4.72). Typically, with the application of a constant potential the MgO content was greater than when a constant current density was used to form the film. The Mg 2p and O 1s spectra of untreated AZ31 (Appendix B, Figure B.6 and B.7) show that the amounts of Mg(OH)₂/MgO decrease after anodic treatment with IL. This is likely due to the limited water available to react with Mg to form Mg(OH)₂ during anodic film growth. The size of the Mg 2p peak does not significantly change after IL treatment, due to the influence of the Mg bonds to components of the IL. It is likely that much of the Mg(OH)₂ and MgO detected in the treated surfaces is from the native oxide/hydroxide surface film. Interestingly, whilst all the surfaces picked up the presence of carbonate (due to a thin IL film on the native oxide), for the film

formed at 2.5 V vs. OCP for 4 hours no carbonate peak was detected (Figure 4.66 b). Since the carbonate peak is related to a film *below* the IL deposited film, this suggests that the film formed using this potential has formed a thicker film than the other techniques analysed. This is consistent with the FIB-SEM cross section in Figure 4.19. The absence of a carbonate peak in the film formed at 2.5 V vs. OCP for 4 hours shows that this film has sufficient thickness such that the XPS spectrum is sampling primarily the IL formed film, as opposed to the substrate. Without sampling of the native film, the O 1s and Mg 2p peaks are significantly reduced. This shows that most of the Mg and O contributions (in the forms of MgO and Mg(OH)₂) are from the native film as opposed to the anodically formed film. In comparison, the large C1s and P 2p show that the film is formed primarily of components of the IL.

The presence of phosphinate in these films suggests that the anion is reacting with the AZ31 surface in order to form some a magnesium phosphinate species. However, the precise way in which this occurs is currently unclear. Our group has previously suggested a mode of reaction based on metal-phosphate interactions[96], which is outlined in Eqn. 1.



With this phosphate species in Eqn. 4, there is a bridging P-O-C bond for the two alkyl chains, but otherwise the compound is very similar with the alkyl phosphinate of the IL anion. Hence, the reaction which occurs between the anion may be similar to Eqn. 4 (except with the phosphinate as opposed to the phosphate). The Mg ions are most likely to form a complex with phosphinate by bonding with the O atoms on the phosphinate, forming a bridging P-O-Mg bond. It is possible that a single Mg atom may coordinate with one both O atoms. The films formed using either constant potential or constant current (based on those that were optically visible) could not be removed by rubbing and required scratching with a hard instrument. This is indicative of a strongly bonded film to the underlying native surface.

Estimate calculations of the amount of different species (obtained from the %area of the fitted peaks) are presented in Appendix C.

4.4.2 XRD

Figure 4.77 shows the diffraction patterns obtained for AZ31 treated for 3 hours at constant potentials of 0 V vs. Pt (green) and 3 V vs. Pt (blue). Due to the crystallisation of the film on the surface, we expect that greater amounts of MgO should be present for surfaces after field crystallisation. Some difficulty in attributing the identity of these peaks was found as the literature often quoted similar positions for the α phase, MgO and Mg(OH)₂. The identities of the peaks and their crystal orientations was adapted from [145] and [31]. The spectra show an increased content for both Mg(OH)₂ and MgO in the IL treated surfaces over the AZ31 base metal, which suggests these compounds are grown due to the anodic potential bias during treatment (from reaction with the residual water in the IL). The higher presence of MgO in the surface treated at 3 V (blue) would be due to the occurrence of field crystallisation on this surface as opposed to that at 0 V vs. Pt. More Mg(OH)₂ is also present on the 3 V surface, which suggests the film formed is thicker than that treated at 0 V vs. Pt.

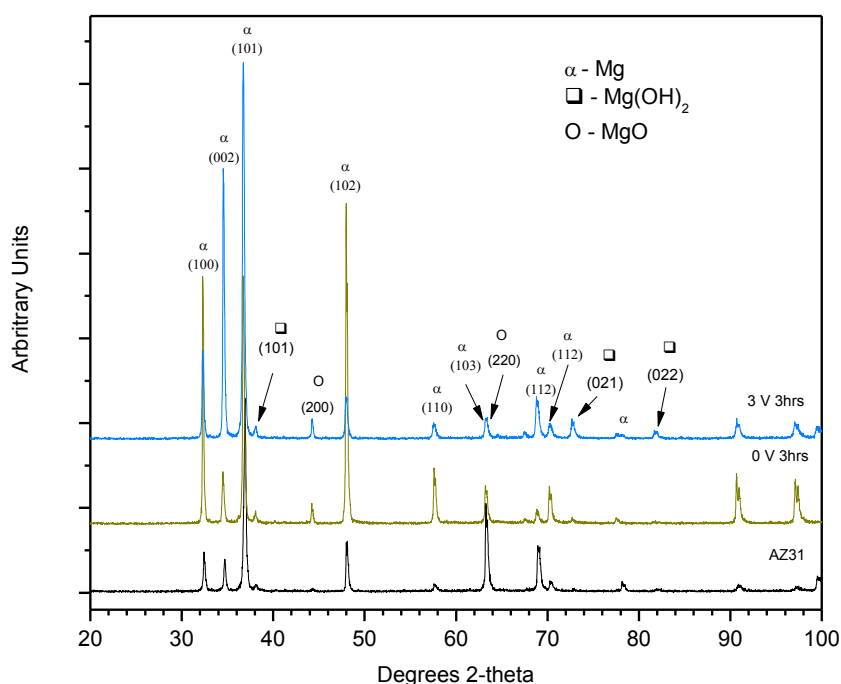


Figure 4.77 – XRD of “as-polished” AZ31 (P4000 grit finish) and AZ31 treated in IL for 3 hours at a constant potential of 0 V vs. Pt (green) and 3 V vs. Pt (blue).

Figure 4.78 shows the diffraction patterns obtained for AZ31 treated at a constant current density of 0.05 mAcm^{-2} in IL and ILAN solutions. If these spectra are compared to Figure 4.77, no MgO is detected over the surface, which shows that the film formed during anodising is comprised of Mg(OH)_2 and components of the IL (see XPS, ATR-FTIR and ToF-SIMS). Interestingly, the peaks of Mg(OH)_2 varied depending on whether the film was formed in neat IL (green line) or ILAN (blue line). In neat IL, Mg(OH)_2 peaks at (approximately) 34° , 54° and 74° are apparent. However, none of these Mg(OH)_2 peaks are present in the diffraction pattern in the film formed in ILAN. Instead, for ILAN, the Mg(OH)_2 peaks occur at 49° and 83° . This suggests that whilst the composition of the films are likely highly similar, the morphology of the films are different. This may account for the different thicknesses observed in FIB-SEM (section 4.2.2) of these anodised films as well as the differences in film stability in section 4.3.

Figure 4.79 compares the diffraction patterns of AZ31 treated at three different current densities of 0.01 mAcm^{-2} (pink line), 0.1 mAcm^{-2} (blue line) and 0.5 mAcm^{-2} (green line). These surfaces are the same as those analysed above in the XPS. Whilst no MgO peak was detected in the blank AZ31 in Figures 4.77 and 4.78, MgO was detected in Figure 4.79 at 45° , not only on the blank AZ31 but also on the three treated surfaces. However, the magnitude for this peak is the same in all cases. Therefore, the films formed under constant current density do not form MgO (or at least not enough to be differentiated). However, in these diffraction patterns there is a dramatic difference in the amount of Mg(OH)_2 detected on the surface treated at 0.1 mAcm^{-2} compared to the other two surfaces. The reason for this dramatic increase in Mg(OH)_2 is currently unclear. What is particularly interesting from the diffraction patterns in Figure 4.79 is the similarity between the film formed at 0.01 mAcm^{-2} and the blank AZ31. In the case of films formed using both 0.1 and 0.5 mAcm^{-2} , peaks are often either smaller or larger than the AZ31 blank, which may suggest anisotropic growth. In comparison, almost every peak, especially

those associated with MgO and Mg(OH)₂, of the diffraction pattern of 0.01 mAcm⁻² is identical to the analogous peak on the blank AZ31 surface. This suggests that an oxide/hydroxide film has not been grown on the surface. However, based on the XPS and optical appearance of films formed at this current density a film is certainly present. This suggests that the film formed at low current density may result in deposition of IL species alone as opposed to a composite of magnesium hydroxide and the anion. The absence of any peaks relating to the IL does not signify absence of the IL on these surfaces. The film formed is likely amorphous and therefore not detected by XRD, especially owing to the nanometre thickness of the films.

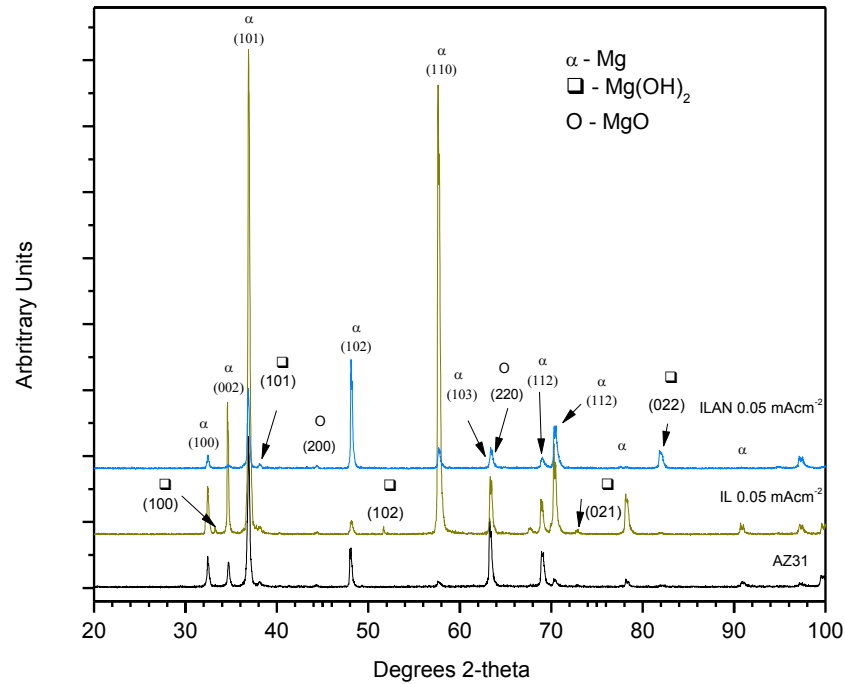


Figure 4.78 - XRD of “as-polished” AZ31 (P4000 grit finish) and AZ31 treated in IL at a constant current of 0.05 mAcm⁻² in IL (green) and ILAN (blue).

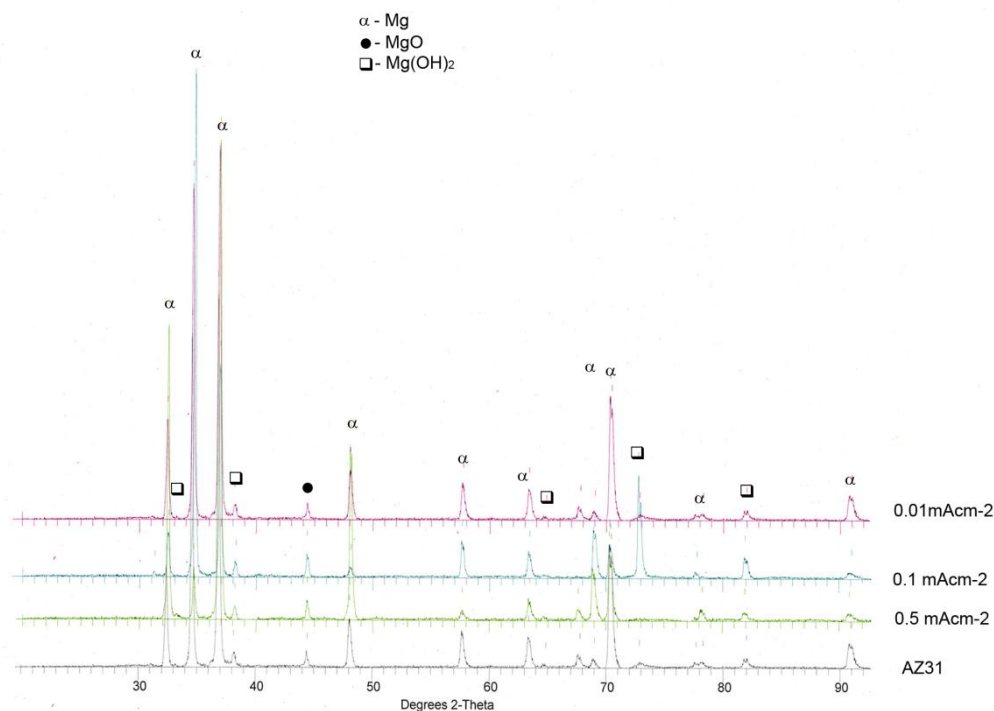


Figure 4.79 - XRD of “as-polished” AZ31 (P4000 grit finish) and AZ31 treated in IL treated at a constant current of 0.5 mAcm^{-2} (green), 0.1 mAcm^{-2} (blue) and 0.01 mAcm^{-2} (pink).

4.4.4 ATR-FTIR

Figure 4.80 presents the ATR-FTIR spectra for neat IL with approximately 1000 ppm of water. The alkyl chains, relating to CH_3 and CH_2 , occur in the range $2800\text{--}3000 \text{ cm}^{-1}$ [90], which include the peaks at 2858 , 2926 and 2954 cm^{-1} in Figure 4.80. The bonds at 1293 , 1260 and 1220 cm^{-1} may be associated with C-P bonds (literature value of 1243 cm^{-1} [146]) however these peaks may also be associated with P=O bonds (at values between $1245\text{--}1275 \text{ cm}^{-1}$)[146-148]. The C-P bond has also been quoted at a frequency of 1439 cm^{-1} [148], which lies within a region of considerable noise (not shown in Figure 4.80) and hence was not observed. The bond at 1166 cm^{-1} corresponds to phosphinate or a P=O bond[146] whilst the bonds at 1049 and 1029 cm^{-1} are quoted in the literature as phosphate bonds [146, 149], most likely corresponding to PO_2 of the phosphinate. For ease of comparison, these assignments have been tabulated in Table 4.11.

Table 4.11 – Bond positions and peak assignments for the neat IL.

Wavenumber (cm^{-1})	Bond identity
1029	R_2PO_2
1049	R_2PO_2
1166	R_2PO_2
1220	C-P
1260	C-P
1293	P=O
2858	CH_2/CH_3
2926	CH_2/CH_3
2954	CH_2/CH_3

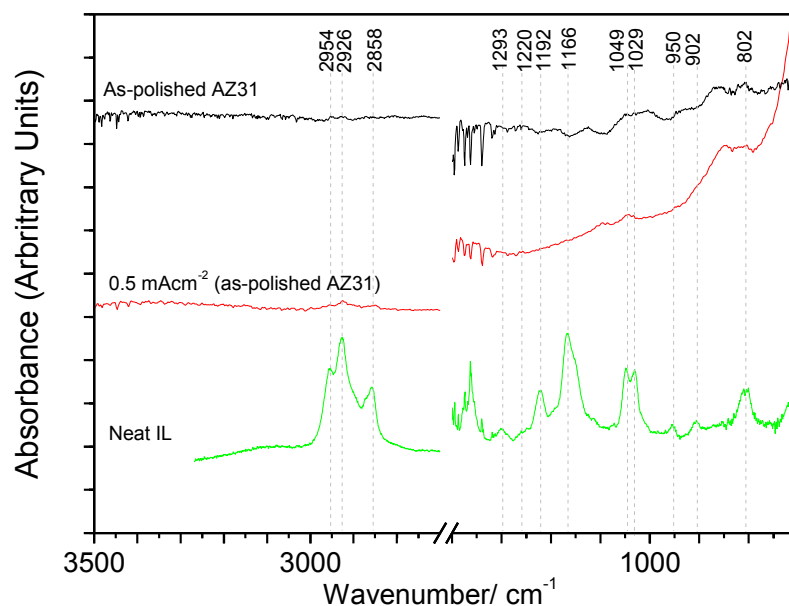


Figure 4.80 - ATR-FTIR of neat $[P_{6,6,6,14}[(^iC_8)_2PO_2]$ IL with approximately 1000 ppm water and bare AZ31 anodised at 0.5 mAcm^{-2} in IL.

The red spectrum in Figure 4.80 indicates that IL species are present on the AZ31 surface after anodising at 0.5 mAcm^{-2} . Other current densities were analysed (0.1 and 0.01 mAcm^{-2} – not shown) and were found to show the same features, with no distinguishable change. The alkyl chains just below 3000 cm^{-1} are present as well as phosphinate species (1029 and 1049 cm^{-1}), which shows species from the IL anion (and possibly cation) are incorporated into the surface film. This figure also shows that the majority of bonds detected in the IL are not present in the anodised film. The black spectra in Figure 4.80 shows the ATR-FTIR response from AZ31 in the ‘as-polished’ condition, ground to a P4000 grit finish. Interestingly, the as-polished surface has a considerable number of peaks, which based on the environment of the native oxide film formation, should correspond to MgO , $Mg(OH)_2$ and $MgCO_3$. However, these peak positions are strange in that literature quotes the presence of MgO at 3700 and 700 cm^{-1} [90], $Mg(OH)_2$ at 3600 - 3700 cm^{-1} [150-152] and $MgCO_3$ at 1500 and 900 cm^{-1} [151]. These peaks were not identified in the spectra, sometimes due to high levels of noise. In addition, literature corresponding to these species at the positions in Figure 4.80 could not be found. Despite this, these peaks can be used to collectively identify the native surface of AZ31, and the following surfaces will be analysed as such.

Figure 4.81 presents the ATR-FTIR spectra for AZ31 anodised in IL in both a dry and wet condition. The main peaks have been indicated with arrows. Peaks just shy of 3000 cm^{-1} can be associated with hydrocarbon structures[146], which have been attributed to the two small peaks at approximately 2924 and 2874 cm^{-1} in Figure 4.81. The presence of these small peaks shows that the alkyl chains from the IL are incorporated into the film during anodising but the intensity of the peak in the ‘wet’ condition is much smaller, which suggests that either less of the alkyl chains have deposited or that no alkyl chains have deposited and residual ethanol from cleaning is still on the surface. The peaks at lower wavenumbers show greater intensities recorded for the wet IL. In addition, a new peak at 1261 cm^{-1} is present when AZ31 is anodised in wet IL as opposed to dry IL. The peaks at 1043 and 1091 cm^{-1} have been associated with phosphinate (due to similarity with phosphate in [146, 149]) as well as the bond at 1261 cm^{-1}

¹[146]. However, the bond at 1261 cm⁻¹ may also be from the C-P bond in the IL[146]. The literature also cites phosphinate at 1066 cm⁻¹ and PO²⁻ at 1075 cm⁻¹[146], which may also account for these two peaks. In general most of the peaks do not match up with the blank AZ31. In the case of the wet IL (which had a very obvious orange coloured film) this may be due to the film formed from the IL. The lack of many of these peaks on the dry anodised surface may be indicative of a detrimental effect of this treatment on as-polished AZ31 (as seen through the corrosion performance in section 4.3). Many of the native film features have been removed from the surface with the action of anodising, which may suggest that anodising to 18 V dissolves the film rather than growing it.

The peak intensities for the phosphinate peaks when the IL is wet suggest significantly more of the anion has reacted with the surface. During anodising in the wet IL the maximum cell potential reached was only 4 V. This suggests that the IL or IL film may be undergoing breakdown through oxidation. The decomposition of the anion is probably the cause of the orange colouration of these surfaces post treatment. An example of this colour was shown in section 4.1 (Figure 4.14) for AZ31 cycled in wet IL. With the addition of water we would expect Mg(OH)₂ to form due to the reaction of water with Mg. The absence of a distinguishable OH peak suggests that much of the water in the IL may be used in hydrolysis of the anion or cation.

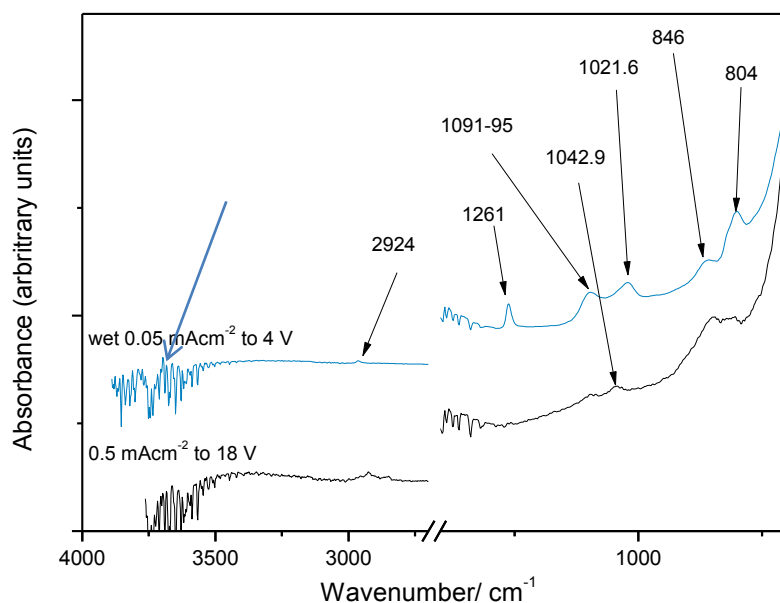


Figure 4.81 – ATR-FTIR of AZ31 anodised at 0.5 mAcm⁻² in neat IL (black) and 0.05 mAcm⁻² in IL containing 6 wt% water (blue). Breakdown occurred in the wet system, leading to a final potential of 4 V with this treatment, as the system could no longer support anodic film growth.

Figure 4.82 shows the ATR-FTIR spectra for AZ31 cycled in wet IL four times between OCP and 3 V vs. Pt. The blue line allows comparison between the film formed due to cyclic voltammetry and anodising (blue spectra in Figure 4.82 is the same as already presented in Figure 4.81). The ‘new’ peak that was present due to the presence of water in Figure 4.81 is also present in the cycled surface in Figure 4.82. All of the peaks present when cycled to 3 V vs. Pt are the same as those present when anodised, however the intensity of the peaks is greater when cycled. This is not particularly surprising as the degree of surface modification (due to this deposition) was identified in the CVs due to intersection of the curve on the return cycle (see

Figure 4.13). In addition, the films formed with wet IL were highly visible. The increased peak intensities show that the reaction/decomposition of the anion has occurred more in the cycled condition. The final potential when anodised (4 V) is only 1 V greater than the final cycled potential. Whilst the treatment was terminated for the anodised surface after reaching 4 V once, the cycled surface was forced to 3 V four consecutive times. Whilst this consecutive cycling would not have greatly altered the surface film formed in a dry IL (due to decreasing current density with cycling) the decomposition process continues with cycling in wet IL. As a result the film deposited appears to be quite thick and obviously is comprised of components of the decomposed IL anion.

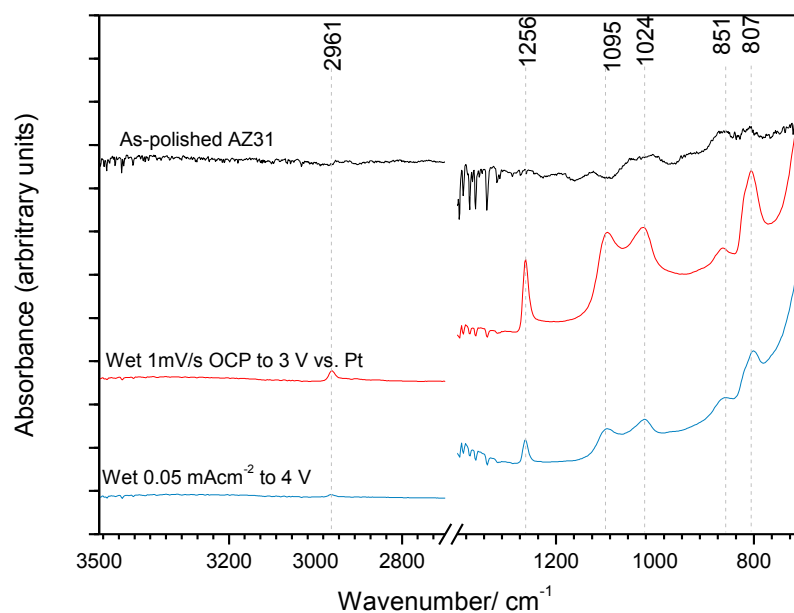


Figure 4.82 – ATR-FTIR of AZ31 cycled between OCP and 3 V vs. Pt (black) and anodised at 0.05 mAcm⁻² to a final potential of 4 V (blue) in wet IL

4.4.4.1 ATR-FTIR of AZ31 Pre-Treatments

The process of acid pickling was introduced in section 4.3.3 and was performed to homogenise the surface to promote film deposition from the IL. The corrosion behaviour presented in 4.3.3 showed that the film formed was far more stable and protective after pickling in the mixture of nitric and phosphoric acid than when formed on ‘as-polished’ AZ31. The corrosion results suggest that the film may be (1) more adherent to the AZ31 substrate, (2) less permeable to ion ingress or (3) less porous. The improvement seen based on the acid pickling was suggested to be due to increased roughness of the surface, greater homogenisation of the surface or improved bonding with the surface (possibly due to the formation of a magnesium phosphate film from the reaction of phosphoric acid with AZ31).

Figure 4.83 compares the surface chemistry of AZ31 after pre-treatment using the two techniques in Table 4.6 (section 4.3.3) as well as immersion in 1 M NaOH for 30s without the subsequent acid immersion. Due to immersion in phosphoric acid, the formation of magnesium phosphate (expected to be Mg₃(PO₄)₂[138]) between 1045-1118 cm⁻¹ has been identified. As expected, these peaks are not present when only treated in NaOH, however when immersed in acid after immersion in NaOH the intensity of the phosphate peak is increased. Interestingly, no

OH⁻ groups were detected after immersion in NaOH. It may be that an immersion time of 30 s is too short to allow for the detectable deposition of hydroxide groups onto the surface.

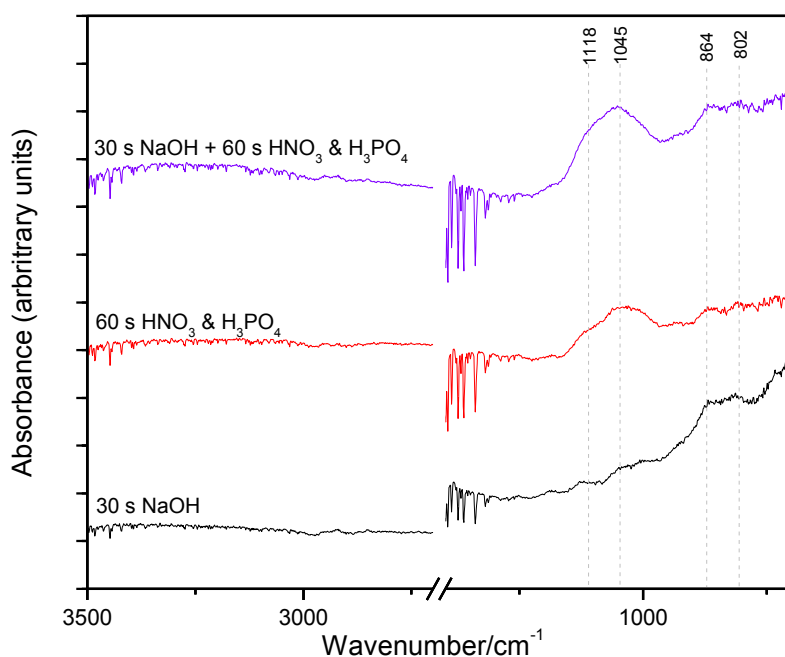


Figure 4.83 – ATR-FTIR of AZ31 after pre-treatment using techniques 1 (red) and 2 (purple) including a surface immersed only in 0.1 M NaOH for 30 s (black).

Figure 4.84 compares AZ31 after pickling for 60 s in the acid mixture (technique 1 – Table 4.6) with and without anodising in IL at 0.1 mAcm⁻². In comparison to AZ31 after pickling, the peaks on the anodised surface are more defined and have greater peak intensity. The anodising step does not appear to alter the presence of magnesium phosphate on the surface, as the large, amorphous bump is still present. With the addition of anodising, another three peaks at 933, 1192 and 1256 cm⁻¹ can be identified. As with the spectra in Figure 4.80, after anodising the presence of hydrocarbon chains are indicated at 2873 and 2930 cm⁻¹. However, whilst the peaks in the fingerprint region in Figure 4.80 reveal phosphinate peaks at 1043 and 1091 cm⁻¹, the peaks in this region in Figure 4.84 are unresolved, such that there are ranges of 1088-1123 cm⁻¹ and 1004-1054 cm⁻¹. These regions correspond very closely with those for the native surface in Figure 4.80. The new peak at 1256 cm⁻¹ is the same peak which occurred in the wet IL and hence corresponds to either phosphate or a C-P bond, whereas the peak at 1192 cm⁻¹ may correspond to a P=O peak[153], but once again lines up with the native surface film. The final new peak at 933 cm⁻¹ can either be attributed to phosphate (quoted at 970 cm⁻¹ in[146]), P-O (quoted at 920 cm⁻¹[147]) or a bridged P-O-C bond (quoted at 936 cm⁻¹[154]), however this peak also appears in the ‘as-polished’ AZ31 surface.

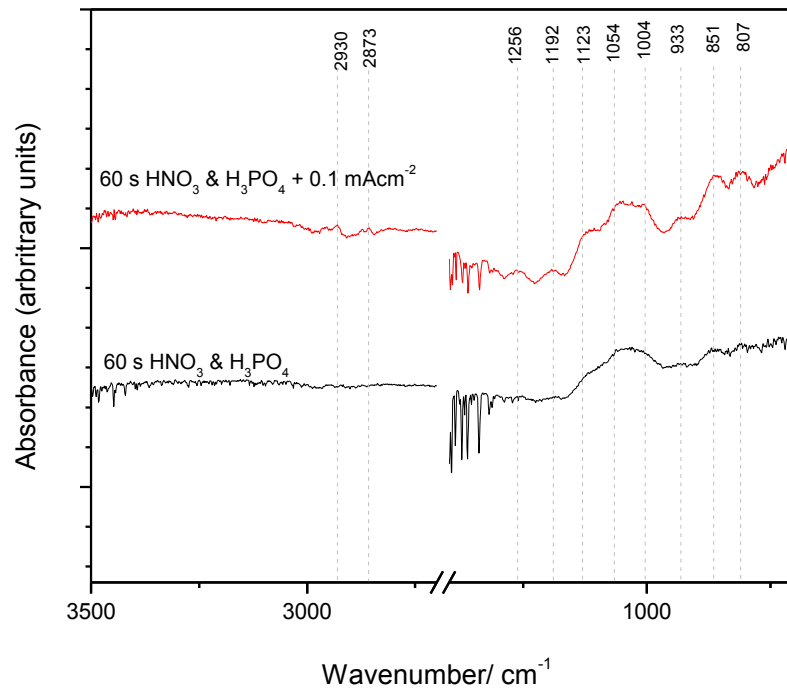


Figure 4.84 – ATR-FTIR of AZ31 anodised in IL at 0.1 mAcm^{-2} after 60s pickling in a solution of nitric and phosphoric acid (red line). A comparison is provided by the pickled AZ31 surface from Figure 4.76 (black).

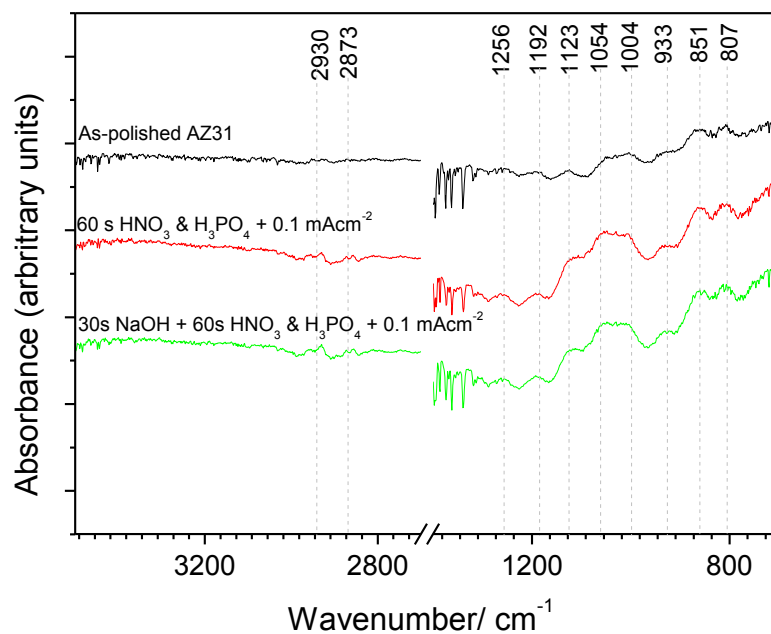


Figure 4.85 - ATR-FTIR of AZ31 with no films (bare - black), AZ31 anodised in IL at 0.1 mAcm^{-2} after pre-treatment in the acid mixture (red line) and AZ31 anodised in IL at 0.1 mAcm^{-2} after pre-treatment in NaOH and the acid mixture (green).

Figure 4.85 compares pre-treated surfaces of AZ31 anodised in IL at 0.1 mAcm^{-2} , with the bare AZ31 surface. No new peaks are developed due to the 30 s immersion in NaOH, and the bonds

on the surface are similar to those on the anodised surface after acid pickling only, which is expected. Due to the lack of a distinguishable OH peak on any of the surfaces it is unlikely that the peaks at similar positions to the 'as-polished' surface correspond to $\text{Mg}(\text{OH})_2$, and their positions may hence be coincidental. In this case the pickling pre-treatments lead to the appearance of additional P-related peaks, which suggest the presence of more of the anion (and possibly cation) on the surface of AZ31. This may be due to improved adhesion or deposition conditions due to the roughening and homogenisation of the surface. However, due to the similarities between the pickled & anodised and 'as-polished' surfaces these results are inconclusive.

4.4.4.2 Summary

The data presented from ATR-FTIR does not conclusively show the chemistry of the film due to conflicting peaks between the treated and untreated surfaces. The identification of alkyl chain peaks, in addition to C-P bond peaks, after anodising shows that the IL film is detected, however other peaks are not as clear. Many of the peaks after anodising on the pickled surface resemble the 'as-polished' AZ31 surface, but they may also be attributed to phosphinate or other P related peaks. Interestingly, anodising on 'as-polished' AZ31 appears to strip the native surface and replace it with components of the IL, namely the alkyl chains, C-P bonds and phosphinate. Therefore we would expect that the increase in peak intensity after anodising the pickled surfaces would be (at least in part) due to the deposition of phosphinate species on the surface.

The use of the IL in a wet state (both through cycling and anodising) appears to result in more components of the IL on the surface, as evidenced by phosphinate, C-P and alkyl chain bond peaks. This is likely due to hydrolysis of the IL from the excess water present. In contrast, anodising on bare AZ31 with 'dry' IL appears to have resulted in only some phosphinate species on the surface. In addition, most features of the native surface are removed.

The application of a pre-treatment to the surface using an acid mixture of nitric and phosphoric acid resulted in the formation of magnesium phosphate on the surface of AZ31 (Figures 4.83-4.85). The deposition of this film appeared to promote the formation of the anodised film. The 30s immersion in NaOH did not result in the formation of detectable OH^- species, however it appeared to promote the formation of the magnesium phosphate film once immersed in the acid solution.

The FTIR shows that the IL film formed on AZ31 after a 60s acid pickle is different to the film formed on bare AZ31. We know from FIB-SEM that anodising in this IL produces a thin, compact film. FTIR shows that this film is composed of alkyl chains from the IL and possibly phosphinates. Improved film growth on pickled AZ31 may account for the improved corrosion properties seen in section 4.3. However, as the same species (with similar intensity of absorbance) were also identified on anodised AZ31 after the base/acid pre-treatment, the improvement in the corrosion properties is likely due to more than the composition of the film. Indeed, the phase angles (Figure 4.67) of the 30 s NaOH & 60 s pickle surfaces were significantly lower than those for the 60 s acid-only pickled surfaces (Figure 4.65), which suggests poor surface coverage of this film on the base-acid surfaces compared to the acid-only surfaces.

Interestingly, despite XRD and XPS (and even ToF-SIMS below) showing the presence of $\text{Mg}(\text{OH})_2$ on the surface, no OH peaks were detected through ATR-FTIR. The reasons for this are unclear.

4.4.5 ToF-SIMS

Time-of-Flight Secondary Ion Mass Spectroscopy (ToF-SIMS) was used to obtain spectra and 2D maps of AZ31 anodised to a cut-off potential of 18 V at 0.1 mAcm⁻² on 'as-polished' and 60s pickled AZ31. The positive ion spectra maps are shown in Figure 4.86 a) and b) for as-polished and pickled treated surfaces respectively. Previously, using XPS we were unable to distinguish the cation from the anion in the surface film, however in Figure 4.86 we can see that intact cation is present in the surface film. The distribution of the cation is mostly uniform on the 'as-polished' surface but more localised on the pickled surface. ToF-SIMS information is affected by the topography of the surface being examined; therefore the high level of roughness of the pickled surface may be contributing to the 'localised' appearance as opposed to the actual presence of the cation over the surface. Whilst both surfaces record a significant amount of the cation, greater counts are observed on the pickled surface. ToF-SIMS obtains elemental data by impacting the surface with ions and measuring the mass of molecules, which are broken away from the surface. As a result, most molecules are fragmented into smaller pieces. Therefore it is interesting that the entire cation was identified on these surfaces.

Figure 4.87 a) and b) compare the negative ion elemental maps for AZ31 anodised at 0.1 mAcm⁻² to 18 V on 'as-polished' and pickled AZ31 respectively. These maps show high levels of O and OH, which are likely from the native film in addition to any Mg(OH)₂ formed due to reaction of Mg with water in the IL during anodising. Unlike the cation, on the treated 'as-polished' surface no anion molecules were detected. However, the presence of PO₂ and PO₃ suggests a uniform, but likely small, amount of the anion is present over the surface. The low intensity of these fragments is interesting as the data obtained from XPS suggested that more of the anion was present than the cation.

Interestingly, with pickling, intact anion compounds were detected in the IL film, although only over a small portion of the surface. This is likely due to considerable fragmentation of most the anion molecule during analysis. If we consider the PO₂ and PO₃ maps, the small area in which the anion was detected is also highlighted. Together these show a uniform coverage of the IL anion. However, much of the contribution of the PO₃ (and possibly some PO₂) could be from the magnesium phosphate film which forms during pickling.

If we consider the location of the cation and anion from Figure 4.86 and 4.87 b), the intact anion and cation occupy the same localised area. This suggests that the IL may have absorbed into, or become entrapped within, the anodic film without dissociation of the molecules.

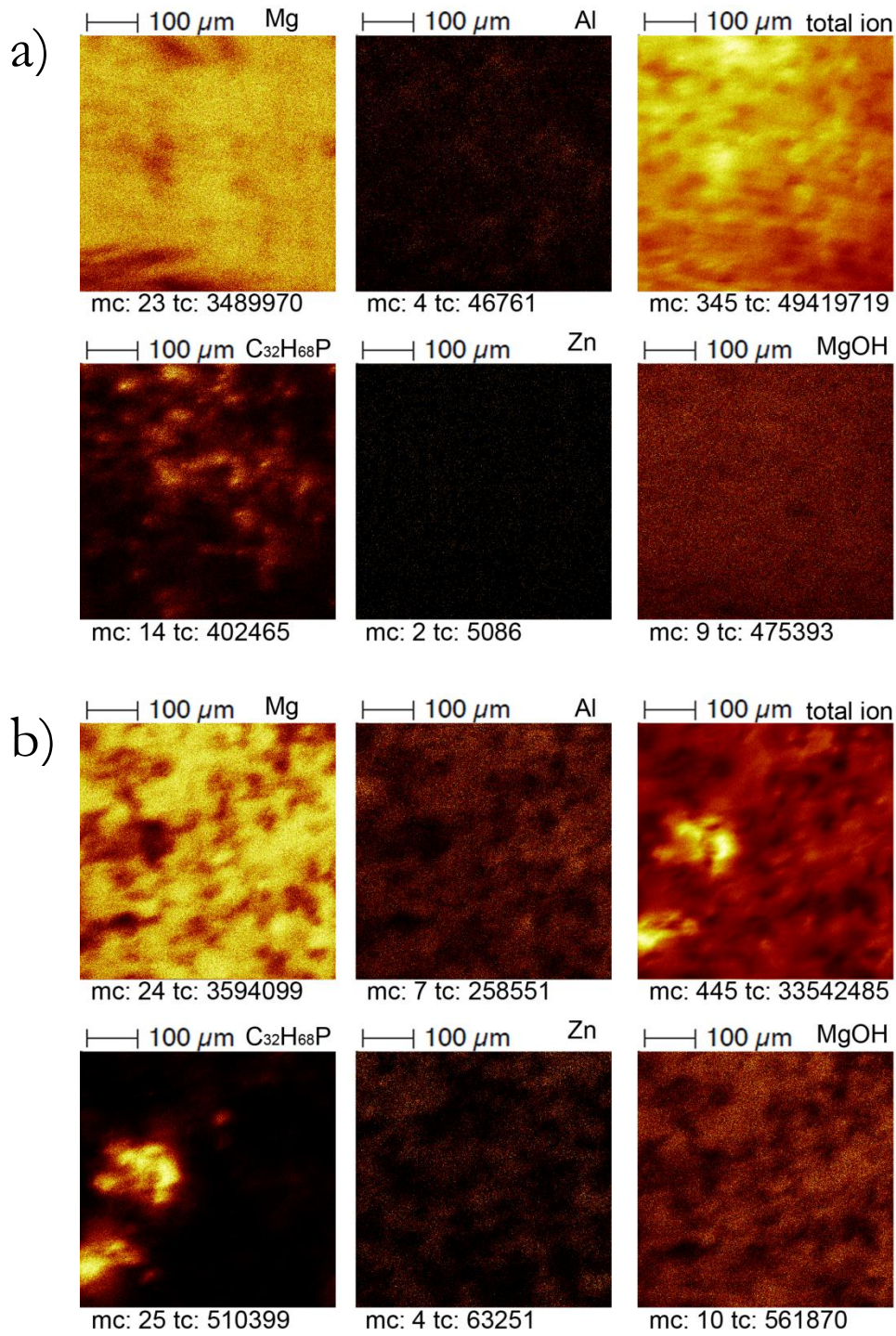


Figure 4.86 – Positive ion ToF-SIMS 2D elemental mapping of AZ31 anodised at 0.1 mAcm^{-2} to 18 V of a) ‘as-polished’ AZ31; b) acid pickled (60s HNO_3 and H_3PO_4) AZ31. $\text{C}_{32}\text{H}_{68}\text{P}$ is the cation molecule.

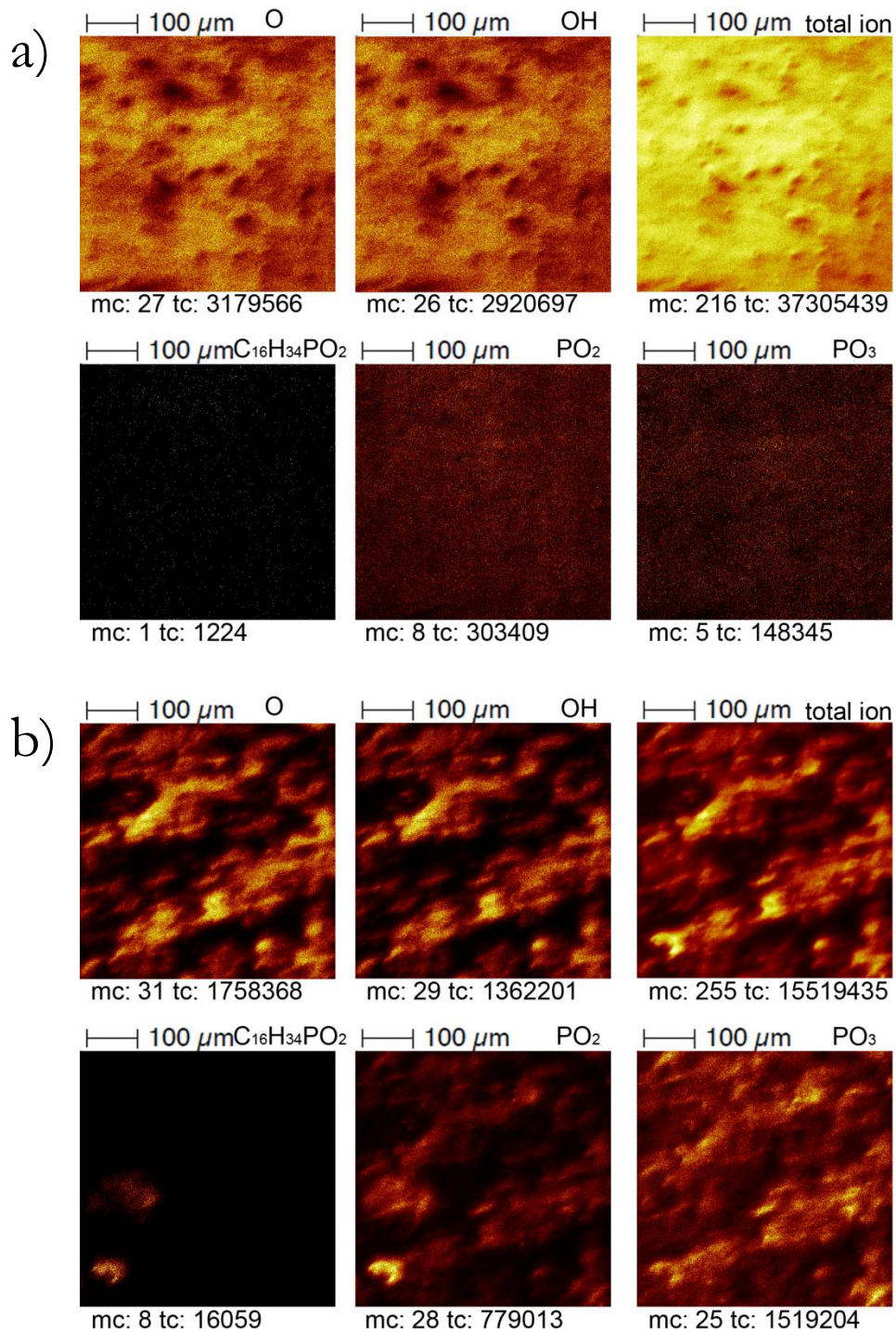


Figure 4.87 - Negative ion ToF-SIMS 2D elemental mapping of AZ31 anodised at 0.1 mAcm^{-2} to 18 V of a) ‘as-polished’ AZ31; b) acid pickled (60s HNO_3 and H_3PO_4) AZ31. $\text{C}_{16}\text{H}_{34}\text{PO}_2$ is the anion molecule.

4.4.6 Section Key Points

From the results presented in this section, the following key points can be made:

- XPS showed that the chemistry of the film formed through anodic means was dominated by interaction of the anion to form phosphinates on the surface whereas ToF-SIMS also showed significant levels of the cation.
- Intact anion was identified over the pickled anodised surface and not on the ‘as-polished’ anodised surface. In addition, greater counts of PO_2 (possible anion fragment)

was also identified on the pickled surface. This suggests that the process of pickling improves the adhesion to, or ability to grow the IL film on, AZ31.

- The films formed through the application of a constant potential have more MgO than films formed through the application of a constant current density.
- The application of greater anodic potential biases led to more incorporation of the IL into the surface film.
- The morphology of the Mg(OH)₂ anodised film formed in ILAN is different to the film formed in neat IL (from XRD).
- Anodic polarisation and anodising in wet IL promotes the breakdown of the IL anion.

Chapter 5

Closing Discussion, Conclusions & Ways Forward

5.1 Overview of the Formation of the Anodic IL Film

Film formation on magnesium alloy AZ31 in the ionic liquid tetradecyltrihexylphosphonium bis(2,4,4-trimethylpentyl)phosphinate ($[P_{6,6,6,14}][[(C_8)_2PO_2]$), benefits from the application of anodic treatments. When scanned positively, the film forming process occurs through two main parts:

1. Oxidation of Mg to Mg^{2+} .
2. Film thickening.

To elaborate, the film thickening process involves the reaction of magnesium with the IL (particularly the anion) in addition to any contribution of residual water to form hydroxides. Due to the positive polarisation of the AZ31 substrate we expect that migration of the anion towards AZ31 will be promoted, whilst the cation will migrate away from the AZ31 surface. However, we know from the ToF-SIMS mapping that there is a substantial amount of cation in the film. There are three main ways the IL can interact with the surface. The interactions will depend on whether the cation or anion coordinate with $Mg(OH)_2$, MgO or Mg^{2+} . Accordingly, the strength of the bonds will be different. The weakest bonds will be between the MgO and the cation. MgO can physically adsorb the cation due to weak electrostatic interactions (like dipoles) due to the negative charge of the O atom and the positive charge of the cation. Slightly stronger hydrogen bonding can occur between the H atom in $Mg(OH)_2$ and an O atom in the phosphinate of the anion. The strongest bond will be chemical adsorption between the Mg^{2+} ions and the O atoms of the phosphinate anion. This last bonding type is shown in Figure 5.1 a). The type of bonding is similar to what we expect from magnesium phosphates (Figure 5.1 b). The Mg atoms will likely coordinate with both O atoms in a single phosphinate molecule. Due to the size of the molecules it is unlikely that a single Mg atom will coordinate with two phosphinate molecules. This structure results in a barrier of hydrocarbons, which we would expect to repel ingress of water. This compound is likely precipitated onto the surface at areas of $Mg \rightarrow Mg^{2+}$ dissolution. It is also possible, if the film is porous, that capillary adsorption of the IL will take place.

The bonding of the film can be either chemical (strong) or physical (weak) adsorption. Physical adsorption involves attraction of charged molecules through Van der Waals interactions and is easily reversible. Comparatively, chemical adsorption requires a relatively large amount of energy

to reverse. As these films do not wash away in solvents, we expect that the film is chemically adsorbed. Chemical adsorption is also more consistent with the irreversible electrochemical nature of the film. We would expect that if the film were physically adsorbed that polarising negatively would result in stripping of the film. The change in polarity of the surface should disrupt the Van der Waals interaction by reversal of charge and hence the attraction of the molecules. Instead, cyclic voltammetry showed that the film is electrochemically stable and robust in the IL environment. With repeated negative/cathodic cycling of AZ31 the process of film growth was not disrupted. However, whilst the film thickened and reduced the anodic current with repeated cycling, the cathodic current increased. With long-term anodic cycling of the surface a zero current is never reached, instead the current stabilises at the leakage current through the film. This leakage current can be the result of two things: (1) the film allows for ion conduction or (2) the presence of pores, which allows for continued Mg dissolution. It is entirely possible that both of these options are true. From the morphology of the field crystallised films we know we can form highly porous structures. In addition, the process of anodising, for which both the constant potential and constant current treatments are included, is known for the formation of porous films. We also know from optical microscopy that film deposition occurs only over the α phase, leaving the cathodic β phase bare, which leaves the cathodes (and hence the cathodic reactions) active.

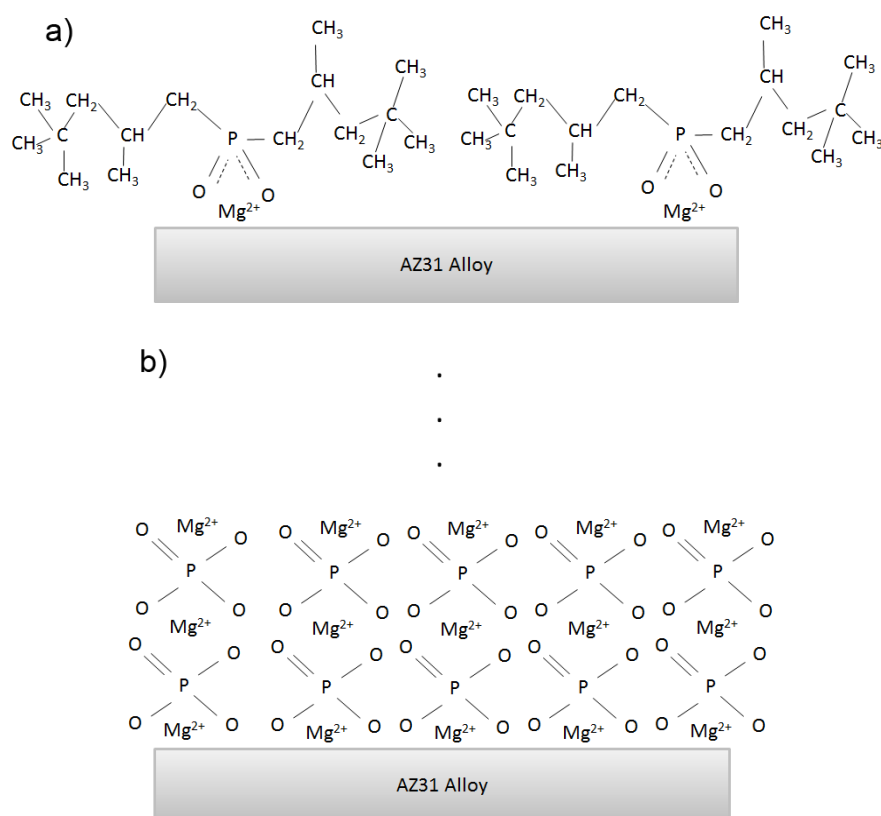


Figure 5.1 – Possible film structures for a) IL film composed of the phosphinate anion and b) magnesium phosphate (taken as $Mg_3(PO_4)_2$) film on the alloy surface. Corresponding reaction of the phosphinate with Mg: $Mg^{2+} + O_2PR_2^- \rightarrow MgO_2PR_2^+$.

The preferential film formation over the α phase was unaffected by the way in which the surface was subjected to anodic current or potential. This is due to the inactivity of the β phase at such low potential values. Anodic films, such as those formed in the IL, will only form over the β phase at potentials greater than 80 V[74]. Whilst the mode of application did not alter where the

film formed it did affect the protection afforded by the films. Films formed using a constant potential < 3 V were able to reduce the corrosion kinetics of the anodic reaction by over half an order of magnitude whilst films formed using constant current densities appeared to worsen the corrosion kinetics. This difference may simply have to do with the potential ranges as opposed to the actual current vs. potential application. It has been mentioned that magnesium is passive below 3 V and above 20 V[74]. Hence, between these two potentials we would expect a high level of reactivity. Above 3 V active dissolution and pitting of magnesium occurs, accompanied by oxygen evolution[74] (although we expect H_2 gas evolution from the corrosion of Mg). This reactivity, in addition to gas evolution processes may disrupt the adhesion of the IL film to AZ31, resulting in delamination in aqueous solutions. This may also explain why the films formed at a lower current density were worse than those formed at higher current density. Those formed more slowly exposed the AZ31 substrate to damaging potentials for a longer period of time. Hence, it would be likely that more corrosion of the AZ31 surface would occur, leading to more gas evolution and hence greater difficulty for the deposition of the film. However, this raises the question: why isn't this process a problem after pickling?

The IL films which were formed on AZ31 after 60 seconds immersion in the acid mixture of nitric and phosphoric acid were very protective, particularly against the anodic dissolution reaction when immersed in neutral aqueous 0.01 M NaCl. In contrast to the constant current density films formed on as-polished AZ31, the IL films formed on pickled AZ31 were also easily reproduced. Part of the contribution to the improved corrosion performance may be the thin, protective magnesium phosphate film which forms due to the reaction of magnesium with phosphoric acid. If AZ31 is polarised anodically above 3 V, Mg dissolution will be reduced by this phosphate layer. We would expect this to reduce gas evolution during anodising, which may result in less disruption during film deposition and hence greater film adhesion. The adhesion of the film may also be due to roughening of the surface or improved bonding between the phosphinate and phosphate species as opposed to phosphinate directly with the AZ31 surface.

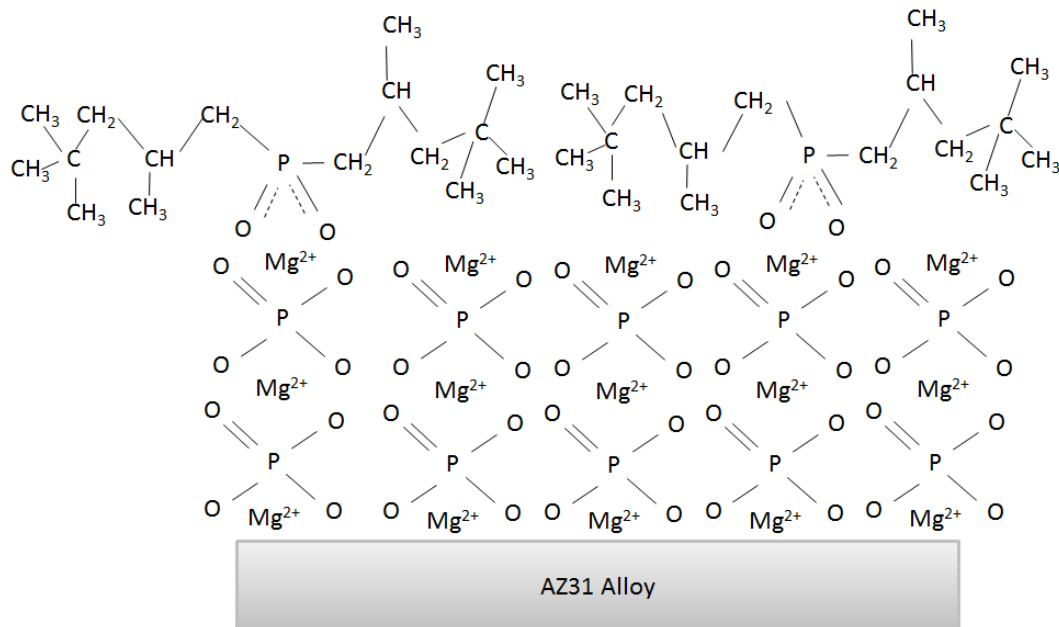


Figure 5.2 – Possible film composition due to deposition of the phosphinate anion onto a pickled surface with a magnesium phosphate ($Mg_3(PO_4)_2$) film.

From the FTIR we know there is an amorphous film of magnesium phosphate on the surface before and after anodising (Figure 4.83-4.85). However, after anodising we see the formation of other small peaks which are likely due to deposition of IL species. Based on the combined information from XPS, XRD, FTIR and ToF-SIMS, after anodising we expect to have a surface layer which is comprised of components of the IL and hydroxide species, essentially resulting in a composite film. The exact morphology of this film cannot be easily interpreted from the data in this thesis due to the thickness of the film. However, it may be possible that a network of magnesium-phosphinate bonds with magnesium hydroxide comprises the film. Whether all of the alkyl chains from the phosphinate remain on the molecule during the anodising step is uncertain. A model for composition of the film (based on the anion) is presented in Figure 5.2. If the phosphinate molecules were to coordinate with the Mg ions in the same way as phosphate molecules, the film may build on the surface as presented in Figure 5.2. However, this is a very simple way of looking at the film as hydroxides as well as the IL cation will be present. As far as the cation is concerned, it may be possible that the cation is trapped as the anion reacts with migrating Mg^{2+} ions, effectively growing the film over the intact cation. Properly understanding exactly what happens to the anion and cation molecules during anodising and the reactions which occur between it and the Mg ions are a topic of ongoing research.

Even with pickling, at these relatively low anodising potentials the film will still only form over anodic α phase and not over any redistributed cathodic particles. As a result the IL films only actively diminish the anodic, magnesium dissolution, reaction when immersed in neutral aqueous 0.01 M NaCl solution. Whilst the cathodic reaction is never reduced, with respect to as-polished AZ31, with the application of these IL films (and in the cases of pickling – increased) the reduction in the anodic kinetics are quite substantial (1.5 orders of magnitude). Furthermore, with the combination of pickling and anodising the films are far more stable in the neutral 0.01 M NaCl solution than the as-polished AZ31 and the pickled AZ31 surfaces. As the anodised films formed on as-polished AZ31 were not stable when immersed in 0.01 M solution there must be improved adhesion of the phosphinate films after pickling. As mentioned previously, this may be due to improved conditions for film deposition (by the phosphate reducing corrosion and hence H_2 evolution). With the phosphinate adhered to the substrate more effectively, the hydrophobic alkyl chains will be able to minimise the passage of water to the surface to reduce the degree of magnesium hydroxide formation. In addition, the surface homogenisation would have led to an increased area applicable for the film to deposit, hence increasing the coverage of the IL film.

One drawback of this IL is that the electrochemical stability of this film and the IL electrolyte relies heavily on the water content in the IL. If left exposed to air the IL will absorb water at levels as high as 5.8 wt% [96]. When AZ31 was cycled anodically to 3 V vs. Pt or anodised to 4 V in IL containing 6 wt% water (40 x more water than in the “dry” condition) breakdown occurred. Unlike films formed under these circumstances in the dry IL, highly visible yellow-orange coloured films were deposited. This suggests that the phosphinate anion may have been hydrolysed.

5.2 Summary of Conclusions

Collectively, this thesis shows that ionic liquid tetradecyltriethylphosphonium bis(2,4,4-trimethylpentyl)phosphinate ($[P_{6,6,6,14}][^{(C_8)_2}PO_2]$) can be successfully used as an electrolyte to form anodic films on magnesium alloy AZ31. Application of appropriate potentials (either through static potential or from current application) can significantly alter the performance of these films when applied to as-polished AZ31. The potential range used for constant current anodising was non-ideal for characterising the prospect of this technique as it has been found to correlate to an active potential range for Mg alloys in aqueous environments. Despite this, the formation of films with fantastic anodic properties were achieved using this method.

The main points from this thesis can be summarised as follows:

1. Magnesium can be passivated in $[P_{6,6,6,14}][^{(C_8)_2}PO_2]$ at anodic potentials, with distinctive film forming behaviour (high-field mechanism) that has also been reported on Bi, Ti, Sn and Zr metals. Dilution of the $[P_{6,6,6,14}][^{(C_8)_2}PO_2]$ IL in a solvent does not disrupt its film forming capabilities.
2. When polarised anodically, the both the cation and phosphinate anion from $[P_{6,6,6,14}][^{(C_8)_2}PO_2]$ are present in the composition of the film.
3. Application of anodic techniques in a wet (6 wt% water) $[P_{6,6,6,14}][^{(C_8)_2}PO_2]$ IL compromised the electrochemical stability of the system, and highly reacted surface films were formed. This is suspected to be due to the hydrolysis of the IL (most likely the anion) due to interaction with excess water.
4. Application of a static potential led to amorphous films which reduce the anodic reaction kinetics by over half an order of magnitude. At long treatment times the films become less protective. This is likely due to the formation of cracks and other defects in the film, which are likely due to internal stresses from ongoing thickening of the films (e.g. 500 μm when treated at 2.5 V vs. OCP (approx. 1 V vs. Pt)).
5. Care must be taken in the magnitude and time of application of the static potential. After approximately 5 hrs at 3 V vs. Pt the amorphous film crystallised and formed a thick oxide on AZ31. The homogeneity of this film was hard to control and large pores in the film allowed for ingress of electrolyte, making the film unsuitable for corrosion protection. The homogeneity of these films could be improved by forming at elevated temperature, but the porosity remains an issue from a corrosion stand-point.
6. Thin films could be formed using a method of constant current density (or galvanostatic anodising) at a number of current densities. A film formed in neat IL (at 0.05 mAcm^{-2}) was found to be approximately 80 nm, whilst a film formed in the dilute IL solution 'ILAN' produced a 30 nm film (at 0.07 mAcm^{-2}). XRD confirmed that the morphology of the two films are different, which suggests viscosity and hence conductivity of the anodising solution alter the morphology of anodised IL films.
7. Use of low current densities led to the formation of defects and ruptures in the galvanostatic films. Large defects resulted in high localised current flow, which in turn led to localised heating and crystallisation of the surrounding film. This often led to termination of film growth.
8. Film formation, despite the different modes of application, always occurred over the α matrix phase in the microstructure.
9. $[P_{6,6,6,14}][^{(C_8)_2}PO_2]$ IL films reduce the anodic corrosion kinetics of AZ31, but do not alter the cathodic reaction when immersed in 0.01 M NaCl solution.

10. Galvanostatically formed films worsen the corrosion performance of 'as-polished' AZ31. This is likely due to film delamination in the 0.01 M NaCl solution.
11. Acid pickling in a mixture of nitric and phosphoric acid led to a 300 mV anodic shift in E_{corr} and a reduction in the anodic reaction kinetics of an order of magnitude. Acid pickling led to greatly improved IL film corrosion properties. This is likely due to a combined effect of surface homogenisation (allowing greater coverage of the IL film over the surface) and the corrosion protection afforded by the magnesium phosphate film (possibly allowing for improved IL film deposition). IL films formed on pickled AZ31 were very stable in 0.01 M NaCl. The anodic reaction was reduced by over 1.5 orders of magnitude and i_{corr} was reduced from 3.6 to 1.1 μAcm^{-2} for pickled AZ31 anodised at 0.1 mAcm^{-2} to 18 V.
12. After acid pickling the cathodic reaction kinetics were accelerated. This is likely due to the redistribution of cathodic Zn particles over the surface.

5.3 What's Next?

Based on the work presented in this thesis, here are some possible suggestions for taking this work further:

1. Investigate a Greater Potential Range:

It has been mentioned in this thesis that magnesium is only stable below 3 V and above 20 V. Between these two potentials magnesium dissolution will readily occur. As the potentiostat used to conduct the constant current anodising is limited to a 20 V, this limits the ability to investigate higher potentials. This is of particular interest as inhomogeneous surface coverage of the IL film, due to the presence of the β phase at these lower potentials must compromise the corrosion performance. If both phases can be anodised the film may act as a more protective barrier to water and corrosive ions. In addition, as a higher potential will be reached the film should also be significantly thicker. This would allow for improved characterisation of the anodically formed IL film. As the threshold is only 20 V, it may be possible to still anodise AZ31 at relatively low potentials and still gain a substantial improvement in the corrosion performance, even with the β phase left bare.

2. Anodise to lower potentials (i.e. < 3V)

Given the behaviour of magnesium alloys between the potentials of 3 and 20 V, it may be worthwhile anodising to low potentials using low current densities.

3. Investigate if IL can be Added to Water as an Anodising Additive

Many ILs are still quite expensive and anodising baths typically require a significant volume, which may be impractical for this material. The performance of the IL in acetonitrile suggests that the dilution of the IL does not affect the film forming ability of the IL on AZ31. However, the IL used in this work is hydrophobic such that only very small concentrations can be achieved in water. It may be worthwhile to investigate hydrophilic ILs in this aspect. By diluting the IL in water, the film would not form as shown in this thesis as most of the anodic reaction will involve the formation of $\text{Mg}(\text{OH})_2$ due to the access to large volumes of water.

4. Investigate Other IL Systems

It may be worthwhile to specifically select an IL that would work well with this technique. For example, one of the main issues in anodising with the phosphonium phosphinate IL was the high viscosity in the dry condition. This limited the range of suitable current densities dramatically. With higher current densities (alongside the use of higher final potentials) the films formed may be less prone to rupture and cracking. In addition, a different chemistry of the IL may improve the corrosion performance of the film. Unfortunately, many of the elements which form protective films are considered environmentally hazardous (i.e. fluorides and phosphates). Research is currently being made into the investigation of silane coatings on Mg alloys. Therefore, it may be possible to synthesise an appropriate Si containing IL. Other alternatives include altering the cation used with the phosphinate anion to reduce the viscosity.

5. Investigate Cleaning Processes

Prior to acid cleaning (pickling) of the AZ31 surface, it was difficult to form consistently good IL films. The investigation on the effect of acid pickling on IL film formation was only conducted with one acid mixture. It may be possible that another acid or acid mixture results in improved results. In addition, due to the formation of the magnesium phosphate film due to reaction of the phosphoric acid with magnesium, it may be of interest to understand what role this film plays in the formation of the IL film in comparison to the surface homogenisation. For example, use nitric acid and phosphoric acid alone. As nitric acid does not form a magnesium complex, if surface homogenisation can be obtained using this acid alone it can be used as a direct comparison for the role of the magnesium phosphate film on the deposition of the IL film.

6. Investigate or Model the Structure of the IL film

The schematic models for the structure of the film formed on AZ31 with this IL are only speculation and do not consider the role of magnesium hydroxide or the cation, which form part of the film. Hence, it may be worthwhile to actively try to understand the structure of the film, especially regarding the interaction with the different surfaces including as-polished and acid pickled. This would require further use of equipment such as transmission electron microscopy (TEM), to obtain the crystal structure of the film.

7. Adhesive Properties Towards Organic Coatings

If the magnesium alloy is going to be used in aggressive environments (e.g. marine) the IL coatings presented in this work will not be sufficient alone. However, in most cases anodised films are formed prior to the application of organic coatings. Therefore, the films need to be adherent not only to the alloy substrate but also to an appropriate organic paint. Hence it would be worthwhile to investigate the coating adhesion and the performance of the IL film-paint system in corrosive conditions (e.g. salt spray test with a scribe through the coating). In addition, adhesion can also be measured physically using tape, as per ASTM standard D3359-09e2.

References

1. B.R. Powell, P.E. Krajewski, and A.A. Luo, *Magnesium Alloys for Lightweight Powertrains and Automotive Structures*, in *Materials, Design and Manufacturing for Lightweight Vehicles*, P.K. Mallick, Editor. 2010, Woodhead Publishing. p. 114-173.
2. I.J. Polmear, *Light Alloys*. 4th Ed.(2006, Elsevier). 237-297.
3. G.-L. Song, *Corrosion Electrochemistry of Magnesium (Mg) and its Alloys*, in *Corrosion of Magnesium Alloys*, G.-L. Song, Editor. 2011, Woodhead Publisher. p. 3-65.
4. A. Pardo, M.C. Merino, A.E. Coy, F. Viejo, R. Arrabal, and S. Feliu Jr., *Electrochim. Acta*, **53** (2008) 7890-7902
5. P. Kurze, *Corrosion and Surface Protections*, in *Magnesium Technology - Metallurgy, Design Data, Applications*, H.E. Friedrich and B.L. Mordike, Editors. 2006, Springer - Verlag. p. 431-433.
6. B.A. Shaw and R.C. Wolfe, *Corrosion of Magnesium and Magnesium-Base Alloys*, in *ASM Handbook*. 2005, ASM International. p. 205-227.
7. R. Winston Revie, *Uhlig's Corrosion Handbook*. 2nd Ed.(2000, John Wiley & Sons). 796-801.
8. B.L. Luan, D. Yang, X.Y. Liu, and G.L. Song, *Corrosion of Magnesium Alloys*, G.-L. Song, Editor. 2011, Woodhead Publisher. p. 543-563.
9. R.G. Buchheit and A.E. Hughes, *Chromate and Chromate-Free Conversion Coatings*, in *ASM Handbook - Corrosion Fundamentals, Testing and Protection*, S.D. Cramer and B.S.C. Jr., Editors. 2003, ASM International. p. 720-735.
10. A. Shkurankov, S. Abedin, and F. Endres, *Aust. J. Chem.*, **60** (2007) 35-42
11. J. Sun, P.C. Howlett, D.R. MacFarlane, J. Lin, and M. Forsyth, *Electrochim. Acta*, **54** (2008) 254-260
12. A.B. Tolstoguzov, U. Bardi, and S.P. Chenakin, *Izv. Ross. Akad. Nauk*, **72** (2008) 641-644
13. P.C. Howlett, D.R. MacFarlane, and A.F. Hollenkamp, *Electrochem. Solid-State Lett.*, **7** (2004) A97-A101
14. P.C. Howlett, N. Brack, A.F. Hollenkamp, M. Forsyth, and D.R. MacFarlane, *J. Electrochem. Soc.*, **153** (2006) A595-A606
15. P. Wang, S.M. Zakeeruddin, J.E. Moser, and M. Gratzel, *J. Phys. Chem. B*, **107** (2003) 13280-13285
16. D.D. Shivagan, P.J. Dale, A.P. Samantilleke, and L.M. Peter, *Thin Solid Films*, **515** (2007) 5899-5903
17. J.L. Sola Cervera and A. Konig, *Chem. Eng. Technol.*, **33** (2010) 1979-1988
18. G. Yue, S. Zhang, Y. Zhu, X. Lu, S. Li, and Z. Li, *AIChE*, **55** (2009) 783-796
19. M. Uerdengen, C. Treber, M. Balsler, G. Schmitt, and C. Werner, *Green Chem.*, **7** (2005) 321-325
20. S. Caporali, F. Ghezzi, A. Giorgetti, A. Lavacchi, A. Tolstogouzov, and U. Bardi, *Adv. Eng. Mater.*, **9** (2007) 185-190
21. M. Forsyth, P.C. Howlett, S.K. Tan, D.R. MacFarlane, and N. Birbilis, *Electrochem. Solid-State Lett.*, **9** (2006) B52-B55
22. N. Birbilis, P.C. Howlett, D.R. MacFarlane, and M. Forsyth, *Surf. Coat. Technol.*, **201** (2007) 4496-4504

23. P.C. Howlett, T. Khoo, G. Mooketsi, J. Efthimiadis, D.R. MacFarlane, and M. Forsyth, *Electrochim. Acta*, **55** (2010) 2377-2383
24. J. Efthimiadis, W.C. Neil, A. Bunter, P.C. Howlett, B.R.W. Hinton, D.R. MacFarlane, and M. Forsyth, *ACS Appl. Mater. Interfaces*, **2** (2010) 1317-1323
25. K. Harboudt, *Magnesium Technology - Metallurgy, Design Data, Applications*, H.E. Friedrich and B.L. Mordike, Editors. 2006, Springer - Verlag. p. 1-25.
26. E. Ghali, *Corrosion Resistance of Aluminum and Magnesium Alloys: Understanding, Performance, and Testing*.(2010, John Wiley & Sons, Inc.). 319-347.
27. *ASM Handbook - Properties and Selection: Nonferrous Alloys and Special-Purpose Materials*, A.I.H. Comitee. Vol. 2.(1990, ASM International).
28. S. Schumann and H. Friedrich, *Magnesium Technology - Metallurgy, Design Data, Applications*, H.E. Friedrich and B.L. Mordike, Editors. 2006, Springer-Verlag. p. 499-526.
29. M. Flores, L. Huerta, R. Escamilla, E. Andrade, and S. Muhl, *Appl. Surf. Sci.*, **253** (2007) 7192-7196
30. F.H. Froes, D. Eliezer, and E. Aghion, *Magnesium Technology - Metallurgy, Design Data, Applications*, H.E. Friedrich and B.L. Mordike, Editors. 2006, Springer - Verlag. p. 607-620.
31. R. Arrabal, A. Pardo, M.C. Merino, S. Merino, M. Mohedano, and P. Casajus, *Mater. Corros.*, **62** (2011) 326-334
32. *Military Handbook - MIL-HDBK-5H: Metallic Materials and Elements for Aerospace Vehicle Structures*.(1998, U.S. Department of Defense).
33. MatWeb. Available from: <http://www.matweb.com/>.
34. E. Ghali, *Activity and Passivity of Magnesium (Mg) and its Alloys*, in *Corrosion of Magnesium Alloys*, G.-L. Song, Editor. 2011, Woodhead Publisher. p. 66-114.
35. Y. Fan, G. Wu, H. Gao, and C. Zhai, *J. Electrochem. Soc.*, **153** (2006) B283-B288
36. T. Zhang, *Corrosion of Magnesium Alloys*, G.-L. Song, Editor. 2011, Woodhead Publisher. p. 166-172.
37. Guangling Song, Andrej Atrens, Xianliang Wu, and Bo Zhang, *Corrosion Science*, **40** (1998) 1769-1791
38. Guangling Song, Andrej Atrens, and Matthew Dargusch, *Corrosion Science*, **41** (1998) 249-273
39. Y.L. Song, Y. H. Liu, S.R. Yu, X.Y. Zhu, and S.H. Wang, *J. Mater. Sci.*, **42** (2007) 4435-4440
40. E. Ghali, *Corrosion Resistance of Aluminium and Magnesium Alloys: Understanding, Performance, and Testing*.(2010, John Wiley & Sons, Inc.). 348-.
41. G. Song and A. Atrens, *Adv. Eng. Mater.*, **5** (2003) 837-858
42. U.C. Nwaogu, C. Blawert, N. Scharnagl, W. Dietzel, and K.U. Kainer, *Corros. Sci.*, **51** (2009) 2544-2556
43. R. Supplit, T. Koch, and U. Schubert, *Corros. Sci.*, **49** (2007) 3015-3023
44. F. Zucchi, V. Grassi, A. Frignani, C. Monticelli, and FG. TrabANELLI, *Surf. Coat. Technol.*, **200** (2006) 4136-4143
45. K. Brunelli, M. Dabala, I. Calliari, and M. Magrini, *Corros. Sci.*, **47** (2005) 989-1000
46. Xiaowei Yang, Guixiang Wang, Guojun Dong, Fan Gong, and Milin Zhang, *Journal of Alloys and Compounds*, **487** (2009) 64-68

47. Lingjie Li, Jinglei Lei, Shenghai Yu, Yujing Tian, Qiquan Jiang, and Fusheng Pan, *Journal of Rare Earths*, **26** (2008) 383-387
48. A. E. Hughes, J. D. Gorman, and P. J. K. Paterson, *Corrosion Science*, **38** (1996) 1957-1976
49. *Corrosion*, L.L. Shreir, R.A. Jarman, and G.T. Burstein, Editors. 1994, Elsevier. p. 108-114.
50. J.E. Gray and B. Luan, *J. Alloys Compd.*, **336** (2002) 88-113
51. D. Hawke and D.L. Albright, *Metal Finishings*, **93** (1995) 34
52. M. Zhao, S. Wu, J. Luo, Y. Fukuda, and H. Nakae, *Surf. Coat. Technol.*, **200** (2006) 5407-5412
53. X. Lei, G. Yu, X. Gao, L. Ye, J. Zhang, and B. Hu, *Surf. Coat. Technol.*, **205** (2011) 4058-4063
54. Yu Shengxue, Lü Qiaoyan, Han Jing, Zhang Zhanwei, and Zhang Qianyun, *Journal of Rare Earths*, **24** (2006) 397-400
55. Amy L. Rudd, Carmel B. Breslin, and Florian Mansfeld, *Corrosion Science*, **42** (2000) 275-288
56. C. S. Lin and S. K. Fang, *Journal of the Electrochemical Society*, **152** (2005) B54-B59
57. R. F. Zheng and C. H. Liang, *Materials and Corrosion*, **58** (2007) 193-197
58. Zhiyi Yong, Jin Zhu, Cheng Qiu, and Yali Liu, *Applied Surface Science*, **255** (2008) 1672-1680
59. Guixiang Wang, Milin Zhang, and Ruizhi Wu, *Applied Surface Science*, **258** (2012) 2648-2654
60. J. D. Gorman, S. T. Johnson, P. N. Johnston, P. J. K. Paterson, and A. E. Hughes, *Corrosion Science*, **38** (1996) 1977-1990
61. L. Yang, M. Zhang, C. Lin, and J. Wu, *Adv. Eng. Mater.*, **308-310** (2011) 2458-2462
62. Xu Yang, Fusheng Pan, and Dingfei Zhang, *Applied Surface Science*, **255** (2008) 1782-1789
63. Xiufang Cui, Qingfen Li, Ying Li, Fuhui Wang, Guo Jin, and Minghui Ding, *Applied Surface Science*, **255** (2008) 2098-2103
64. Xiaoming Chen, Guangyu Li, Jianshe Lian, and Qing Jiang, *Applied Surface Science*, **255** (2008) 2322-2328
65. R.-G. Hu, S. Zhang, J.-F. Bu, C.-J. Lin, and G.-L. Song, *Prog. Org. Coat.*, **73** (2012) 129-141
66. S.V. Lamaka, M.F. Montemor, A.F. Galio, M.L. Zheludkevich, C. Trindade, L.F. Dick, and M.G.S. Ferreira, *Electrochim. Acta*, **53** (2008) 4773-4783
67. Z.-L. Wang and R.-C. Zeng, *Trans. Nonferrous Met. Soc. China*, **20** (2010) s655-s669
68. L.-P. Wu, J.-J. Zhao, Y.-P. Xie, and Yang Z.-D, *Trans. Nonferrous Met. Soc. China*, **20** (2010) s630-s637
69. Z. Zhang, G. Yu, Y. Ouyang, X. He, B. Hu, J. Zhang, and Z. Wu, *Appl. Surf. Sci.*, **255** (2009) 7773-7779
70. C.A. Huang, T.H. Wang, T. Weirich, and V. Neubert, *Electrochim. Acta*, **53** (2008) 7235-7241
71. X.L. Gao, G. Yu, Y.J. Ouyang, J.L. Chen, X.P. Lei, and Y. Chen, *Surface Eng.*, **24** (2008) 295-300
72. P. Zhu, X. Zhang, J. Wu, Y. Xu, and M. Zhou, *Adv. Mater. Research*, **145-147** (2011) 1390-1397
73. Hui Zhao, Zhanghong Huang, and Jianzhong Cui, *Microelectronic Engineering*, **85** (2008) 253-258

74. G.L. Song and Z. Shi, *Overview of Anodizing Techniques*, in *Corrosion of Magnesium Alloys*, G.L. Song, Editor. 2011, Woodhead Publishing. p. 565-614.
75. Z. Shi, G. Song, and A. Atrens, *Corros. Sci.*, **48** (2006) 1939-1959
76. Z. Shi, G. Song, and A. Atrens, *Corros. Sci.*, **48** (2006) 3531-3546
77. Y. Zhang, C. Yan, F. Wang, H. Lou, and C. Cao, *Surf. Coat. Technol.*, **161** (2002) 36-43
78. C.S. Wu, Z. Zhang, F.H. Cao, L.J. Zhang, J.Q. Zhang, and C.N. Cao, *Appl. Surf. Sci.*, **253** (2007) 3893-3898
79. S.J. Xia, R. Yue, R.G. Rateieck, and V.I. Birss, *J. Electrochem. Soc.*, **151** (2004) B179-B187
80. G.-L. Song, *Surf. Coat. Technol.*, **203** (2009) 3618-3625
81. K.N. Marsh, J.A. Boxall, and R. Lichtenhaler, *Fluid Phase Equilib.*, **219** (2004) 93-98
82. T. Welton, *Chem. Rev.*, **99** (1999) 2071-2083
83. K.J. Fraser and D.R. MacFarlane, *Aust. J. Chem.*, **62** (2009) 309-321
84. M.C. Buzzeo, C. Hardacre, and R.G. Compton, *Chem. Phys. Chem.*, **7** (2006) 176-180
85. Yunqiao Pu, Nan Jiang, and Arthur J. Ragauskas, *Journal of Wood Chemistry and Technology*, **27** (2007) 23-33
86. Zhao-Tie Liu, Li-Hong Shen, Zhong-Wen Liu, and Jian Lu, *Journal of Materials Science*, **44** (2009) 1813-1820
87. P.-Y. Chen and C.L. Hussey, *Electrochim. Acta*, **52** (2007) 1857-1864
88. J. Mun, T. Yim, C.Y. Choi, J.H. Ryu, Y.G. Kim, and S.M. Oh, *Electrochem. Solid State Lett.*, **13** (2010) A109-A111
89. J.M. Wang, J.B. Wang, H.B. Shao, X.X. Zheng, J.Q. Zhang, and C.N. Cao, *Mater. Corros.*, **60** (2009) 977-981
90. T. Khoo, P.C. Howlett, M. Tsagouria, D.R. MacFarlane, and M. Forsyth, *Electrochim. Acta*, **58** (2011) 583-588
91. H. Ashassi-Sorkhabi and M. Es'haghi, *Mater. Chem. Phys.*, **114** (2009) 267-271
92. P.-C. Lin, I.-W. Sun, J.-K. Chang, C.-J. Su, and J.-C. Lin, *Corros. Sci.*, **53** (2011) 4318-4323
93. Tseng C.-H, J.-K. Chang, J.-R. Chen, W.T. Tsai, M.-J. Deng, and I.-W. Sun, *Electrochem. Commun.*, **12** (2010) 1091-1094
94. U. Bardi, S.P. Chenakin, S. Caporali, A. Lavacchi, I. Perissi, and A. Tolstogousov, *Surf. Interface Anal.*, **38** (2006) 1768-1772
95. I. Perissi, U. Bardi, S. Caporali, and A. Lavacchi, *Corros. Sci.*, **48** (2006) 2349-2362
96. P.C. Howlett, S. Zhang, D.R. MacFarlane, and M. Forsyth, *Aust. J. Chem.*, **60** (2007) 43-46
97. P.C. Howlett, W. Neil, T. Khoo, J. Sun, M. Forsyth, and D.R. MacFarlane, *Israel J. Chem.*, **48** (2008)
98. P. Zanello, *Voltammetric Techniques*, in *Inorganic Electrochemistry: Theory, Practice and Application*. 2003, The Royal Society of Chemistry. p. 49-134.
99. S. Higson, *Analytical Chemistry*. 2004, Oxford University Press. p. 295-299.
100. Robert J. Flanagan, David Perrett, and Robin Whelpton, *Electrochemical Detection in HPLC - Analysis of Drugs and Poisons*. 2005, Royal Society of Chemistry.
101. P. Zanello, *Voltammetric techniques*, in *Inorganic Electrochemistry*. 2003, The Royal Society of Chemistry. p. 49-136.

102. D.C. Silverman, *Practical Corrosion Prediction Using Electrochemical Techniques*, in *Uhlig's Corrosion Handbook*, R. Revie, Editor. 2011, John Wiley & Sons. p. 1129-1166.
103. E.C. Bucharsky and J.R. Vilche, *Laboratory Corrosion Monitoring of Zn-Rich Paint Coatings on Naval Steel in Seawater by Electrochemical Methods*, in *Organic and Inorganic Coatings for Corrosion Prevention - Research and Experiences: (EFC 20)*, L. Fedrizzi and L. Bonora, Editors. 1997, Maney Publishing. p. 2-22.
104. D. A. Jones, *Electrochemical Kinetics of Corrosion*, in *Principles and Prevention of Corrosion*. 1996, Prentice Hall: U.S.A. p. 75-115.
105. R. Amini and A.A. Sarabi, *Appl. Surf. Sci.*, **257** (2011) 7134-7139
106. M. Mahdavian and M. M. Attar, *Corrosion Science*, **48** (2006) 4152-4157
107. M. Anik and G. Celikten, *Corros. Sci.*, **49** (2007) 1878-1894
108. M. Zhao, S. Wu, P. An, and J. Luo, *Appl. Surf. Sci.*, **253** (2006) 468-475
109. X.G. Han, X.P. Zhu, and M.K. Lei, *Surf. Coat. Technol.*, **206** (2011) 874-878
110. M.A Jingling, W. Jiuba, L.I. Gengxin, and X.V. Chunhua, *Corros. Sci.*, **52** (2010) 534-539
111. F. Mansfeld, *Electrochim. Acta*, **38** (1993) 1891-1897
112. M.C. Isa, M.Y. Ahmad, A.R. Daud, and M. Daud, *Key Eng. Mater.*, **442** (2010) 322-329
113. P.L. Cabot, J.A. Garrido, E. Perez, A.H. Moreira, P.T.A. Sumodjo, and W. Proud, *Electrochim. Acta*, **40** (1995) 447-454
114. D. Britz, *J. Electroanal. Chem.*, **88** (1978) 309-352
115. Z. Guo and X. Lin, *J. Electroanal. Chem.*, **568** (2004) 45-53
116. C. Amatore, E. Maisonhaute, and G. Simonneau, *J. Electroanal. Chem.*, **486** (2000) 141-155
117. V. Brunetti and M.L. Teijelo, *J. Electroanal. Chem.*, **613** (2008) 16-22
118. O.E. Linarez Perez, V.C. Fuertes, M.A. Perez, and M.L. Teijelo, *Electrochem. Commun.*, **10** (2008) 433-437
119. Hochun Lee, Feng Xu, Carol S. Jeffcoate, and Hugh S. Isaacs, *Electrochemical and Solid-State Letters*, **4** (2001) B31-B34
120. D.E. Williams and G.A. Wright, *Electrochim. Acta*, **21** (1975) 1009-1019
121. M. Santamaria, F. Di Quarto, S. Zanna, and P. Marcus, *Electrochimica Acta*, **56** (2011) 10533-10542
122. R. Kirchheim, *Kinetics of Film Formation on Fe-Cr Alloys*, in *Modifications of Passive Films: (EFC 12)*, P. Marcus, B. Baroux, and M. Keddam, Editors. 1994, Maney Publishing. p. 102-107.
123. Runduo Zhang, Houshang Alamdari, and Serge Kaliaguine, *Applied Catalysis A: General*, **340** (2008) 140-151
124. Chett J. Boxley and Henry S. White, *Journal of the Electrochemical Society*, **151** (2004) B265-B270
125. O. Khaselev and J. Yahalom, *J. Electrochem. Soc.*, **145** (1998) 190-193
126. D.A. Vermilyea, *J. Electrochem. Soc.*, **102** (1955) 207-214
127. D.A. Vermilyea, *J. Electrochem. Soc.*, **104** (1957) 542-546
128. Q. Van Overmeere and J. Proost, *Electrochim. Acta*, **55** (2010) 4653-4660
129. J. Yahalom and J. Zahavi, *Electrochim. Acta*, **15** (1970) 1429-1435
130. S. Verdier, M. Boinet, S. Maximovitch, and F. Dalard, *Corros. Sci.*, **47** (2005) 1429-1444
131. K. Shimizu, G.E. Thompson, and G.C. Wood, *Thin Solid Films*, **92** (1982) 231-241
132. V.R. Howes, *Corros. Sci.*, **14** (1974) 491-502
133. A.K. Vijh, *Corros. Sci.*, **11** (1971) 411-417

134. L. C. Archibald and J. S. L. Leach, *Electrochimica Acta*, **22** (1977) 15-20
135. S. Feliu Jr., C. Mattiotte, J.C. Galvan, and V. Barranco, *Corros. Sci.*, **53** (2011) 1865-1872
136. G. Song, A. Atrens, D. St John, X. Wu, and J. Nairn, *Corros. Sci.*, **39** (1997) 1981-2004
137. L. Wu and Z. Yang, *Adv. Mater. Research*, **189-193** (2011) 279-285
138. Y. Zhu, G. Yu, B. Hu, X. Lei, H. Yi, and J. Zhang, *Appl. Surf. Sci.*, **2010** (2010) 2988-2994
139. D. Orlov, K.D. Ralston, N. Birbilis, and Y. Estrin, *Acta Mater.*, **59** (2011) 6176-6186
140. B. Rodgers. 23/03/12]; Available from: <http://www.consultsr.com/resources/eis/cpecalc.htm>.
141. D. Tie, F. Feyerabend, N. Hort, R. Willumeit, and D. Hoeche, *Adv. Eng. Mater.*, **12** (2010) B699-B704
142. J.F. Moulder, W.F. Stickle, P.E. Sobol, and K.D. Bomben, *Handbook of X-Ray Photoelectron Spectroscopy*, J. Chastain and R.C.K. Jr.(1995, Chigasaki, ULVAC-PHI).
143. A. M. Puziy, O.I. Poddubnaya, R.P. Socha, J. Gurgul, and M. Wisniewski, *Carbon*, **46** (2008) 2113-2123
144. H.S. Liu, T.S. Chin, and S.W. Yang, *Mater. Chem. Phys.*, **50** (1997) 1-10
145. H.-Y. Hsiao and W.-T. Tsai, *Surf. Coat. Technol.*, **190** (2005) 299-308
146. U. Braun, B. Schartel, M.A. Fichera, and C. Jager, *Polym. Degrad. Stabil.*, **92** (2007) 1528-1545
147. S. Mohapatra and P. Pramanik, *Colloid Surface A*, **339** (2009) 35-42
148. Q. Li, X. Wang, D. Wang, W. Xiong, G. Zhong, and Y. Wang, *J. Appl. Polym. Sci.*, **117** (2010) 3066-3074
149. M.E. Fleet, X. Liu, and X. Wang, *J. Non-Cryst. Solids.*, **355** (2009) 2604-2609
150. H. Yan, X. Zhang, L. Wei, X. Liu, and B. Xu, *Powder Technol.*, **193** (2009) 125-129
151. S.S. Singh, *Mat. Sci. Eng. B-Solid*, **176** (2011) 1695-1702
152. Yanying Zhu, Guangming Wu, Yun-Hong Zhang, and Qing Zhao, *Applied Surface Science*, **257** (2011) 6129-6137
153. K. Faghihi and K. Zamani, *Appl. Polym. Sci.*, **101** (2006) 4263-4269
154. X. Wang, Y. Hu, L. Song, W. Xing, and H. Lu, *Prog. Org. Coat.*, **71** (2011) 72-82
155. J.-A. Latham, P. C. Howlett, D.R. MacFarlane, and M. Forsyth, *Electrochim. Acta*, **56** (2011) 5328-5334

Appendices

Appendix A: Electrochemical Behaviour of GC in Wet IL and in an Argon Glovebox.

Figure A.1 shows two plots of the anodic and cathodic response of glassy carbon polarised to 3 V and -3 V vs. Pt with excess water. The differences between a and b exist from the use of two different batches of IL. Both ILs were purified using the same method.

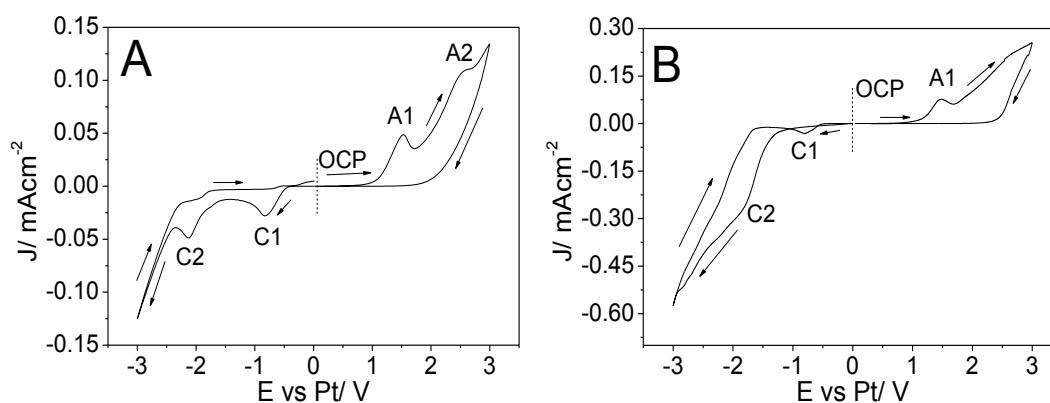


Figure A. 1 – Cyclic voltammogram of two separate scans on glassy carbon: 1) polarised from OCP (approx 0 V vs. Pt) to 3 V vs. Pt at 1 mV/s and 2) polarised from OCP to -3 V vs. Pt at 1 mV/s. C1 and C2 denote the cathodic reaction peaks and A1 and A2 the anodic peaks. Arrows indicate the direction of the scans. Dashed line indicates OCP.

The general behaviour of the curves are similar to the dried condition (Figure 4.1); however, in both of the cathodic scans a new peak (C1) has appeared at approximately -0.8 V vs. Pt and the original water peak in Figure A.1 a) has been shifted to -2.1 V vs. Pt (C2). In comparison, the water peak in Figure A.1 b) is still at -1.7 V, coinciding with the dry condition.

Similar behaviour is observed in the anodic scans. However, in both scans the water peak remains in the same position at approximately 1.5 V vs. Pt (A1). However, particularly in Figure A.1 a), a new peak (A2) at approximately 2.5 V vs. Pt is observed. This peak is not resolved in Figure A.1 b), but the change in slope at 2.5 V vs. Pt may be from the same reaction as the distinct peak formed in Figure A.1 a). With the addition of significant levels of water the current densities of the reactions, particularly those involved directly with the water, should increase. Figure 4.1 a shows a current density of approximately -0.02 mAcm^{-2} for the reduction of water and approximately 0.005 mAcm^{-2} for oxidation. Figure A.1 shows the cathodic reaction increasing by a factor of 2.6 and the anodic reaction increasing by a factor of 10.

One possible explanation for the new shapes of the curves may be due to different physical states of the water. That is, bound water and free water. Since the only change to the system was the introduction of 60,000 ppm water, it would be a logical assumption to say that the new reaction peaks are related to the water in the IL. Despite $[\text{P}_{6,6,6,14}][(\text{C}_8)_2\text{PO}_2]$ being classified as a hydrophobic IL (due to primarily hydrocarbon chains), during drying the IL does not easily give up water: requiring several hours at very low vacuum to remove to levels around 200 ppm. If the container the dried IL is kept in is not maintained under vacuum or a dry atmosphere the IL will quickly absorb up to 1000 ppm of water more readily than desiccant. Hence, the IL has a high affinity for water at lower levels. As mentioned previously, the IL's equilibrium water content from the atmosphere is approximately 6 wt% (60,000 ppm). Therefore, with all of this

in mind the IL must have a strong interaction with water at low levels. It is expected that water levels between a minimum 0-2500 ppm are physically bound to the IL through electrostatic interactions. Water molecules that interact with the IL will require a greater potential to reduce than those which are not directly interacting (free water). In the dry condition the water peaks exist at approximately ± 1.7 V vs. Pt, which is relatively high. However, whilst this is interesting in itself regarding the nature of water reactions in the IL system at different concentrations, the focus of this thesis lies primarily on the behaviour on AZ31. Hence, the analysis of this reaction on GC is beyond the scope of this work and will not be further tackled here.

Figure A.2 shows a CV of GC in the dry IL (approx. 950-1000 ppm water) cycled between OCP and 3 V vs. Pt (a and b) and OCP and -3 V vs. Pt (a and c). Interestingly, as with the behaviour of GC with 6 wt% water (Figure 4.12) the behaviour is slightly different from a past CV measurement (Figure A.2 a) to more recently performed CVs using a different batch of IL and experimental set-up (Figure 4.15 b & c).

In Figure A.2 a), no water reaction peaks are visible, despite the IL containing at least 1000 ppm at the time of the experiment. As a result, this scan shows the electrochemical window to be approximately 4 V. In comparison, the scans in Figure A.2 b) and c) show water peaks in both the anodic and cathodic scans (A2, C1 and C2). The peaks are the same as those which appear in the wet condition in Figure A.1, however the anodic water peak A2 is more prominent in the argon environment. This anodic water peak is present in the subsequent cycles in Figure 16 b, however in the cathodic scan in Figure 16 c the water reduction peaks are only present in the initial scan. It was initially hypothesised that the lack of water peaks in Figure A.2 a) was due to oxygen being directly involved in the reduction of water, as per Eqn. A.1[155].

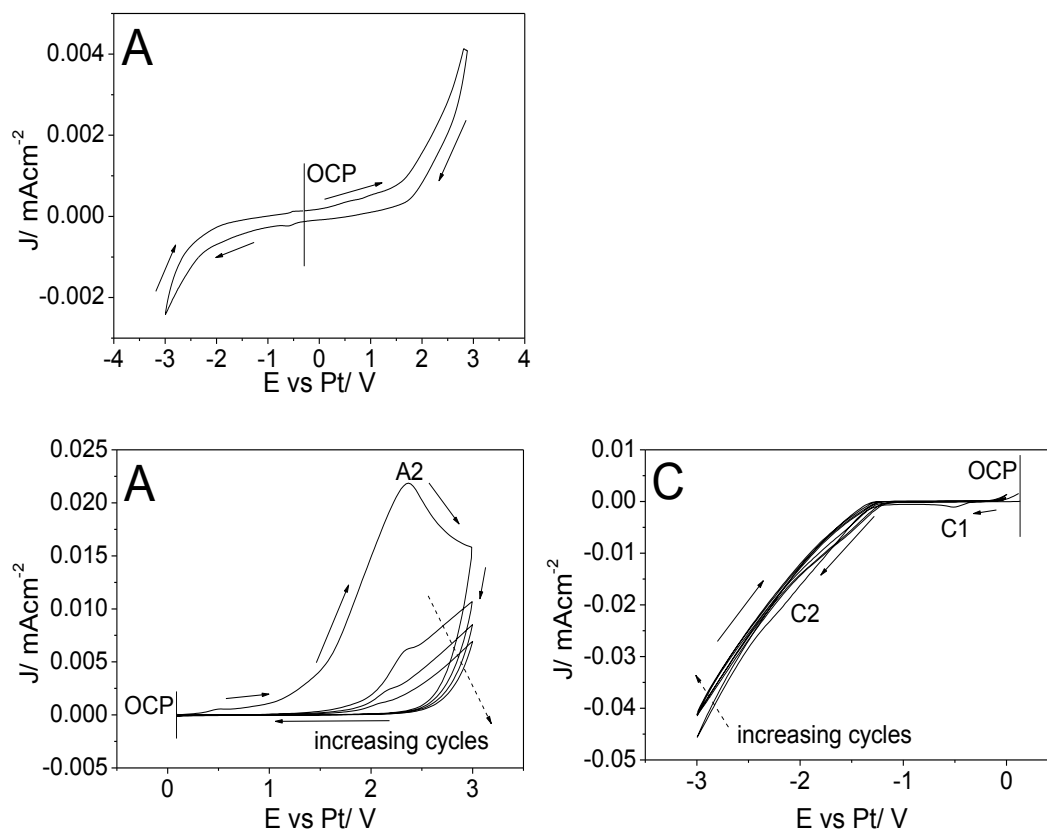
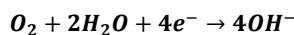


Figure A. 2 - Cyclic voltammograms of glassy carbon in dry IL in glovebox a) OCP to 3 V \leftrightarrow -3 V vs. Pt at 1 mV/s (old IL batch), b) OCP to 3 V at 1 mV/s (new IL batch) and c) OCP to -3 V at 1 mV/s (new IL batch).



Eqn. A. 1

However, the difference between Figure A.2 a) and c) suggests that this may not be the case. As just mentioned, the cathodic peaks are not only very small in their respective currents (C2 hardly more than a slight bump along the way to IL reduction) but they only appear in the first scan (whereas in the 6 wt% condition the water peaks continue to occur in following scans). Hence, small amounts of dissolved oxygen may be available to react with the system, which is exhausted by the subsequent cycles. However, it is not clear why the behaviour in Figure A.2 b) has changed. In particular, why the oxidation reaction occurs only at approximately 2.5 V vs. Pt, as opposed to 1.5-1.7 V vs. Pt (dry and open to air) or both (wet).

Appendix B: XPS of Neat $[\text{P}_{6,6,6,14}][(\text{C}_8)_2\text{PO}_2]$ IL and Untreated AZ31

In order to set a baseline for the species present on IL-treated AZ31 surfaces, XPS was initially conducted on the neat IL. This is possible due to the very low volatility of ILs, allowing them to be placed under high vacuum. We were lucky enough to perform this XPS at the Australian Synchrotron, and were thus able to use a variety of energies for the incident X-ray beam for surface analysis (see literature review for more information on Synchrotron XPS vs. regular XPS). Control over the beam energy meant the technique can be made more or less surface sensitive, thus effectively allowing for depth analysis. E.g. using energy of 790 eV obtains spectra from a shallower cross section of the surface as opposed to 1486 eV, which is the energy used in typical XPS instruments.

The IL was prepared by placing a small volume of IL into a gold (Au) foil dish. Excess IL was removed using a Kimwipe®: leaving a small layer of the IL for analysis. Figure B.1 shows the chemical structure of the IL used in this work. The structure shows the presence of four separate elements: H, C, P and O. However, spectra can only be obtained for C, P and O, which will hence be presented and discussed.

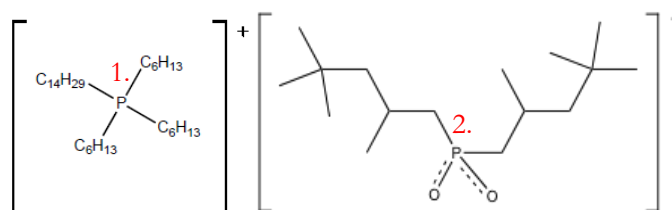


Figure B. 1 – Structure of [P_{6,6,6,14}][(i-C₈)₂PO₂].

Figure B.2 compares the XPS surveys of the IL at 1486 eV and 790 eV. C, O and P from the IL are all indicated on the image. However, along with these expected peaks two Si peaks were also identified at approximately 100 eV (2p) and 150 eV (2s). Prior to analysis via XPS, this IL was passed through a purification column containing a very fine filter agent comprised of SiO₂. Therefore some of the SiO₂ must have been dissolved into the collected IL. Table 4.7 shows the atomic composition of the IL based on 1486 eV survey spectrum.

Table B. 1 - at% of elements found in XPS survey and the expected quantity based on chemical composition.

Element	O 1s	C 1s	P 2p	Si 2p
Survey	10.9	78.1	3.3	7.6
Excl. Si	11.8	84.6	3.6	-
Expected	2.5	95	2.5	-

Whilst we expect a measurable amount of Si due to purification, the at% calculated from the data suggests there is a significant amount of Si in solution. In addition, the Si count is even higher in the 790 eV survey (Figure B.2 b). Inductively coupled plasma spectroscopy (ICP) analysis of the IL after purification revealed only a small amount of Si at < 1 mg/L in 1 mL/L of IL in solvent.

With approximately 892 mg IL per mL[83] this equates to 0.0011 wt% and approximately 0.00004 at% Si, which is much lower than the values from XPS. Hence, the excess Si may be due to contamination on the surface due to adventitious Si or Si from silicon grease used in the instrument.

The O 1s count in Table C.1 is also unexpectedly high. Based on the chemical structure of this IL there should be 95 at% C and 2.5 at% each of O and P. The P 2p count was close to the expected levels (3.6 at%), however the O 1s count was considerably greater (11.8 at%) than it should be. This is likely the result of the presence of dissolved water in the IL (which may have been around 6 wt % at the time of the test).

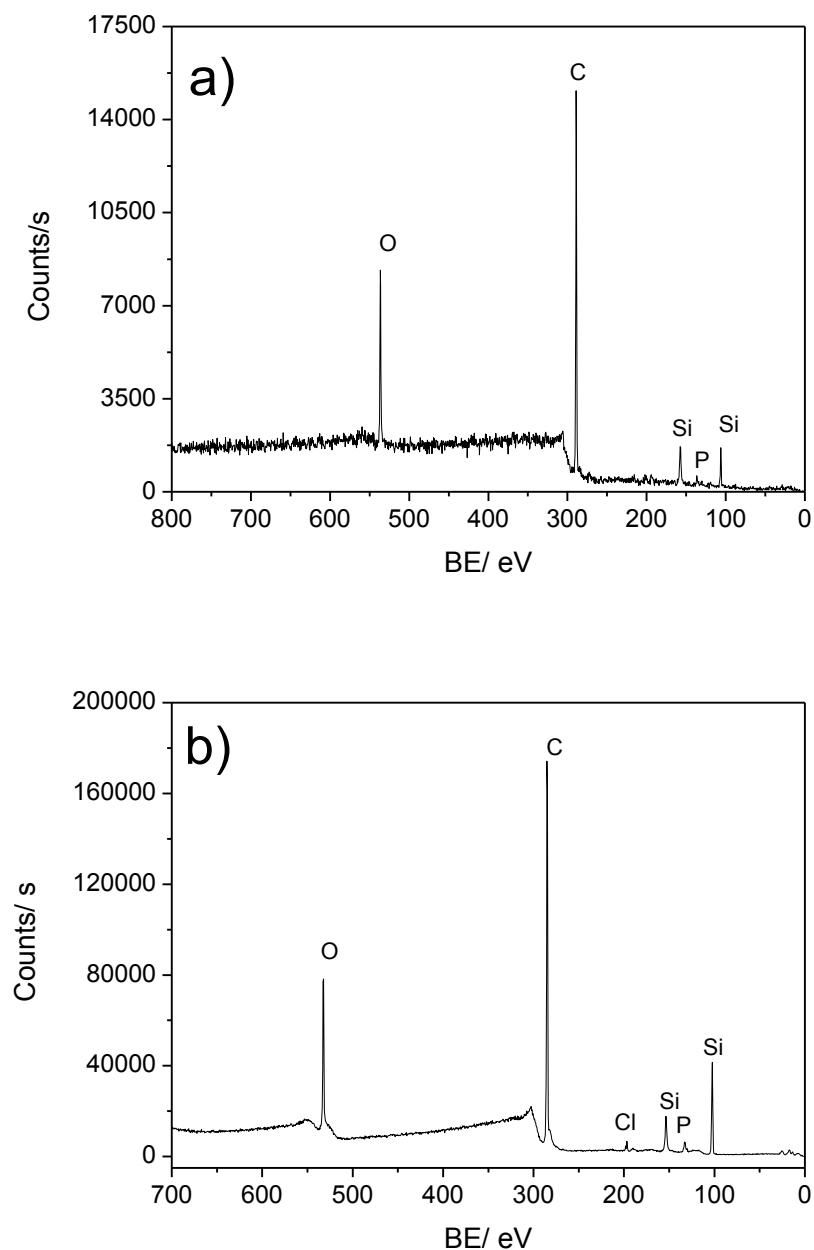


Figure B. 2 – XPS survey of purified neat IL on Au foil at a) 1486 eV and b) 790 eV.

Figure B.3 a)-d) compares the P spectra at 180 eV, 330 eV, 530 eV and 1486 eV respectively. As illustrated in Figure B.1 the P atom in $[P_{6,6,6,14}][[(C_8)_2PO_2]$ exists in two states (red numbers), based on whether it is from the anion or the cation. Two main peaks were identified at binding energies of 129.3-131.1 and 132.1-133.8 eV (as well as the doublets at slightly higher binding energy). The bonding of P to O is more electronegative than P to C (due to O being more electronegative than C), therefore the shift from elemental P (129.9 eV[142]) will be greater. Hence, the peak between 132.1-133.8 eV can be associated with the alkylphosphate in the anion of the IL. Hence, the peak at the lower binding energy (129.3-131.1 eV) must be the organophosphorus bond of the cation.

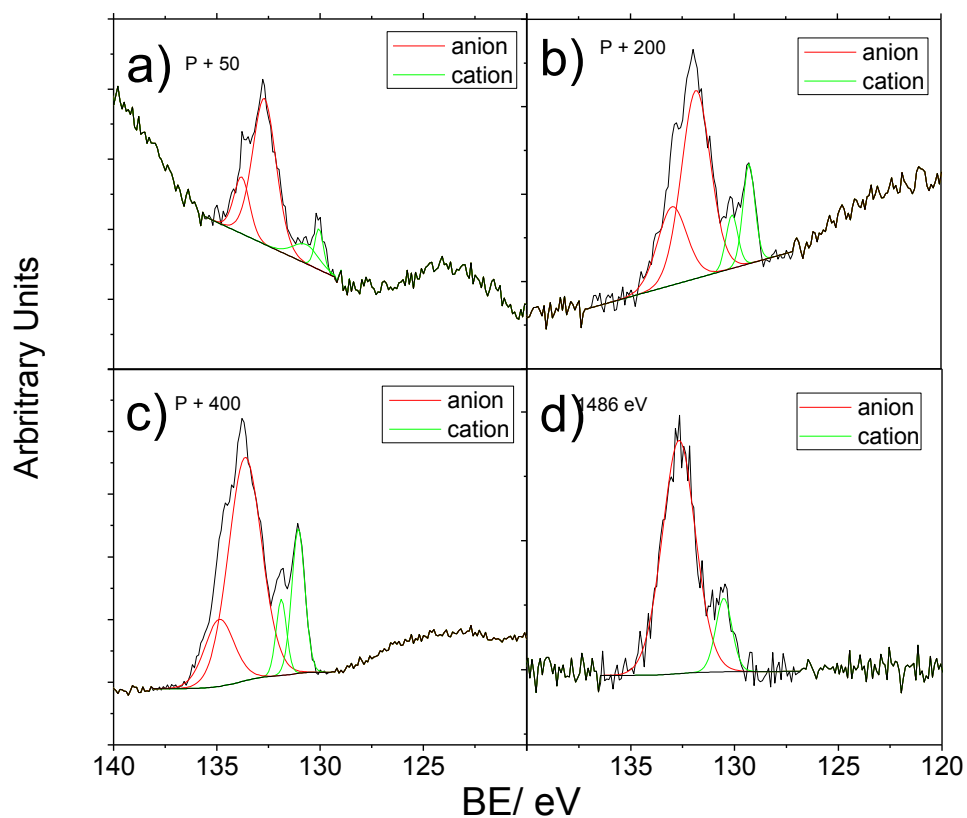


Figure B. 3 – XPS spectra of P2p region at a) 180 eV; b) 330 eV; c) 530 eV; d) 1486 eV.

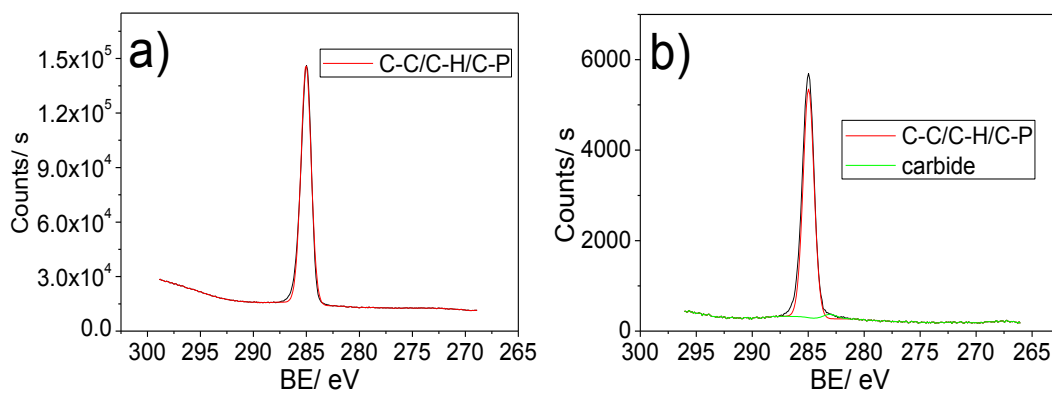


Figure B. 4 – XPS spectra of C1s region at a) 335 eV; b) 1486 eV.

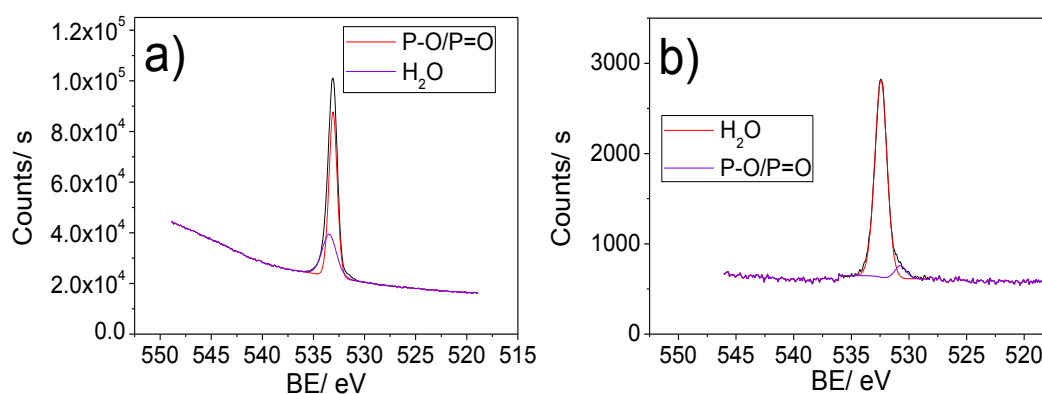


Figure B. 5 – XPS spectra of O1s region at a) 580 eV; b) 1486 eV.

Figure B.4 compare the C 1s regions of the IL at 335 and 1486 eV. In $[P_{6,6,6,14}][[(C_8)_2PO_2]$, carbon is bonded to H atoms, other C atoms and P atoms. C-C and C-H bonds exist at 285 eV, which are exhibited by the large peak in Figure B.4. A small peak at approximately 282.9 eV corresponds to carbide[142]. The carbide may have come about through the same means as the Si, as activated carbon was also used in the purification column. However, the surface sensitivity of this peak suggests the contamination may have occurred during handling or from the instrument.

Figure B.5 compares XPS spectra in the O 1s region at 580 and 1486 eV. The state of O in the IL exists in a shared single and double bond with the P atom in the anion: P-O and P=O. However, water present in the IL will also contribute to the peak. The literature notes P-O and P=O bonds have binding energies at 531.2 eV[144] and water has a binding energy of 533.2 eV[142]. The two peaks in Figure 4.50 do not sit exactly where expected, being at 533.5 and 533.08 eV and 532.4 and 530.7 for Figure B.5 a) and b) respectively. However, there should be no other bond types in the IL. The area ratios for the two peaks show larger amounts of the anion at the surface than in the bulk. However, in the bulk of the IL there is considerably more H_2O , which considering this IL likely had several thousand ppm of water at the time of analysis is not surprising.

Summary

Due to the basic structure of the IL, the XPS data associated with this compound is also very basic. This means that the process of peak fitting is relatively simple, but it also means that differentiating between components of the anion from those of the cation is extremely difficult.

From the chemical structure in Figure B.1 we know that there are only two P atoms per IL. Hence, the relative intensities of the alkylphosphinate and the organophosphorus should be equal. However, the relative intensity of the alkylphosphinate peak is significantly greater at all energies (often more than 100% larger), which suggests the presence of excess anion. However, the possibility of excess anion does not adequately explain this dramatic difference. Instead, this may be indicative of the morphology of the IL in its liquid state. The application of a range of energies, varying from very low to very high, eliminates the hypothesis of the effect of layering of the anion and cation (as there is no trend). The anion appears to be shielding the cation from interaction with the x-ray beam of the XPS, reducing its sensitivity. This could mean that the long-range order of the IL involves the anion encapsulating the cation.

Also, despite the presence of C-P bonds in the IL from both the anion and cation, no distinguishable C-P peak was identified in the C 1s region in Figure 4.47. However, these C-P bonds occur a lot less than the C-C and C-H bonds and thus the intensity of this peak will be

much lower. However, the energy of the C-P bond is very close to the C-C and C-H bonds[143], making it hard to distinguish. In particular the C1s peak is highly symmetrical, which makes it very hard to fit a peak for the C-P bond.

Untreated AZ31

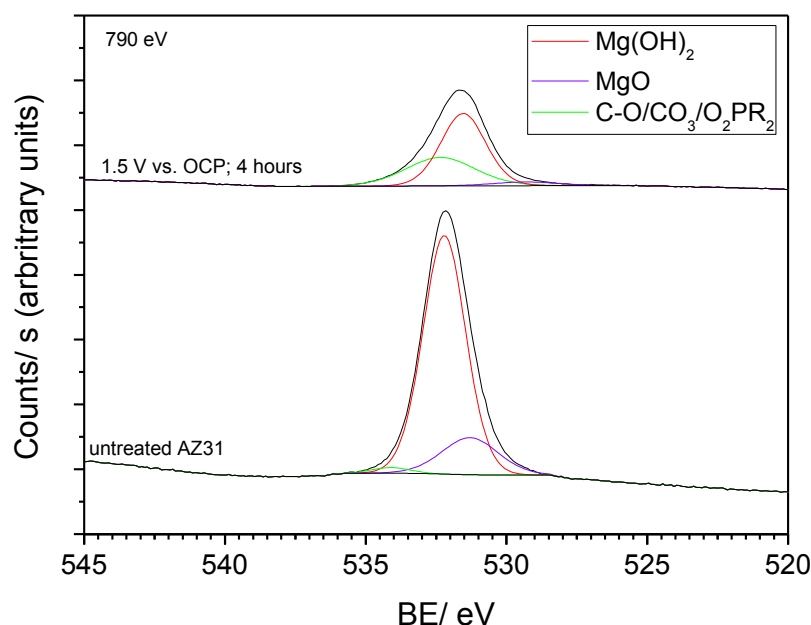


Figure B. 6 – O 1s spectra obtained at 790 eV of untreated AZ31 and AZ31 treated in IL at 1.5 V vs. OCP for 4 hours. O_2PR_2 = phosphinate.

The O 1s spectra of the untreated AZ31 surface (Figure B.6) shows magnesium hydroxide ($Mg(OH)_2$) and magnesium oxide (MgO) as the main constituents. These species exist as part of the native film on magnesium alloys. The higher proportion of $Mg(OH)_2$ to MgO is due to the reaction of water with MgO from the moisture in the air. Also, a small quantity of carbonate (CO_3^{2-}) is also present from the reaction of CO_2 in the air with the substrate. As a comparison, the O 1s spectrum for a treated AZ31 surface is also present. The treated surface has significantly reduced peak intensity than the blank AZ31 surface. This suggests that the IL film formed during treatment may mask much of the signal originally from the native film on AZ31.

Figure B.7 compares the Mg 2p spectra of the same surfaces. Interestingly, the Mg 2p peak is larger after treatment than when bare. The amount of $Mg(OH)_2$ is reduced after treatment and the peak at higher energy is larger, which may be due to the bonding between Mg and the IL anion.

These spectra suggest that most of the Mg present in the IL treated surfaces is due to the interaction with the IL. Mg is forced to oxidise to Mg^{2+} under the influence of the anodic current, which causes it to migrate through the surface film to react with IL at the electrolyte/surface interface. Due to the relatively small quantity of water in the IL we would expect that some $Mg(OH)_2$ would be produced. As there insufficient water present to support considerable growth of $Mg(OH)_2$ the quantity is decreased with anodic treatment (as the IL film covers the majority from the native film).

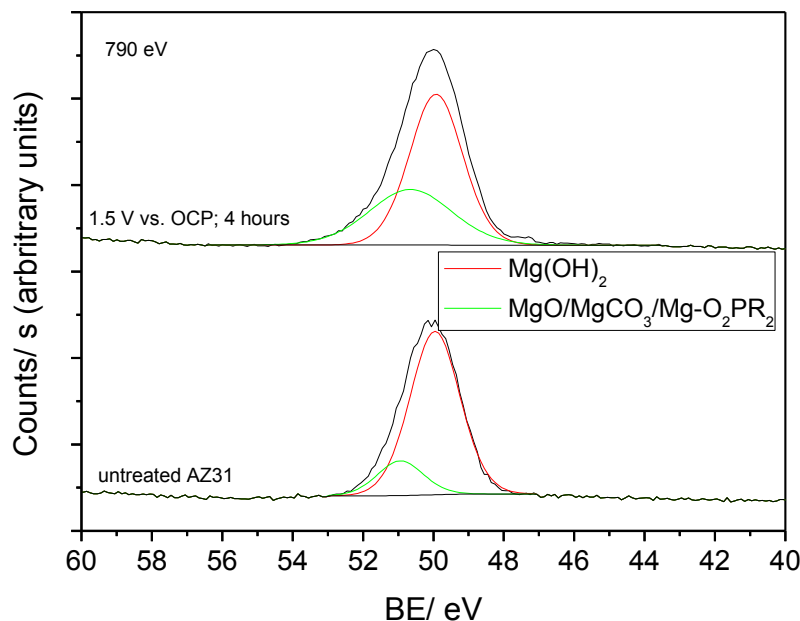


Figure B. 7 – Mg 2p spectra obtained at 790 eV of untreated AZ31 and AZ31 treated in IL at 1.5 V vs. OCP for 4 hours. O₂PR₂ = phosphinate.

Appendix C: Table of XPS %area Fits

Table C. 1 - % area of separate peaks in the C 1s and O 1s spectrums at 790 and 1486 eV for CP 1 and 2. Binding energies for the peaks are indicated in brackets in eV.

Peaks		-0.4 V vs. OCP; 4 hours		1.5 V vs. OCP; 4 hours	
		790	1486	790	1486
C 1s	C-C/C-H	50.5 (284.9)	47.3(284.9)	50.6 (284.9)	57.19 (285.0)
	CO ₃ ⁻	8.2 (289.4)	13.1 (289.2)	3.9 (289.8)	7.9 (289.5)
	Carbide	20.4 (281.1)	-	17.2 (280.9)	-
O 1s	Mg(OH) ₂	73.9 (531.7)	82.3 (531.6)	59.5 (531.5)	71.6 (531.4)
	MgO	2.7 (529.2)	3.0 (528.9)	4.4 (529.3)	3.6 (529.0)
	PO ₄ ⁻ /CO ₃ ⁻	23.4 (532.5)	14.7 (532.6)	36.1 (532.3)	24.8 (532.4)

Table C. 2 - %area composition of numerous species from the C1s and O 1s spectra. Binding energies for the peaks are indicated in brackets in eV.

Peaks		0.1 mAcm ⁻²	0.01 mAcm ⁻²	0.5 mAcm ⁻²	0.01 mAcm ⁻² ; 18V 4 hours
C 1s	C-C/C-H	61.1 (285.1)	57.1 (285)	49.4 (285)	35.4 (284.9)
	CO ₃ ⁻	26.8 (290)	18.4 (290)	21.2 (290.4)	23.0 (290.2)
	CO ₂ [?]	12.2 (287)	24.6 (286.2)	23.4 (285.9)	34.0 (285.2)
O 1s	Mg(OH) ₂	66.3 (531.9)	79.6 (531.9)	76.8 (531.9)	80.6 (531.8)
	MgO	0.7 (529.8)	-	1.1 (529.6)	4.7 (529.9)
	PO ₄ ⁻ /CO ₃ ⁻	33.1 (532.6)	20.4 (533.4)	22.1 (532.9)	14.7 (532.4)

Appendix D: Fits of Equivalent Circuits of IL Films

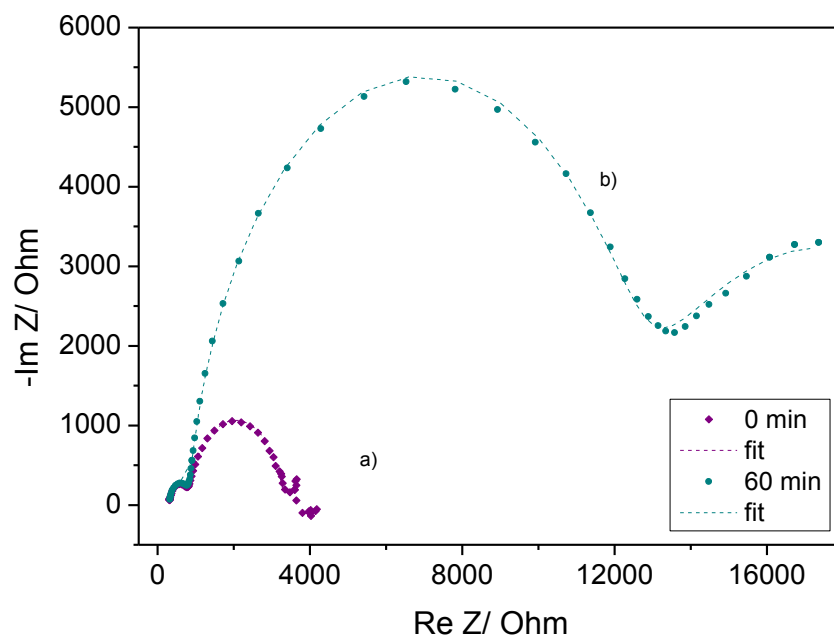


Figure D. 1 - Example of the correlation of the proposed model of the equivalent circuit in Figure 4.61 a) and b) on as-polished AZ31.

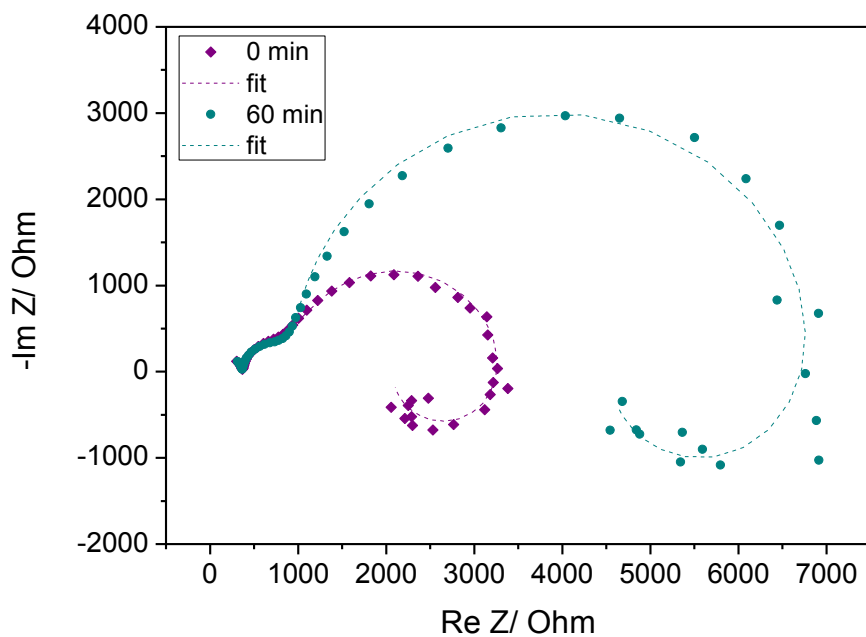


Figure D. 2 – Example of the correlation of the proposed model of the equivalent circuit in Figure 4.61 c) on AZ31 surfaces showing low frequency inductive behaviour.

Appendix E: SEM and EDS of Field Crystallised Films

Figure E.1 shows a secondary electron image for field crystallised AZ31 treated at 3 V and 50°C for 96 hours (corresponding to Figure 4.29 c) of the optical profilometry). Figure E.1 b) and c) show the corresponding EDS of points 1 and 2 on Figure E.1 a). Figure E.1 b) shows the response generated from the bulk of the uniformly crystallised film. The counts for Mg and O are close, which suggest the film is predominantly comprised of MgO. Point 2 on Figure E.1 a) is a point of localised breakdown shown earlier in Figure 4.28 d) in section 4.2.1.2.1. The EDS spectrum for this region has more O than Mg. Given this is a point of breakdown it would not be surprising if a large constituent of it is Mg(OH)₂ as well as MgO, which would give rise to the greater O count.

In general, whilst high counts for Mg and O were observed over the entire surface, no detectable amount of P was identified. Due to the considerable thickness of these films this absence is unlikely to be due to the depth of interaction of the x-ray beam. Therefore, field crystallisation must result in the formation of oxides on the AZ31 surface as opposed to a film containing components of the IL. This suggests the typically amorphous Mg(OH)₂ film has been crystallised to MgO. Of course it is still possible that a small amount of IL is present that has not been detected by this method.

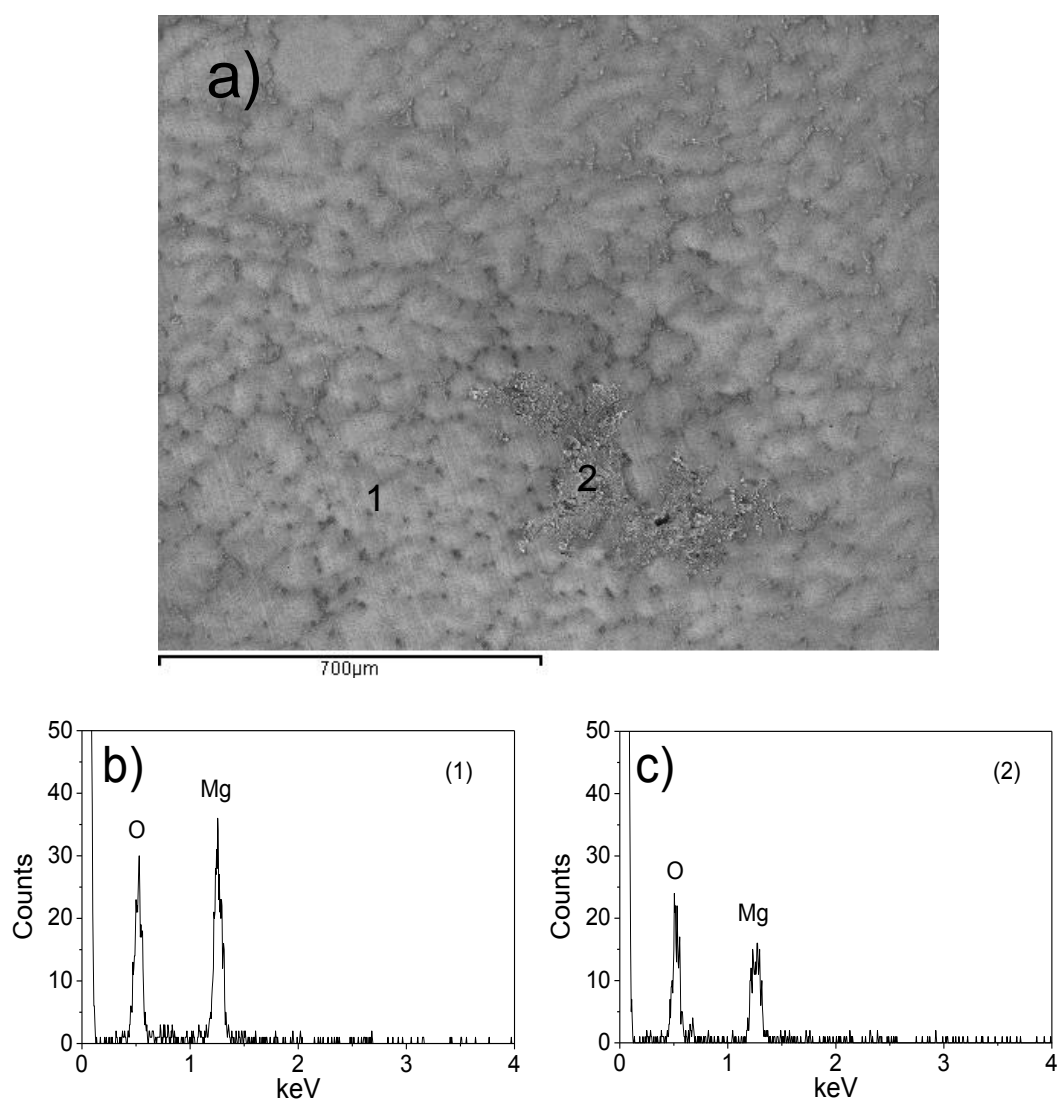


Figure E. 1 – a) Secondary electron image of AZ31 anodised at a constant voltage of 3 V vs. Pt at 50°C for 96 hours after field crystallisation; b) EDS of point 1 and c) EDS of point 2.

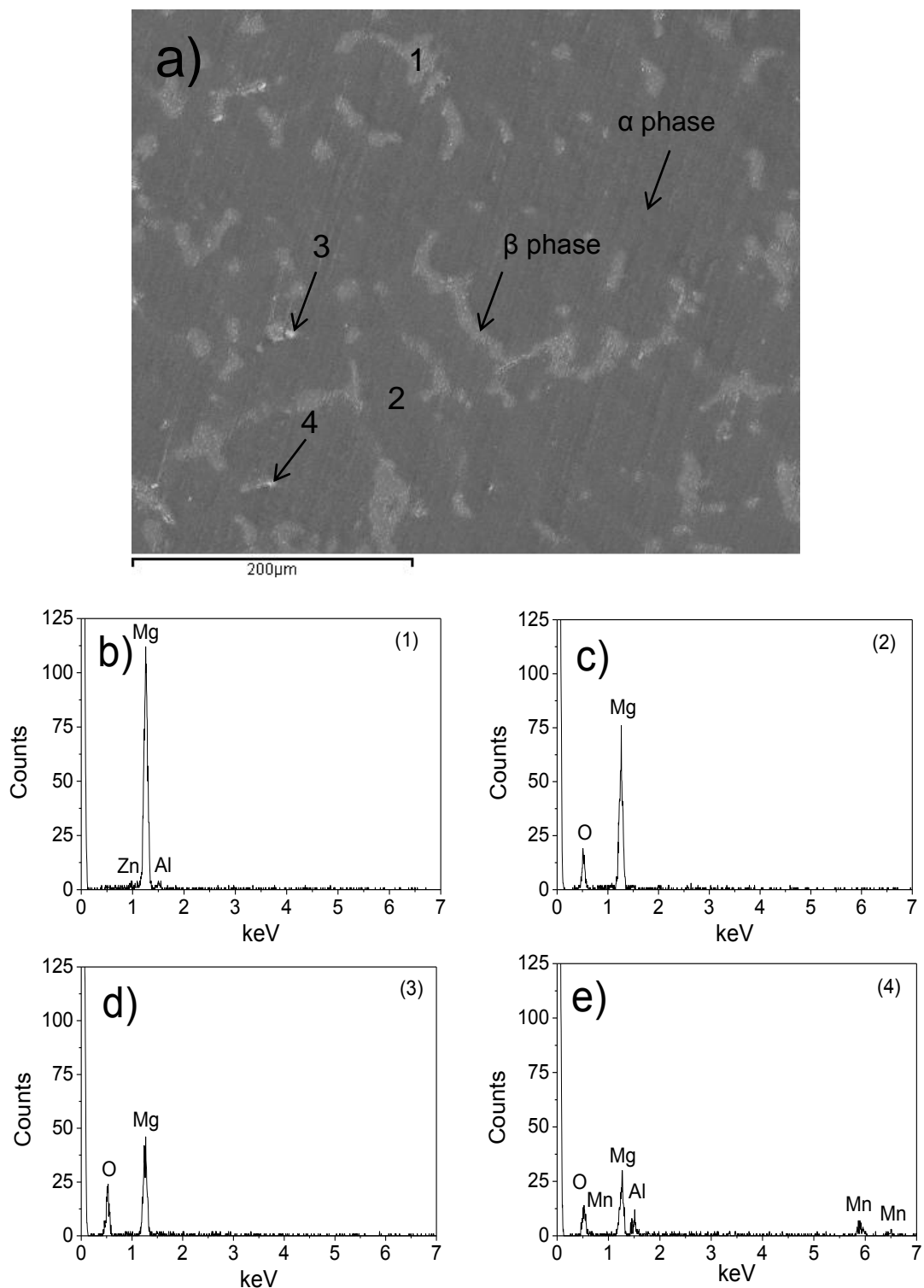


Figure E. 2 – a) Secondary electron image of AZ31 anodised at a constant voltage of 3 V vs. Pt at 50°C for 48 hours after field crystallisation; b) EDS of point 1; c) EDS of point 2; d) EDS of point 3 and e) EDS of point 4.

Figure E.2 shows the appearance of a crystallised film formed at 3 V and 50°C for 48 hours. EDS spectra taken from points 1-4 on Figure E.2 are presented in Figures E.2 b)-e) respectively. The surface film in Figures E.1 a) and E.2 a) show that the films formed are fairly uniform in deposition, at least over the α phase. The optical profilometry presented in section 4.2.1.2.1 showed preferential film deposition over α phase as opposed to β phase based on height and roughness information. EDS analysis in Figure E.2 confirms this. Spectral information over the β phase (Figure E.2 b) shows the presence of Mg, Al and Zn without a distinct O peak. The

especially large Mg peak is most likely due to interaction of the electrons with α phase below the β phase analysed. The lack of O and any other elements apart from those present in the base alloy confirms that the crystalline oxide does not nucleate over the β phase. This is especially apparent when the spectrum is compared to the spectrum in Figure E.2 c) of the α phase. In this case a large O peak and larger Mg peak are detected. The difference in qualitative ratio (Mg:O) in Figure E.2 c) vs. Figure E.1 b) is likely due to film thickness (with greater thickness for 96 hours as opposed to 48).

Figures E.2 d) and e) are the spectra obtained from particles identified on the surface. Unlike the spectra over the β phase there is a considerable amount of O detected in both cases. These particles likely act as nucleation points in the microstructure for film crystallisation. The lack of O over the β phase is not surprising. As pointed out previously in section 4.2, anodic film growth does not occur over the β phase at potentials less than 80 V. Therefore, due to the amorphous film growth being preferential over the α phase there is no film over the β phase to crystallise.

Appendix F: $[P_{6,6,6,14}][(^iC_8)_2PO_2]$ as an Inhibitor

Despite $[P_{6,6,6,14}][(^iC_8)_2PO_2]$ being a hydrophobic IL, small concentrations can still be dissolved into water. When this IL was dissolved into an organic solvent (ILAN – 0.1 M IL in acetonitrile) it was still able to act in the same manner as the neat IL and passivate the AZ31 surface (section 4.1.2). This raised the question, can $[P_{6,6,6,14}][(^iC_8)_2PO_2]$ form a film when dilute in water and hence act as an inhibitor against corrosion in a corrosive aqueous media?

To answer this, solutions of 10^{-4} , 1.2×10^{-4} (100 ppm), 6.4×10^{-4} (500 ppm) and 10^{-3} M IL in 0.01M NaCl were prepared. This section outlines a brief look into the possible use of this IL as an inhibitor in corrosive media. EIS, PP, optical microscopy and optical profilometry will be presented to characterise the behaviour of the IL in 0.01 M NaCl.

Electrochemical Inhibitor behaviour: EIS and PP

Figure F.1 shows Nyquist plots of the EIS response obtained from AZ31 exposed to 0.01 M NaCl with and without the addition of a small concentration of IL (1, 1.2, 6.4, 10×10^{-4} M IL). Immediately after immersion (Figure F.1 a) the EIS response consists of a single high frequency capacitive arc and an inductive arc at low frequency. This is a typical EIS response for AZ31 in NaCl solutions, where the capacitive arc can be attributed to a resistor and capacitor in series, which represent the charge transfer resistance and double layer capacitance through the surface film. The low frequency inductive loop indicates that the film on AZ31 (the native oxide layer) is defective and localised corrosion (e.g. pitting) is occurring through these defects.

After 3 hours immersion in the solutions the high frequency capacitive arc has increased for all solutions. In addition, there is no longer a low frequency inductance loop. The order of resistance of the films deposited onto AZ31 in this time is control > 1.2×10^{-4} M > 10^{-4} M > 6.4×10^{-4} M > 10^{-3} M. This suggests the lower concentrations of IL in solution provide better inhibition. However, due to the similar resistance values as the control surface it is hard to distinguish whether the resistance increase of the lower inhibitor solutions (and in fact of any of

the solutions) is due to IL film formation or simply due to the formation of a thick layer of corrosion products.

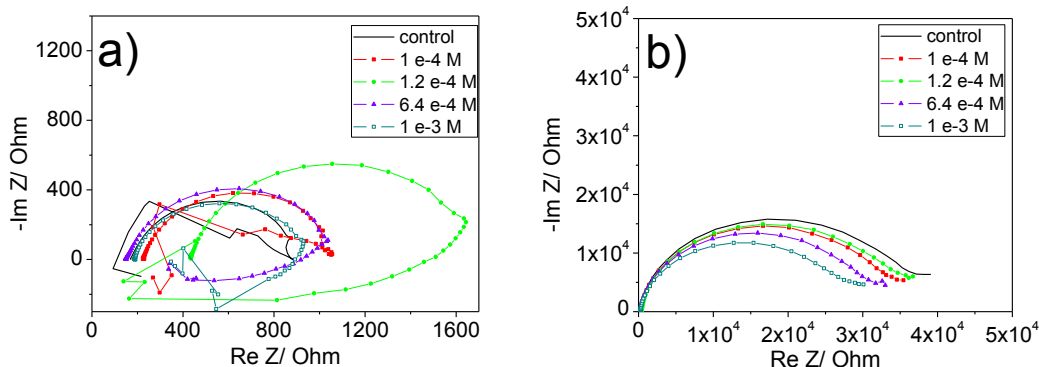


Figure F. 1 – Nyquist plots of AZ31 immersed in 0.01 M NaCl with and without 1, 1.2, 6.4 and 10×10^{-4} M IL after a) immediate immersion and b) 3 hours after immersion.

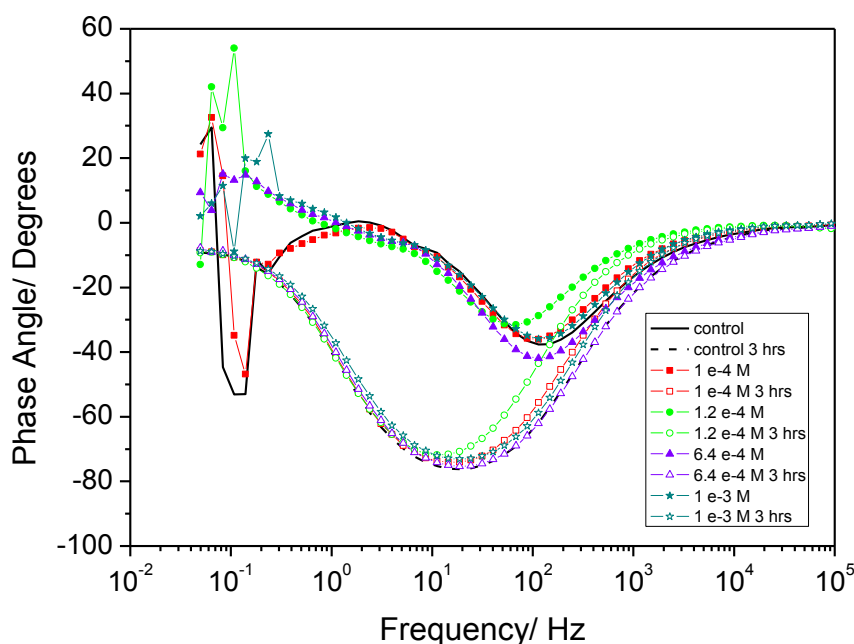


Figure F. 2 - Bode plot of phase angle of AZ31 immersed in 0.01 M NaCl with and without 1, 1.2, 6.4 and 10×10^{-4} M IL for 0 and 3 hours after immersion.

Figure F.2 shows a Bode plot of the phase angles of AZ31 in these solutions immediately after immersion and 3 hours after immersion. Initially the phase angles of the surface films are 37.7° , 36° , 31.6° , 42° and 35.7° for the control solution and IL solutions with 1, 1.2, 6.4 and 10×10^{-4} M concentrations respectively. After 3 hours these values increase to 76.2° , 74.1° , 71.8° , 75.3° and 73.1° . As mentioned previously, the deposition of corrosion products onto the AZ31 surface during corrosion alter the corrosion properties by forming a resistive film. As the phase angles are all very close to the control values, it cannot be said whether any change in these values is due to the IL or the deposition of corrosion product.

Figure F.3 shows PP curves of AZ31 immersed in 0.01 M NaCl (within a pipette cell) with and without the addition of 1.2 and 6.4 $\times 10^{-4}$ M IL for 30 minutes. Tafel fitting was performed 20 mV either side of E_{corr} and the calculated values are tabulated in Table F.1.

With 1.2 $\times 10^{-4}$ M IL the system appears to behave as a weak cathodic inhibitor as there is a consistent cathodic shift in E_{corr} , although the cathodic kinetics (based on β_c) are not lower than the control in all cases. In general the pitting potential is reduced in comparison to the controls. However, most changes between the control scans and those conducted with 1.2 $\times 10^{-4}$ M IL are within experimental scatter ranges.

With 6.4 $\times 10^{-4}$ M IL the system appears to behave as a weak anodic inhibitor. On average the kinetics of the anodic arm have been reduced (β_a being higher), but not significantly. Conversely, the cathodic reaction kinetics have increased (β_c being lower).

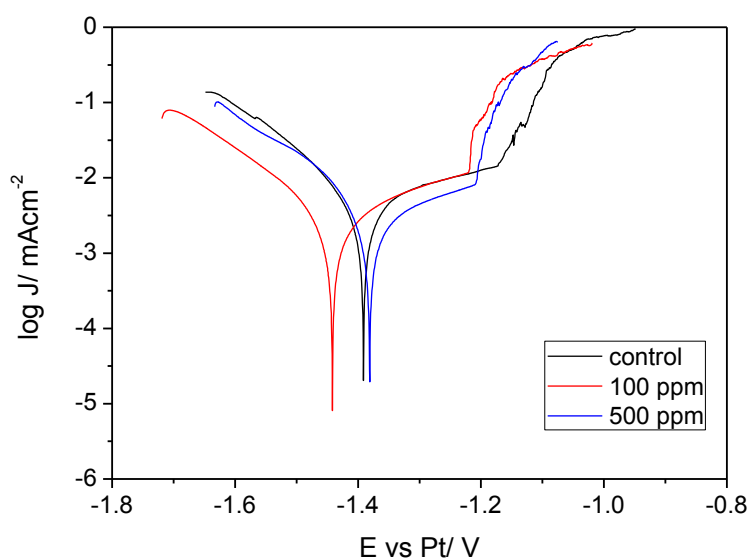


Figure F. 3 – Potentiodynamic polarisation of AZ31 in solutions containing 0.01 M NaCl and 0 (control), 100 and 500 ppm added [P_{6,6,6,14}][(C₈)₂PO₂].

Table F. 1 – Tafel extrapolations of solutions of 0.01 M NaCl containing no (control), 100 and 500 ppm IL.

Solution	E_{corr}	i_{corr}
Control	-1.398 ± 0.011	1.45 ± 0.09
100 ppm	-1.453 ± 0.012	1.3 ± 0.4
500 ppm	-1.41 ± 0.03	1.4 ± 0.5

Immersion Test Within the Pipette Cell

Figure F.4 a)-e) shows optical micrographs of AZ31 exposed to 0.01 M NaCl solution for 3 hours (in the pipette cell) without and with 1, 1.2, 6.4 and 10 $\times 10^{-4}$ M IL respectively. The main mode of corrosion on AZ31 occurs through the formation of clusters of shallow pits over the α phase. The α phase in Figure F.4 a) (the control) is very dark, which suggests considerable levels

of corrosion on this surface. Whilst Figure F.4 b) and c) (10^{-4} M and 1.2×10^{-4} M) are also dark, Figure F.4 d) and e) (6.4×10^{-4} M and 10^{-3} M) are considerably lighter. In fact, if the darkening of the α phase is darkened by the build-up of corrosion product, it appears as though the surface exposed to the solution containing 6.4×10^{-4} M IL has sustained the least amount of corrosion. However, the differences between the degree of corrosion on these surfaces is minor.

Figure F.5 a)-e) show optical profilometry images of AZ31 exposed to 0.01 M NaCl solution for 3 hours (in the pipette cell) without and with 1, 1.2, 6.4 and 10×10^{-4} M IL respectively. Optical profilometry was performed in order to gain a better understanding of the differences in corrosion performance between the surfaces by assessing pit depth. Figure F.5 a) of the control AZ31 immediately displays the degree of the corrosion attack on this surface. This image shows a number of large clusters of pits over the α phase with depths up to $3.37 \mu\text{m}$ (indicated by arrow).

The lowest concentration IL solution (10^{-4} M – Figure F.5 b) was the worst performing of the inhibitor solutions; however the pits on this surface were measured at $1.52 \mu\text{m}$, which is less than half the depth of the pits measured on the control surface.

With increasing IL concentration, the maximum pit depth drops to a minimum of $1.24 \mu\text{m}$ (6.4×10^{-4} M) and rises to $1.27 \mu\text{m}$ for 10^{-3} M IL. Whilst this particular IL is aprotic[83] it is not easily soluble in an aqueous solution. In fact, at higher concentrations the IL will separate as oily conglomerates in the solution. At a concentration of 10^{-3} M the IL is not fully dissolved, which may account for the worsened performance in comparison to the slightly lower concentration of 6.4×10^{-4} M. No noticeable conglomeration of the IL in the 6.4×10^{-4} M was noticed, hence the increased concentration with miscibility likely accounts for the improved resistance to corrosion with this solution.

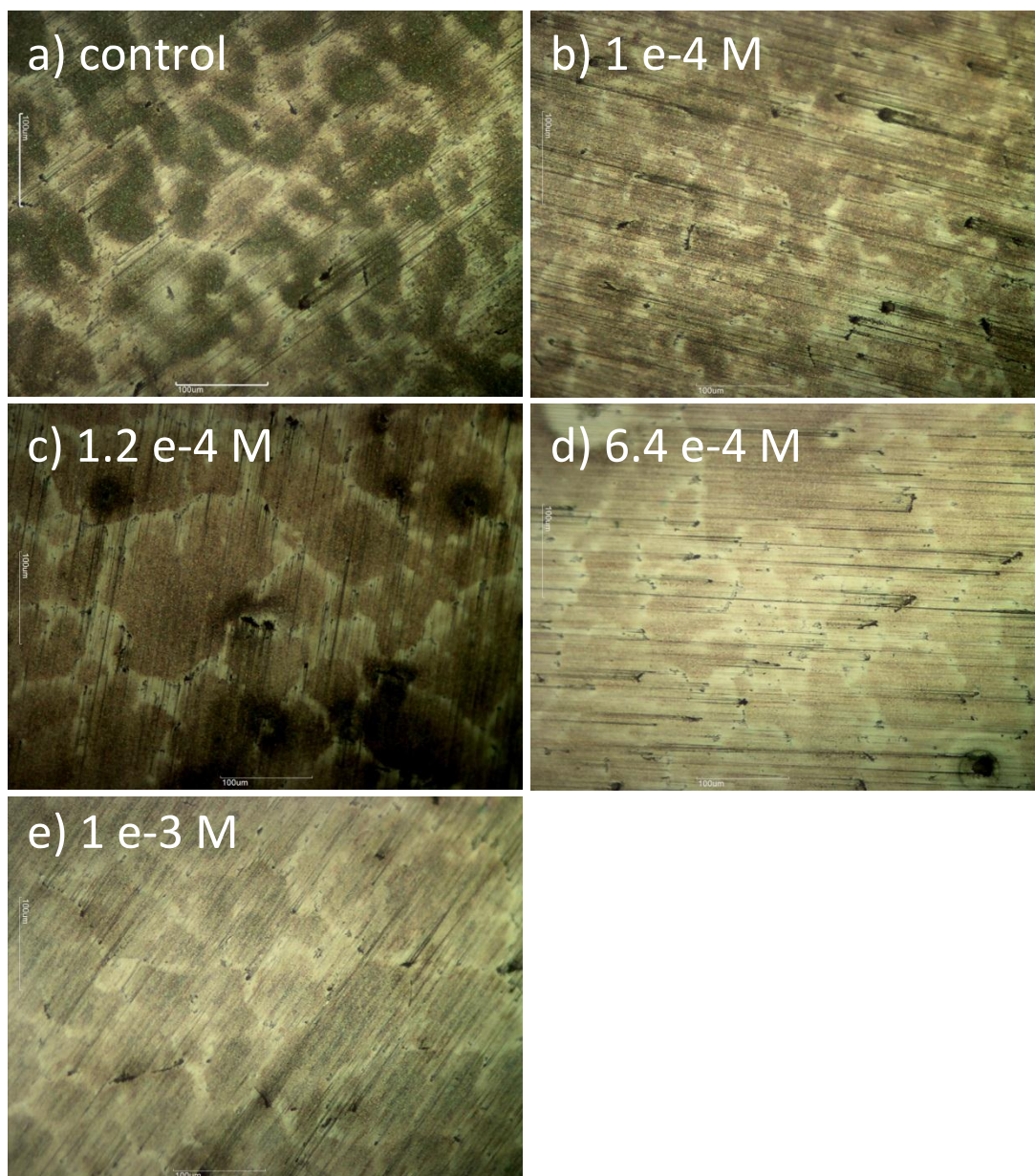
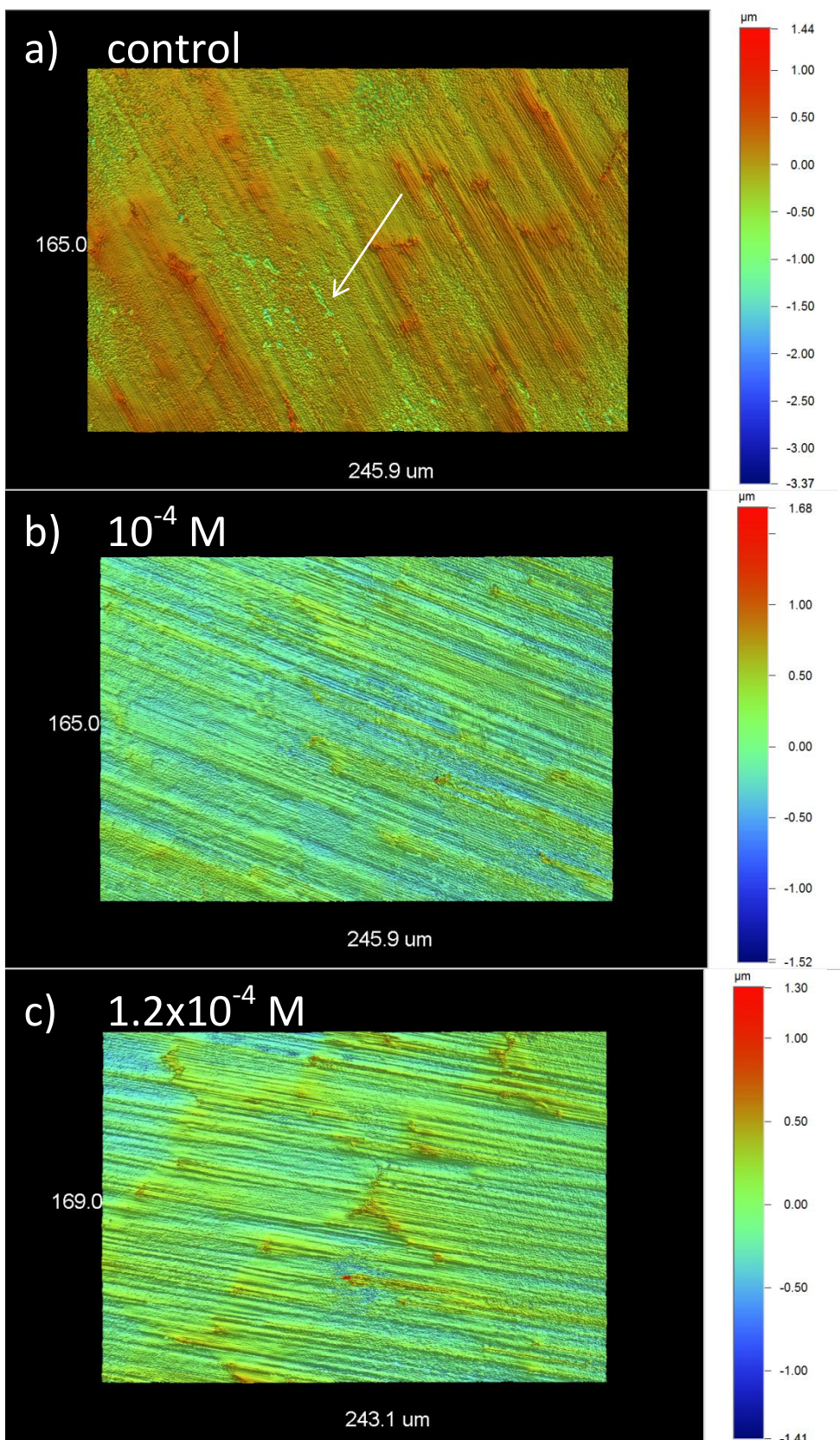


Figure F. 4 – Optical micrographs of AZ31 immersed for 3 hours in a) 0.01 M NaCl; b) 0.01 M NaCl and 10^{-4} M IL; c) 0.01 M NaCl and 1.2×10^{-4} M IL; d) 0.01 M NaCl and 6.4×10^{-4} M IL; e) 0.01 M NaCl and 10^{-3} M IL.



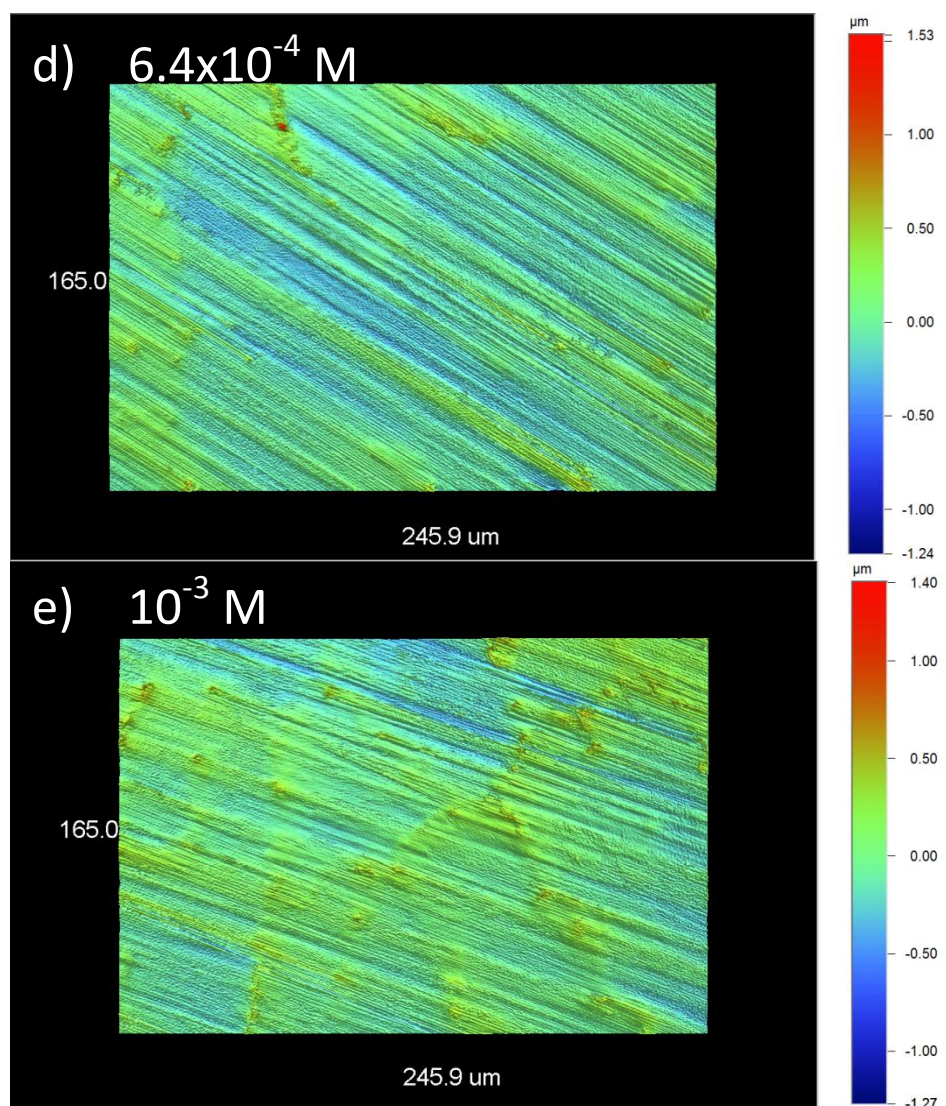


Figure F. 5 – Optical profilometry of AZ31 after 3 hours immersion in neutral 0.01 M with a) 0 M IL; b) 10^{-4} M IL; c) 1.2×10^{-4} M IL; d) 6.4×10^{-4} M IL; e) 10^{-3} M IL.

SEM images in Figures F.6 and F.7 show these surfaces after 3 hours immersion. These images are consistent with the optical profilometry. Clusters of pits are readily visible in Figures F.6 b) and e) and F.7 b) and c).

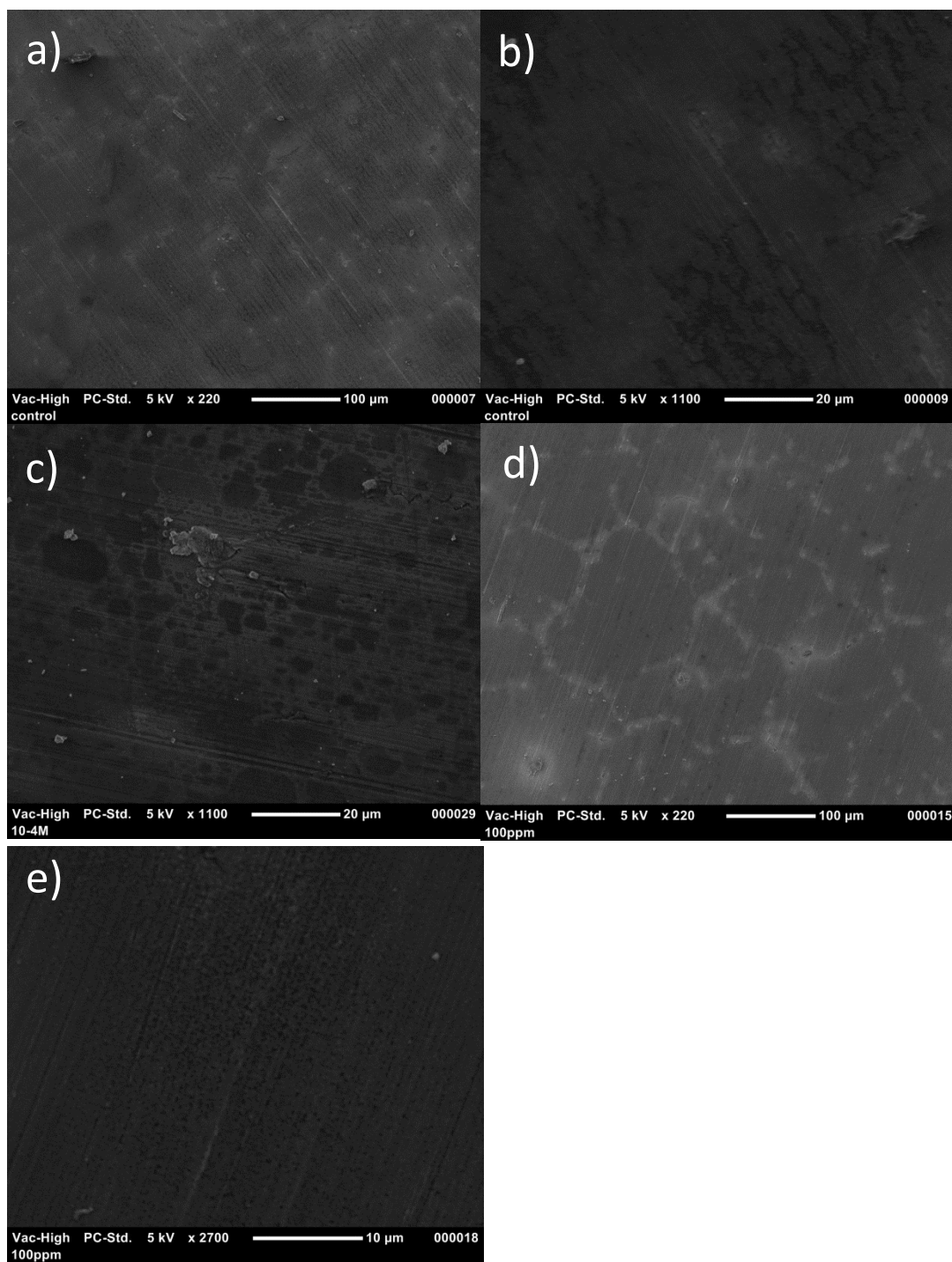


Figure F. 6 – SEM images at 5 keV of AZ31 after 3 hours immersion in a)-b) 0.01 M NaCl; c) 0.01 M NaCl + 10⁻⁴ M IL; d)-e) 0.01 M NaCl + 1.2 x 10⁻⁴ M IL.

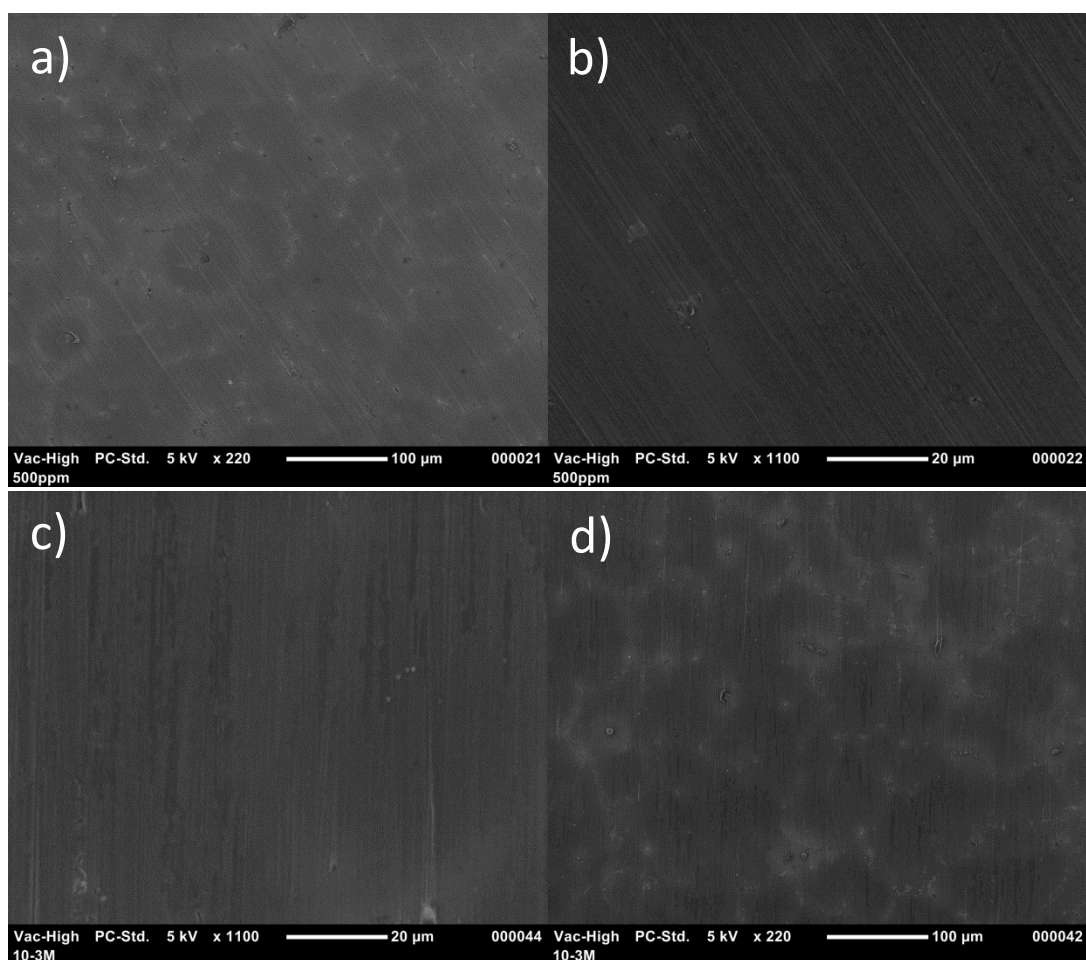


Figure F. 7 – SEM images at 5 keV of AZ31 after 3 hours immersion in a)-b) 0.01 M NaCl + 6.4×10^{-4} M IL; c)-d) 0.01 M NaCl + 10^{-3} M IL.

Key Points

From the results presented in this section, the following key points can be made:

- $[P_{6,6,6,14}][C_8)_2PO_2]$ IL is not a strong inhibitor of AZ31 corrosion in 0.01 M NaCl.
- Electrochemical analysis via EIS and PP did not adequately indicate any change in corrosion performance when IL was introduced into the solutions. However, this may simply be due to the weak inhibiting effect of the IL.
- Visual examination via optical profilometry revealed a reduction of over 50% in pit depth due to the presence of IL, with the greatest reduction of 63% for the solution containing 6.4×10^{-4} M IL.

Whilst the improvement reported here is not particularly high, it shows that it is possible for ILs to be added to an aqueous solution to slow corrosion. Of course, improved IL selection (e.g. hydrophilic, water miscible ILs) is required to take this further, as this data shows that this particular IL is not a suitable candidate for inhibition.

Droplet Corrosion Test

Droplet corrosion tests were conducted. 5 μL droplets of solutions of 0.01 M NaCl without and with the addition of 1.2 and 6.4 $\times 10^{-4}$ M IL were deposited on AZ31 and left in a container containing saturated KCl. Recorded humidity returned levels between 80-90 % R.H. The surfaces were exposed to these droplets for 24 hours. SEM images were obtained and are shown for the control, 1.2 $\times 10^{-4}$ M and 6.4 $\times 10^{-4}$ M IL in Figures F.8, F.9 and F.10 respectively.

The surface in Figure E.3 is considerably corroded and is covered in numerous pits, which can be identified by the large clouds of corrosion product (white dots). However, the remainder of the surface is covered in far more numerous shallow pits. These shallow pits appear as clusters of small corrosion product clouds over the majority of the surface and are particularly visible in Figure F.8 b. The large pits are surrounded by large areas of mudcracking, which shows a large build-up of corrosion product has deposited around this site. Small intermetallics are visible in Figure F.8 and appear not to influence the corrosion.

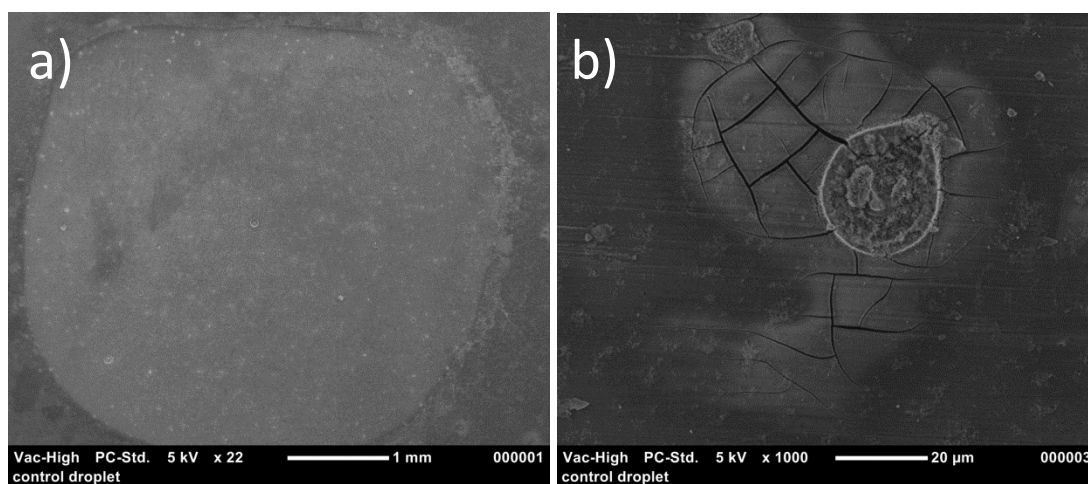


Figure F. 8 – SEM images of AZ31 exposed to a 5 μL droplet of 0.01 M NaCl for 24 hours at 80-90 %R.H. a) the entire droplet (lighter area) b) corrosion product over a large pit surrounded by mud-cracking of magnesium hydroxide/oxide.

With the addition of 1.2 $\times 10^{-4}$ M IL the number of large pits over the surface is essentially the same as when there is no IL present. However, the amount of corrosion over the surrounding areas appears to be significantly decreased. Figure F.8 b) and F.9 b) have very similar magnifications (1000x vs. 1100x) and the large pits in each appear essentially identical. Both have large clouds of corrosion product and are surrounded by mud-cracked corrosion deposition. However, whilst many small clouds of discrete corrosion product are visible in Figure F.8 b), very few examples of these are visible in Figure F.9 b). This suggests that the degree of corrosion is less when 1.2 $\times 10^{-4}$ M of IL is present.

The level of corrosion on the surface exposed to 6.4 $\times 10^{-4}$ M IL in 0.01 M NaCl sits in between the 1.2 $\times 10^{-4}$ M surface and the control. There appears to be fewer large pits on the surface but over the matrix the shallow pits are still present (indicated by the little tufts of corrosion product). Interestingly, over other regions of the droplet the surface looks similar to 100 ppm, in that the shallow pitting is not obvious (Figure F.10 c).

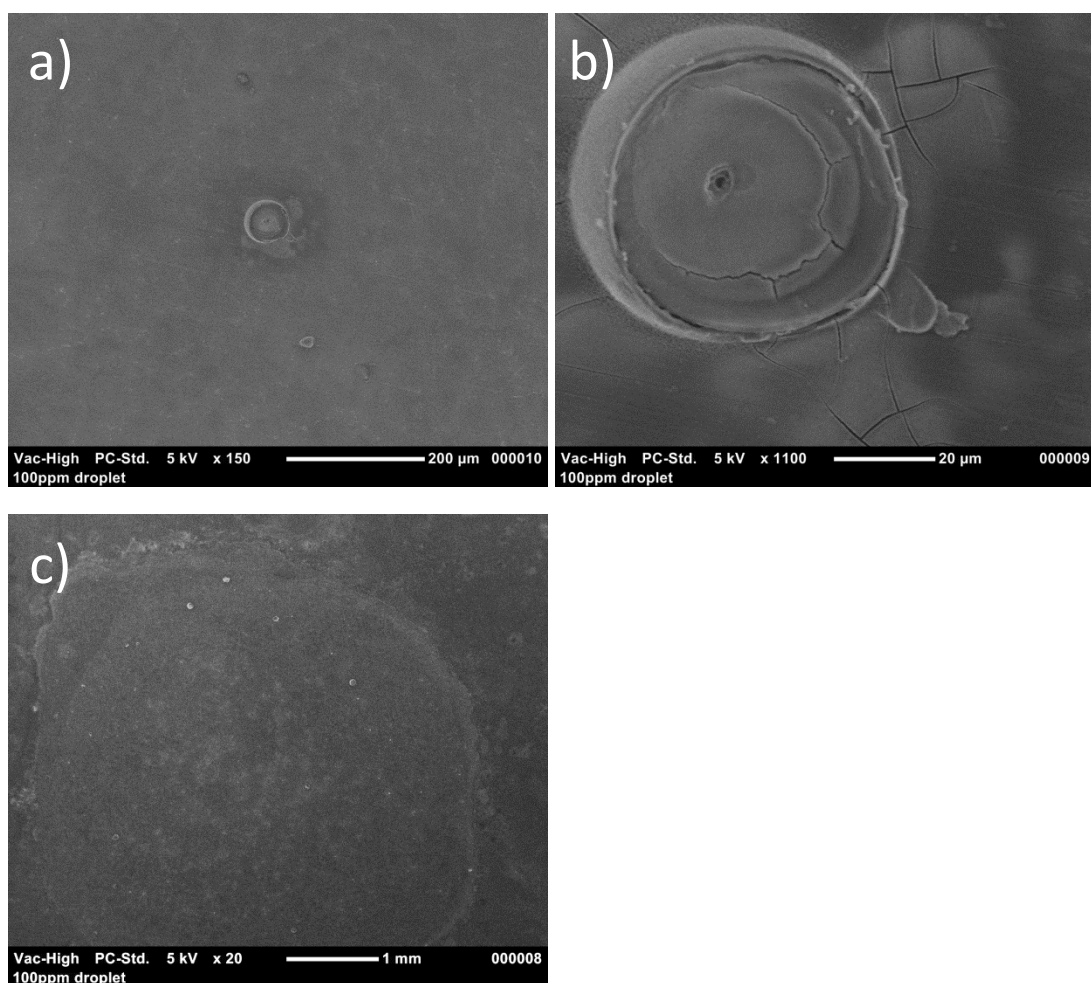


Figure F. 9 - SEM images of AZ31 exposed to a 5 μL droplet of 0.01 M NaCl containing 1.2×10^{-4} M $[\text{P}_{6,6,6,14}][(\text{C}_8)_2\text{PO}_2]$ for 24 hours at 80-90 %R.H. a) a large pit and surrounding area b) zoomed in image of corrosion product over the large pit, surrounded by mud-cracking of magnesium hydroxide/oxide.

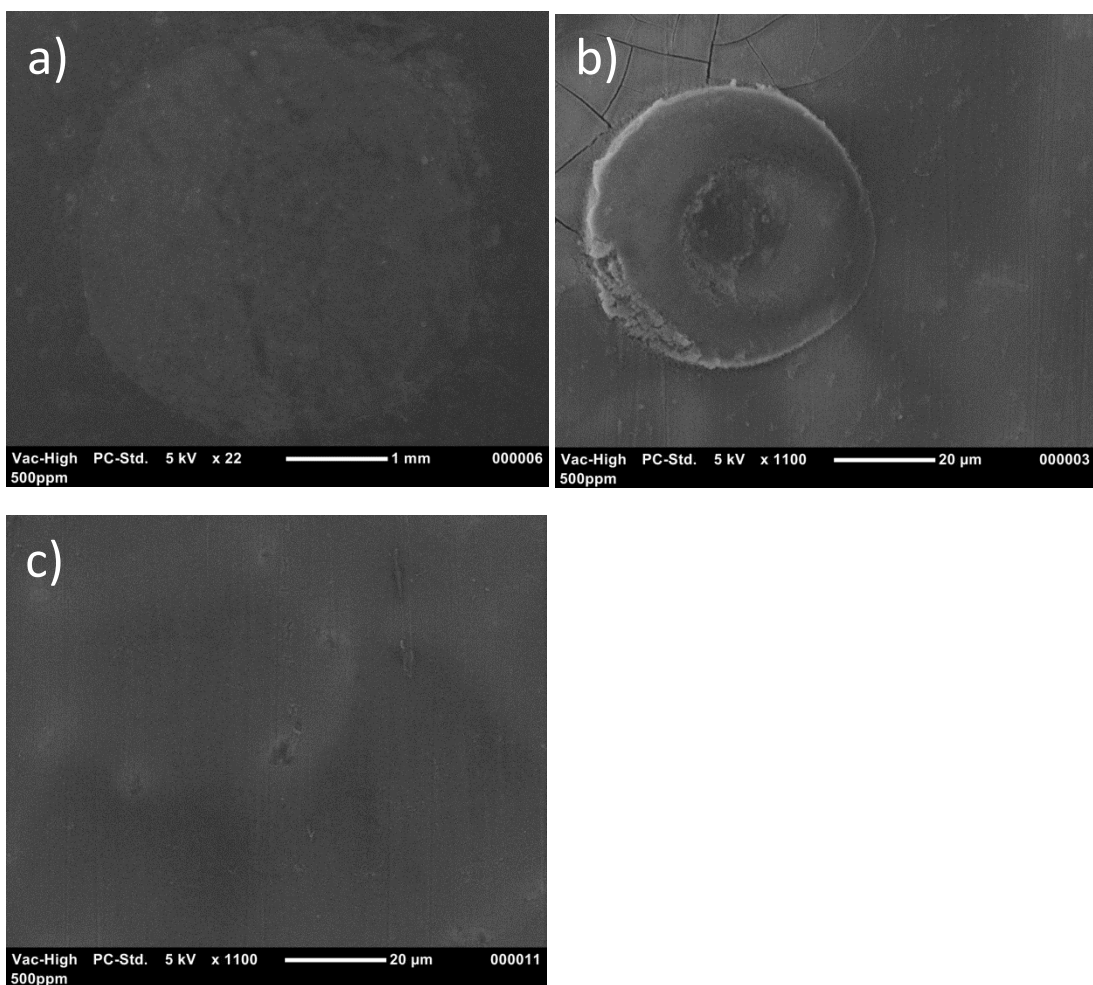


Figure F. 10 - SEM images of AZ31 exposed to a 5 μL droplet of 0.01 M NaCl containing 6.4×10^{-4} M $[P_{6,6,6,14}][iC_8)_2PO_2]$ for 24 hours at 80-90 %R.H. a) a large pit and surrounding area b) zoomed in image of corrosion product over the large pit, surrounded by mud-cracking of magnesium hydroxide/oxide.

Appendix G: ICP Analysis Results

Sample 1: As received Cytec [P_{6,6,6,14}][(C₈)₂PO₂]

Sample 2: Purified [P_{6,6,6,14}][(C₈)₂PO₂]

Table G. 1 - impurities between as received Cytec IL and purified IL. (1mL IL: 1000mL solution)

Laboratory Identification		243213	243214	243215	243216	243217	243218	243213d	243213r	243214s	ics
Sample Identification		1	2	3	4	5	6	QC	QC	QC	QC
Depth (m)		--	--	--	--	--	--	--	--	--	--
Sampling Date recorded on COC		15/12/09	15/12/09	15/12/09	15/12/09	15/12/09	15/12/09	--	--	--	--
Laboratory Extraction (Preparation) Date		24/12/09	24/12/09	24/12/09	24/12/09	24/12/09	24/12/09	24/12/09	--	24/12/09	24/12/09
Laboratory Analysis Date		30/12/09	30/12/09	30/12/09	30/12/09	30/12/09	30/12/09	30/12/09	--	30/12/09	24/12/09
Method : E022.1/E030.1											
Unfiltered metals		EQL									
Arsenic	5	*<25	<5	<5	<5	<5	<5	*<25	--	98%	75%
Cadmium	0.5	*<0.25	<0.5	<0.5	<0.5	<0.5	<0.5	*<0.25	--	94%	103%
Copper	5	*<25	<5	7	6	6	14	*<25	--	104%	93%
Lead	5	*<25	<5	<5	<5	<5	<5	*<25	--	103%	123%
Manganese	5	*<25	<5	7	9	8	92	*<25	--	106%	82%
Zinc	5	*<25	9	5	<5	5	6	*<25	--	99%	112%

Results expressed in ug/l unless otherwise specified

Laboratory Identification		mb								
Sample Identification		QC								
Depth (m)		--								
Sampling Date recorded on COC		--								
Laboratory Extraction (Preparation) Date		24/12/09								
Laboratory Analysis Date		24/12/09								
Method : E022.1/E030.1										
Unfiltered metals		EQL								
Arsenic	5	<5								
Cadmium	0.5	<0.5								
Copper	5	<5								
Lead	5	<5								
Manganese	5	<5								
Zinc	5	<5								

Laboratory Identification		243213	243214	243215	243216	243217	243218	243213d	243213r		
Sample Identification		1	2	3	4	5	6	QC	QC		
Depth (m)		--	--	--	--	--	--	--	--		
Sampling Date recorded on COC		15/12/09	15/12/09	15/12/09	15/12/09	15/12/09	15/12/09	--	--		
Laboratory Extraction (Preparation) Date		23/12/09	23/12/09	23/12/09	23/12/09	23/12/09	23/12/09	23/12/09	--		
Laboratory Analysis Date		23/12/09	23/12/09	23/12/09	23/12/09	23/12/09	23/12/09	23/12/09	--		
Method : E018.1											
pH in water		EQL									
pH (pH units)	0.1	7.9	7.6	4.3	4.2	3.6	4.5	7.9	0%		

Results expressed in pH units unless otherwise specified

Laboratory Identification		243213	243214	243215	243216	243217	243218	243213d	243213r	243214s	ics
Sample Identification		1	2	3	4	5	6	QC	QC	QC	QC
Depth (m)		--	--	--	--	--	--	--	--	--	--
Sampling Date recorded on COC		15/12/09	15/12/09	15/12/09	15/12/09	15/12/09	15/12/09	--	--	--	--
Laboratory Extraction (Preparation) Date		23/12/09	23/12/09	23/12/09	23/12/09	23/12/09	23/12/09	23/12/09	--	23/12/09	23/12/09
Laboratory Analysis Date		23/12/09	23/12/09	23/12/09	23/12/09	23/12/09	23/12/09	23/12/09	--	23/12/09	23/12/09
Method : E033.1/E045.1/E047.1											
Chloride		EQL									
Chloride	1	1	2	*<5	*<5	*<5	1	1	0%	114%	103%

Results expressed in mg/l unless otherwise specified

Laboratory Identification		mb								
Sample Identification		QC								
Depth (m)		--								
Sampling Date recorded on COC		--								
Laboratory Extraction (Preparation) Date		23/12/09								
Laboratory Analysis Date		23/12/09								
Method : E033.1/E045.1/E047.1										
Chloride		EQL								
Chloride	1	<1								

Results expressed in mg/l unless otherwise specified

Laboratory Identification		243213	243214	243215	243216	243217	243218	243213d	243213r	243214s	ics
Sample Identification		1	2	3	4	5	6	QC	QC	QC	QC
Depth (m)		--	--	--	--	--	--	--	--	--	--
Sampling Date recorded on COC		15/12/09	15/12/09	15/12/09	15/12/09	15/12/09	15/12/09	--	--	--	--
Laboratory Extraction (Preparation) Date		23/12/09	23/12/09	23/12/09	23/12/09	23/12/09	23/12/09	23/12/09	--	23/12/09	23/12/09
Laboratory Analysis Date		23/12/09	23/12/09	23/12/09	23/12/09	23/12/09	23/12/09	23/12/09	--	23/12/09	23/12/09
Method : E034.1/E045.1											
Fluoride		EQL									
Fluoride	0.1	*<0.5	*<0.5	*<0.5	*<0.5	*<0.5	*<0.5	*<0.5	--	100%	98%

Results expressed in mg/l unless otherwise specified

Laboratory Identification		mb								
Sample Identification		QC								
Depth (m)		--								
Sampling Date recorded on COC		--								
Laboratory Extraction (Preparation) Date		23/12/09								
Laboratory Analysis Date		23/12/09								
Method : E034.1/E045.1										
Fluoride	EQL 0.1	<0.1								

Results expressed in mg/l unless otherwise specified

Laboratory Identification		243213	243214	243215	243216	243217	243218	243213d	243213r	243214s	ics
Sample Identification		1	2	3	4	5	6	QC	QC	QC	QC
Depth (m)		--	--	--	--	--	--	--	--	--	--
Sampling Date recorded on COC		15/12/09	15/12/09	15/12/09	15/12/09	15/12/09	15/12/09	--	--	--	--
Laboratory Extraction (Preparation) Date		24/12/09	24/12/09	24/12/09	24/12/09	24/12/09	24/12/09	24/12/09	--	24/12/09	24/12/09
Laboratory Analysis Date		29/12/09	29/12/09	29/12/09	29/12/09	29/12/09	29/12/09	29/12/09	--	29/12/09	29/12/09
Method : E020.1/E030.1											
Unfiltered metals		EQL									
Iron	0.05	*<0.25	<0.05	<0.05	<0.05	<0.05	0.30	*<0.25	--	101%	101%
Phosphorus	0.1	7.0	1.1	148	95.5	72.2	0.7	8.4	18%	105%	100%
Silicon	1	*<5	<1	<1	<1	<1	<1	*<5	--	100%	101%

Results expressed in mg/l unless otherwise specified

Appendix H: Pt Pseudo Metal Reference Internal Referencing and Stability

Due to the use of a pseudo Pt metal reference electrode throughout the research presented in this thesis, ferrocene and cobaltocenium were used to internally reference the Pt metal.

Figure H.1 shows the CV conducted in the IL using GC as the working electrode with ferrocene as the internal reference. The region of the CV where the ferrocene peaks should appear is highlighted in the inset of Figure H.1. In the inset the peaks we expect to see from the oxidation and reduction of ferrocene (Sigma Aldrich 98% purity) are not present. The electrochemical window of the IL is smaller than the potential for the oxidation of ferrocene and as a result the reactions of the ferrocene are buried in the reaction of the IL.

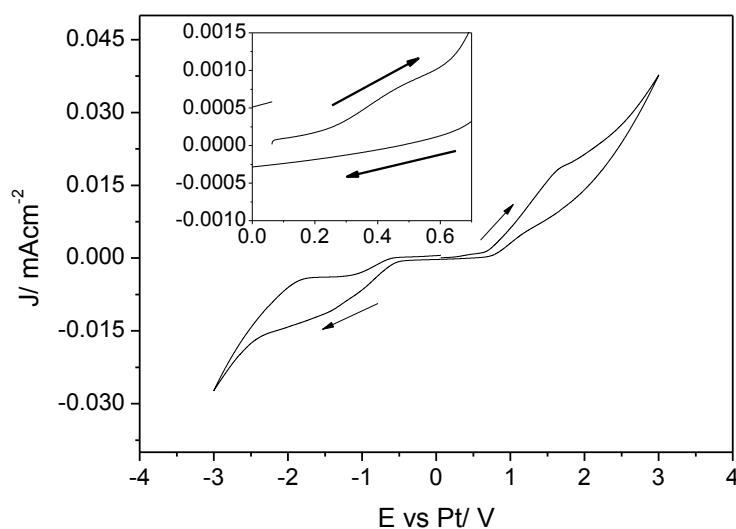


Figure H. 1 – Cyclic voltammetry of $[P_{6,6,6,14}][(C_8)_2PO_2]$ on glassy carbon with the addition of 5 mM ferrocene. Scanned from OCP \rightarrow 3 V \rightarrow -3 V. Inset is zoomed portion of the curve.

Cobaltocenium (bis(cyclopentadienyl)cobalt(III) hexafluorophosphate – Sigma Aldrich 96% purity) was also tried as an internal reference and the cyclic voltammogram is shown in Figure H.2. In this case the reduction of the compound could be identified (arrow 1); however the reactivity of the IL solution causes this reaction to be irreversible. Therefore the potential cannot be used to act as an internal reference.

Whilst the exact potential at which reactions are occurring cannot be compared to other systems, the Pt metal pseudo reference is able to hold a relatively stable potential in the IL so long as it is immersed for over 48 hours. The IL appears to react with the fresh IL to form a passive film on the surface which stabilises the potential of the metal (Figure H.3).

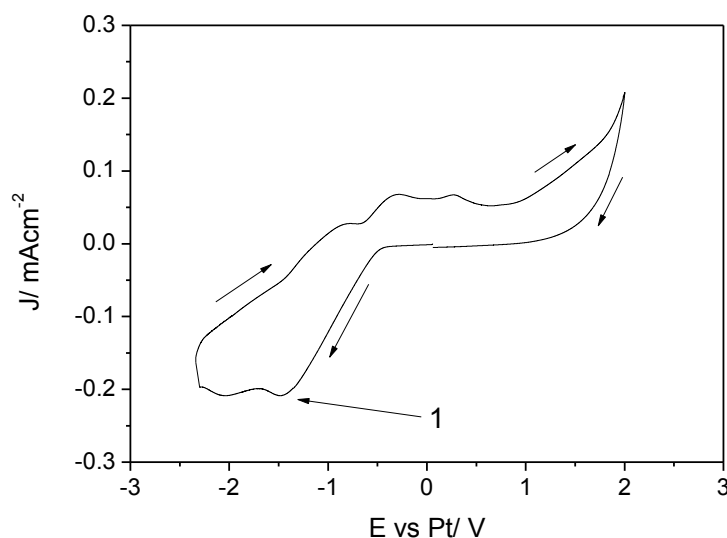


Figure H. 2 - Cyclic voltammetry of $[P_{6,6,6,14}][C_8)_2PO_2]$ on glassy carbon with the addition of 10 mM cobaltocenium. Scanned from OCP \rightarrow -2.5 V \rightarrow 2.5 V.

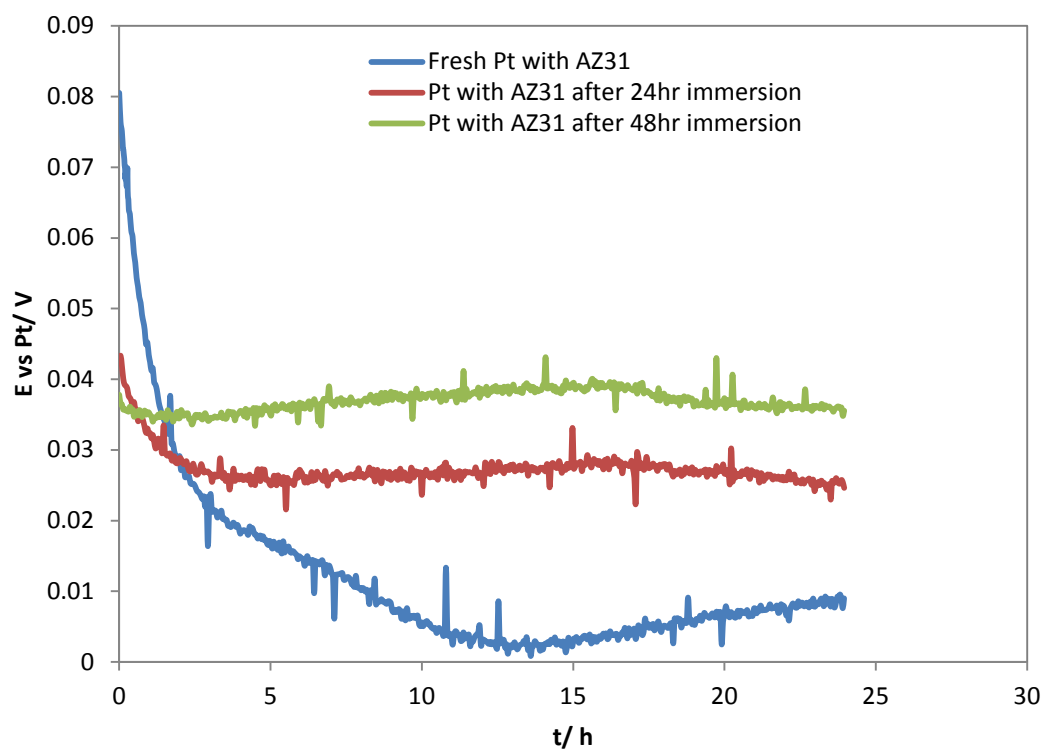


Figure H. 3 – Open Circuit Potential vs. time curves for Pt reference electrode immersed in $[P_{6,6,6,14}][(C_8)_2PO_2]$ IL. “After 24hrs” and “After 48hrs” refer to electrodes stored in IL prior to this test for 24 and 48 hours respectively. “Fresh Pt” refers to Pt polished just prior to the test.